THÈSE

Pour obtenir le grade de

DOCTEUR DE L'UNIVERSITÉ GRENOBLE ALPES

École doctorale : EEATS - Electronique, Electrotechnique, Automatique, Traitement du Signal
Spécialité : Nano électronique et Nano technologies
Unité de recherche : Laboratoire des Technologies de la Microélectronique

Développement du Dopage Compensatoire au Cu et d'une Filière d'Intégration de Nanofils de ZnO pour des Nano-générateurs Piézoélectriques de Haute Performance

Development of the Cu Compensatory Doping and Integration Process of ZnO Nanowires for High-Performance Piezoelectric Nanogenerators

Présentée par :

Manuel MANRIQUE REYES

Direction de thèse :

Bassem SALEM Directeur de recherche au CNRS, CNRS	Directeur de thèse
Vincent CONSONNI DIRECTEUR DE RECHERCHE, CNRS	Co-directeur de thèse
Gwenaël LE RHUN Ingénieur chercheur HDR, CEA-Leti	Co-encadrant de thèse

Rapporteurs :

Sylvain BOLLAERT
PROFESSEUR DES UNIVERSITES, Université de Lille
Guylaine POULIN-VITTRANT
DIRECTRICE DE RECHERCHE, CNRS CENTRE LIMOUSIN POITOU-CHARENTES

Thèse soutenue publiquement le **5 décembre 2024**, devant le jury composé de :

Lionel PETIT, PROFESSEUR DES UNIVERSITES, INSA Lyon	Président
Bassem SALEM, DIRECTEUR DE RECHERCHE, CNRS DELEGATION ALPES	Directeur de thèse
Vincent CONSONNI, DIRECTEUR DE RECHERCHE, CNRS DELEGATION ALPES	Co-directeur de thèse
Sylvain BOLLAERT, PROFESSEUR DES UNIVERSITES, Université de Lille	Rapporteur
Guylaine POULIN-VITTRANT, DIRECTRICE DE RECHERCHE, CNRS CENTRE LIMOUSIN POITOU-CHARENTES	Rapporteure
Skandar BASROUR, PROFESSEUR DES UNIVERSITES, Université Grenoble Alpes	Examinateur

Invités :

Gwenael LE RHUN
INGENIEUR DE RECHERCHE, CEA
Gustavo ARDILA
MAITRE DE CONFERENCES, UGA

“Persevera hasta tu último aliento, porque es en el esfuerzo continuo donde se revela la verdadera fe.”

(Apóstol Santiago el Mayor)

“Persevere until your last breath, for it is in continuous effort that true faith is revealed.”

(Apostle James the Great)

Acknowledgments

The following pages represent three years of experimental research, a work that would not have been possible without the unconditional support of my thesis supervisors: Vincent CONSONNI, Bassem SALEM, and Gwenaël LE RHUN, to whom I will be forever grateful. You gave me the opportunity to grow scientifically through your expertise, guidance, and, above all, immense patience. Thank you for always accompanying me on this adventure filled with challenges and rewarding experiences.

I would also like to express my gratitude to the jury members, Sylvain BOLLAERT and Guylaine POULIN-VITTRANT as reviewers, and Lionel PETIT, Skandar BASROUR, and Gustavo ARDILA as examiners, for dedicating their time to evaluating this thesis. Their constructive feedback has helped improve the content of this manuscript and has raised valuable questions worthy of further exploration.

I also extend my gratitude to the members of my CSI, Gustavo ARDILA, and Ahmad BSIESY, for their trust in the successful development of this thesis and for their favorable advice over these three years.

This thesis has also extensively benefited from the invaluable technical support of Isabelle GELARD (LMGP), Hervé ROUSSEL (LMGP), Laetitia RAPENNE (LMGP), Sébastien LABAU (LTM), Sébastien CAVALAGLIO (LTM), Catherine PUDDA (CEA), Dominique LAURO (CEA), Jouhaiz ROUCHOU (CEA), Thierry FARJOT (CEA), Fabrice PERRIN (CEA), Fabrice DONATINI (Institut Néel), Fabrice WILHELM (ESRF), Véronique JACOB (IUT1 Chimie), Anthony VELLA (IUT1 Chimie), and Gustavo ARDILA (CROMA), for which I am deeply grateful.

I would like to express my sincere appreciation to the NNS team at LMGP: Eirini, Estelle, José, Guislain, Alexandre, Adrien, Quang Chieu, Lisa, Marielena, Émilien, Andy and Ilyas, and the members of the PROSPECT division at LTM: Sarah, Mohammed, Liliane, Aymen, Badreddine, Hala, and Riadh. This enriching collaboration has enabled the dissemination of our work within the scientific community.

I am also immensely grateful to my family, bound by strong ties of friendship: Antonio, Vanessa, Paula, Alejandra, Antonella, Fiorella, Juan Manuel, Camila, Sofia, Furhan, Zeineb, Ramzi, and Malika. You lightened the burden of this journey by sharing your joy.

These words are dedicated exclusively to you, Nazareth CARIGGA, for making my dreams your own, standing by my side through every challenge without hesitation. I will be eternally

grateful for your emotional support and love. This 2025 is your year, and I eagerly await the moment when all your sacrifices and dedication are rightfully rewarded. It will be a moment to celebrate with our little cats, Lomita and Yukita, who bring us into a world full of laughter.

Finalmente, siento un profundo e incontenible deseo de expresar mi más sincero agradecimiento a mi familia por su apoyo incondicional desde el día en que llegué a este mundo. Por ello, dedico este trabajo a estas personas tan especiales: Marcos, Dalila, Miguel, Marco Antonio, María Jesús, Yoel, Milene, Nataly, Américo Miranda, Isabel Reyes, Victoria Reyes, Rosario Manrique, Manuel Manrique y Flor Manrique. ¡Que Dios los bendiga siempre!

Contents

Acknowledgments **2**
Contents **4**
Nomenclature **5**
Introduction – The promising of piezoelectric nanogenerators for self-powered devices **7**
Abstract **10**
Résumé **11**
Chapter I – Piezoelectric Nanogenerators based on ZnO nanowire arrays **14**
I.1 Piezoelectricity – An overview 16
I.2 ZnO nanowires – An overview 24
I.3 Piezoelectric nanogenerators based on nanowires 36
I.4 ZnO nanowires grown by chemical bath deposition 45
Bibliography 57
Chapter II – Cu-doping and thermal annealing of ZnO nanowires grown by chemical bath deposition for piezoelectric applications **67**
II.1 State-of-the-art: strategies for extrinsic doping of ZnO nanowires in Chemical Bath Deposition – theoretical and experimental approaches 69
II.2 Cu-doping of ZnO nanowires grown by Chemical Bath Deposition – adsorption and incorporation mechanisms 71
II.3 Effect of thermal annealing treatment in Cu-doped ZnO nanowires 93
II.4 In-depth discussion of Cu-doping and thermal annealing effects on the optical and electrical properties of ZnO nanowires 104
II.5 Enhancing the output voltage of piezoelectric nanogenerators based on ZnO nanowire matrix through Cu-doping and thermal annealing 107
II.6 Conclusion 120
Bibliography 121
Chapter III – Investigation of nanocomposites based on ZnO nanowire/Parylene-C/Al_2O_3 to enhance the performance of piezoelectric nanogenerators **128**
III.1 State-of-the-art: impact of polymer thickness and surface passivation on the performance of ZnO nanowire-based piezoelectric nanogenerators 130
III.2 Influence of parylene-C top layer thickness on the output voltage of piezoelectric nanogenerators 134
III.3 Effect of Al_2O_3 shell layers on the surface defects of ZnO nanowires grown by chemical bath deposition 145
III.4 Enhancing the performance of piezoelectric nanogenerators based on ZnO nanowire matrix with Al_2O_3 shell passivation layers 154
III.5 Conclusion 169
Bibliography 170
Chapter IV – Synthesis of ZnO nanowires on Au and AZO seed layers for piezoelectric applications **175**
IV.1 State-of-the-art: electrical interface and morphology of ZnO nanowires for piezoelectric nanogenerators 177
IV.2 Effect of AZO seed layers on the morphological properties of ZnO nanowires for piezoelectric applications 182
IV.3 Effect of Au seed layers on the morphological and structural properties of ZnO nanowires for piezoelectric applications 196
IV.4 Conclusion 205
Bibliography 206
IV.5 Supporting information 208
General conclusion and perspectives **212**

Nomenclature

Acronyms/Abbreviation

AM	Additional Mode
AFM	Atomic Force Microscopy
ANR	Agence Nationale de la Recherche
AZO	Aluminum-doped Zinc Oxide
CBD	Chemical Bath Deposition
CBM	Conduction Band Minimum
CEA	Commissariat à l'énergie atomique et aux énergies alternatives
CMTC	Consortium des Moyens Technologiques Communs
CROMA	Centre de Radiofréquences, Optique et Micro-nanoélectronique des Alpes
DAP	Donor-acceptor Pair
DFT	Density-functional theory
DLE	Deep Level Emission
DOS	Density Of States
EDS	Energy Dispersive X-ray Spectroscopy
ESRF	European Synchrotron Radiation Facility
FA	Free electron-to-acceptor
FEM	Finite Element Method
FESEM	Field-emission Scanning Electron Microscopy
FWHM	Full Width at Half Maximum
HMTA	Hexamethylenetetramine
HRTEM	High-Resolution Transmission Electron Microscopy
LETI	Laboratoire d'électronique et de technologie de l'information
LGEF	Laboratoire de Génie Electrique et Ferroélectricité
LING	Laterally Integrated Nanogenerator
LMGP	Laboratoire des Matériaux et du Génie Physique
LTM	Laboratoire des Technologies de la Microeléctronique
MEA	Monoethanolamine
MOCVD	Metalorganic Chemical Vapor Deposition
NBE	Near-band Edge

NW	Nanowire
NW/μm²	Nanowire per μm² (density)
PDMS	Polydimethylsiloxane
PFM	Piezoresponse Force Microscopy
PNG	Piezoelectric NanoGenerator
PMMA	Polymethyl Methacrylate
PTA	Plateforme Technologique Avancée
PVD	Physical Vapor Deposition
PZC	Point-of-zero-charge
STEM	Scanning Transmission Electron Microscopy
TEM	Transmission Electron Microscopy
TES	Two-electron Satellite
VBM	Valence Band Maximum
VING	Vertically Integrated Nanogenerator
XANES	X-ray absorption near-edge spectroscopy
XLD	X-ray Linear Dichroism
XRD	X-ray Diffraction
ZPL	Zero Phonon Line

Introduction – The promising of piezoelectric nanogenerators for self-powered devices

Over the last decades, the development of the Internet of Things (IoT) - a term introduced in 1999 by Kevin Ashton from Procter & Gamble, which defines the IoT as the network connecting physical objects ("things") with digital technologies, schematic languages, and virtual identities to share information[1] – has transformed the society into a smart city, revolutionizing healthcare, agriculture, informatics, and everyday life.[2,3] However, the rise of the IoT necessitates large-scale sensor networks or systems with numerous sensor nodes that require wireless, sustainable, and independent operation.[4]

The development of Wireless Sensor Networks (WSNs) enhances the efficiency of the IoT. As these networks become miniaturized, their reduced power consumption makes the conventional use of batteries as a power source less suitable due to issues of cost, reliability, and sustainability. This has led to increased interest in ambient energy harvesting as an alternative power supplier for WSNs.

Among various energy harvesting technologies, piezoelectric nanogenerators (PNGs) have emerged as a viable option for converting omnipresent mechanical energy from vibrations, human motion, and fluid flow into electrical energy. Although PNGs have potential applications in self-powered systems and active sensors for human motion monitoring, biomedical uses, environmental monitoring, and artificial intelligence, their generated low-power density requires further research and improved strategies.[4,5]

Recent advancements in nanotechnology have shown that the use of piezoelectric nanowires (NWs) significantly improves the performance of PNGs.[6] These NWs, due to their unique structural properties, exhibit increased piezoelectric coefficients and reduced dielectric constants, leading to higher energy conversion efficiencies.

Zinc oxide (ZnO), an abundant, biocompatible, and cost-effective material, has become notable for piezoelectric applications since its first integration into a PNG in 2006 by Z. Wang and J. Song.[7] Since then, piezoelectric composites involving ZnO NWs embedded within a dielectric matrix have attracted attention due to their scalable, low-temperature manufacturing potential. However, the piezoelectric performance of these composites is highly dependent on the electrical and morphological properties of each component.

This thesis examines the piezoelectric response of PNGs incorporating a ZnO NW-based nanocomposite, with ZnO NWs grown through chemical bath deposition (CBD). Although CBD is a green chemistry process that allows ZnO NW growth at low temperatures, defects incorporated during synthesis result in a high density of free carriers. These carriers cause screening effects that degrade the overall performance of the PNG. Therefore, the focus of this work is on achieving electrically resistive ZnO NWs suitable for integration into a PNG, while also addressing issues such as electrode interfaces and the properties of the embedding polymer. This thesis explores distinct strategies to boost the piezoelectric response of these devices, detailed in the following chapters.

This work continues the research initiated by Dr. Clément LAUSECKER, who pursued his PhD at the LMGP, LTM, and CEA Leti between 2018 and 2021. His studies focused on the synthesis and integration of ZnO NWs for fabricating PNGs, addressing topics such as developing a copper (Cu) doping strategy for ZnO NWs via CBD, synthesizing of ZnO NWs on gold (Au) layers through CBD, and advancing a technological process for fabricating PNGs based on vertically integrated ZnO NW-based nanocomposites.

This thesis presents three years of work in four chapters.

Chapter I provides a detailed state-of-the-art of PNGs based on NWs, particularly ZnO NWs. It starts with the theoretical background on piezoelectricity and a general overview of piezoelectric materials. Then, the chapter discusses the advantages of ZnO NWs for piezoelectric applications and evaluates the NW-based PNG performance, justifying the PNG structure chosen for this thesis, and providing strategies to enhance this device. The chapter concludes with a description of the ZnO NW synthesis by the CBD method, highlighting the origin of the main issue to overcome: the screening effect caused by the high density of free carriers in these nanostructures.

Chapter II investigates achieving resistive ZnO NWs through compensatory Cu-doping and thermal annealing processes. The chapter provides an in-depth exploration of how Cu is incorporated into ZnO NWs coupled with thermal annealing. The incorporation mechanisms and effects are examined using lab-scale characterization techniques (electronic microscopy, 5 K cathodoluminescence spectroscopy, two-point probe electrical measurements, etc.) and X-ray Absorption Spectroscopy at the European Synchrotron Radiation Facility (ESRF). The chapter concludes with the characterization of PNGs integrating Cu-doped and thermally annealed ZnO NWs.

Chapter III explores modifying the surface properties of ZnO NWs with a dielectric coating layer to improve the PNG performance. The chapter investigates the optimal thickness of a parylene-C layer embedding the ZnO NWs into a PNG *via* piezoelectric characterizations. Furthermore, PNGs integrating ZnO/Al_2O_3 core-shell heterostructures coated with the optimized parylene-C layer are studied, showing promising results.

Chapter IV examines the morphological properties of ZnO NWs grown by CBD on Aluminum-doped ZnO (AZO) and Au seed layers, which should serve as the bottom electrode of a PNG for creating, respectively, Ohmic and Schottky interfaces with the ZnO NWs. The chapter explores the selective area growth (SAG) method for controlling ZnO NWs growth on AZO layers, and presents characterizations of a PNG based on an Au film acting as a seed layer and bottom electrode, revealing unexplored mechanical effects on the device's output voltage.

This thesis, supported by a LabEx MINOS funding from the UGA – France, took place at the LMGP, LTM, and CEA Leti laboratories, with additional support from collaborators such as PTA and CMTC technological platforms, CROMA (formerly IMEP-LaHC), Institut Néel, ESRF, and IUT 1 Chimie – UGA.

[1] F. H. Cabrini, F. V. Filho, P. Rito, A. B. Filho, S. Sargento, A. V. Neto, S. T. Kofuji, *Sensors* **2021**, *21*, 1–19.

[2] A. Zanella, N. Bui, A. Castellani, L. Vangelista, M. Zorzi, *IEEE Internet Things J.* **2014**, *1*, 22–32.

[3] I. Izadgoshasb, *Sensors* **2021**, *21*, 8332.

[4] X. Cao, Y. Xiong, J. Sun, X. Zhu, Q. Sun, Z. L. Wang, *Adv. Funct. Mater.* **2021**, *31*, 1–31.

[5] K. K. Das, B. Basu, P. Maiti, A. K. Dubey, *Acta Biomater.* **2023**, *171*, 85–113.

[6] B. Zaarour, L. Zhu, C. Huang, X. Jin, H. Alghafari, J. Fang, T. Lin, *J. Ind. Text.* **2021**, *51*, 297–340.

[7] Z. L. Wang, J. Song, *Science (80-.).* **2006**, *312*, 242–246.

Abstract

Since the development of the first Zinc Oxide Nanowire (ZnO NW) based piezoelectric nanogenerator (PNG) by Z. Wang and J. Song in 2006,[1] the ability of ZnO NWs to convert mechanical energy into electrical energy has been demonstrated, revolutionizing the field of energy harvesting. Nowadays, ZnO NW arrays are integrated into electronic devices, offering efficient and sustainable energy sources that are particularly well-suited to Internet-of-Things (IoT) applications.

This thesis focuses on enhancing the performance of PNGs based on vertically integrated ZnO NW arrays grown in an aqueous medium by chemical bath deposition (CBD). The latter, a green chemistry-compatible process, offers potential industrial viability at a large scale for the growth of ZnO NWs at low temperatures (60 – 100 °C) on flexible and rigid substrates. However, the unintentional formation of mainly hydrogen-related defects in CBD-grown ZnO NWs results in a high density of free electrons in their bulk ($5 \times 10^{17} – 1.5 \times 10^{19}$ cm^{-3}),[2] leading to the detrimental screening effect of piezoelectric potential. This screening effect originates from electrostatic interactions between free electrons and the positive poles created within bent ZnO NWs.[3]

This thesis explores distinct approaches for boosting the energy conversion efficiency of PNGs based on ZnO NWs grown by CBD. The first strategy involves developing electrically resistive ZnO NWs through compensatory Cu-doping and thermal annealing processes, followed by their integration into PNGs to evaluate their piezoelectric properties. The second approach modifies the surface properties of ZnO NWs by coating them with Alumina (Al_2O_3) shell and parylene-C layers, assessing their effects on piezoelectric properties through PNG characterizations. Finally, the thesis examines the synthesis of ZnO NWs on Aluminum-doped ZnO and gold seed layers, aiming to create, respectively, Ohmic and Schottky interfaces with ZnO NWs for piezoelectric applications.

This fully experimental work provides promising ways to enhance ZnO NW-based PNGs, offering potential possibilities for sustainable energy harvesting applications.

[1] Z. L. Wang, J. Song, *Science (80-.).* **2006**, *312*, 242–246.

[2] A. J. L. Lopez Garcia, M. Mouis, V. Consonni, G. Ardila, *Nanomaterials* **2021**, *11*, 941.

[3] R. K. Pandey, J. Dutta, S. Brahma, B. Rao, C. P. Liu, *JPhys Mater.* **2021**, *4*, DOI 10.1088/2515-7639/ac130a.

Résumé

Depuis le développement du premier nanogénérateur piézoélectrique (PNG) à base de nanofils d'oxyde de zinc (ZnO) par Z. Wang et J. Song en 2006,[1] la capacité des nanofils de ZnO à convertir l'énergie mécanique en énergie électrique a été démontrée, révolutionnant ainsi le domaine de la récupération d'énergie. Actuellement, les réseaux de nanofils de ZnO sont intégrés dans des dispositifs électroniques, offrant des sources d'énergie durables et performantes, particulièrement adaptées aux applications de l'Internet des objets.

Ce travail de thèse vise à améliorer les performances d'un PNG intégrant verticalement un réseau de nanofils de ZnO, lesquels sont synthétisés en milieu aqueux par dépôt en bain chimique (CBD). Ce dernier, un procédé compatible avec la chimie verte, présente un potentiel industriel pour la croissance des nanofils de ZnO à basse température (60 – 100 °C) à grande échelle sur des substrats flexibles et rigides. Cependant, l'incorporation non intentionnée de défauts principalement liés à l'hydrogène pendant le CBD, mène à une densité élevée d'électrons libres ($5 \times 10^{17} – 1.5 \times 10^{19}$ cm^{-3}) dans les NFs de ZnO,[2] provoquant un effet d'écrantage indésirable du potentiel piézoélectrique. Cet effet résulte des interactions électrostatiques entre les électrons libres et les pôles positifs générés dans les nanofils de ZnO sous sollicitations mécaniques.[3]

Cette thèse explore différentes approches pour optimiser l'efficacité de conversion énergétique des PNGs à base de nanofils de ZnO synthétisés par CBD. La première stratégie aborde l'élaboration de nanofils de ZnO électriquement résistifs via un dopage compensatoire au cuivre (Cu) et recuits thermiques, suivi de leur intégration dans des PNGs afin d'évaluer leurs propriétés piézoélectriques. La deuxième approche consiste à modifier les propriétés de surface des nanofils de ZnO en les revêtant d'une coquille en alumine (Al_2O_3) et de couches de parylène-C. Leurs effets sur les performances piézoélectriques sont étudiés à travers des caractérisations des PNGs. Enfin, cette thèse examine la synthèse de nanofils de ZnO sur des couches de nucléation d'or et de ZnO dopé à l'aluminium (AZO), afin de créer respectivement une interface Schottky et ohmique avec les nanofils de ZnO, pour des applications piézoélectriques.

Cette étude expérimentale ouvre des perspectives prometteuses pour améliorer les PNGs à base de nanofils de ZnO, offrant ainsi des solutions intéressantes pour des applications durables de récupération d'énergie.

The page was intentionally left blank.

The page was intentionally left blank.

Chapter I – Piezoelectric Nanogenerators based on ZnO nanowire arrays

Content

I.1 Piezoelectricity – An overview 16
I.1.1 Principle of piezoelectricity 16
I.1.2 Piezoelectric phenomenon (equations) 18
I.1.3 Piezoelectric materials 20
I.1.3.1 Ceramics 20
I.1.3.2 Crystals 21
I.1.3.3 Polymers 22
I.1.3.4 Composites 22
I.2 ZnO nanowires – An overview 24
I.2.1 Properties of ZnO nanowires 24
I.2.1.1 Structural properties 24
I.2.1.2 Semiconducting properties 26
I.2.1.2.1 Electronic properties 26
I.2.1.2.2 Native point defects 27
I.2.1.2.3 Electrical properties 30
I.2.1.3 Dielectric, mechanical, and piezoelectric properties 32
I.2.2 Detrimental piezoelectric screening effect in ZnO nanowires 34
I.3 Piezoelectric nanogenerators based on nanowires 36
I.3.1 Laterally Integrated NanoGenerator 37
I.3.2 Vertically Integrated NanoGenerator 39
I.3.3 Strategies to enhance the performance of a ZnO nanowire-based piezoelectric nanogenerator 41
I.3.3.1 Doping 41
I.3.3.2 Areal density 42
I.3.3.3 Surface engineering 43
I.3.3.4 Interfacial modification 44
I.4 ZnO nanowires grown by chemical bath deposition 45
I.4.1 Chemical bath deposition 45
I.4.1.1 Principle of chemical bath deposition 45
I.4.1.2 Chemical reactions in chemical bath deposition 46
I.4.2 Nucleation mechanism and morphological control of ZnO nanowires grown by chemical bath deposition 48
I.4.2.1 Spontaneous growth 49
I.4.2.2 Selective area growth 51
I.4.3 Extrinsic point defects in ZnO nanowires grown by chemical bath deposition 52
I.4.3.1 Unintentional doping of ZnO nanowires 52
I.4.3.1.1 Hydrogen-related defects 53
I.4.3.1.2 Nitrogen-related defects 53
I.4.3.2 Intentional doping of ZnO nanowires 54
Bibliography 57

This chapter provides the background knowledge to understand the working principle and fabrication of piezoelectric nanogenerators based on nanowires as building blocks. Mathematical formulations are provided to explain the piezoelectricity, as well as a brief discussion of piezoelectric materials. The structural and semiconducting properties of ZnO in the form of nanowires (NW) are particularly discussed in detail due to their multifunctional coupling to piezoelectric applications. At last, the growth of ZnO NWs by the chemical bath deposition (CBD), the method used throughout this thesis, is exhaustively presented, illustrating the problems to overcome for the development of an optimal piezoelectric device.

I.1 Piezoelectricity – An overview

The term piezoelectricity comes from two Greek words: “piezein”, which means press or squeeze, and “electron”, referring to static electricity. Thus, etymologically, “piezoelectricity” refers to “electricity originated from press”. This phenomenon was observed for the first time by the brothers Curie in 1880. They observed the accumulation of positive and negative charges in the surfaces of quartz crystals compressed in specific directions.[1] The reverse piezoelectric effect, i.e. the appearance of a compression in the piezoelectric crystal under electrical polarization, was predicted by Gabriel Lippmann months later the piezoelectricity discovery,[2] and was experimentally proven by the brothers Curie.[3] Through the contributions of different researchers, particularly W. Voigt, the thermodynamic equations explaining piezoelectricity were established around 1910.[4,5] This contributed to the development of the first piezoelectric application before 1921, such as sonar for submarine detection and oscillators with quartz crystals.[6,7] Researches focused on piezoelectricity rapidly created interest in industrial market, having shown the possibility of inventing man-made piezoelectric materials. Nowadays, the development of new performing piezoelectric materials is being investigated for distinct applications in medicine, military, energy, information, etc.

I.1.1 Principle of piezoelectricity

The piezoelectric effect involves the interaction between the mechanical and electrical properties of a material. According to the excitation of this material, two distinct effects occur, named direct or reverse piezoelectric effect. **Figure I.1-1(a-b)** illustrates the difference between both effects. Direct piezoelectricity refers to the generation of electric charges in response to external mechanical stress, which leads to a positive or negative electric voltage depending on the deformation direction. In contrast, the reverse piezoelectric effect refers to the mechanical deformation of a piezoelectric crystal under electrical polarization. Both effects can be explained by a simple molecular model based on the structural features of a material,[8] which can be centrosymmetric or non-centrosymmetric.

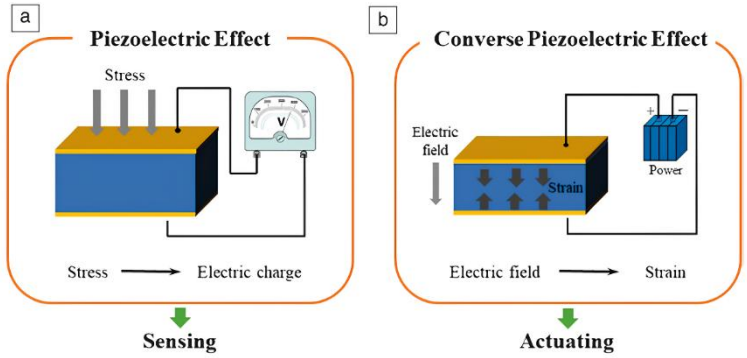

Figure I.1-1. (a) *Direct and* ***(b)*** *reverse piezoelectric effect. Adapted from REF [9].*

Figure I.1-2 depicts the electrical polarization induced in both types of materials under mechanical stress. At the beginning state, i.e. without mechanical deformation, the center of positive and negative charges coincides in the primitive unit cell of both types of materials, leading to a null total dipole moment ($\Sigma p_i=0$). When an external force is applied, the positively- and negatively-charged center always coincides in the centrosymmetric crystal, leading to a zero net polarization (P=0) inside its structure, and consequently, no piezoelectric effect is observed in this non-polar material. In contrast, a non-centrosymmetric crystal exhibits a no-zero total dipole moment in its primitive unit cell under external force, leading to a net non-zero polarization. This piezoelectric polarization arises in non-centrosymmetric and polar materials.

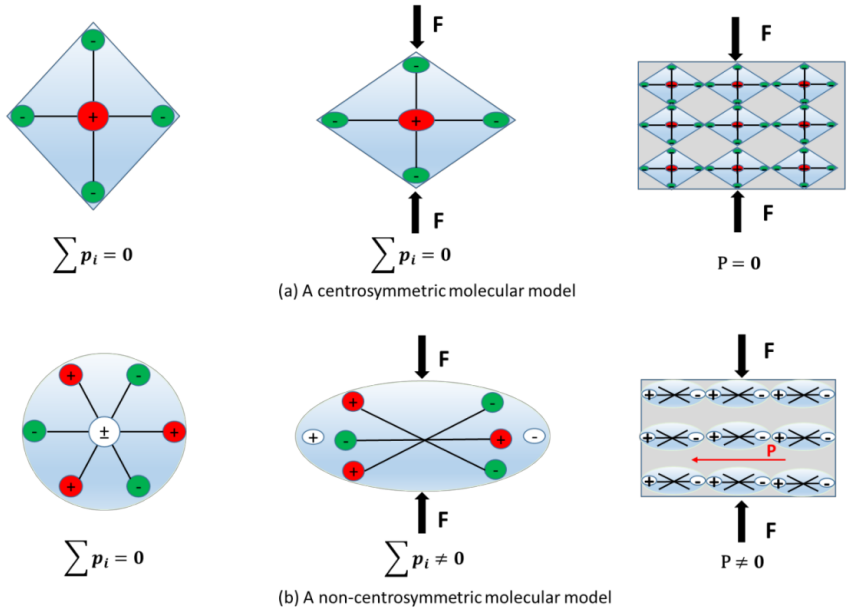

Figure I.1-2. *Molecular model of* ***(a)*** *centrosymmetric and* ***(b)*** *non-centrosymmetric materials under mechanical stress. Adapted from REF [10].*

I.1.2 Piezoelectric phenomenon (equations)

According to the Institute of Electrical and Electronics Engineers (IEEE) standard for piezoelectricity,[11] due to the anisotropic properties of piezoelectric materials, they are referenced in an orthogonal system, as illustrated in **Figure I.1-3**. The three axes numbered as 1, 2, and 3 correspond to the conventional *x*, *y*, and *z*-axis, respectively. The piezoelectric polarization in materials is generally chosen along the z-axis. Then, this orthogonal system allows three translation movements along axes 1, 2, and 3, and three rotation movements numbered as 4, 5, and 6 around axes 1, 2, and 3, respectively.

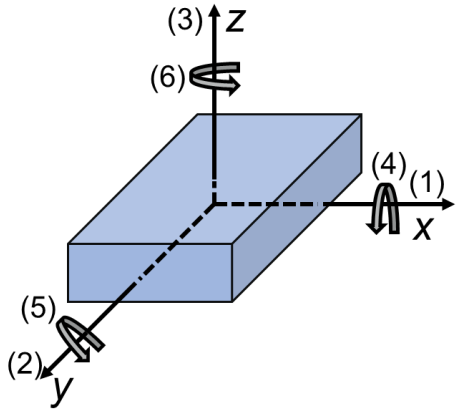

Figure I.1-3. *Orthogonal system to reference piezoelectric materials.*

By considering a linear response of piezoelectric materials at low mechanical and electrical fields, and by coupling Hooke's equations with the electric displacement equation, the direct and reverse piezoelectric effects are expressed in **Equation I.1-1** and **Equation I.1-2**, respectively.[12]

$$D_i = d_{ijk} T_{jk} \qquad \textit{Equation I.1-1}$$

$$S_{jk} = d_{ijk} E_i \qquad \textit{Equation I.1-2}$$

where each term is summarized in **Table I.1-1**. The index i, j, and k refers to the three orthogonal directions 1, 2, and 3.

Table I.1-1. *Mechanical and electrical tensors involved in the mathematical formulation of the piezoelectricity. Adapted from REF [13].*

Category	Term	Meaning	Unit	Dimension
Electrical	D	Electric displacement	C/m²	1st order tensor, 1×3
	E	Electric field	N/C	
Mechanical	T	Stress	N/m²	2nd order tensor, 3×3
	S	Strain		
Piezoelectric	d	Piezoelectric coefficient	C/N	3rd order tensor, 3×3×3

The symmetry of the crystal allows the reduction of the Stress and Strain tensors in 1st order tensors of 1×6 dimension. Similarly, the piezoelectric coefficient is represented as a 2nd-order tensor "d_{ij}", where "*i*" represents the applied field direction (i=1, 2, 3), and "*j*" indicates the direction in which mechanical stress is applied (j=1, 2, 3, 4, 5, 6). For instance, d_{31} indicates the appearance of an electrical polarization along axis 3 when mechanical stress is applied along axis 1. Thus, the thermodynamic formulation explaining the piezoelectricity is defined by 8 equations using the Voigt notation and four piezoelectric constants named *d*, *e*, *g*, and h, presented in **Table I.1-2**.[13]

Table I.1-2. *Thermodynamic equations of piezoelectricity taking into account the crystal symmetry and Voigt notation. $(A)^t$ is the transpose of the tensor A. $(A)^X$ is the tensor A at constant or null X (X=T, S, E, D). Inspired from REF [14].*

	T	S
D	$S = s^D.T + g^t.D$ $E = -g.T + (\varepsilon^{-1})^T.D$	$T = c^D.S + h^t.D$ $E = -h.S + (\varepsilon^{-1})^S.D$
E	$S = s^E.T + d^t.E$ $D = d.T + \varepsilon^T.E$	$T = c^E.S - e^t.E$ $D = e.S + \varepsilon^S.E$

The description of each term and the dimensions involved in the equations of **Table I.1-2** are summarized in **Table I.1-3**.

Table I.1-3. *Terms used in **Table I.1-2**. Inspired from REF [14].*

Category	Term	Meaning	Unit	Dimension
Electrical	D	Electric displacement	C/m^2	1 × 3
	E	Electric field	N/C	
	ε	Permittivity	F/m	3 × 3
Mechanical	T	Stress	N/m^2	1 × 6
	S	Strain		
	c	Elastic stiffness	N/m^2	6 × 6
	s	Elastic compliance	m^2/N	6 × 6
Piezoelectric	d	Piezoelectric constants	C/N	3 × 6
	e		C/m^2	
	g		N^2/C	
	h		N/C	

In this thesis, the piezoelectric coefficient *d* will be referenced frequently, particularly d_{33}. This coefficient represents the electrical displacement along axis 3 when mechanical stress is applied in the same direction. In the case of ZnO, axis 3 refers to its polar direction, i.e. the *c*-axis.

In addition, the efficiency of converting the supplied mechanical energy into recovered electrical energy by a piezoelectric crystal is quantified by the electromechanical coupling coefficient k_{ij}. Then, for practical considerations, k_{33} will be considered, whose mathematical equation involves mechanical and piezoelectric coefficients of the material:[13]

$$k_{33} = \frac{d_{33}}{\sqrt{\varepsilon_{33}^{T} s_{33}^{E}}} \qquad \textit{Equation I.1-3}$$

Where ε_{33}^{T} is the permittivity at constant mechanical stress (T≠ 0), and s_{33}^{E} is the strain coefficient at constant electric field. Therefore, according to **Equation I.1-3**, a material with intrinsic properties such as a high piezoelectric constant, low permittivity, and low strain constants, will provide performant piezoelectric devices. However, depending on the piezoelectric applications, additional factors involving the acoustic impedance, the velocity of longitudinal or shear wave propagation, and the density of the active piezoelectric material also account for the design of performant piezoelectric devices.[15,16]

I.1.3 Piezoelectric materials

In material science, there is a total of 32 crystallographic classes that can be classified according to crystal symmetry: centrosymmetric (11 classes) and non-centrosymmetric (21) classes. As previously seen, solely non-centrosymmetric crystals (20 classes) with a polar axis exhibit piezoelectric properties. The latter can be categorized into natural, such as quartz (SiO_2) and Rochelle salt ($KNaC_4H_4O_6.4H_2O$), and synthetic types. According to Kenji Uchino's work, piezoelectric materials are divided into ceramics, crystals, polymers, and composites.[16]

I.1.3.1 Ceramics

These materials are widely preferred because of their excellent piezoelectric characteristics and simple manufacturing process. Among these, lead zirconate titanate ($PbZr_xTi_{1-x}O3$, PZT) is one of the most commonly used material in industry. PZT, a perovskite of hexagonal symmetry (class 6mm), is found as hard (PZT-4) or soft (PZT-5A, PZT-5H) type, offering a broad range of applications at temperatures lower than 200 °C.[17] Then, the titanate of barium ($BaTiO_3$), widely enhanced since its discovery around 1940's, exhibit piezoelectric properties below 125 °C.[18] Additionally, lead-free ceramics arranged in perovskite structure are also developed by replacing the lead in PZT by other elements, resulting, for instance, in $K_{1/2}Na_{1/2}NbO_3$ (KNN).[19] Recently, by manipulating the morphotropic phase boundary and

introducing local structural heterogeneity, the researchers developed a Sm-modified $0.15Pb(Mg_{1/3}Nb_{2/3})O_3$-$(0.85-x)PbZrO_3$-$xPbTiO_3$ ceramic (named A* in **Table I.1-4**) with the highest piezoelectric and electromechanical coupling coefficients ever recorded for a temperature below 293 °C.[20]

***Table I.1-4**. Piezoelectric properties of selected ceramics. REFs [17–20].*

	PZT-4	PZT-5A	PZT-5H	$BaTiO_3$	KNN	A*
d_{33} (pC/N)	290 – 330	370 – 425	590 – 650	190	200 – 280	720
k_{33}	0.65 – 0.70	0.70 – 0.72	0.75 – 0.78	0.48 – 0.5	-	0.8

I.1.3.2 Crystals

The piezoelectric crystals composed of a single macroscopic crystal often exhibits superior piezoelectric properties compared to ceramics. Quartz (SiO_2), a natural piezoelectric crystal, was the first material to be used, with small piezoelectric-related coefficients for temperatures lower than 573 °C.[12] Around 1949, the discovery of other piezoelectric crystals as lithium niobate ($LiNbO_3$) garnered attention because of its interesting properties below 1140 °C.[21] Nowadays, the perovskite-structured family of lead magnesium niobate doped with lead titanate ($[Pb(Mg_{1/3}Nb_{2/3})O_3]_{(x)}$-$[PbTiO_3]_{(1-x)}$ - (PMN-PT)), and related combinations ($[Pb(I_{1/2}Nb_{1/2})O_3]_{(y)}$-$[Pb(Mg_{1/3}Nb_{2/3})O_3]_{(x)}$-$[PbTiO_3]_{(1-x-y)}$ - (PIN-PMN-PT)) surged as promising piezoelectric materials for application lower than 150 °C.[22] Although single crystals display the highest piezoelectric-related coefficients, their toxicity or high manufacturing costs are factors that require significant attention. In contrast, piezoelectric semiconductors with a wurtzite structure, including III-V group elements (such as GaN, AlN, InN, and BN) and II-VI group elements (such as ZnO and CdS), have earned significant attention from researchers due to their multifunctional properties and the ease of their integration into novel devices at low cost.[23–30] In particular, ZnO, widely used since the beginning of this century, will be described in **Section I.2**, owing to the easy synthesis in distinct form of nanostructures well oriented along a polar axis.[31]

***Table I.1-5.** Piezoelectric properties of selected single crystals. REFs [12,21,22].*

	Quartz	$LiNbO_3$	PMN-PT	PIN-PMN-PT
d_{33} (pC/N)	2.3	7.5	1500 – 2800	2000
k_{33}	0.1	0.56	0.9 – 0.94	0.94

Table I.1-6. *Piezoelectric properties of selected semiconductors. REFs [24,25,28,30,32].*

	GaN	AlN	InN	ZnO	CdS
d_{33} (pC/N)	2.8 – 3.7	5.0 – 6.8	3.5 – 10.1	12.4	-10.3
k_{33}	0.38	0.23 – 0.30	0.31	0.48	0.26

I.1.3.3 Polymers

Piezoelectric polymers are known for their flexibility and ease of manufacturing, ideal for large-area sensors and actuators. The one most used is polyvinylidene fluoride (PVDF), which melts at around 170°C.[33] In addition, by coupling PVDF with trifluoroethylene (PVDF-TrFE), this resulting copolymer enhances their piezoelectric related coefficients below 100 °C.[33] A polymer consisting of a single chlorinated benzene ring, commonly known as parylene-C, becomes a piezoelectric polymer when its structure is crystallized trough a poling process. This process involves applying high electrical field while heating the material at temperatures below 120 °C.[34] Particularly, this polymer will be used in the present thesis because of the ease of deposition providing reliable devices.

Table I.1-7. *Piezoelectric properties of selected polymers. REFs [33,34].*

	PVDF	PVDF-TrFE	Parylene-C
d_{33} (pC/N)	20 – 30	30 – 40	2.1
k_{33}	0.12	0.15	0.02

I.1.3.4 Composites

The composite materials offer significant benefits by combining the high piezoelectric properties of ceramics or single crystals with the flexibility of polymers, all at a controlled volume fraction.[35] According to the arrangement and interconnection of different phases within a composite material, there are 10 dimensional connectivity whose phases are labeled in the form *a*-*b*.[36] **Figure I.1-4** illustrates these connectivity, where *a* refers to the piezoelectric ceramic or crystal (shadow region), and *b* designs the polymer phase (clear phase). Each phase can connect itself along the *x*, *y*, and *z*-direction. For instance, if a phase connects itself along the *x*- and *y*- directions, so *a* (or *b*) equals two. The most common connectivities of piezoelectric composites are the 1-3 (piezoelectric pillars within a polymer matrix), 2-2 (alternate stack of piezoelectric and polymer layers), and 0-3 (piezoelectric particles within a polymer matrix).

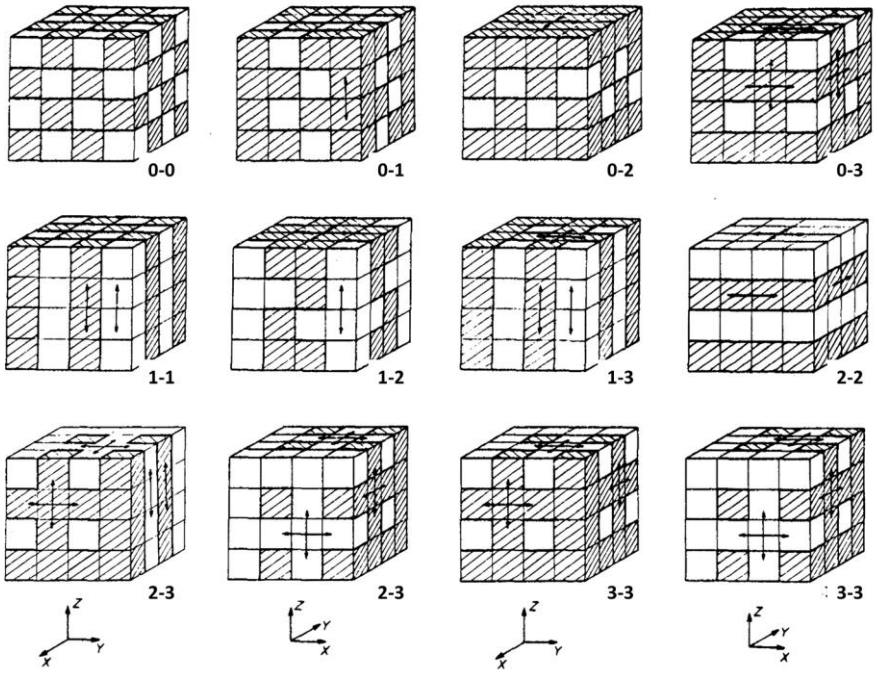

Figure I.1-4. *Schematic of composite's connectivity. Adapted from REF [36].*

As mentioned, the properties of piezoelectric composites depend on the volume fraction of the active phase, connectivity, and mechanical and piezoelectric properties of the crystals, ceramics, and polymers, as illustrated in **Table I.1-8**.

Table I.1-8. *Piezoelectric properties of selected piezocomposites. Adapted from REF [35].*

	PZT-5H		PMN-PT	PMN-PT	PMN-PT
Connectivity	1-3		1-3	2-2	2-2
Volume fraction	0.1	0.51	0.27	0.39	0.4
d_{33} (pC/N)	225	610	521	-	-

It is crucial to mention that, owing to benefit size effects, piezoelectric materials are developed at nanometer scale in the form of thin film (2D), nanorods (1D), or nanoparticles (0D), which enhances their piezoelectric properties and promoting their integration into devices. This size effect benefit will be discussed in detail in **Section I.2.1.3** for ZnO. Additionally, in the following chapters, piezoelectric devices based on nanocomposites with 1-3 connectivity, i.e. ZnO nanowires within a matrix polymer of parylene-C, will be presented.

I.2 ZnO nanowires – An overview

Zinc oxide is a notable II-VI semiconductor due to its wide direct bandgap of 3.37 eV, a relatively high excitation binding energy of 60 meV at room temperature, and good electron mobility.[37,38] These properties render ZnO an interesting material for optoelectronic components in the UV spectral range and as transparent conducting oxides (TCO).[39] Additionally, ZnO can be used as an additive in ceramics, concrete, polymers, cosmetics, food, and paintings.[40]

Owing to the crystallographic structure of ZnO, the latter can be synthesized by vapor phase deposition techniques or wet chemistry techniques.

In the context of this thesis, a comprehensive explanation of fundamental information regarding ZnO will be conducted. This section will therefore include an analysis of its structural, semiconducting, and piezoelectric properties, with a specific focus on ZnO nanowires.

I.2.1 Properties of ZnO nanowires

I.2.1.1 Structural properties

ZnO, found in nature as a zincite mineral, is a crystal with a wurtzite structure. The latter, unlike the zinc-blende and rocksalt crystallographic structures, is the only one thermodynamically stable under ambient conditions.[38] **Figure I.2-1(a)** illustrates the non-centrosymmetric wurtzite structure of ZnO belonging to the space group C_{6v}^4 or $P6_3mc$. This structure consists of alternating hexagonal planes of positively-charged zinc atoms and negatively-charged O atoms along the $\langle 0001 \rangle$ direction, known as the *c*-axis. The unit hexagonal cell of the wurtzite structure is defined by two lattice parameters, *a* and *c*, with a ratio of $\frac{c}{a} = \sqrt{\frac{8}{3}} = 1.633$. In this structure, Zn atoms bond with four O atoms in a tetrahedral coordination, and vice versa. The length of the Zn-O bond along the *c*-axis is measured by the internal parameter u, given as the ratio $u = 3/8 = 0.375$ (in units of *c*), in an ideal wurtzite structure. Therefore, the ideal values for the lattice parameters *a* and *c* are 3.2501 and 5.2071 Å, respectively.[38] However, Zn-O bonds are not equal in all directions; the distances are slightly greater along the *c*-axis. This isotropic bond distance of Zn and O atoms in single tetrahedral coordination arises from disturbances caused by next-nearest neighbors.[38] The

partly ionic and partly covalent bonding character between Zn and O atoms can also account for structural disturbances.[41] Indeed, the ionic-covalent Zn-O bonds with a value of 0.616 on the Phillips♣ scale arises from the difference in electronegativity between zinc (1.65) and oxygen (3.44) on the Pauling scale,[41] which leads to not uniformly charge distributions in the material, resulting in a spontaneous polarization of -0.057 C/m² along the *c*-axis.[28,42] This intrinsic polarization within the crystal affects severely the chemical and physical properties of ZnO.[42–45] Indeed, the $[0001]$ planes (or *c*-planes) exhibit a nonzero charge leading to a nonzero dipole moment (i.e. *c*-polar surfaces), whereas the $[10\bar{1}0]$ and $[11\bar{2}0]$ planes, known as *m*- and *a*-planes, respectively, are electrically neutral, depicting non-polar surfaces, as illustrated in **Figure I.2-1(b)**.

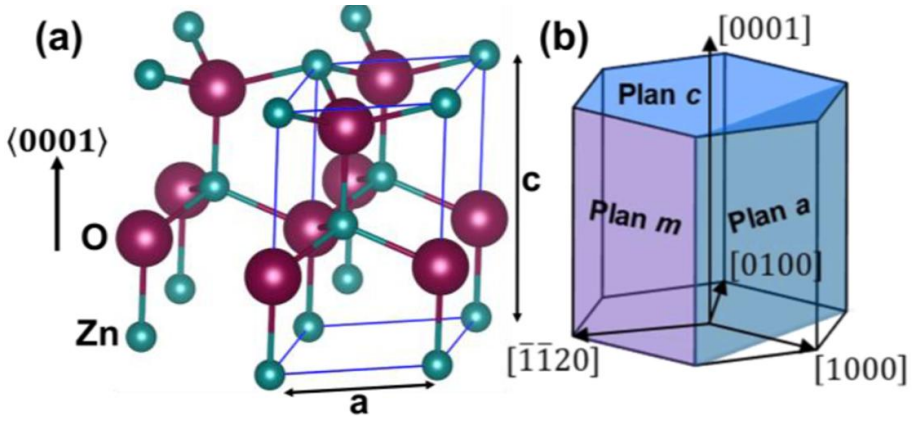

Figure I.2-1. (a) *Wurtzite crystallographic structure of ZnO and* ***(b)*** *related crystalline planes. Adapted from [46].*

The polar character creates an electrostatic instability and leads to a divergence in the surface energy of the planes, as shown in **Table I.2-1**. Thus, *c*-planes, which are more unstable than *m*-planes, form faster than the non-polar planes, favoring the formation, of nanostructures with high aspect ratio such as nanowires.[43–45,47]

Table I.2-1. *Calculated surface energy of different planes of wurtzite ZnO. Adapted from REF [47].*

	$[0001] - Zn$ Polar *c*-plane	$[10\bar{1}0]$ Non-polar *m*-plane	$[11\bar{2}0]$ Non-polar *a*-plane
Surface energy (J/m²)	2.25	1.12	1.06

Moreover, owing to the lack of an inversion center in wurtzite ZnO, the polar *c*-surfaces differ according to the direction $\langle 0001 \rangle$. Thus, two different *c*-polar surfaces arise: Zn-polarity

♣ **Phillips ionicity** quantifies the ionic character degree in a chemical bond by spectroscopic measurements. It's calculated as the ratio of the ionic gap (E_i) to the total energy gap (E). E_i involves solely electrostatic interactions between ions, while E includes both ionic and covalent contributions. Higher Phillips ionicity values indicate stronger ionic bonding.

for $[0001]$-planes, and O-polarity for $[000\bar{1}]$-planes. Zn- and O-polarity exhibit different physical-chemical characteristics and stabilization mechanisms, where Zn-polar surfaces are more reactive than O-polar surfaces in an aqueous medium.[45,48]

I.2.1.2 Semiconducting properties

I.2.1.2.1 Electronic properties

ZnO has a direct band gap of 3.37 eV at room temperature and without mechanical pressure,[49] with a free-exciton binding energy of 60 meV.[37] **Figure I.2-2(a)** illustrates the calculated energy levels that electrons can occupy in ZnO given by the band diagram.[50] Thus, the band gap, referring to the lowest difference in energy between the conduction and valence band, is located at the Γ-point (wave vector $\vec{k} = 0$) in the Brillouin zone, where coincidently the lowest conduction band and the maximum valence band are found.[51] The lowest conduction band is formed by empty 4s states of Zn^{2+} or antibonding♣ sp^3 hybrid states, whereas the maximum valence band originates from occupied 2p orbitals of O^{2-} or bonding sp^3 orbitals.[39] However, due to the hexagonal crystal field and spin-orbit coupling, the valence band splits into three twofold-degenerate bands of symmetries $\Gamma 7$ (A), $\Gamma 9$ (B), and $\Gamma 7$ (C), separated by 4.9 (A-B) and 43.7 (B-C) meV,[39,51] as depicted in **Figure I.2-2(b)**.

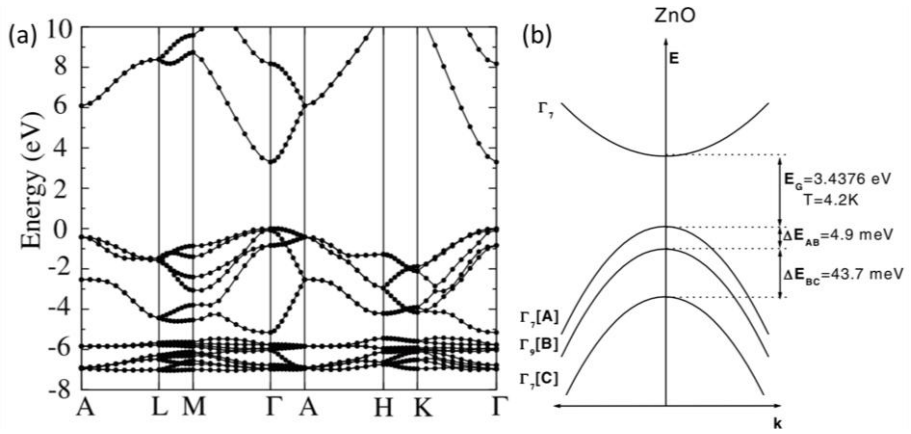

Figure I.2-2. (a) *Band diagram of wurtzite ZnO calculated by density functional theory (DFT). The energy of the valence band maximum was set to zero. Adapted from REF [50].* ***(b)*** *Schematic of the respective electronic band diagram at the Γ-point. Adapted from REF [51].*

It is important to mention that, according to the $\vec{k}.\vec{p}$ theory, a method used to calculate the band structure in solids, the effective mass of electrons and holes influences the

♣ **Antibonding** (*bonding*) sp3 hybrid states refer to the combination of atomic orbitals of zinc and oxygen atoms in the ZnO crystal lattice, where the electrons are more likely to be found between the atoms, weakening (*strengthening*) the chemical bond, responsible for the formation of the conduction (*valence*) band in ZnO.

conduction and valance band energy bending, respectively. Thus, under pressure, the electron in the conduction band is tightly bound to the atom, which increases its effective mass and modifies the conduction band bending, resulting in a band bap with higher energy.[49]

I.2.1.2.2 Native point defects

In a crystalline material, imperfections in its orderly structure of atoms are known as crystallographic defects. These defects are categorized as planar (grain boundaries and stacking faults), line (edge and screw dislocations), and point defects.[52] The latter, referred to as 0-dimensional defects♦, are localized disruptions in the crystal structure. In ZnO, point defects can greatly influence its electrical and optical properties.[50,51] It should to noted that point defects are classified as either intrinsic (or native) or extrinsic (from the introduction of external impurities). The latter will be further detailed in **Section I.4.3**.

Native point defects in ZnO involve imperfections in the crystal structure related solely to Zn and O atoms. There are three types of native defects:[53]

i) Vacancies: these occur when atoms are missing from their regular lattice positions, denoted as V_{Zn} and V_O for Zn- and O-vacancy, respectively.

ii) Interstitials: these are extra atoms occupying spaces between regular lattice positions (interstitial). They are denoted as Zn_i or O_i for interstitial Zn and O, respectively.

iii) Antisites: these arise when a Zn atom occupies an O lattice site or vice versa. They are denoted as X_Y, where *X* represents the misplaced atom and *Y* represents the site it occupies (either Zn or O).

Furthermore, the electrical properties of a defect are determined by its charge state. In semiconductor physics, “donor” defects refer to positively charged defects that “added extra free electrons” to the material, whereas “acceptor” defects are negatively charged defects that “accepted free electrons” through the incorporation of holes. Thus, donor and acceptor defects act as n-type and p-type dopants, respectively. It is worth mentioning that an electrical compensation process between donors and acceptors can occur in the material.

In thermodynamic equilibrium, the concentration of a point defect depends on its formation energy, given by the equation:[50,53,54]

♦ Tec-Science. (n.d.). Crystallographic defects. Retrieved August 29, 2024, from https://www.tec-science.com/material-science/structure-of-metals/crystallographic-defects/

$$c = N_{sites} e^{-\frac{E^f}{k_B T}}$$ ***Equation I.2-4***

where E^f is the formation energy, N_{sites} the number of sites on which the defect can be incorporated (cm^{-3}), k_B the Boltzmann constant, and T the temperature. It is predictable from **Equation I.2-4** that point defects with high formation energy are less likely to be present and, consequently, their concentration will be lower. However, in ZnO, the formation energy of point defects varies with the Fermi level of the crystal, the charge state of the defect, and the chemical potential μ_{Zn} and μ_O determining the abundance of Zn and O atoms, respectively.[50,53] Thus, through DFT calculations, the formation energies of native point defects in ZnO are determined as a function of the Fermi level in **Figure I.2-3(a-b)**. As previously mentioned, the formation energies differ according to the Zn- and O-rich conditions. For instance, in Zn-rich conditions, the low abundance of oxygen atoms leads higher probability of forming V_o (low formation energy), while the excess of Zn atoms could increase the probability of forming Zn_i. In contrast, in O-rich conditions, following the same reasoning, the low abundance of Zn atoms results in a high probability of forming V_{Zn}, whereas the excess of oxygen atoms would favor the formation of O_i as well as O_{Zn}.

The Fermi level, an important parameter to calculate the energy formation of point defects previously discussed, represents a reservoir for electron exchange which ensures the charge neutrality of the system.[54] When ZnO is grown in a chemical solution, the Fermi level can be modified by changing the O or H partial pressure, the pH value, or by applying a bias voltage.[55] Particularly, by increasing the pH, the chemical potential of H decreases, which in turn increases the Fermi level of the chemical growth solution, indicating the likely control in the formation of point defects.

Figure I.2-3(c) depicts the Fermi level at which charge state transitions occur for defects in ZnO, i.e. the energy required to remove or add an electron to the native defect. Thus, donor defects are classified as “shallow” or “deep” based on how close their charge state transitions are to the conduction band. Shallow donor defects have energy transitions near the conduction band, suggesting that these defects can ionize at room temperature. In contrast, deep donors usually require thermal activation for ionization because their energy transitions are distant from the conduction band. Similarly, shallow and deep acceptor defects are distinguished, respectively, by their energy transitions near and far from the valence band. Therefore, for a defect to be spontaneously electrically active in the crystal, it must

simultaneously exhibit low formation energy and shallow energy transitions, which would conduct the electric behavior of ZnO.

ZnO is widely recognized for its inherent n-type electrical conductivity, which has been extensively studied.[38,50,56–58] It should be noted that, according to the diagram of thermodynamic transition levels shown in **Figure I.2-3(c)**, the native defects do not appear to have a major role in the conductivity of ZnO in its natural state. For instance, Zn_i and Zn_O are shallow donors, but their high formation energy makes them thermodynamically unstable. In contrast, V_o, while having low formation energy, acts as a deep donor due to its level transition, meaning it is not ionized at room temperature and can compensate for p-type doping. Similar behavior is expected for acceptor defects: both O_i and O_{Zn} are deep acceptors with high formation energy, while Zn_i is a deep acceptor with low formation energy and can also compensate for n-type doping.

Thus, the n-type conductivity in ZnO is mainly related to extrinsic defects involving hydrogen atoms. Additionally, the intentional incorporation of dopants other than H also contributes to the electrical behavior of ZnO. This will be discussed further in **Section I.4.3**, focusing on ZnO nanowires grown by chemical bath deposition.

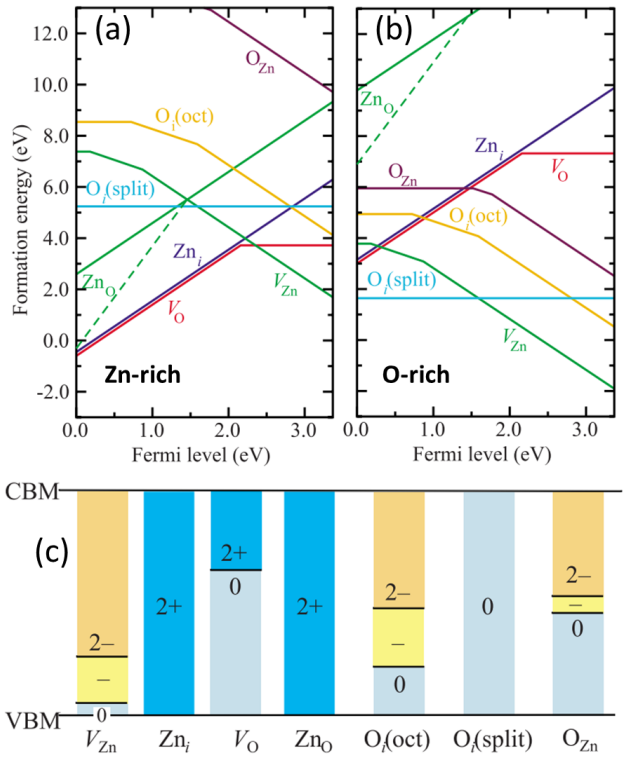

Figure I.2-3. *Formation energies of native point defects as a function of the Fermi level in ZnO for* ***(a)*** *Zn-rich and* ***(b)*** *O-rich conditions. The zero of the Fermi level corresponds to the valence band maximum.* ***(c)*** *Thermodynamic transition levels for defects in ZnO. Adapted from REF [53].*

I.2.1.1.2.3 Electrical properties

ZnO is characterized by its n-type electrical conductivity,[38,50,56–58] which is significant for various applications. It is worth mentioning that p-type conductivity in ZnO does not exist owing to the high compensation mechanism induced by n-type defects.[39,50] In addition, the growth method and morphology of ZnO severely affect its electrical behavior, notably its free carrier concentration and electrical mobility. Indeed, bulk ZnO samples synthesized by seeded-chemical-vapor transport (CVT), high-pressure melt (HPM), and hydrothermal (HYD) methods exhibit different Hall electron mobility,[59] as presented in **Figure I.2-4(a)**. These differences arise from different scattering interactions specific to each sample. In addition, at room temperature, the mobility of intrinsic ZnO samples can lie between 350 – 400 cm^2/Vs, which is dominated by polar-optical phonon scattering interaction, according to mobility calculations.[59,60] The morphology of the material also plays a role in the electrical behavior of ZnO, as depicted in **Figure I.2-4(b)**. The presence of extended defects within the structure and the surface roughness affect the mobility of ZnO differently depending on its dimensions.[61,62] Furthermore, the conventional Hall measurement method could not be adapted for 1D ZnO nanostructures.[62] Consequently, optional techniques such as terahertz spectroscopy, electromechanical impedance spectroscopy, etc., are used to study the electrical properties of NWs. Particularly, the integration of single 1D ZnO nanostructures into field effect transistor (FET) devices has advanced significantly for assessing their electrical properties.[63] In these devices, ZnO is typically contacted by two electrodes to measure its resistivity, free carrier concentration, and mobility. The electrical properties of ZnO 1D nanostructures can be also studied through 4-point or 2-point probe electrical measurements, where ZnO requires at least 4 or 2 electrodes, respectively.

Given that this thesis will present the resistivity values of single ZnO NWs assessed by 2-point probes, for illustrative purposes, **Table I.2-2** depicts the resistivity reported by different techniques of ZnO NWs grown by different methods.

For practical reasons, this thesis will compare our resistivity result with those reported in ZnO NWs assessed by 4-point probes measurements in Chapter 2.

The resistivity is calculated under the hypothesis of bulk-like conduction in a flat-band regime in the NW.[64]

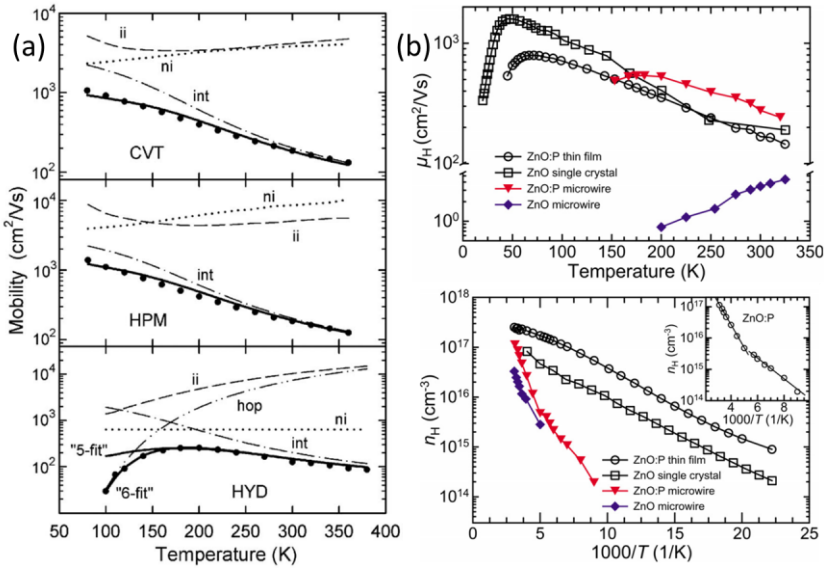

Figure I.2-4. (a) *Hall electron mobility* vs *temperature of bulk ZnO grown by different methods. Scattering interactions related to ionized impurity (ii), neutral impurity (ni), and hopping (hop) are calculated. Adapted from REF [59].* ***(b)*** *Hall mobility and carrier concentration of single crystal, thin film, and microwire ZnO. Adapted from REF [62].*

Table I.2-2*. Resistivity, mobility, and free carrier density of ZnO NWs grown by carbothermal reduction (CR), chemical vapor deposition (CVD), thermal evaporation (TE), electrodeposition (ED), metal-organic CVD (MOCVD), chemical bath deposition (CBD), vapor-phase (VP), and Hydrothermal (HT) investigated by FET, Fourier transform infrared reflectance (FTIR) spectroscopy, electrochemical impedance spectroscopy (EIS), scanning spreading resistance microscopy (SSRM), electron holography (EH), terahertz time-domain spectroscopy (THz-TDS), scanning capacitance microscopy (SCM), longitudinal optical phonon-plasmon (LPP) fit, and 4-point probe method. CBD (Zn), CBD (O), CBD refer to ZnO NWs grown by CBD having Zn-, O-, or unknown polarity, respectively.*

	Resistivity (mΩ.cm)	Mobility ($cm^2/V/s$)	Free carrier concentration (cm^{-3})	Measurement method	REF
CR	0.2 – 2	13 ± 5	$(5.2 \pm 2.5) \times 10^{17}$	FET	[65]
CVD	-	30.22 – 5.41	-	FET	[66]
	-	39 - 60	$(0.12 - 1.1) \times 10^{18}$	FET	[67]
TE	0.15 – 0.29	-	-	4-point probes	[68]
	-	65.5 – 88.2	$(0.75 – 1.3) \times 10^{18}$	FET	[69]
ED	-	23	10^{20}	FTIR	[70]
	-	-	6.2×10^{19}	EIS	[71]
	-	-	8×10^{19}	EIS	[72]
MOCVD	60	100	$(1 – 5) \times 10^{18}$	4-point probes	[64]
	-	-	$(1 – 3) \times 10^{18}$	SSRM	[73]
	-	-	$(1 – 2) \times 10^{18}$	EH	[74]
CBD (Zn)	0.11		$(0.54 – 1.1) \times 10^{19}$	4-point probes	[75]
CBD (O)	0.98		$(0.64 – 1.3) \times 10^{18}$	4-point probes	[75]
CBD	-	138	2.0×10^{16}	THz-TDS	[76]
	-	-	$(0.5 – 2) \times 10^{18}$	SCM	[77]
	4.1 – 28.4	-	$(0.27 – 3.1) \times 10^{19}$	4-point probes	[78]
	-	31.3	1.2×10^{18}	LPP	[79]
VP	25 - 3000	-	$(0.03 – 6) \times 10^{18}$	4-point probes	[80]
HT	18 – 450	-	$(0.2 – 6) \times 10^{18}$	4-point probes	[80]

I.2.1.3 Dielectric, mechanical, and piezoelectric properties

The nanostructuring of ZnO enhances its properties for piezoelectric applications through surface-related effects. Yang et al. showed, through scanning conductance microscopy (SCM) measurements, that the dielectric constant ε (in units of the permittivity of free space $\varepsilon_0 = 8.85 \times 10^{-12}$ F/m), which indicates a material's ability to store electrical energy, decreases from 6.4 to 2.7 as the diameter of ZnO NWs decreases from 285 nm to 85 nm, significantly lower than the reported 8.6 for bulk ZnO,[81] as presented in **Figure I.2-5(a)**. This reduction in dielectric constant is explained by a core-shell composite nanowire model: the nanowire has a core with a high dielectric constant surrounded by a shell layer with a low dielectric constant due to a depletion in carriers. Then, as the diameter decreases, the influence of the shell layer becomes more significant, reducing the NW's dielectric constant.[81]

Surface effects also impact Young's modulus of ZnO according to the diameter dimension of the NW, as illustrated in **Figure I.2-5(b)**. Micromechanical measurements have shown that as the NW diameter decreases from 80 to 20 nm, Young's modulus of ZnO increases from 140 to 160 GPa.[82] This increase is attributed to surface reconstruction and long-range ionic interactions. Surface reconstruction, which is the rearrangement of atoms at the surface to more stable positions due to lack of bonding with other atoms, reduces the NW's volume,[83] leading to surfaces stiffer than the bulk. Long-range ionic interactions also contribute to this effect by inducing high compressive stress in surface atoms, resulting in higher Young's modulus.[82] Surface effects are not significant in ZnO NWs with diameters larger than 100 nm, exhibiting a bulk-like behavior with Young's modulus of 140 GPa. Interestingly, molecular dynamics simulations suggest that Young's modulus could further increase from 170 to 195 GPa as the diameter is reduced from 20 to 5 nm.

ZnO nanowires have been found to exhibit higher piezoelectric properties compared to other ZnO nanostructures, as presented in **Table I.2-3**.[84] This was firstly supported by Zhao's work, where the piezoelectric coefficient of ZnO nanobelts was measured by PFM and found to be frequency-dependent, ranging from 14.3 to 26.7 pm/V, significantly higher than the reported 9.93 pm/V of bulk ZnO, as depicted in **Figure I.2-5(c)**.[85] Zhao suggested that this piezoelectric enhancement is due to the nanobelt's perfect single-crystallinity, freedom of dislocation, and the potential influence of size effects. Additionally, Ghosh et al. suggested that the enhancement of piezoelectric response as well as its dependency on frequency could

be attributed to V_{Zn} and V_o defects in ZnO, which lead to a discontinuity in the organization of crystallographic plans along the *c*-axis, generating magnetic moments induced by unpaired neighboring O atoms, which induces reversible electric dipoles and enhances the piezoelectric coefficients.[86] Li et al. found through PFM measurements that by decreasing the diameter of micropillars from 7 µm to 1.5 µm, the piezoelectric coefficient increases from 18.2 to 46.9 pm/V.[83] This is attributed to the rearrangement of atoms at the surface, reducing the overall volume of the NW, and consequently enhancing the polarization per unit volume leading to higher piezoelectric coefficients. Hoang et al. also demonstrated, through first-principles calculations, that by decreasing the diameter of ZnO NW from 4 to 1 nm, residual stress appears at the NW surface, leading to increasing piezoelectric coefficients from 2 to 8 C/m².[87] These dimensions are, however, too difficult to obtain experimentally.

Therefore, according to previous works, ZnO NWs are highly suitable for integration into piezoelectric-related devices, due to their enhanced dielectric and piezoelectric properties enhancing the electromechanical coupling coefficient k_{33}, as described in **Equation I.1-3**.

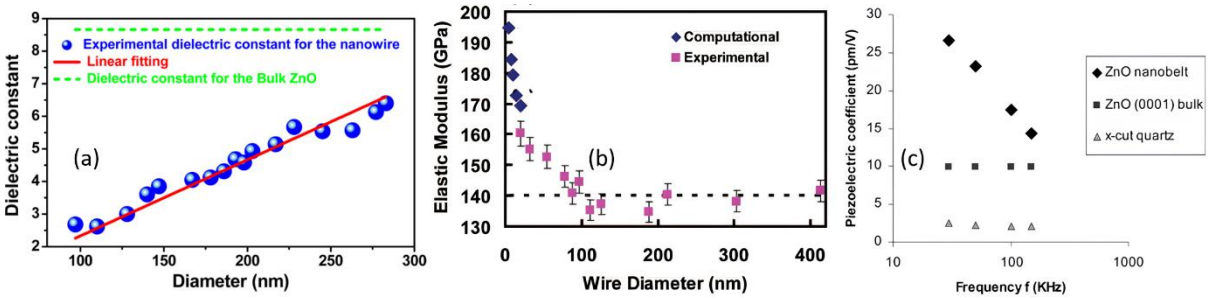

Figure I.2-5. (a) *Dielectric constant,* ***(b)*** *Young's Modulus, and* ***(c)*** *piezoelectric coefficient of ZnO NWs. Adapted from REFs [81], [82], and [85], respectively.*

Table I.2-3. *Piezoelectric coefficient d_{33} for pure ZnO nanostructures. Adapted from [84].*

	d_{33} (pm/V)	Dimensions	Measurement method
ZnO bulk	12.4	♣	♣
Film	5 – 5.3	Thickness 285 – 710 nm	AFM/PFM
Nanosheet	6.48 – 18.9	Thick 1.5 – 4.5 nm Triangular side length ~8 µm	AFM
Nanobelt	14.3 – 26.7	Diameter 65 – 360 nm Length: tens of µm	PFM
Nanowire	0.4 – 49.7	Diameter: 20 – 500nm Length: 0.4 – 2.4 µm	AFM/PFM

♣ Dimension and measurement method not specified. The paper only mention "conventional techniques" to measure the d_{33} coefficient. (DOI: 10.1109/PROC.1968.6246)

I.2.2 Detrimental piezoelectric screening effect in ZnO nanowires

When mechanical stress is applied to ZnO, it generates a piezopotential with positive and negative poles within its structure. The screening effect occurs when this piezopotential is reduced or "screened" by the migration of free electrons towards the positive pole within the structure of ZnO,[88,89] whose magnitude is directly correlated with the density of free charge carriers.

Several studies have explored this effect in single ZnO NWs. Gao et al. simulated the behavior of free charges in bent ZnO NWs with varying doping levels between 0.6 and 2.0 $\times 10^{17}$ cm^{-3}, showing that the compressive side is fully depleted due to negative voltage, while the tensile side is partially screened by free electrons.[90] Similarly, Araneo et al. demonstrated that laterally bent ZnO NWs (in form of cylinder) experience a decrease in piezopotential as doping levels increase from 1×10^{14} to 1×10^{18} cm^{-3}, while conical NWs (low diameter) maintain higher piezopotential even at high donor concentrations (1×10^{16} cm^{-3}).[91] Romano et al. further observed that vertically compressed NWs show reduced piezopotential with increasing donor concentration from 1×10^{16} to 5×10^{17} cm^{-3}, while the influence of dielectric materials, like PMMA, is negligible at higher doping levels (1×10^{16} cm^{-3}).[92]

Moreover, Tian et al. explored how the screening effect affects ZnO NW arrays integrated in a device.[88] Its simulations illustrated that piezopotential decreases with increasing carrier concentration, as free electrons screen the piezopotential and degrade the device performance, as illustrated in **Figure I.2-6**.

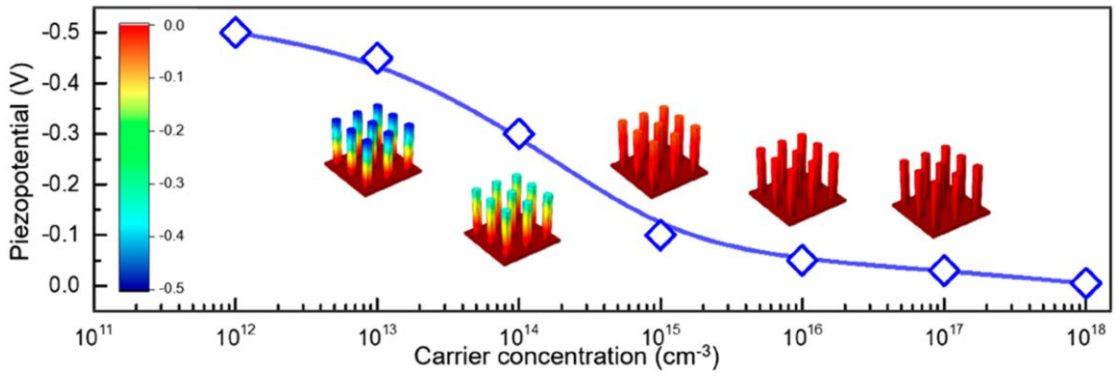

Figure I.2-6. *Simulation results illustrating the piezoelectric potential in ZnO nanorods with varying carrier concentrations, ranging from 10^{12} to 10^{18} cm^{-3}. The piezopotential decreases with increasing carrier concentration, highlighting how free electrons screen the piezopotential and degrade device performance. Adapted from REF [88].*

In the case of ZnO NWs grown by CBD, a high density of free electrons lying in the range of 5×10^{17} – 1.5×10^{19} cm^{-3} has been measured,[75–77,93,94] as discussed in **Section I.2.1.2.3**,

indicating that the screening effect is strongly manifested. Therefore, addressing the screening effect is essential for enhancing the efficiency of ZnO-based nanogenerators and other piezoelectric devices, whose strategies to mitigate its impact will be discussed in **Section I.3.3**.

I.3 Piezoelectric nanogenerators based on nanowires

The first piezoelectric nanogenerator based on nanowires was developed in 2006 by Z. Wang and J. Song.[95] In this study, ZnO NWs were synthesized by vapor-liquid-solid (VLS) process on catalyst Au particles, and subsequently characterized under mechanical deflection using an atomic force microscope (AFM) tip coated with platinum (Pt), as depicted in **Figure I.3-1(a)**. The deflection of NW by the AFM tip induced tensile stress on the outer surface and compressive stress on the inner surfaces of ZnO NWs. The strain generated the separation of charges across the NW due to the piezoelectric effect, leading to the generation of an electrical current. Interestingly, the authors estimated an energy conversion efficiency between 17 and 30% for a single ZnO NW.

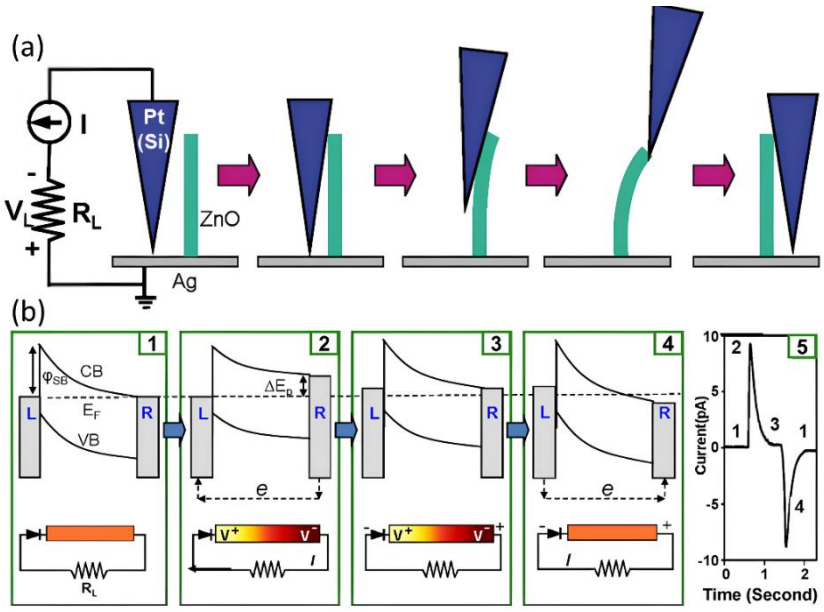

Figure I.3-1. (a) *Experimental setup to generate electricity by deforming ZnO NWs with an AFM tip. Adapted from REF [95].* ***(b)*** *Current generation mechanism by a single ZnO NW in a nanogenerator. Adapted from REF [96].*

Figure I.3-1(b) illustrates the generation of electrical current by a single piezoelectric ZnO NW integrated into a nanogenerator, a principle applicable to other piezoelectric materials.[96] The NW is contacted by two electrodes, L and R, with the L-contact forming a Schottky barrier (φ_{SB}), as shown in the energy band diagram of **Figure I.3-1(b-1)**. When the NW is subjected to tensile stress, a piezoelectric polarization arises in its structure, creating a potential difference (ΔE_p) between the two ends of the NW (**Figure I.3-1(b-2)**). This ΔE_p induces the flow of electrons in the external circuit from electrode R to L, generating the first output signal. Due to the Schottky barrier, external electrons cannot flow through the NW; as a result, they accumulate in the L-electrode. Once compensation of the piezoelectric potential

is reached by the flow of external electrons, the current ceases (**Figure I.3-1(b-3)**). Upon release of the NW, the piezoelectric polarization disappears, disrupting the equilibrium with the electrons accumulated at the L-electrode (**Figure I.3-1(b-4)**). Consequently, electrons flow from the accumulated region (L) to the depleted region (R), generating the second output signal in the opposite direction. Finally, the system reaches stabilization, and no further current flows.

Having exhibited interesting piezoelectric properties, the integration of piezoelectric nanowires into nanogenerators has been largely explored since the early 2000s, offering potential applications in a wide range of fields, including sensor networks, energy harvesting, self-powered systems, piezotronics, and more.[97]

Typically, piezoelectric nanogenerators are designed with two main architectures depending on whether the nanowires are integrated laterally or vertically relative to the substrate within the device. These two different configurations will be discussed in the following section.

I.3.1 Laterally Integrated NanoGenerator

The Laterally Integrated NanoGenerator (LING) architecture comprises nanowires arranged laterally on a substrate, with two electrodes contacting the opposite sides of the nanowires. This configuration was first developed by Zhong Lin Wang's group around 2010 using ZnO NWs, as presented in **Figure I.3-2**.[98,99] Xu et al. created a LING device by growing ZnO NWs via a wet chemical method on the exposed surfaces of ZnO layers, as depicted in **Figure I.3-2(a)**.[98] This device was subjected to cyclic stretching and releasing at a strain rate of 0.05% s^{-1}, producing an output voltage of 1.26 V, a current of 28.8 nA, and a power density of 70 nW/cm^3. In a different approach, Zhu et al. synthesized ZnO NWs on Si substrates using the chemical vapor deposition (CVD) method. The NWs were subsequently aligned laterally on a flexible substrate by a mechanical bench, and metallic electrodes contacted their opposite sides, as illustrated in **Figure I.3-2(b)**.[99] This device generated a voltage of 2.03 V, a current of 107 nA, and a power density of 11 mW/cm^3.

Following the pioneering work by Wang's group, several studies have discussed the performances of LING based on different piezoelectric nanofibers and flexible substrates,[100] as summarized in **Table I.3-1**. It is worth noting that the performances listed in the latter table are not normalized, as comprehensive details about the test conditions used are unavailable.

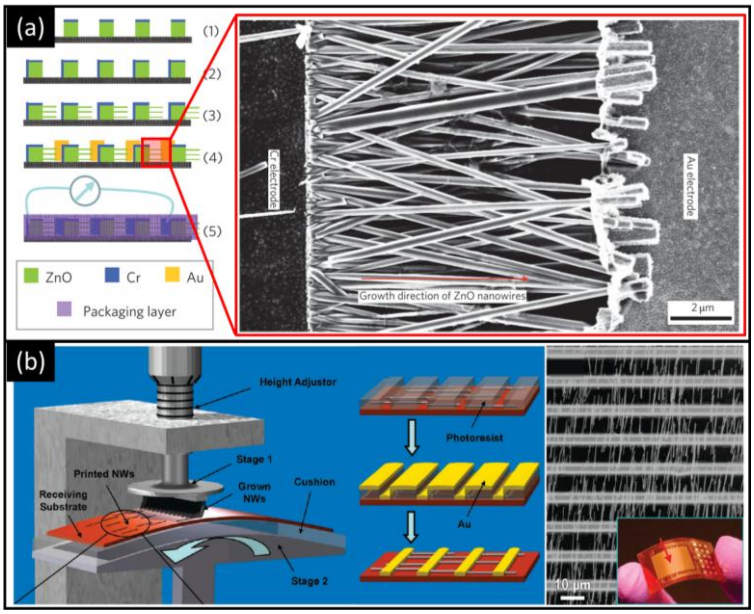

Figure I.3-2. *LING manufactured by* ***(a)*** *directly growing or* ***(b)*** *transferring ZnO NWs between two metal electrodes. Adapted from REFs [98] and [99], respectively.*

Table I.3-1. *Output electrical performance of LINGs reported in the literature.* ***Note****: performances listed in this table are not normalized as details about the test conditions used are unavailable.*

Piezoelectric Material	Electrical Output	Synthesis and integration method	Test condition	REF
Single $BaTiO_3$ NW	0.21 V 1.3 nA	Electrospinning♣	Bending from 5 to 200 mm at 0.33 Hz	[101]
Single $BaTiO_3$ NW	10 mV 2.3 nA	Hydrothermal and drop dispersion	Periodic deformation by bending machine	[102]
Single ZnO NW	3 mV 30 pA	Physical Vapor deposition	Rat's heartbeat	[103]
Single PMN-PT NW	9 mV 1.5 nA 175.4 W/cm^3	Hydrothermal method and drop dispersion	Strain of 0.283% at strain rate of 2.32% s^{-1}	[104]
500 PVDF microfibers	1.7 V 300 nA	Electrospinning	Stretching-releasing deformation of 0.5 % at 15 Hz	[105]
BaTiO3 microfibers	0.86 V	Sol-gel process and continuous spinning method	Harmonic excitation by applying a dynamic load with a finger	[106]
PZT nanofiber	1.63 V 0.03 μW	Electrospinning	Impulsive loading, dynamic loading, and free vibration	[107]
KNN nanofibers	0.3 V 50 NA	Electrospinning	Bending strain	[108]
PZT NWs	6 V 45 nA	Electrospinning	Periodic release-bending	[109]

♣ Electrospinning is a technique at lab-scale for producing nanofibers and microfibers from polymer solutions or melts.

ZnO NWs	2.03 V 107 nA 11 mW/m^3	CVD and mechanic transfer	Cyclic stretching-releasing agitation (0.33 Hz) at strain rate of 0.05 s^{-1}	[99]
ZnO NWs	1.26 V 28.8 nA 70 nW/cm²	Wet chemical method	Cyclic stretching–releasing deformation	[98]
500 PVDF NW array	0.2 mV 350 nA	Electrospinning	Repeated external strain of 0.06 ± 0.02 % at 1 Hz	[110]

I.3.2 Vertically Integrated NanoGenerator

The Vertically Integrated NanoGenerator (VING) configuration consists of nanowires disposed vertically on a substrate, with two electrodes contacting their opposite sides. Due to the ease of fabrication, VINGs are largely developed,[100,111,112] whose first related publication was in 2007 by X. Wang from Z. L. Wang's group.[113] This device, shown in **Figure I.3-3(a)**, integrated a ZnO NW array grown on Au catalyst particles between two electrodes. The bottom electrode consisted of a ZnO film, while a parallel zigzag electrode of platinum (Pt) was used as the top electrode. When subjected to ultrasonic waves of 41 kHz, the device generated a voltage of 0.7 mV and a current of 0.15 nA. Following this work, Wang's group continued to develop ZnO NW-based VINGs integrating pyramid-shaped metal-coated electrodes, aiming to investigate the carrier density and transport of a Schottky barrier under UV illumination,[114] the simultaneous conversion of mechanical and solar energy into electrical energy,[115] and the energy conversion efficiency of multilayer VINGs.[116]

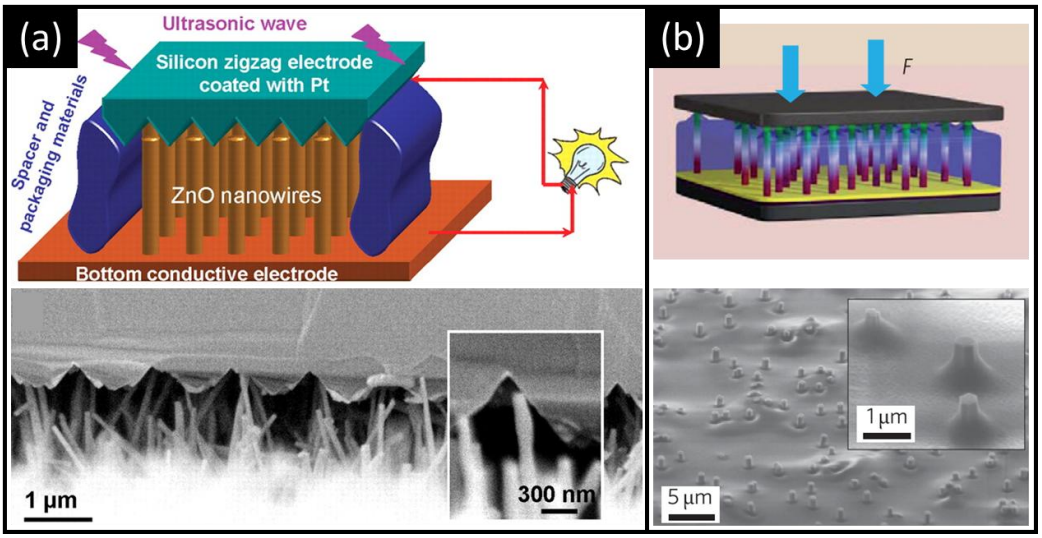

Figure I.3-3. (a) *VING integrating a ZnO NW matrix with a zigzag top electrode. Adapted from REF [113].* ***(b)*** *VING based on ZnO NWs embedded in PMMA polymer. Adapted from REF [98].*

In the next years to 2009, other groups created VINGs based on different piezoelectric nanowires. Given the large amount of work reported in this field, a few studies are summarized for illustrative purposes in **Table I.3-2**, focused particularly on ZnO NW-based VINGs. The performances shown in the latter table are not normalized due to a lack of detailed information about the test conditions employed.

Table I.3-2. *Output electrical performance of VINGs reported in the literature.* ***Note****: performances listed in this table are not normalized as details about the test conditions used are unavailable.*

Piezoelectric Material	Electrical Output	Synthesis and integration method	Test condition	REF
PZT NWs	1 Vpp	Hydrothermal reaction	Sinusoidal base excitation (0.7 g RMS base acceleration	[117]
BaTiO3 NW array	90 V 1.2 µA	Hydrothermal	Bending of 5 mm at 0.2 m/s strain rate	[102]
ZnO NWs	0.7 mV 0.15 nA	(Probably by CVD)	Ultrasonic waves at 41 kHz	[113]
ZnO NWs	10 V 0.6 µA 10 mW/cm^3	Wet chemical method	Strained to 0.12 % at strain rate 3.56% s-1	[118]
ZnO NWs	1.5 V 25 nA 70 µW/cm^3	Hydrothermal	Turning and compressing by a tire	[119]
ZnO NWs	58 V 134 µA 0.78 W/cm^3	Wet chemical method on selected areas	Compressive stress with a linear motor	[120]
PZT NWs	0.7 V 4 µA/cm² 2.8 mW/cm^3	Hydrothermal	Periodic pressing and releasing between 1-50 HZ by linear motor	[121]
(K,Na)NbO3 NRs	0.38 V 6.4 nA 101 mW/cm^3	Hydrothermal	Compressive force of 1 kgf at 1 Hz	[122]
Mg-doped GaN NWs	228 ± 120 mV 6.35 mW/cm^3	Plasma-assisted molecular beam epitaxy (MBE)	Flexion strain at 3 and 6 Hz	[123]
ZnO NW array	62 mV 0.11 µW/cm²	Wet chemical process	Ultrasonic wave excitation	[116]

In this thesis, VING is developed due to its ease of fabrication and superior performance compared to LING. Particularly, a device integrating a ZnO NW embedded in parylene-C, as schematized in **Figure I.3-3(b)**, is fabricated.

I.3.3 Strategies to enhance the performance of a ZnO nanowire-based piezoelectric nanogenerator

As previously discussed, the size-dependent enhancement of the piezoelectric properties in ZnO renders it suitable for integration into piezoelectric nanogenerators (PNGs), where ZnO NWs are arranged vertically as a matrix. However, a significant challenge remains: the screening effects degrading the device performance. Thus, distinct approaches have been developed to overcome this issue, including doping, controlling area density, surface treatment, and interfacial modification of ZnO NWs.[124] It is worth mentioning that the substrate also plays an important role in the performance of PNGs, with flexible substrates being advantageous due to their ability to deform easily.[125] However, this thesis focuses on ZnO NWs vertically synthesized on rigid substrates by chemical bath deposition. The advantage of this approach is that the technology developed for rigid substrates can be promptly adapted for flexible substrates.

I.3.3.1 Doping

The doping process involves the intentional introduction of impurities into ZnO NWs to modify their piezoelectric properties. These impurities can be halogen ions (F, Cl, Br, I), rare earth elements, metalloids (Sb), and metallic elements (Al, Ga, Cu, Fe, Mg, Mn, Cr), which either introduce holes (p-type doping) or electrons (n-type doping).[125–130] P-type dopants such as K, Li, Na, and rare earth elements basically reduce the density of free electrons by recombining with them in ZnO NWs, minimizing screening effects and enhancing the piezoelectric properties of ZnO NWs.[128,129] The piezoelectric properties of ZnO NW are further influenced by the ionic radii of the dopants,[125] as schematized in **Figure I.3-4**. When dopant ions (Mn^{+}) substitute Zn in the crystal lattice, they form M-Oxygen bonds in ZnO. Smaller ions enable easier rotation of these bonds, enhancing the piezoelectric displacement and increasing the d_{33} value in ZnO. In contrast, larger ions obstruct bond rotation, reducing the piezoelectric response. However, larger ions improve c-axis orientation and decrease the lattice constant in ZnO, enhancing its overall piezoelectric behavior along with its d_{33} coefficient. Thus, the choice of dopant and its concentration significantly influence the lattice strain and subsequent piezoelectric response.

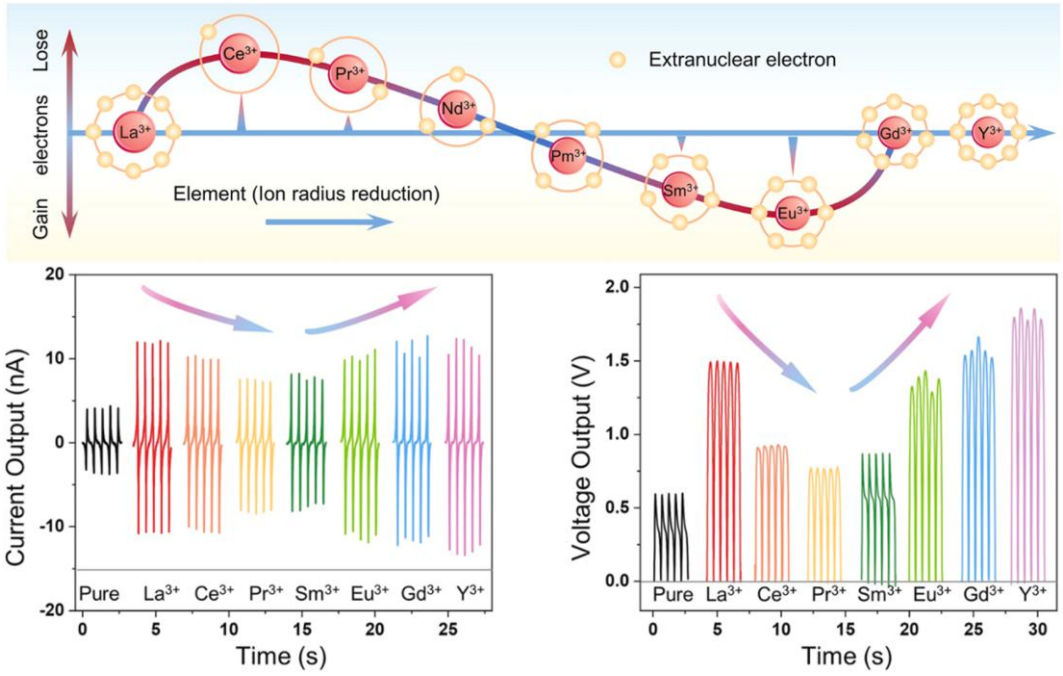

Figure I.3-4. *Output current and voltage of PNGs based on ZnO NW doped with rare earth (RE) ions with different ionic radii. Adapted from REF [129].*

I.3.3.2 Areal density

The density of ZnO NWs directly affects both the mechanical and electrical properties of PNGs, highlighting the importance of controlling it for optimal functionality of the device. A lower density of ZnO NW allows for easier mechanical deformation in PNGs, enhancing the mechanical energy transfer.[131] In contrast, a higher NW density ensures structural robustness and improves the device's effectiveness in storing electrical energy.[120,131] Thus, this balance between efficient mechanical energy transfer and electrical energy storage is essential for PNGs. However, a high NW density can cause free electron tunneling between adjacent NWs, leading to screening effects and reducing the piezoelectric response of a PNG, as illustrated in **Figure I.3-5(a)**. Therefore, the effective isolation of inactive NWs from active NWs is achieved by using the selective area growth (SAG) method, further discussed in **Section I.4.2.2**, allowing good control of NW density, decreasing the screening effects, and improving the PNG performance,[88,120,132,133] as illustrated in **Figure I.3-5(b)**. The SAG method highlights the importance of carefully tuning the NW density to reduce undesirable screening effects, maximizing the efficiency of ZnO NW-based PNGs.

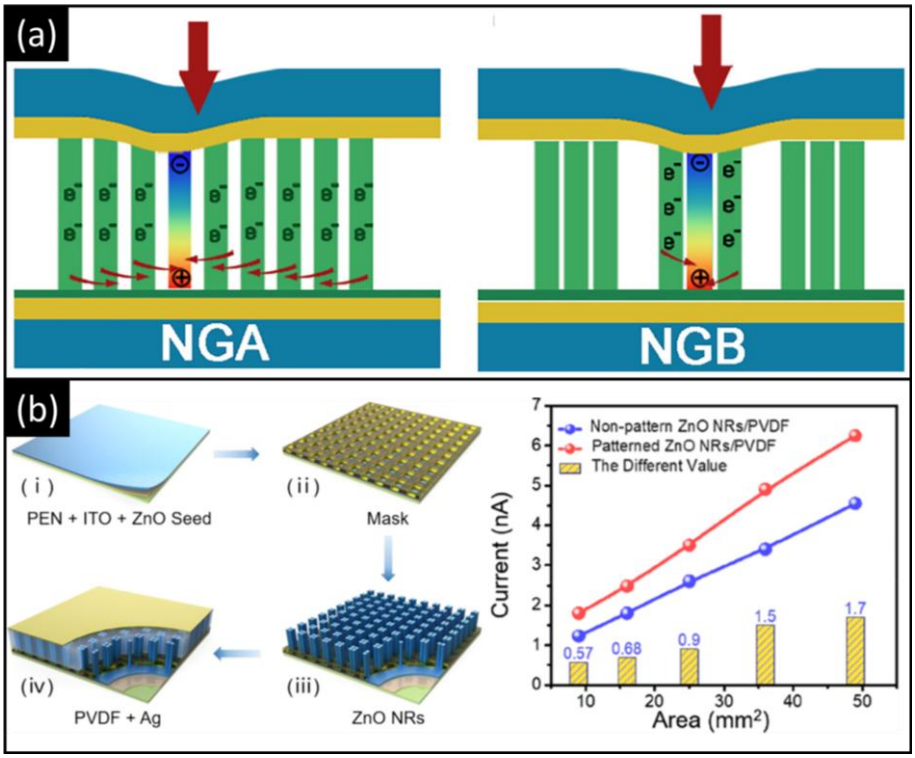

Figure I.3-5. (a) *Screening effects led by free electron tunneling between neighboring NW in (left) dense and (right) controlled density. Adapted from REF [133].* ***(b)*** *Fabrication steps of a patterned PNG for SAG method, along with its output current compared to a non-patterned PNG based on ZnO NWs. Adapted from REF [88].*

I.3.3.3 Surface engineering

Surface engineering involves strategic modifications of the surface properties of ZnO NWs integrated in PNGs to optimize the device performance. This modification is achieved through the interaction of ZnO NWs with other material in contact, such as PMMA, a commonly used electrically inert polymer in PNGs. Lu et al. demonstrated that incorporating Au nanoparticles on the surface of ZnO NWs forms Schottky junctions, creating an electron depletion region, which enhances both the piezopotential and electrical output of a PNG.[134] Following the same approach, p-type materials, including polymers (P3HT♣) and semiconductors (PEDOT:PSS♦, Cu_2O), form p-n heterojunctions with ZnO, effectively depleting free electrons from its surface and reducing screening effects.[135,136] Other approaches uses piezoelectric polymers (PVDF♠) to amplify the overall piezoelectric response of PNGs.[88,136] Therefore, each material contributes either by enhancing piezoelectric synergy or suppressing

♣ Poly(3-hexylthiophene)
♦ Poly(3,4-ethylenedioxythiophene) polystyrene sulfonate
♠ Poly(vinylidene fluoride)

screening effects, improving the performance of PNGs compared to those based on inert polymers like PMMA, as schematized in **Figure I.3-6**.

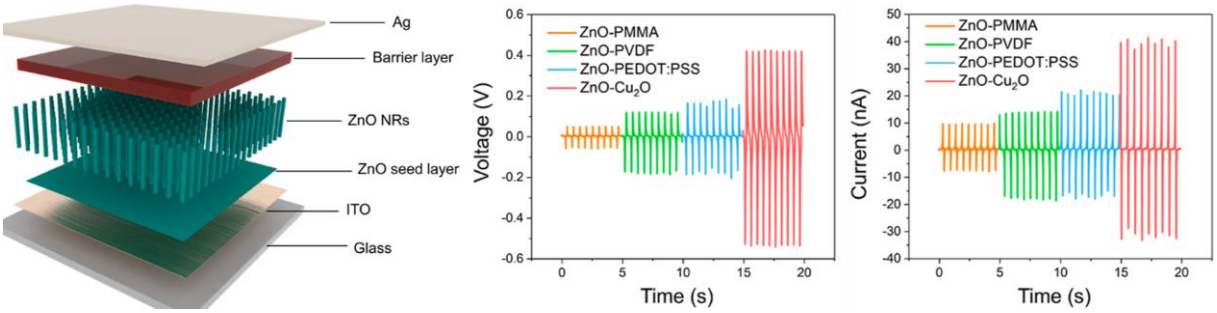

***Figure I.3-6**. Structure, output voltage, and current of PNG with different barrier layers modifying the electrical surface of ZnO NWs. Adapted from REF [136].*

I.3.3.4 Interfacial modification

Interface engineering consists in the creation of electrical couplings between ZnO NWs and the electrodes of a PNG, which can be capacitive, ohmic, p-n, and Schottky. As previously discussed, p-n and Schottky junctions deplete the excess of electrons in ZnO, improving the piezoelectric performance of a PNG. In addition, they serve as electrical barriers, preventing electron flow from ZnO NWs to external circuits, protecting the device from leakage current. Studies have demonstrated that using electrodes incorporating CuI, Cu_2O, CuO, and NiO layers to form p-n junctions with ZnO NWs significantly enhances PNG performance.[137–140] The integration of a Schottky interface between Au and ZnO NWs can further double the output voltage of a PNG compared to one based on ZnO NWs grown on ZnO seed layers deposited on ITO substrates, as illustrated in **Figure I.3-7**.[132] The use of ITO and AZO as electrodes also exhibits interesting properties, but they are generally less effective than Schottky barriers incorporating Au layers.[132,141] Thus, these findings highlight the importance of interface engineering in fine-tuning the performance of ZnO-based nanogenerators.

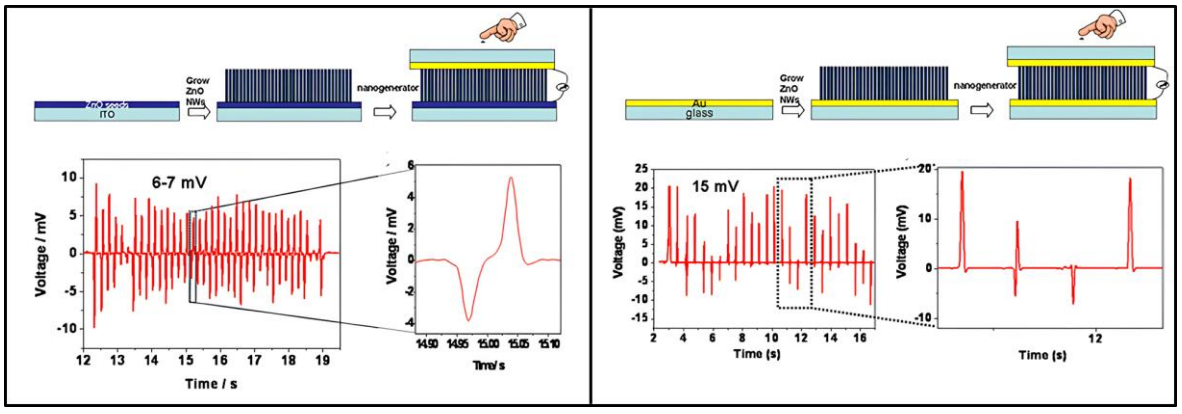

***Figure I.3-7**. Output voltage of a VING based on ZnO NWs with a single (left) and double (right) Schottky barrier. Adapted from REF [132].*

I.4 ZnO nanowires grown by chemical bath deposition

A wide range of techniques based on vapor phase and wet chemistry deposition methods have been employed to grow ZnO nanowires (NWs), each offering distinct functional properties.[142,143] Among these, chemical bath deposition (CBD) is recognized as an environmentally friendly process,[144] and is considered promising for large-scale industrial applications due to its ability to grow ZnO NWs at low temperatures (60 – 100 °C) on flexible and rigid substrates.[143,145]

Given the environmental advantages and benefits of the CBD method, along with the extensive expertise of the LMGP in this area, ZnO NWs are synthesized using CBD in this thesis. The following sections will provide a detailed discussion of the CBD process, as well as the unintentional and intentional incorporation of extrinsic defects in the ZnO NW structure.

I.4.1 Chemical bath deposition

The first study related to CBD was reported in 1984 by Fujita et al., who demonstrated how synthetic conditions affect the crystal morphology of ZnO grown via a homogeneous precipitation method, resulting in ZnO NWs formed directly in the chemical solution.[146] Following in this research direction, M. Andrés Vergés et al. in 1990 explored the effect of reactant concentrations, pH, and temperature on the hydrolysis of zinc nitrate and the formation of ZnO microcrystals.[147] However, it was not until 2001 that Vayssieres et al. successfully synthesized a well-oriented ZnO NW array on a substrate using the CBD method,[148,149] opening perspectives in the synthesis of ZnO by a green chemistry technique.

I.4.1.1 Principle of chemical bath deposition

The process for growing ZnO NWs via the CBD method is illustrated in **Figure I.4-1**. A flexible or rigid substrate, coated with a seed layer that facilitates the nucleation of ZnO NWs, is essential. The seed layer reduces the system's surface energy, promoting thus the growth of ZnO NWs.[150] The substrate is immersed in a chemical solution containing zinc and oxygen precursors – zinc nitrate $Zn(NO_3)_2$ and hexamethylenetetramine ($(CH_2)_6N_4$, HMTA), respectively – in deionized water, within a sealed reactor. This reactor is introduced into a regular oven to heat the chemical solution between 60 and 100 °C,[145] promoting both the growth of ZnO NWs on the seed layer (heterogeneous growth) and the precipitation of

suspended ZnO NWs in the solution (homogeneous growth). This precipitation during the CBD process can contaminate the NWs grown on the substrate, so the substrate is placed face-down on an inert glass support to minimize this contamination.

Kinetic and thermodynamic factors drive the synthesis of longer ZnO NWs.[151] These nanostructures exhibit a polar *c*-plane top facet and non-polar *m*-plane sidewalls. Since the polar *c*-planes have surface energies higher than the non-polar *m*-planes,[47] the total free energy of ZnO is minimized by extending the non-polar *m*-plane vertical sidewalls at the expense of the polar *c*-plane top facet, leading to greater axial growth along the *c*-axis compared to radial growth along the *m*-axis.[152] Furthermore, due to the polar nature of the *c*-planes, electrostatic interactions occur between the Zn- and O-terminated bonds on the *c*-planes, and the Zn^{2+} and OH^- ions of the chemical bath, promoting rapid axial growth,[43,47,153,154] favoring the formation of nanostructures with a high aspect ratio, such as ZnO NWs.

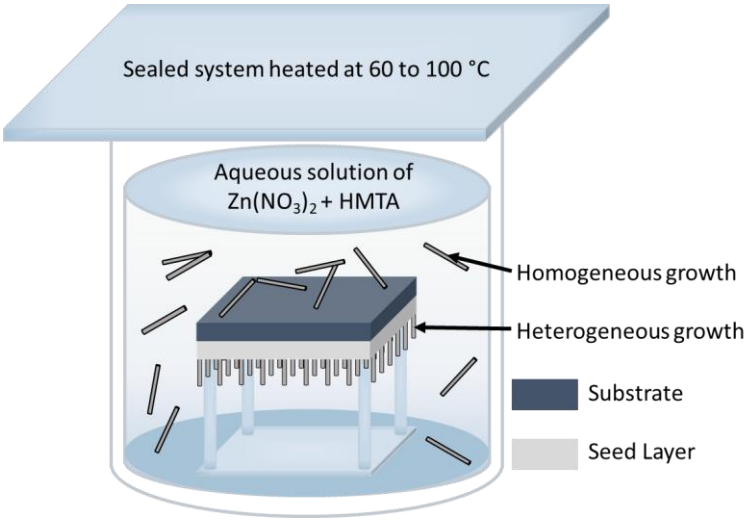

Figure I.4-1. *Schematic representation of ZnO NW growth by CBD method in a sealed system. A substrate coated with a seed layer is placed face-down into a chemical solution mixing the precursors $Zn(NO_3)_2$ and HMTA in deionized water. ZnO NWs form in a heterogeneous (since the seed layer) or heterogeneous (suspended in solution) after heating the chemical solution.*

I.4.1.2 Chemical reactions in chemical bath deposition

The reactions during the CBD process leading to the formation of ZnO NWs are described by the following equations:[150]

$$(CH_2)_6N_4 + 6H_2O \leftrightarrow 6HCHO + 4NH_3 \qquad \textbf{Equation 1.4-1}$$

$$NH_3 + H_2O \leftrightarrow NH_4^+ + HO^- \qquad \textbf{Equation 1.4-2}$$

$$Zn(NO_3)_2 \leftrightarrow Zn^{2+} + 2NO_3^- \qquad \textbf{Equation 1.4-3}$$

$$Zn^{2+} + 2HO^- \leftrightarrow ZnO_s + H_2O \qquad \textbf{Equation 1.4-4}$$

Reaction **(Equation 1.4-1)** depicts the hydroxylation of HMTA during the heating of the chemical solution, forming formaldehyde (HCHO) and ammonia (NH_3). Subsequently, ammonia hydrolyzes, forming ammonium (NH_4^+) and hydroxide (HO^-) ions **(Equation 1.4-2)**. It has been found that HMTA acts as a pH buffer,[155] affecting thus the supersaturation of the chemical precursors. HMTA also inhibits the development of non-polar *m*-planes through interactions such as covalent and hydrogen bonding, electrostatic interactions with adsorbates, and steric hindrance, reducing consequently the radial growth of ZnO NWs.[151] Reaction **(Equation 1.4-3)** illustrates the solubilization of zinc nitrate, forming NO_3^- and Zn^{2+} ions. The latter reacts with HO^- ions to finally form ZnO **(Equation 1.4-4)**. It should be noted that Zn^{2+} is the limiting reactant, meaning that the synthesis of ZnO NWs depends strongly on the concentration of Zn^{2+} in the chemical bath. Thus, the supersaturation ratio (S_r) is a crucial parameter that dictates the ZnO NW formation. This parameter is defined as the ratio between the initial concentration of Zn^{2+} in the bath ($[Zn^{2+}]_i$) and the concentration of Zn^{2+} at the thermodynamic equilibrium ($[Zn^{2+}]_{eq}$),[156] i.e. $S_r = [Zn^{2+}]_i/[Zn^{2+}]_{eq}$, and varies as a function of the pH of the chemical bath, the precursor concentration, and the temperature. The precipitation of suspended ZnO NWs as well as the formation of ZnO NWs on the substrates is dictated by S_r, as illustrated in **Figure I.4-2**. When $S_r < 1$, it indicates that all the $[Zn^{2+}]_i$ is solubilized in the solution and do not reach a saturation limit ($[Zn^{2+}]_{eq}$), so no NWs are formed. By increasing the $[Zn^{2+}]_i$, its solubilization reaches a saturation limit, giving $S_r = 1$. Since this point, an increase in $[Zn^{2+}]_i$ leads to a light excess of precursor in the chemical bath, leading to the formation of ZnO NWs from a seed layer with low formation energy,[150] until $S_r \leq A$. If this limit is exceeded, so ZnO NWs have enough energy to nucleate as precipitates in the bath at expense of the heterogeneous growth to compensate the excess of precursor. Finally, when $S_r > B$, ZnO NWs rapidly precipitates in the chemical bath, inhibiting the heterogeneous growth of ZnO NWs. This indicates the importance to define carefully the precursor conditions and temperature in the chemical bath.

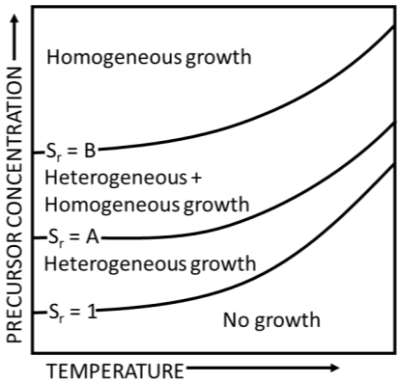

Figure I.4-2. *Schematic representation of the effect of the supersaturation on the growth of ZnO NWs. Inspired from REF [157].*

It is important to mention that by adding ammonia in the chemical bath, the pH increases, and when the pH exceeds 7, the main formed Zn(II)-related species in the bath are amine complexes such as $\mathrm{Zn(NH)_n^{2+}}$.[151,155,157,158] These species then follow an additional reaction before to form ZnO (**Equation 1.4-5)**. Additionally, under conventional temperature conditions and in a low pH range (pH < 7), $\mathrm{Zn(NO_3)_2}$ experimentally could dissociate in $\mathrm{Zn^{2+}}$ and $\mathrm{[Zn(H_2O)_6]}$ complexes.[159,160] The latter would need a dehydration process involving no formation of long-lived intermediates, as supported by *in situ* XANES studies.[161] Chapter 2 will present speciation diagrams as a function of the pH involved in the growth of ZnO NWs.

$$\mathrm{Zn(NH_3)_n^{2+}} \leftrightarrow \mathrm{Zn^{2+} + nNH_3} \qquad \textit{Equation 1.4-5}$$

I.4.2 Nucleation mechanism and morphological control of ZnO nanowires grown by chemical bath deposition

As previously mentioned, the seed layer plays a crucial role in promoting the growth of ZnO NWs via CBD by lowering the surface energy of the thermodynamic system that control their formation. In addition, when the crystal properties of the seed layer are close to those of ZnO NWs, the energy required for NW formation is minimized,[150] indicating that the nucleation layer's characteristics directly affect the morphological properties of the resulting ZnO NWs. For instance, crystallographic mismatch between the seed layer and ZnO NWs affect the nucleation density, which affect the volume of growth solution available for each NW, and alter consequently their morphological properties such as density, diameter and length.[162]

For practical purposes, this thesis will focus on ZnO and Au seed layers, since they will be used to develop piezoelectric nanogenerators (PNGs).

It has been shown that ZnO NWs can grow homoepitaxially via CBD on the polar *c*-faces of ZnO nanoparticles, where polarity transfer occurs from the nanoparticle to the NW.[163–165]

This Zn- and O-polarity transfer, facilitated by CBD, can be strategically employed in the development of PNGs. Given that Zn- and O-polarity compensate each other in terms of piezoelectricity, it is optimal for the ZnO seed layer to exhibit a predominant (or exclusive) polarity. This preferential polarity can be achieved through thermal treatments at high temperatures,[163,166] resulting in ZnO NWs with uniform polarity, improving consequently the performance of the related PNG. ZnO NWs can be also grow on $(10\bar{1}2)$ and $(20\bar{2}1)$ semi-polar surfaces of ZnO nanoparticles, resulting in tilted NWs.[167]

Furthermore, ZnO NWs can also grow vertically as dense arrays on Au layers by hydrothermal method.[132,162,168–170] Clement et al. demonstrated that vertical ZnO NWs grow heteroepitaxially on the (111)-facets of Au (111) grains through CBD processes.[171] In addition, a Schottky barrier can arise at the interface between Au and hydrothermal-grown ZnO NWs,[172–174] which is advantageous for the fabrication of PNGs.[132,141,175–178] This will be discussed in detail in **Chapter IV**.

The control of the ZnO NW's morphology is a crucial parameter to enhance the performance of the related PNG. In the CBD method, the morphological properties of ZnO NWs can be modified by adjusting the chemical bath conditions and engineering the seed layer, which can or cannot be patterned, as described below.

I.4.2.1 Spontaneous growth

Spontaneous growth refers to the random nucleation of ZnO NWs across the entire surface of non-patterned seed layers. Under this condition, the morphological properties of ZnO NWs are determined solely by the chemical bath conditions and the characteristics of the seed layer.

The increase in temperature of the chemical bath raises the solubility of the precursors in the solution, modifies the growth rate of ZnO NWs, and increases the mobility of atoms on their surfaces, which can result in ZnO NWs with tipped top faces,[179–182] as shown in **Figure I.4-3(a)**. Additionally, the precursor concentration in $Zn(NO_3)_2$ and HMTA significantly affects the supersaturation level in the chemical bath, affecting the aspect ratio and density of ZnO NWs,[151,170,183,184] as illustrated in **Figure I.4-3(b)**. Given that ZnO NWs grow in a single chemical bath, i.e. neither $Zn(NO_3)_2$ nor HMTA is added to renew the solution, the growth time becomes a crucial factor due to the depletion of reactants.[185–187] For instance, if the reactant depletion is minimal, extended growth time can lead to the coalescence of ZnO NWs,[186] as

schematized in **Figure I.4-3(c)**. The pH of the chemical bath does not only alter the supersaturation level but also affects the electrical charge of the ZnO NW surfaces and their growth rate, influencing their morphological shapes,[188–192] as exampled in **Figure I.4-3(d)**. This topic will be detailed in the **Section I.4.3**. Therefore, the simultaneous control of the temperature, growth time, precursor concentration, and pH in the chemical bath govern the final shape of ZnO NWs. It is important to mention that longer ZnO NWs with low diameters are preferred to enhance the performance of PNGs.

In this thesis, standard ZnO NWs were grown by CBD for 3h at 85 °C. The pH values and the precursor concentrations were varied depending on the specific objective of each experiment.

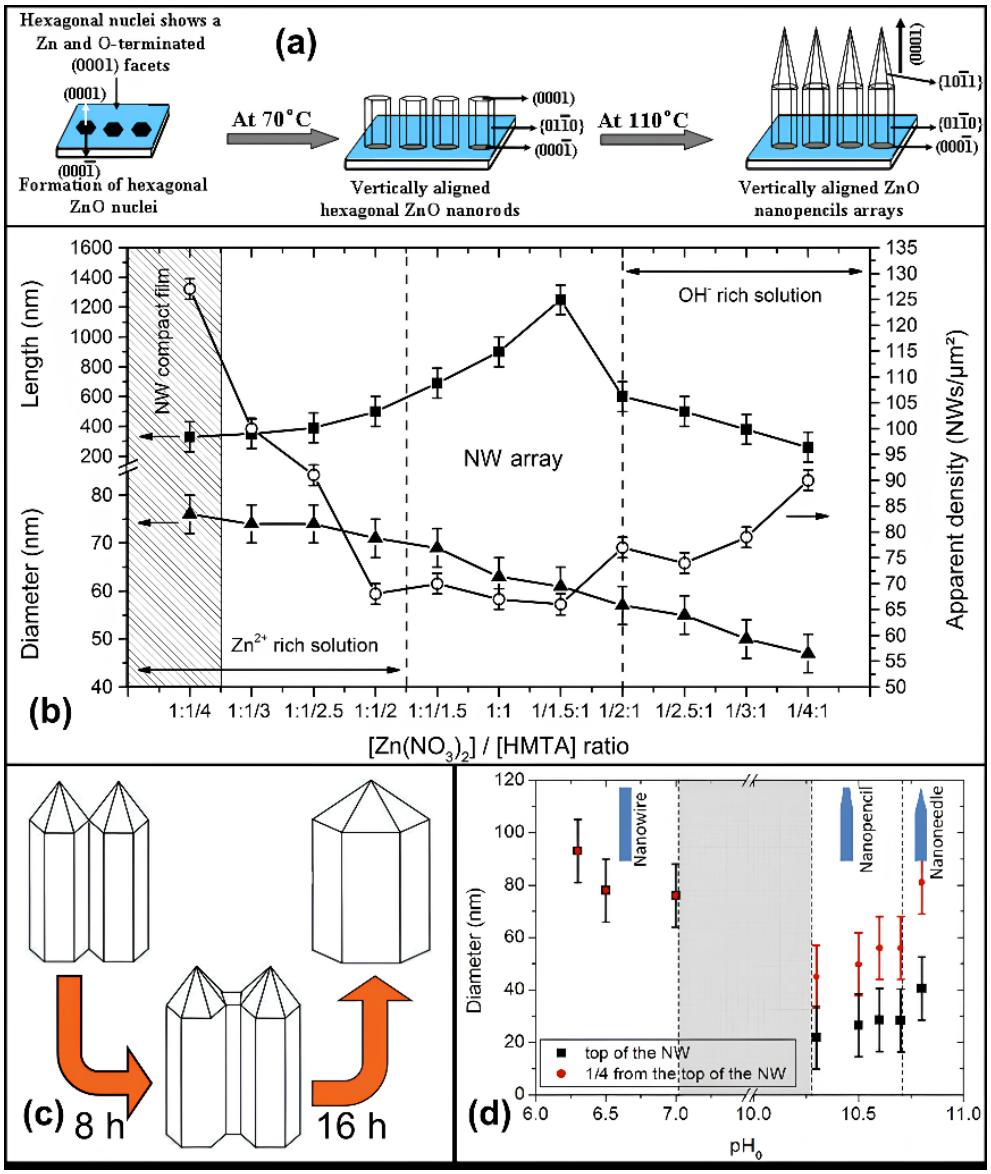

Figure I.4-3. *Morphological properties of ZnO NWs grown by CBD as a function of the* ***(a)*** *solution temperature,* ***(b)*** *chemical precursor concentration,* ***(c)*** *growth time, and* ***(d)*** *pH of the chemical bath. Adapted from REFs [180], [151], [186], and [193], respectively.*

I.4.2.2 Selective area growth

The selective area growth (SAG) method, as the name indicates, consists of localized growth of ZnO NWs in patterned seed layers. These seed layers are patterned using inkjet lithography,[194] microcontact printing photolithography,[195] nanosphere photolithography,[196] nanoimprint lithography,[197] beam-laser interference lithography,[198] conventional photolithography,[133] and electron-beam-assisted lithography.[48,199,200]

Since this thesis had access to the electron-beam-assisted lithography process, this method will be detailed. In addition, it is important to distinguish between "selective growth" and "surface-selective growth". Selective growth refers to the nucleation of multiple NWs in a pattern of large size or a single region (**Figure I.4-4(a)**). Surface-selective growth, in contrast, consists of the formation of a single NW on a single pattern (**Figure I.4-4(b)**). This second case is more interesting for the fabrication of PNGs since it allows the control of both the position and diameter of each ZnO NW.

By fixing the nucleation sites through surface-selective growth, the growth of ZnO NWs by CBD is mostly influenced by both diffusion and reaction rates, which are affected by factors such as nanowire density, polarity, and the availability of reactants.[48,200] When NWs are densely arranged, diffusion of precursors is the limiting factor, i.e. the growth rate depends on how rapidly reactants like Zn^{2+} ions can reach the nanowire surface, whereas, in spaced NWs, the growth rate is dictated by how fast these ions are incorporated into the crystal structure, as illustrated in **Figure I.4-4(c)**.[200] The polarity of ZnO NWs also plays a critical role, as depicted in **Figure I.4-4(d)**. Zn-polar surfaces, with a higher number of dangling bonds per oxygen atom, facilitate more efficient Zn incorporation, leading to faster growth rates compared to O-polar surfaces. This surface reaction rate along with ionic interactions between charged polar surfaces and ionic species, such as Zn^{2+} and HO^- ions in the solution, contributes to the difference in growth kinetics.[48]

As a consequence, the SAG method must consider the properties of the seed layer and the growth rate dictated by the diffusion and reaction rates. This will be more detailed in Chapter 4.

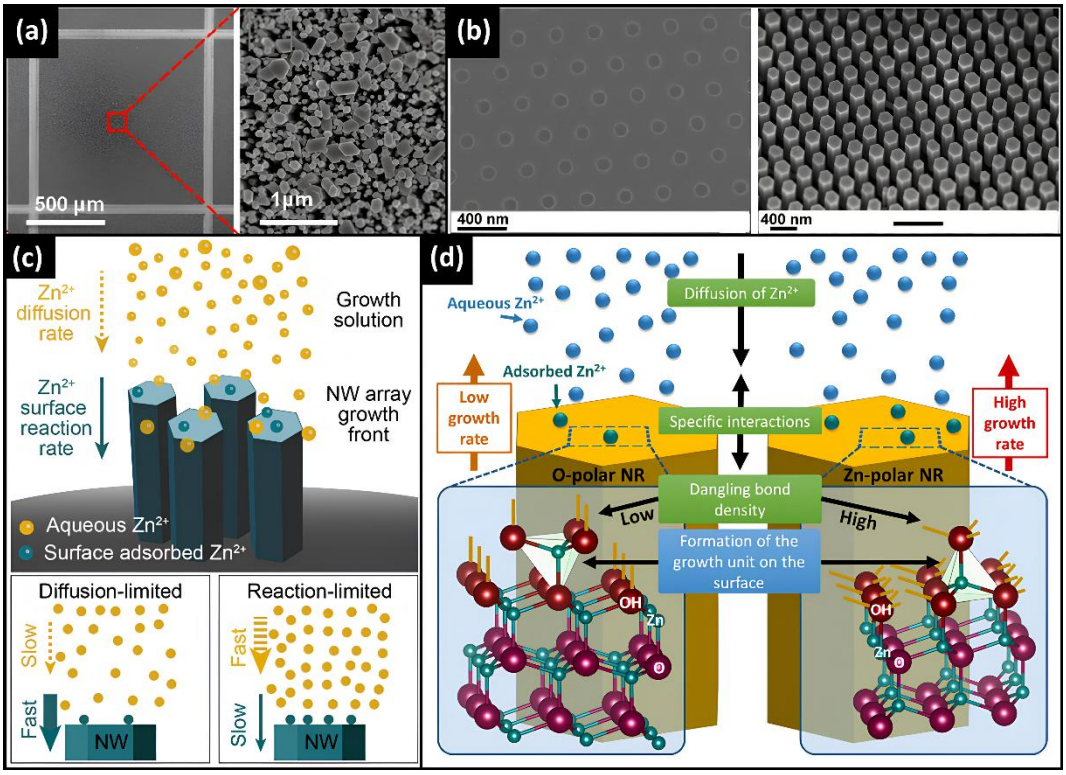

Figure I.4-4. *ZnO NWs grown by CBD on* ***(a)*** *single-region and* ***(b)*** *surface-selective patterned seed layers.* ***(c)*** *Schematic showing serial processes of diffusion and reaction in the vicinity of the NW array growth front.* ***(d)*** *Schematic representation of the possible mechanisms accounting for the polarity-dependent growth of ZnO NRs. Adapted from REFs [120], [201], [200], and [48], respectively.*

I.4.3 Extrinsic point defects in ZnO nanowires grown by chemical bath deposition

In contrast to the intrinsic defects mentioned in **Section I.2.1.2.2**, which involve solely Zn and O atoms, extrinsic point defects arise from impurities introduced in ZnO. These impurities can be introduced unintentionally, such as hydrogen (H), or intentionally, such as metallic species further discussed, both of which modify the electronic structure of Zn and O atoms. A special case occurs with nitrogen (N), as it can be incorporated either unintentionally or intentionally, depending on the conditions of the chemical bath used to synthesize ZnO NWs.

I.4.3.1 Unintentional doping of ZnO nanowires

ZnO NWs grown by CBD are typically n-type nanostructures, whose behavior is primarily attributed to the presence of H in their structure. The incorporation of both H and N during the CBD process leads to the formation of distinct types of defects in ZnO NWs, which affect their optical and electrical properties.

I.4.3.1.1 Hydrogen-related defects

The unintentional incorporation of H in ZnO NWs originates from the hydrogen-rich environment during the CBD growth process. This incorporation occurs during the crystallization of ZnO NWs following the hydroxylation of Zn^{2+} ions,[155] as depicted in **Equation I4.4** in **Section I.4.1.2**. Moreover, DFT calculations indicate that H^+ is the most stable state for hydrogen in ZnO, contributing to its n-type conductivity.[202] Nowadays, the main H-related defects formed in ZnO NWs grown by CBD were identified, including interstitial H in bon-centered sites (H_{BC}), O-H bonds in a zinc vacancy (V_{Zn}-nH), and substitutional H on the O lattice site (H_O),[75] as illustrated in **Figure I.4-5(a)**. Among these, both H_{BC} and V_{Zn}-3H defects are the main responsible for the high density of free charge carriers in as-grown ZnO NWs, as they act as shallow donors with low formation energies,[78] as depicted in **Figure I.4-5(b)**. As a result, ZnO NWs grown by CBD exhibit carrier density in the range of 5×10^{17} – 1.5×10^{19} cm^{-3},[75–77,93,94] highlighting the need for compensatory doping to enhance their performance for piezoelectric applications.

I.4.3.1.2 Nitrogen-related defects

The incorporation of N in ZnO NWs is promoted by its abundant presence, originating from the precursors $Zn(NO_3)_2$ and $(CH_2)_6N_4$ – HMTA used in the chemical bath. Dr. José VILLAFUERTE, a former PhD candidate at LMGP, conducted an in-depth study that provided valuable insights into the engineering of N-related defects in ZnO NWs grown by CBD.[79] His research revealed that N occupies O lattice sites (N_O) and forms deep acceptor complexes, such as V_{Zn}-N_O-H (**Figure I.4-5(c)**), with low formation energy under H-rich conditions, as depicted in **Figure I.4-5(d)**. In addition, he demonstrated that by increasing the pH of the chemical bath via the addition of ammonia, a massive incorporation of V_{Zn}-N_O-H defects along with the formation of V_{Zn}-H complexes in ZnO NW occurs, contributing to p-type compensatory doping.[203] These N- and H-related defects will be frequently referenced in Chapter 2 to further examine the electrical properties of ZnO NWs.

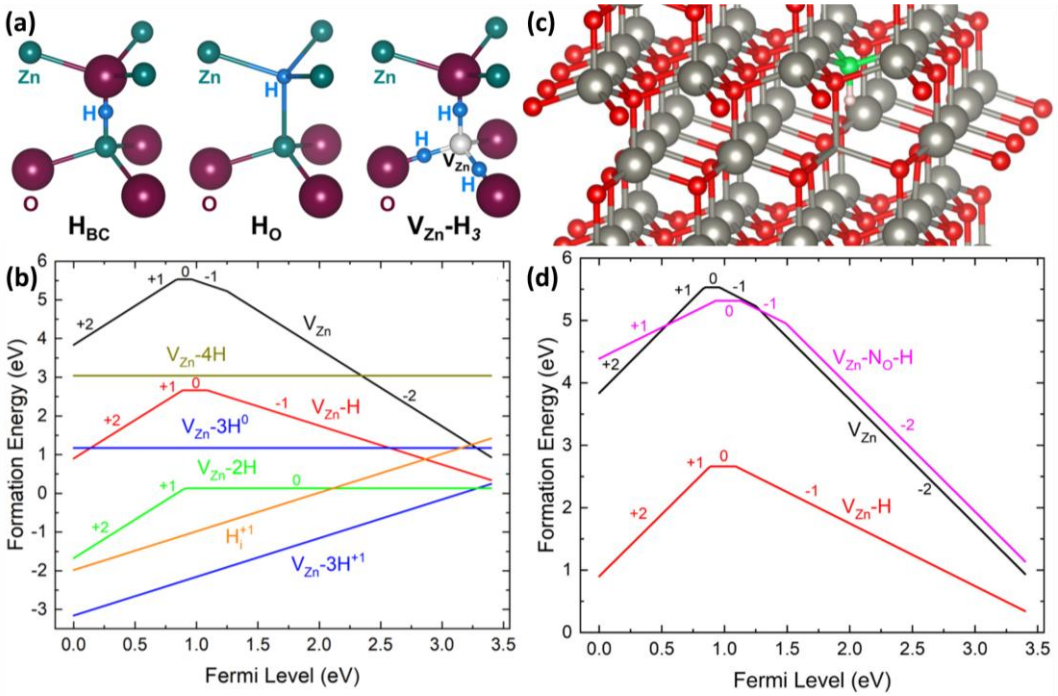

Figure I.4-5. (a) *Main hydrogen-related defects in ZnO NWs grown by CBD. Adapted from REF [75].* ***(b)*** *Formation energies of hydrogen-related defects in ZnO as a function of the Fermi level in intermediate O-conditions from DFT calculations. Adapted from REF [78].* ***(c)*** *Structural model for the most stable atomic configuration of the axial V_{Zn}-N_O-H defect complex.* ***(d)*** *Formation energies of nitrogen- and hydrogen-related defects in ZnO as a function of the Fermi level in intermediate O-conditions from DFT calculations. The zero of Fermi level corresponds to the valence band maximum. Adapted from REF [79].*

I.4.3.2 Intentional doping of ZnO nanowires

At LMGP, the doping of ZnO NWs via CBD follows the face-selective electrostatic interaction method developed by Joo et al.,[204] as illustrated in **Figure I.4-6**. By introducing non-zinc sulfates in the chemical solution, A-type (positively charged) and B-type (negatively charged) ions form charged complexes that electrostatically interact with oppositely charged ZnO NW surfaces. This interaction inhibits the axial growth along the negatively-charged (0002) *c*-polar face, promoting platelet formation, or obstructs the sidewall growth along the positively-charged $(10\bar{1}0)$ non-polar *m*-plane face, resulting in high-aspect-ratio structures. Thus, the LMGP uses this approach to control the morphology of ZnO NWs and promote the incorporation of metallic species into their structure.

The first intentional doping of ZnO NWs by CBD at LMGP was conducted by Verrier et al., incorporating aluminum (Al) through electrostatic interactions between $Al(OH)_4^-$ complexes and the positively charged *m*-faces of ZnO NWs by adjusting the pH of the chemical bath.[191] Following the same approach, gallium (Ga) atoms were used for doping ZnO NWs, which showed higher incorporation efficiency than Al atoms, likely due to lower formation energies, as suggested by DFT calculations.[192,205] It is important to mention that Al and Ga are

n-type dopants, which significantly increase the free carrier density in ZnO NWs.[206] However, given that resistive ZnO NWs are necessary for piezoelectric applications, the following paragraphs focus on p-type dopants.

Elements from groups IA (Li, Na, K), IB (Cu, Ag, Au), and VB (N, P, As, Sb) are potential candidates for p-type doping in ZnO.[50,207] However, p-type doping in ZnO NWs remains challenging due to the incorporation mechanisms and the formation of electrically inactive compensating defects.

From group-IA elements, lithium (Li) is the most promising dopant for piezoelectric applications.[208–210] Indeed, when ZnO NWs are synthesized in a chemical bath with equimolar $Zn(NO_3)_2$, HMTA, and $LiNO_3$, Li occupies Zn sites under favorable thermodynamic conditions, creating a shallow acceptor level (90 meV).[208,209,211,212]

Concerning group-VB elements, nitrogen (N) preferentially occupies O sites (N_O) due to similar ionic radii, with low formation energies under oxygen-rich conditions.[79,211,213] However, according to DFT calculations, group-IA elements exhibit shallower acceptor levels than VB elements.[211] Although phosphorus (P), arsenic (As), and antimony (Sb) create deeper acceptor levels at O sites than N_O defects,[211] they form acceptor complexes when substituting Zn in the form of X_{Zn}-$2V_{Zn}$ (X: P, As, Sb) with ionization energies of 150–180 meV, establishing their viability as effective p-type dopants for ZnO.[214–216] Interestingly, a flexible PNG incorporating Sb-doped ZnO NWs grown via CBD has recently outperformed devices based on $BaTiO_3$ and PZT materials, based on the piezoelectric coefficient and volume of active piezoelectric material.[130]

For group-IB elements, according to DFT calculations, copper (Cu), silver (Ag), and gold (Au) are expected to occupy Zn sites with high transition energies $\varepsilon(0/-)$ of 0.7, 0.4, and 0.5 eV above the valence band maximum, respectively, under oxygen-rich conditions.[217] In particular, Cu, due to its ionic radius similar to Zn, can easily be incorporated at Zn sites without forming self-compensating interstitial donors.[217,218] Among distinct studies based on Cu-doped ZnO NWs synthesized via CBD,[219–221] the work of Dr. Clement LAUSECKER, an ancient PhD candidate at the LMGP – LTM – CEA Leti, provided valuable insights into the physicochemical and incorporation mechanisms of Cu, highlighting the importance of controlling the pH of the chemical bath.[222] Therefore, in the framework of this thesis, Cu was selected as the compensatory dopant for ZnO NWs using the CBD method. A detailed

discussion of the Cu-doping implications for the overall properties of ZnO NWs can be found in **Chapter II**.

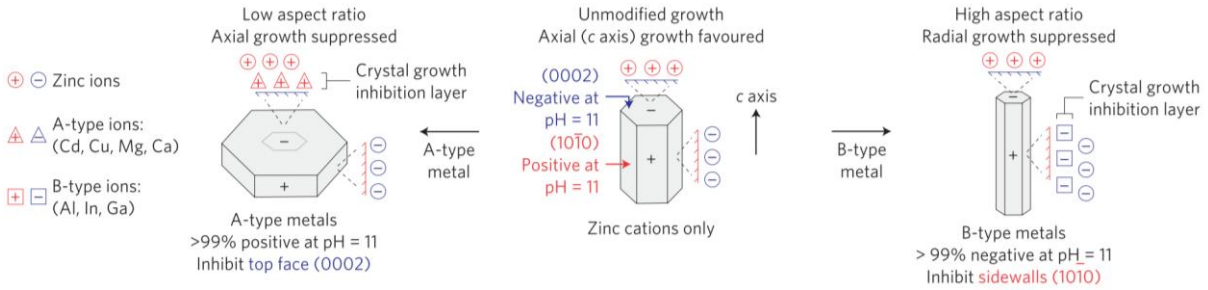

Figure I.4-6. *Face-selective electrostatic control for doping with non-zinc metal sulfates of ZnO NWs by hydrothermal method. Adapted from REF [204].*

Thesis Objective

This thesis was partially supported by LabEx MINOS[♣] funding under the contract ANR-10-LABX-55-01 and the French RENATECH network through the PTA technological platforms. Following the work of Dr. Clement LAUSECKER, whose thesis also received LabEX MINOS funding, the main objective of this thesis was to develop a performant PNG based on ZnO NWs grown by CBD. As previously discussed, these nanostructures exhibit a high density of free carriers, which promotes screening effects and degrades their piezoelectric properties. This thesis addresses this challenge through three complementary approaches for improving the energy conversion efficiency of PNGs:

1- **Reduce the free carrier density in ZnO NWs** to weaken screening effects.

2- **Modify the surface properties of ZnO NWs** using coating layers.

3- **Evaluate and control the morphological properties of ZnO NWs** on seed layers that can potentially function as bottom electrodes.

The first approach is developed in Chapter 2, focusing on altering the intrinsic properties of ZnO NWs to improve PNG performance. The second approach investigates the influence of coating polymers on the optical and structural properties of ZnO NWs, and the consequences on the related PNG behavior, discussed in Chapter 3. Finally, the third approach is detailed in Chapter 4, where promising initial results to tune the morphology of ZnO NWs are presented.

[♣] The LabEx – MINOS (Laboratories of Excellence – MInatec NOvel devices Scaling) program is a French government's funding to support scientific research.

Bibliography

[1] J. Curie, P. Curie, *Bull. la Société minéralogique Fr.* **1880**, *3*, 90–93.

[2] G. Lippmann, *J. Phys. Théorique Appliquée* **1881**, *10*, 381–394.

[3] P. Curie, J. Curie, *CONTRACTIONS ET DILATATIONS PRODUITES PAR DES TENSIONS ÉLECTRIQUES DANS LES CRISTAUX HÉMIÈDRES À FACES INCLINÉES*, Gauthier-Villars, **1908**.

[4] W. Voigt, *Abh. Gott* **1890**, *1*.

[5] W. Voigt, in *Lehrb. Der Krist.*, Vieweg+Teubner Verlag, Wiesbaden, **1966**, pp. 560–800.

[6] W. P. Mason, *J. Acoust. Soc. Am.* **1981**, *70*, 1561–1566.

[7] A. Ballato, in *1996 IEEE Ultrason. Symp. Proc.*, IEEE, **1996**, pp. 575–583.

[8] A. Arnau, D. Soares, in *Piezoelectric Transducers Appl.*, Springer Berlin Heidelberg, Berlin, Heidelberg, **2008**, pp. 1–38.

[9] J. Rödel, J.-F. Li, *MRS Bull.* **2018**, *43*, 576–580.

[10] X. Zhang, Characterization and Structuration of Piezoelectric ZnO-Based Composites : Toward Medical Applications, **2022**.

[11] A. N. S. Institute, *IEEE Trans. Sonics Ultrason.* **1984**, *31*, i–i.

[12] J. Li, *Lead-Free Piezoelectric Materials*, Wiley, **2021**.

[13] C. Falconi, G. Mantini, A. D'Amico, V. Ferrari, in *Fundam. Piezoelectric Sensorics Mech. Dielectr. Thermodyn. Prop. Piezoelectric Mater.*, Springer Berlin Heidelberg, Berlin, Heidelberg, **2012**, pp. 93–133.

[14] G. Poulin, **2004**.

[15] J. D. N. Cheeke, J. D. N. Cheeke, *Fundamentals and Applications of Ultrasonic Waves*, CRC Press, **2010**.

[16] K. UCHINO, *Advanced Piezoelectric Materials: Science and Technology*, Woodhead Publishing, **2017**.

[17] W. Hooker, *Properties of PZT-Based Piezoelectric Ceramics between -150 and 250 ° C*, **1998**.

[18] R. Lay, G. S. Deijs, J. Malmström, *RSC Adv.* **2021**, *11*, 30657–30673.

[19] P. Zhao, B.-P. Zhang, J.-F. Li, *Appl. Phys. Lett.* **2007**, *90*, 1–4.

[20] Q. Guo, F. Li, F. Xia, P. Wang, X. Gao, H. Hao, H. Liu, H. Sun, S. Zhang, *J. Mater.* **2021**, *7*, 683–692.

[21] W. Yue, J. Yi-jian, *Opt. Mater. (Amst).* **2003**, *23*, 403–408.

[22] Y. Guo, H. Luo, T. He, X. Pan, Z. Yin, *Mater. Res. Bull.* **2003**, *38*, 857–864.

[23] A. Dadgar, M. Weyers, in *Met. Vap. Phase Ep.*, Wiley, **2019**, pp. 109–147.

[24] S. Trolier-Mckinstry, P. Muralt, *J. Electroceramics* **2004**, *12*, 7–17.

[25] Z. L. Wang, *J. Phys. Condens. Matter* **2004**, *16*, DOI 10.1088/0953-8984/16/25/R01.

[26] M. Catti, Y. Noel, R. Dovesi, *J. Phys. Chem. Solids* **2003**, *64*, 2183–2190.

[27] I. Vurgaftman, J. R. Meyer, *J. Appl. Phys.* **2003**, *94*, 3675–3696.

[28] F. Bernardini, V. Fiorentini, D. Vanderbilt, *Phys. Rev. B* **1997**, *56*, R10024–R10027.

[29] I. B. Kobiakov, *Solid State Commun.* **1980**, *35*, 305–310.

[30] D. Berlincourt, H. Jaffe, L. R. Shiozawa, *Phys. Rev.* **1963**, *129*, 1009–1017.

[31] L. Schmidt-Mende, J. L. MacManus-Driscoll, *Mater. Today* **2007**, *10*, 40–48.

[32] H. Morkoç, *Handbook of Nitride Semiconductors and Devices*, Wiley, **2008**.

[33] J. S. Harrison, Z. Ounaies, *Piezoelectric Polymers*, 2001.

[34] J. Y. H. Kim, A. Cheng, Y. C. Tai, *Proc. IEEE Int. Conf. Micro Electro Mech. Syst.* 2011, 473–476.

[35] P. Kabakov, T. Kim, Z. Cheng, X. Jiang, S. Zhang, *Annu. Rev. Mater. Res.* 2023, *53*, 165–193.

[36] R. E. Newnham, D. P. Skinner, L. E. Cross, *Mater. Res. Bull.* 1978, *13*, 525–536.

[37] D. C. Reynolds, D. C. Look, B. Jogai, *Solid State Commun.* 1996, *99*, 873–875.

[38] Ü. Özgür, Y. I. Alivov, C. Liu, A. Teke, M. A. Reshchikov, S. Doğan, V. Avrutin, S.-J. Cho, H. Morkoç, *J. Appl. Phys.* 2005, *98*, 1–103.

[39] C. Klingshirn, *ChemPhysChem* 2007, *8*, 782–803.

[40] A. Moezzi, A. M. McDonagh, M. B. Cortie, *Chem. Eng. J.* 2012, *185–186*, 1–22.

[41] C. R. A. Catlow, A. M. Stoneham, *J. Phys. C Solid State Phys.* 1983, *16*, 4321–4338.

[42] C. Noguera, F. Finocchi, J. Goniakowski, *J. Phys. Condens. Matter* 2004, *16*, S2509–S2537.

[43] J. Goniakowski, F. Finocchi, C. Noguera, *Reports Prog. Phys.* 2008, *71*, 016501.

[44] J. Zúñiga-Pérez, V. Consonni, L. Lymperakis, X. Kong, A. Trampert, S. Fernández-Garrido, O. Brandt, H. Renevier, S. Keller, K. Hestroffer, M. R. Wagner, J. S. Reparaz, F. Akyol, S. Rajan, S. Rennesson, T. Palacios, G. Feuillet, *Appl. Phys. Rev.* 2016, *3*, DOI 10.1063/1.4963919.

[45] V. Consonni, A. M. Lord, *Nano Energy* 2021, *83*, DOI 10.1016/j.nanoen.2021.105789.

[46] T. COSSUET, 2019, 309.

[47] S.-H. Na, C.-H. Park, *J. Korean Phys. Soc.* 2009, *54*, 867–872.

[48] T. Cossuet, E. Appert, J. L. Thomassin, V. Consonni, *Langmuir* 2017, *33*, 6269–6279.

[49] A. Mang, K. Reimann, S. Rübenacke, *Solid State Commun.* 1995, *94*, 251–254.

[50] A. Janotti, C. G. Van De Walle, *Reports Prog. Phys.* 2009, *72*, DOI 10.1088/0034-4885/72/12/126501.

[51] B. K. Meyer, H. Alves, D. M. Hofmann, W. Kriegseis, D. Forster, F. Bertram, J. Christen, A. Hoffmann, M. Straßburg, M. Dworzak, U. Haboeck, A. V. Rodina, *Phys. Status Solidi Basic Res.* 2004, *241*, 231–260.

[52] A. Kelly, K. M. Knowles, *Crystallography and Crystal Defects*, Wiley, 2012.

[53] A. Janotti, C. G. Van de Walle, *Phys. Rev. B* 2007, *76*, 165202.

[54] C. G. Van de Walle, *Phys. B Condens. Matter* 2001, *308–310*, 899–903.

[55] M. Todorova, J. Neugebauer, *Surf. Sci.* 2015, *631*, 190–195.

[56] C. Jagadish, S. Pearton, *Zinc Oxide Bulk, Thin Films and Nanostructures*, Elsevier, 2006.

[57] N. H. NICKEL, E. TERUKOV, *Zinc Oxide-A Material for Micro-and Optoelectronic Applications*, Springer, n.d.

[58] M. D. McCluskey, S. J. Jokela, *J. Appl. Phys.* 2009, *106*, 1–13.

[59] X. Yang, N. C. Giles, *J. Appl. Phys.* 2009, *105*, DOI 10.1063/1.3079336.

[60] T. Makino, Y. Segawa, A. Tsukazaki, A. Ohtomo, M. Kawasaki, *Appl. Phys. Lett.* 2005, *87*, 1–4.

[61] W.-K. Hong, G. Jo, S.-S. Kwon, S. Song, T. Lee, *IEEE Trans. Electron Devices* 2008, *55*, 3020–3029.

[62] C. P. Dietrich, M. Brandt, M. Lange, J. Kupper, T. Böntgen, H. von Wenckstern, M. Grundmann, *J. Appl. Phys.* 2011, *109*, 1–6.

[63] Y. W. Heo, D. P. Norton, L. C. Tien, Y. Kwon, B. S. Kang, F. Ren, S. J. Pearton, J. R. LaRoche, *Mater. Sci. Eng. R Reports* 2004, *47*, 1–47.

[64] A. De Luna Bugallo, F. Donatini, C. Sartel, V. Sallet, J. Pernot, *Appl. Phys. Express* 2015, *8*, 025001.

[65] J. Goldberger, D. J. Sirbuly, M. Law, P. Yang, *J. Phys. Chem. B* 2005, *109*, 9–14.

[66] P. C. Chang, C. J. Chien, D. Stichtenoth, C. Ronning, J. G. Lu, *Appl. Phys. Lett.* 2007, *90*, DOI 10.1063/1.2712507.

[67] S. Song, W. K. Hong, S. S. Kwon, T. Lee, *Appl. Phys. Lett.* 2008, *92*, 2–5.

[68] S. P. Chiu, H. F. Chung, Y. H. Lin, J. J. Kai, F. R. Chen, J. J. Lin, *Nanotechnology* 2009, *20*, DOI 10.1088/0957-4484/20/10/105203.

[69] W. K. Hong, J. Yoon, T. Lee, *Nanotechnology* 2015, *26*, DOI 10.1088/0957-4484/26/12/125202.

[70] R. Könenkamp, K. Boedecker, M. C. Lux-Steiner, M. Poschenrieder, F. Zenia, C. Levy-Clement, S. Wagner, *Appl. Phys. Lett.* 2000, *77*, 2575–2577.

[71] I. Mora-Seró, F. Fabregat-Santiago, B. Denier, J. Bisquert, R. Tena-Zaera, J. Elias, C. Lévy-Clément, *Appl. Phys. Lett.* 2006, *89*, 1–4.

[72] T. Voss, C. Bekeny, J. Gutowski, R. Tena-Zaera, J. Elias, C. Ĺvy-Cĺment, I. Mora-Seró, J. Bisquert, *J. Appl. Phys.* 2009, *106*, DOI 10.1063/1.3211294.

[73] L. Wang, J. M. Chauveau, R. Brenier, V. Sallet, F. Jomard, C. Sartel, G. Brémond, *Appl. Phys. Lett.* 2016, *108*, DOI 10.1063/1.4945100.

[74] M. Den Hertog, F. Donatini, R. McLeod, E. Monroy, C. Sartel, V. Sallet, J. Pernot, *Nanotechnology* 2018, *29*, DOI 10.1088/1361-6528/aa923c.

[75] T. Cossuet, F. Donatini, A. M. Lord, E. Appert, J. Pernot, V. Consonni, *J. Phys. Chem. C* 2018, *122*, 22767–22775.

[76] J. B. Baxter, C. A. Schmuttenmaer, *J. Phys. Chem. B* 2006, *110*, 25229–25239.

[77] L. Wang, S. Guillemin, J. M. Chauveau, V. Sallet, F. Jomard, R. Brenier, V. Consonni, G. Brémond, *Phys. Status Solidi Curr. Top. Solid State Phys.* 2016, *13*, 576–580.

[78] J. Villafuerte, F. Donatini, J. Kioseoglou, E. Sarigiannidou, O. Chaix-Pluchery, J. Pernot, V. Consonni, *J. Phys. Chem. C* 2020, *124*, 16652–16662.

[79] J. Villafuerte, O. Chaix-Pluchery, J. Kioseoglou, F. Donatini, E. Sarigiannidou, J. Pernot, V. Consonni, *Phys. Rev. Mater.* 2021, *5*, 1–15.

[80] A. M. Lord, T. G. Maffeis, A. S. Walton, D. M. Kepaptsoglou, Q. M. Ramasse, M. B. Ward, J. Köble, S. P. Wilks, *Nanotechnology* 2013, *24*, DOI 10.1088/0957-4484/24/43/435706.

[81] Y. Yang, W. Guo, X. Wang, Z. Wang, J. Qi, Y. Zhang, *Nano Lett.* 2012, *12*, 1919–1922.

[82] R. Agrawal, B. Peng, E. E. Gdoutos, H. D. Espinosa, *Nano Lett.* 2008, *8*, 3668–3674.

[83] T. Li, Y. T. Li, W. W. Qin, P. P. Zhang, X. Q. Chen, X. F. Hu, W. Zhang, *Nanoscale Res. Lett.* 2015, *10*, 394.

[84] N. Bhadwal, R. Ben Mrad, K. Behdinan, *Sensors* 2023, *23*, DOI 10.3390/s23083859.

[85] M.-H. Zhao, Z.-L. Wang, S. X. Mao, *Nano Lett.* 2004, *4*, 587–590.

[86] M. Ghosh, S. Ghosh, M. Seibt, K. Y. Rao, P. Peretzki, G. Mohan Rao, *CrystEngComm* 2016, *18*, 622–630.

[87] M. T. Hoang, J. Yvonnet, A. Mitrushchenkov, G. Chambaud, *J. Appl. Phys.* 2013, *113*, DOI 10.1063/1.4773333.

[88] G. Tian, D. Xiong, Y. Su, T. Yang, Y. Gao, C. Yan, W. Deng, L. Jin, H. Zhang, X. Fan, C. Wang, W. Deng, W. Yang, W. Yang, *Nano Lett.* 2020, *20*, 4270–4277.

[89] R. K. Pandey, J. Dutta, S. Brahma, B. Rao, C.-P. Liu, *J. Phys. Mater.* **2021**, *4*, 044011.

[90] Y. Gao, Z. L. Wang, *Nano Lett.* **2009**, *9*, 1103–1110.

[91] R. Araneo, C. Falconi, *Nanotechnology* **2013**, *24*, 265707.

[92] G. Romano, G. Mantini, A. Di Carlo, A. D'Amico, C. Falconi, Z. L. Wang, *Nanotechnology* **2011**, *22*, DOI 10.1088/0957-4484/22/46/465401.

[93] A. M. Lord, T. G. Maffeis, A. S. Walton, D. M. Kepaptsoglou, Q. M. Ramasse, M. B. Ward, J. Köble, S. P. Wilks, *Nanotechnology* **2013**, *24*, DOI 10.1088/0957-4484/24/43/435706.

[94] C. Opoku, A. S. Dahiya, F. Cayrel, G. Poulin-Vittrant, D. Alquier, N. Camara, *RSC Adv.* **2015**, *5*, 69925–69931.

[95] Z. L. Wang, J. Song, *Science (80-.).* **2006**, *312*, 242–246.

[96] Z. L. Wang, R. Yang, J. Zhou, Y. Qin, C. Xu, Y. Hu, S. Xu, *Mater. Sci. Eng. R Reports* **2010**, *70*, 320–329.

[97] Z. L. Wang, *Adv. Mater.* **2012**, *24*, 4632–4646.

[98] S. Xu, Y. Qin, C. Xu, Y. Wei, R. Yang, Z. L. Wang, *Nat. Nanotechnol.* **2010**, *5*, 366–373.

[99] G. Zhu, R. Yang, S. Wang, Z. L. Wang, *Nano Lett.* **2010**, *10*, 3151–3155.

[100] B. Zaarour, L. Zhu, C. Huang, X. Jin, H. Alghafari, J. Fang, T. Lin, *J. Ind. Text.* **2021**, *51*, 297–340.

[101] X. Ni, F. Wang, A. Lin, Q. Xu, Z. Yang, Y. Qin, *Sci. Adv. Mater.* **2013**, *5*, 1781–1787.

[102] C. Baek, H. Park, J. H. Yun, D. K. Kim, K.-I. Park, *MRS Adv.* **2017**, *2*, 3415–3420.

[103] Z. Li, G. Zhu, R. Yang, A. C. Wang, Z. L. Wang, *Adv. Mater.* **2010**, *22*, 2534–2537.

[104] B. Moorthy, C. Baek, J. E. Wang, C. K. Jeong, S. Moon, K. Il Park, D. K. Kim, *RSC Adv.* **2017**, *7*, 260–265.

[105] Y. K. Fuh, S. Y. Chen, J. C. Ye, *Appl. Phys. Lett.* **2013**, *103*, DOI 10.1063/1.4813909.

[106] P. Hu, Z. Xiong, H. Xue, J. Pan, Q. Lu, X. Xiao, in *2011 Int. Symp. Adv. Packag. Mater.*, IEEE, **2011**, pp. 43–46.

[107] X. Chen, S. Xu, N. Yao, Y. Shi, *Nano Lett.* **2010**, *10*, 2133–2137.

[108] H. B. Kang, J. Chang, K. Koh, L. Lin, Y. S. Cho, *ACS Appl. Mater. Interfaces* **2014**, *6*, 10576–10582.

[109] W. Wu, S. Bai, M. Yuan, Y. Qin, Z. L. Wang, T. Jing, *ACS Nano* **2012**, *6*, 6231–6235.

[110] J. Chang, L. Lin, *2011 16th Int. Solid-State Sensors, Actuators Microsystems Conf. TRANSDUCERS'11* **2011**, 747–750.

[111] J. Briscoe, S. Dunn, *Nano Energy* **2014**, *14*, 15–29.

[112] Z. Wang, X. Pan, Y. He, Y. Hu, H. Gu, Y. Wang, *Adv. Mater. Sci. Eng.* **2015**, *2015*, 1–21.

[113] X. Wang, J. Song, J. Liu, Z. L. Wang, *Science (80-.).* **2007**, *316*, 102–105.

[114] J. Liu, P. Fei, J. Song, X. Wang, C. Lao, R. Tummala, Z. L. Wang, *Nano Lett.* **2008**, *8*, 328–332.

[115] C. Xu, X. Wang, Z. L. Wang, *J. Am. Chem. Soc.* **2009**, *131*, 5866–5872.

[116] S. Xu, Y. Wei, J. Liu, R. Yang, Z. L. Wang, *Nano Lett.* **2008**, *8*, 4027–4032.

[117] M. H. Malakooti, Z. Zhou, H. A. Sodano, *Act. Passiv. Smart Struct. Integr. Syst. 2016* **2016**, *9799*, 97991Z.

[118] Y. Hu, Y. Zhang, C. Xu, L. Lin, R. L. Snyder, Z. L. Wang, *Nano Lett.* **2011**, *11*, 2572–2577.

[119] Y. Hu, C. Xu, Y. Zhang, L. Lin, R. L. Snyder, Z. L. Wang, *Adv. Mater.* **2011**, *23*, 4068–4071.

[120] G. Zhu, A. C. Wang, Y. Liu, Y. Zhou, Z. L. Wang, *Nano Lett.* **2012**, *12*, 3086–3090.

[121] S. Xu, B. J. Hansen, Z. L. Wang, *Nat. Commun.* **2010**, *1*, DOI 10.1038/ncomms1098.

[122] P. G. Kang, B. K. Yun, K. D. Sung, T. K. Lee, M. Lee, N. Lee, S. H. Oh, W. Jo, H. J. Seog, C. W. Ahn, I. W. Kim,

J. H. Jung, *RSC Adv.* 2014, *4*, 29799–29805.

[123] L. Lu, N. Jamond, P. Chrétien, F. Houzé, L. Travers, J. C. Harmand, F. Glas, F. H. Julien, E. Lefeuvre, N. Gogneau, M. Tchernycheva, *J. Phys. Conf. Ser.* 2016, *773*, 012010.

[124] A. T. Le, M. Ahmadipour, S. Y. Pung, *J. Alloys Compd.* 2020, *844*, 156172.

[125] D. Hu, M. Yao, Y. Fan, C. Ma, M. Fan, M. Liu, *Nano Energy* 2019, *55*, 288–304.

[126] Y. Fu, Y. Zhao, P. Wang, L. Xing, X. Xue, *Phys. Chem. Chem. Phys.* 2015, *17*, 2121–2126.

[127] O. Synhaivskyi, D. Albertini, P. Gaffuri, J. M. Chauveau, V. Consonni, B. Gautier, G. Bremond, *J. Phys. Chem. C* 2021, *125*, 15373–15383.

[128] M. Ahmad, M. K. Ahmad, M. H. Mamat, A. Mohamed, A. B. Suriani, N. M. A. N. Ismail, C. F. Soon, N. Nafarizal, *Micromachines* 2022, *13*, DOI 10.3390/mi13091450.

[129] Y. Sun, S. Shen, W. Deng, G. Tian, D. Xiong, H. Zhang, T. Yang, S. Wang, J. Chen, W. Yang, *Nano Energy* 2023, *105*, 108024.

[130] J. Villafuerte, X. Zhang, E. Sarigiannidou, F. Donatini, O. Chaix-Pluchery, L. Rapenne, M.-Q. Le, L. Petit, J. Pernot, V. Consonni, *Nano Energy* 2023, *114*, 108599.

[131] R. Hinchet, S. Lee, G. Ardila, L. Montès, M. Mouis, Z. L. Wang, *Adv. Funct. Mater.* 2014, *24*, 971–977.

[132] J.-H. Tian, J. Hu, S.-S. Li, F. Zhang, J. Liu, J. Shi, X. Li, Z.-Q. Tian, Y. Chen, *Nanotechnology* 2011, *22*, 245601.

[133] D. Yang, Y. Qiu, Q. Jiang, Z. Guo, W. Song, J. Xu, Y. Zong, Q. Feng, X. Sun, *Appl. Phys. Lett.* 2017, *110*, DOI 10.1063/1.4975477.

[134] S. Lu, Q. Liao, J. Qi, S. Liu, Y. Liu, Q. Liang, G. Zhang, Y. Zhang, *Nano Res.* 2016, *9*, 372–379.

[135] K. Y. Lee, B. Kumar, J. Seo, K.-H. Kim, J. I. Sohn, S. N. Cha, D. Choi, Z. L. Wang, S. Kim, *Nano Lett.* 2012, *12*, 1959–1964.

[136] H. Zhang, G. Tian, D. Xiong, T. Yang, S. Zhong, L. Jin, B. Lan, L. Deng, S. Wang, Y. Sun, W. Yang, W. Deng, *ACS Appl. Mater. Interfaces* 2022, *14*, 29061–29069.

[137] S. Shin, M. H. Lee, J. Jung, J. H. Seol, J. Nah, *J. Mater. Chem. C* 2013, *1*, 8103.

[138] B. Yin, Y. Qiu, H. Zhang, J. Lei, Y. Chang, J. Ji, Y. Luo, Y. Zhao, L. Hu, *Nano Energy* 2015, *14*, 95–101.

[139] J. Lei, B. Yin, Y. Qiu, H. Zhang, Y. Chang, Y. Luo, Y. Zhao, J. Ji, L. Hu, *RSC Adv.* 2015, *5*, 59458–59462.

[140] C. Liu, M. Peng, A. Yu, J. Liu, M. Song, Y. Zhang, J. Zhai, *Nano Energy* 2016, *26*, 417–424.

[141] C. Justeau, T. S. Tlemcani, G. Poulin-Vittrant, K. Nadaud, D. Alquier, *Materials (Basel).* 2019, *12*, DOI 10.3390/ma12162511.

[142] Ü. Özgür, Y. I. Alivov, C. Liu, A. Teke, M. A. Reshchikov, S. Doğan, V. Avrutin, S.-J. Cho, H. Morkoç, *J. Appl. Phys.* 2005, *98*, 1–103.

[143] S. Xu, Z. L. Wang, *Nano Res.* 2011, *4*, 1013–1098.

[144] P. Anastas, N. Eghbali, *Chem. Soc. Rev.* 2010, *39*, 301–312.

[145] C. Lausecker, B. Salem, X. Baillin, V. Consonni, *J. Phys. Chem. C* 2019, *123*, 29476–29483.

[146] K. Fujita, K. Murata, T. Nakazawa, I. Kayama, *Yogyo Kyokai Shi/Journal Ceram. Soc. Japan* 1984, *92*, 227–230.

[147] M. A. Vergés, A. Mifsud, C. J. Serna, *J. Chem. Soc. Faraday Trans.* 1990, *86*, 959–963.

[148] L. Vayssieres, K. Keis, S.-E. Lindquist, A. Hagfeldt, *J. Phys. Chem. B* 2001, *105*, 3350–3352.

[149] L. Vayssieres, K. Keis, A. Hagfeldt, S. E. Lindquist, *Chem. Mater.* **2001**, *13*, 4395–4398.

[150] D. Lincot, *MRS Bull.* **2010**, *35*, 778–789.

[151] R. Parize, J. Garnier, O. Chaix-Pluchery, C. Verrier, E. Appert, V. Consonni, *J. Phys. Chem. C* **2016**, *120*, 5242–5250.

[152] S. Guillemin, L. Rapenne, H. Roussel, E. Sarigiannidou, G. Brémond, V. Consonni, *J. Phys. Chem. C* **2013**, *117*, 20738–20745.

[153] J. Zúñiga-Pérez, V. Consonni, L. Lymperakis, X. Kong, A. Trampert, S. Fernández-Garrido, O. Brandt, H. Renevier, S. Keller, K. Hestroffer, M. R. Wagner, J. S. Reparaz, F. Akyol, S. Rajan, S. Rennesson, T. Palacios, G. Feuillet, *Appl. Phys. Rev.* **2016**, *3*, DOI 10.1063/1.4963919.

[154] V. Consonni, A. M. Lord, *Nano Energy* **2021**, *83*, DOI 10.1016/j.nanoen.2021.105789.

[155] M. N. R. Ashfold, R. P. Doherty, N. G. Ndifor-Angwafor, D. J. Riley, Y. Sun, *Thin Solid Films* **2007**, *515*, 8679–8683.

[156] D. Kashchiev, G. M. van Rosmalen, *Cryst. Res. Technol.* **2003**, *38*, 555–574.

[157] J. J. Richardson, F. F. Lange, *Cryst. Growth Des.* **2009**, *9*, 2570–2575.

[158] C. Verrier, E. Appert, O. Chaix-Pluchery, L. Rapenne, Q. Rafhay, A. Kaminski-Cachopo, V. Consonni, *J. Phys. Chem. C* **2017**, *121*, 3573–3583.

[159] S. P. Dagnall, D. N. Hague, A. D. C. Towl, *J. Chem. Soc. Faraday Trans. 2* **1982**, *78*, 2161.

[160] I. Persson, *Pure Appl. Chem.* **2010**, *82*, 1901–1917.

[161] K. M. McPeak, M. A. Becker, N. G. Britton, H. Majidi, B. A. Bunker, J. B. Baxter, *Chem. Mater.* **2010**, *22*, 6162–6170.

[162] J. B. Cui, C. P. Daghlian, U. J. Gibson, R. Püsche, P. Geithner, L. Ley, *J. Appl. Phys.* **2005**, *97*, DOI 10.1063/1.1854206.

[163] S. Guillemin, V. Consonni, E. Appert, E. Puyoo, L. Rapenne, H. Roussel, *J. Phys. Chem. C* **2012**, *116*, 25106–25111.

[164] S. Guillemin, E. Appert, H. Roussel, B. Doisneau, R. Parize, T. Boudou, G. Bremond, V. Consonni, *J. Phys. Chem. C* **2015**, *119*, 21694–21703.

[165] S. Guillemin, R. Parize, J. Carabetta, V. Cantelli, D. Albertini, B. Gautier, G. Brémond, D. D. Fong, H. Renevier, V. Consonni, *Nanotechnology* **2017**, *28*, 1–10.

[166] Q. C. Bui, G. Ardila, H. Roussel, C. Jiménez, I. Gélard, O. Chaix-Pluchery, X. Mescot, S. Boubenia, B. Salem, V. Consonni, *Mater. Adv.* **2022**, *3*, 498–513.

[167] T. Cossuet, H. Roussel, J. M. Chauveau, O. Chaix-Pluchery, J. L. Thomassin, E. Appert, V. Consonni, *Nanotechnology* **2018**, *29*, DOI 10.1088/1361-6528/aadf62.

[168] S. Xu, C. Lao, B. Weintraub, Z. L. Wang, *J. Mater. Res.* **2008**, *23*, 2072–2077.

[169] S. Boubenia, A. S. Dahiya, G. Poulin-Vittrant, F. Morini, K. Nadaud, D. Alquier, *Sci. Rep.* **2017**, *7*, 1–10.

[170] C. Lausecker, B. Salem, X. Baillin, V. Consonni, *Cryst. Growth Des.* **2023**, *23*, 2941–2950.

[171] C. Lausecker, B. Salem, X. Baillin, H. Roussel, E. Sarigiannidou, F. Bassani, E. Appert, S. Labau, V. Consonni, *Nanotechnology* **2019**, *30*, DOI 10.1088/1361-6528/ab1d6e.

[172] M. W. Allen, M. M. Alkaisi, S. M. Durbin, *Appl. Phys. Lett.* **2006**, *89*, 1–4.

[173] L. J. Brillson, Y. Lu, *J. Appl. Phys.* 2011, *109*, DOI 10.1063/1.3581173.

[174] A. M. Lord, V. Consonni, T. Cossuet, F. Donatini, S. P. Wilks, *ACS Appl. Mater. Interfaces* 2020, *12*, 13217–13228.

[175] S. Xu, Y. Qin, C. Xu, Y. Wei, R. Yang, Z. L. Wang, *Nat. Nanotechnol.* 2010, *5*, 366–373.

[176] A. Yu, H. Li, H. Tang, T. Liu, P. Jiang, Z. L. Wang, *Phys. Status Solidi - Rapid Res. Lett.* 2011, *5*, 162–164.

[177] K. H. Kim, K. Y. Lee, J. S. Seo, B. Kumar, S. W. Kim, *Small* 2011, *7*, 2577–2580.

[178] C. Opoku, A. S. Dahiya, C. Oshman, F. Cayrel, G. Poulin-Vittrant, D. Alquier, N. Camara, *Phys. Procedia* 2015, *70*, 858–862.

[179] R. B. Peterson, C. L. Fields, B. A. Gregg, *Langmuir* 2004, *20*, 5114–5118.

[180] Q. Ahsanulhaq, A. Umar, Y. B. Hahn, *Nanotechnology* 2007, *18*, 115603.

[181] Y. M. Lee, H. W. Yang, *J. Solid State Chem.* 2011, *184*, 615–623.

[182] D. Singh, A. A. Narasimulu, L. Garcia-Gancedo, Y. Q. Fu, N. Soin, G. Shao, J. K. Luo, *Nanotechnology* 2013, *24*, DOI 10.1088/0957-4484/24/27/275601.

[183] M. Guo, P. Diao, S. Cai, *J. Solid State Chem.* 2005, *178*, 1864–1873.

[184] V. Strano, R. G. Urso, M. Scuderi, K. O. Iwu, F. Simone, E. Ciliberto, C. Spinella, S. Mirabella, *J. Phys. Chem. C* 2014, *118*, 28189–28195.

[185] C. Xu, P. Shin, L. Cao, D. Gao, *J. Phys. Chem. C* 2010, *114*, 125–129.

[186] H. Wang, J. Xie, K. Yan, M. Duan, *J. Mater. Sci. Technol.* 2011, *27*, 153–158.

[187] L. Chen, X. Li, L. Qu, C. Gao, Y. Wang, F. Teng, Z. Zhang, X. Pan, E. Xie, *J. Alloys Compd.* 2014, *586*, 766–772.

[188] D. Vernardou, G. Kenanakis, S. Couris, E. Koudoumas, E. Kymakis, N. Katsarakis, *Thin Solid Films* 2007, *515*, 8764–8767.

[189] W. Wu, G. Hu, S. Cui, Y. Zhou, H. Wu, *Cryst. Growth Des.* 2008, *8*, 4014–4020.

[190] G. Amin, M. H. Asif, A. Zainelabdin, S. Zaman, O. Nur, M. Willander, *J. Nanomater.* 2011, *2011*, DOI 10.1155/2011/269692.

[191] C. Verrier, E. Appert, O. Chaix-Pluchery, L. Rapenne, Q. Rafhay, A. Kaminski-Cachopo, V. Consonni, *Inorg. Chem.* 2017, *56*, 13111–13122.

[192] P. Gaffuri, E. Appert, O. Chaix-Pluchery, L. Rapenne, M. Salaün, V. Consonni, *Inorg. Chem.* 2019, *58*, 10269–10279.

[193] C. Verrier, E. Appert, O. Chaix-Pluchery, L. Rapenne, Q. Rafhay, A. Kaminski-Cachopo, V. Consonni, *Inorg. Chem.* 2017, *56*, 13111–13122.

[194] R. Kitsomboonloha, S. Baruah, M. T. Z. Myint, V. Subramanian, J. Dutta, *J. Cryst. Growth* 2009, *311*, 2352–2358.

[195] C. H. Wang, A. S. W. Wong, G. W. Ho, *Langmuir* 2007, *23*, 11960–11963.

[196] Z. Szabó, J. Volk, E. Fülöp, A. Deák, I. Bársony, *Photonics Nanostructures - Fundam. Appl.* 2013, *11*, 1–7.

[197] C. Zhang, X. Huang, H. Liu, S. J. Chua, C. A. Ross, *Nanotechnology* 2016, *27*, 485604.

[198] X. Chen, P. Lin, X. Yan, Z. Bai, H. Yuan, Y. Shen, Y. Liu, G. Zhang, Z. Zhang, Y. Zhang, *ACS Appl. Mater. Interfaces* 2015, *7*, 3216–3223.

[199] S. Xu, Y. Wei, M. Kirkham, J. Liu, W. Mai, D. Davidovic, R. L. Snyder, L. W. Zhong, *J. Am. Chem. Soc.* 2008,

130, 14958–14959.

[200] J. J. Cheng, S. M. Nicaise, K. K. Berggren, S. Gradečak, *Nano Lett.* 2016, *16*, 753–759.

[201] V. Consonni, E. Sarigiannidou, E. Appert, A. Bocheux, S. Guillemin, F. Donatini, I. C. Robin, J. Kioseoglou, F. Robaut, *ACS Nano* 2014, *8*, 4761–4770.

[202] C. G. Van De Walle, *Phys. Rev. Lett.* 2000, *85*, 1012–1015.

[203] J. Villafuerte, E. Sarigiannidou, F. Donatini, J. Kioseoglou, O. Chaix-Pluchery, J. Pernot, V. Consonni, *Nanoscale Adv.* 2022, *4*, 1793–1807.

[204] J. Joo, B. Y. Chow, M. Prakash, E. S. Boyden, J. M. Jacobson, *Nat. Mater.* 2011, *10*, 596–601.

[205] Y. K. Frodason, K. M. Johansen, T. S. Bjørheim, B. G. Svensson, A. Alkauskas, *Phys. Rev. B* 2018, *97*, 104109.

[206] O. Synhaivskyi, D. Albertini, P. Gaffuri, J. M. Chauveau, V. Consonni, B. Gautier, G. Bremond, *J. Phys. Chem. C* 2021, *125*, 15373–15383.

[207] M. D. McCluskey, S. J. Jokela, *J. Appl. Phys.* 2009, *106*, DOI 10.1063/1.3216464.

[208] J. I. Sohn, S. N. Cha, B. G. Song, S. Lee, S. M. Kim, J. Ku, H. J. Kim, Y. J. Park, B. L. Choi, Z. L. Wang, J. M. Kim, K. Kim, *Energy Environ. Sci.* 2013, *6*, 97–104.

[209] S. H. Shin, Y. H. Kim, M. H. Lee, J. Y. Jung, J. H. Seol, J. Nah, *ACS Nano* 2014, *8*, 10844–10850.

[210] V. A. Cao, M. Kim, S. Lee, C. G. Kim, P. Cao Van, T. N. Thi, J. R. Jeong, J. Nah, *ACS Appl. Mater. Interfaces* 2022, *14*, 26824–26832.

[211] C. H. Park, S. B. Zhang, S. H. Wei, *Phys. Rev. B - Condens. Matter Mater. Phys.* 2002, *66*, 1–3.

[212] E. C. Lee, K. J. Chang, *Phys. Rev. B - Condens. Matter Mater. Phys.* 2004, *70*, 1–4.

[213] X. Yang, A. Wolcott, G. Wang, A. Sobo, R. C. Fitzmorris, F. Qian, J. Z. Zhang, Y. Li, *Nano Lett.* 2009, *9*, 2331–2336.

[214] S. Limpijumnong, S. B. Zhang, S. H. Wei, C. H. Park, *Phys. Rev. Lett.* 2004, *92*, 1–4.

[215] W.-J. Lee, J. Kang, K. J. Chang, *Phys. B Condens. Matter* 2006, *376–377*, 699–702.

[216] B. Puchala, D. Morgan, *Phys. Rev. B - Condens. Matter Mater. Phys.* 2012, *85*, 1–5.

[217] Y. Yan, M. M. Al-Jassim, S. H. Wei, *Appl. Phys. Lett.* 2006, *89*, 87–90.

[218] F. Gallino, C. Di Valentin, *J. Chem. Phys.* 2011, *134*, DOI 10.1063/1.3575198.

[219] L. Chow, O. Lupan, G. Chai, H. Khallaf, L. K. Ono, B. Roldan Cuenya, I. M. Tiginyanu, V. V. Ursaki, V. Sontea, A. Schulte, *Sensors Actuators, A Phys.* 2013, *189*, 399–408.

[220] I. Polat, S. Yilmaz, I. Altin, E. Bacaksiz, M. Sökmen, *Mater. Chem. Phys.* 2014, *148*, 528–532.

[221] A. H. Rakhsha, H. Abdizadeh, E. Pourshaban, M. R. Golobostanfard, V. R. Mastelaro, M. Montazerian, *Materialia* 2019, *5*, DOI 10.1016/j.mtla.2019.100212.

[222] C. Lausecker, B. Salem, X. Baillin, O. Chaix-Pluchery, H. Roussel, S. Labau, B. Pelissier, E. Appert, V. Consonni, *Inorg. Chem.* 2021, *60*, 1612–1623.

The page was intentionally left blank.

The page was intentionally left blank.

Chapter II – Cu-doping and thermal annealing of ZnO nanowires grown by chemical bath deposition for piezoelectric applications

Contents

II.1 State-of-the-art: strategies for extrinsic doping of ZnO nanowires in Chemical Bath Deposition – theoretical and experimental approaches 69
II.2 Cu-doping of ZnO nanowires grown by Chemical Bath Deposition – adsorption and incorporation mechanisms 71
II.2.1 Experimental procedure: Cu-doping of ZnO NWs with different Cu-dopant levels 71
II.2.2 Morphological properties 72
II.2.3 Physicochemical adsorption process of Cu (II)-related species 73
II.2.4 Structural properties 76
II.2.5 Raman spectroscopy 78
II.2.6 Cathodoluminescence at 5 K 82
II.2.7 XANES and XLD spectroscopy 85
II.2.8 Electrical properties assessed by two-point probe measurements on single NW 88
II.3 Effect of thermal annealing treatment in Cu-doped ZnO nanowires 93
II.3.1 Experimental procedure: thermal annealing of Cu-doped ZnO nanowires grown at fixed Cu-dopant level 93
II.3.2 Morphological properties 93
II.3.3 Raman spectroscopy 95
II.3.4 X-ray photoelectron spectroscopy 98
II.3.5 XANES and XLD spectroscopy 99
II.3.6 Electrical properties assessed by 2-point probes measurements on single NW 101
II.4 In-depth discussion of Cu-doping and thermal annealing effects on the optical and electrical properties of ZnO nanowires 104
II.5 Enhancing the output voltage of piezoelectric nanogenerators based on ZnO nanowire matrix through Cu-doping and thermal annealing 107
II.5.1 Piezoelectric characterizations on the LTM's test bench 107
II.5.2 Output voltage of piezoelectric nanogenerators based on a Cu-doped ZnO nanowire matrix 109
II.5.2.1 Fabrication of piezoelectric nanogenerators based on Cu-doped ZnO nanowires 109
II.5.2.2 Characterization of piezoelectric nanogenerators based on Cu-doped ZnO nanowires 110
II.5.3 Output voltage of piezoelectric nanogenerators based on thermally annealed ZnO nanowire matrix 115
II.5.3.1 Fabrication of piezoelectric nanogenerators based on thermally annealed ZnO nanowires 115
II.5.3.2 Characterization of piezoelectric nanogenerators based on thermally annealed ZnO nanowires 118
II.6 Conclusion 120
Bibliography 121

This chapter investigates the incorporation process of Cu atoms in ZnO NWs via CBD to compensate for their high free electron density. It aims to reduce the screening effect in ZnO NWs for piezoelectric applications. This work is based on previous research by Dr. Clément LAUSECKER, conducted at the LMGP, LTM, and CEA Leti between 2018 and 2021. In addition, the effect of thermal annealing on the electrical properties of ZnO NWs is also studied. Both the compensatory Cu-doping and thermal annealing present promising strategies to improve PNGs.

II.1 State-of-the-art: strategies for extrinsic doping of ZnO nanowires in Chemical Bath Deposition – theoretical and experimental approaches

As discussed in **Chapter I**, the high density of free electrons in ZnO nanowires (NWs) degrades their piezoelectric properties through detrimental screening effects. To address this issue, compensatory doping with acceptors has been identified as a promising solution. Among various acceptor elements from the I-A, V-A, and I-B groups,[1] copper (Cu) emerges as a promising candidate due to its abundance, low cost, and ionic radii similar to Zn, which allows Cu to easily substitute Zn in the lattice (Cu_{Zn}) with relatively low ionization energy.[2,3] Joo et al. proposed an effective approach to modify the aspect ratio of ZnO NWs using metallic dopants via adsorption processes, where pH-dependent electrostatic interactions guide the selective attachment of different metallic species,[4] such as Al, Ga, and Cu, to the polar *c*-plane and non-polar *m*-plane of ZnO NWs in aqueous solutions.[5–7]

In recent years, the doping of ZnO NWs via chemical bath deposition (CBD) with various metallic species has been well studied. This process relies on favorable thermodynamic conditions, such as low supersaturation♣ in the chemical bath[6,8,9] and reduced free energy of the adsorption process, which is influenced by chemical, coulombic, and solvation energies.[10,11] Therefore, the pH of the bath plays a critical role in controlling the nucleation, growth, and doping of ZnO NWs. Lausecker et al. demonstrated that in the presence of Zn(II) and Cu(II) species, different pH ranges significantly affect the formation of ZnO NWs and Cu-related phases, as schematized in **Figure II.1-1(a)**.[7] At low pH (5.2–5.7), shorter ZnO NWs are formed, while high supersaturation in the intermediate-pH range (5.7–8.0) results in excessive precipitation, inhibiting NW growth. In contrast, a high pH (8.0–8.7) favors the growth of longer ZnO NWs with minimal Cu precipitation. Under these high-pH conditions, i.e. oxygen-rich conditions, Cu is more likely to substitute Zn as a Cu_{Zn} acceptor, reducing free electron density and enhancing the piezoelectric properties of ZnO NWs, as suggested by density functional theory (DFT) calculations depicted in **Figure II.1-1(b)**.[12]

♣ Supersaturation refers to the difference between the initial concentration of metallic M^{X+} ions and the concentration at the thermodynamic equilibrium of soluble M(X) species in the chemical bath. More details will be provided in **Section 2.2.3**.

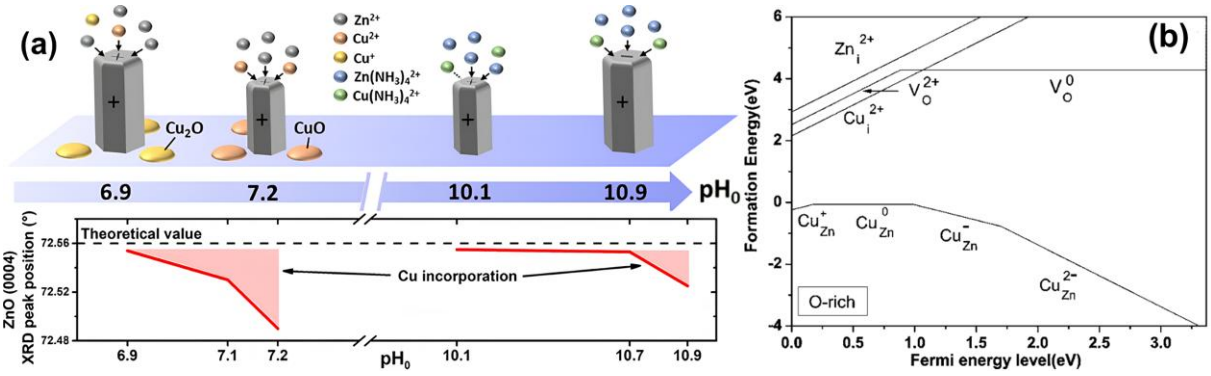

Figure II.1-1. (a) *Schematic diagram representing the incorporation mechanisms of Cu in ZnO NWs grown by CBD, along with the evolution of the (0004) diffraction peak of ZnO with the initial pH.* ***(b)*** *Formation energy of CuZn in ZnO under oxygen-rich conditions from DFT. Adapted from REFs [7] and [12], respectively.*

Objective

This chapter will present two distinct methods to achieve more electrically resistive ZnO NWs for piezoelectric applications. The objectives are as follows:

1- Compensatory Cu(II) doping: Investigate the adsorption and incorporation processes of Cu(II) in ZnO NWs grown by CBD in a high pH region, and examine how this affects their electrical properties. Additionally, fabricate and characterize a PNG based on a Cu-doped ZnO NW matrix using the test bench available at the Cameleon Platform – LTM.

2- Thermal annealing in a controlled O_2 atmosphere: Explore the impact of thermal annealing on the electrical properties of ZnO NWs grown via CBD in a high pH region. Similar to the 1st objective, evaluate the output voltage of PNGs integrating thermally annealed ZnO NW matrix.

II.2 Cu-doping of ZnO nanowires grown by Chemical Bath Deposition – adsorption and incorporation mechanisms

This section discusses the incorporation mechanisms of Cu(II) species in ZnO NWs during chemical bath deposition and their effects before and after a thermal annealing in an O_2 atmosphere at 500 °C.

The results presented in section II.2 and II.4 have been published in: Manrique, Manuel, et al. "Incorporation and Compensatory Doping Processes of Cu into ZnO Nanowires Investigated at the Local Scale." *Small Structures* (2024): 2400534.

II.2.1 Experimental procedure: Cu-doping of ZnO NWs with different Cu-dopant levels

The polycrystalline ZnO seed layers were firstly grown by sol-gel process on pre-cleaned (100) Si substrates. A solution mixing 375 mM of zinc acetate dehydrate ($Zn(CH_3COO)_2{\cdot}2H_2O$, Sigma-Aldrich) and 375 mM of monoethanolamine (MEA, Sigma-Aldrich) in pure ethanol was prepared and stirred for 12 h at 60 °C and then at room temperature. The (100) Si substrates, pre-cleaned in an ultrasonic bath with acetone and isopropyl alcohol, were subsequently dipped into the solution under a controlled atmosphere (<16% hygrometry) and finally annealed at 300 °C for 10 min on a hot plate and at 500 °C for 1 h in a regular oven. Then, ZnO NWs were grown by CBD in an aqueous solution of 54 ml mixing $Zn(NO_3)_2$ and HMTA with an equimolar ratio of 30 mM. The initial pH of the chemical bath (pH_0) was fixed at ~11.0 by adding ~800 mM of ammonia. In addition, Cu-dopant solutions with a concentration of 0.3, 0.9, 1.5, and 3 mM, previously prepared by dissolving copper nitrate hemi-pentahydrate ($Cu(NO_3)_2{\cdot}2.5H_2O$, Sigma Aldrich) in deionized water, were added to the chemical bath to fix the $[Cu(NO_3)_2]/[Zn(NO_3)_2]$ ratio at 1, 3, 5, and 10%, respectively. The growth of ZnO NWs was achieved by keeping the sealed reactors in a regular oven heated at 85 °C for 3 h. Finally, the synthesized ZnO NWs were thermally annealed in a tubular furnace at 500 °C under an O_2 atmosphere for 1h. **Table II.2-1** summarizes the growth conditions and the labels of the samples.

Table II.2-1. *Growth conditions of ZnO NWs with different $[Cu]/[Zn]_{bath}$ ratios.*

$[Cu]/[Zn]_{bath}$ (%)	$[Zn(NO_3)_2]_{bath}=[HMTA]_{bath}$ (mM)	$[Cu(NO_3)_2]_{bath}$ (mM)	$[NH_3]_{bath}$ (mM)	Comments
0	30	0	800	Total volume of solution: 54ml Growth time: 3h Temperature: 85 °C
1		0.3		
3		0.9		
5		1.5		
10		3		

II.2.2 Morphological properties

The homoepitaxial and heterogeneous growth of unintentionally n- and Cu-doped ZnO NWs was achieved by CBD on polycrystalline ZnO seed layers oriented along the polar *c*-axis.[13] The morphological properties of ZnO NWs with a $[Cu]/[Zn]_{bath}$ ratio varying in the range of 0 to 10% are presented in **Figure II.2-1(a-e)**. The resulting mean diameter measured at half of the height of the pristine ZnO NWs, their mean length, their aspect ratio defined as the ratio of their mean length over their mean diameter, and their number density are summarized in **Figure II.2-2**.

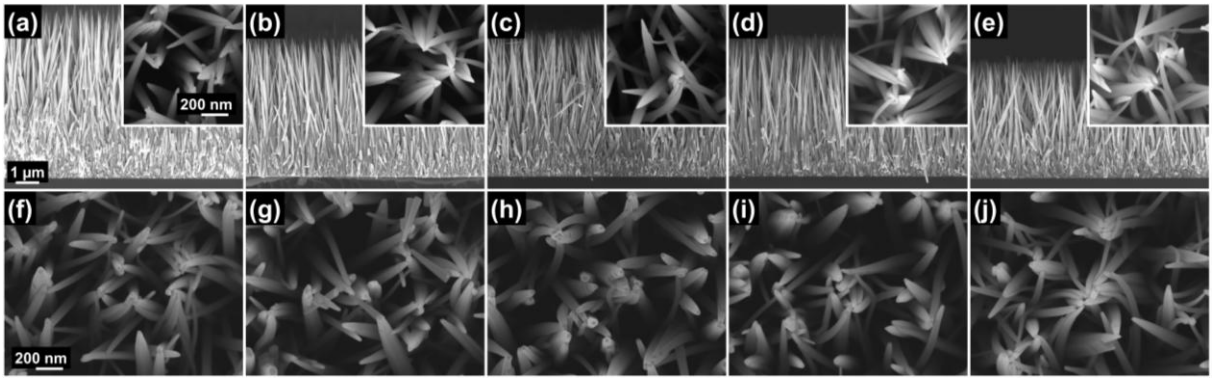

Figure II.2-1*. Cross-sectional and top-view (inset) FESEM images of ZnO NWs grown by CBD at 85 °C for 3h with [Cu]/[Zn]bath ratios of (a) 0, (b) 1, (c) 3, (d) 5, and (e) 10%, respectively. (f)-(j) Corresponding top-view FESEM images of these ZnO NWs after thermal annealing in an O_2 atmosphere at 500 °C for 1h.*

The ZnO NWs are vertically-aligned and exhibit a pencil-shaped top face, owing to the axial growth rate along the polar *c*-axis that is higher than the radial growth rate along the non-polar *m*-axis. Through the gradual increase in the $[Cu]/[Zn]_{bath}$ ratio, a progressive increase in the mean diameter of ZnO NWs from about 105 to 142 nm occurs, along with a progressive decrease in their mean length from about 7.8 to 5.6 µm. Hence, the aspect ratio of ZnO NWs is found to decrease from about 74.8 to 39.1 as the $[Cu]/[Zn]_{bath}$ ratio is increased from 0 to 10%. The number density of ZnO NWs lies in the range of 30 to 40 NW/µm^2 and does not show any particular tendency as a function of the $[Cu]/[Zn]_{bath}$ ratio. The present finding

is consistent with the fact that the number density of unintentionally n- and Cu-doped ZnO NWs is governed by the number of nucleation sites on the polycrystalline ZnO seed layers.[14]

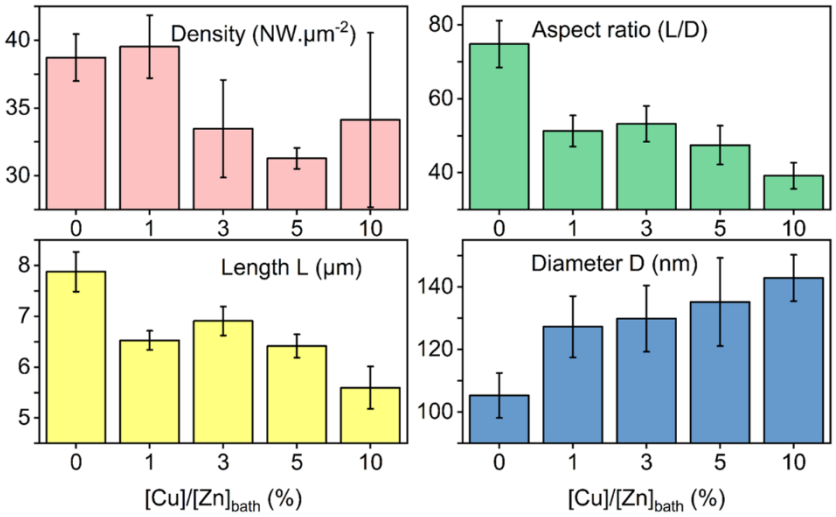

Figure II.2-2. *Resulting mean diameter, length, aspect ratio, and number density of ZnO NWs grown by CBD at different [Cu]/[Zn]$_{bath}$ ratios.*

In addition, no morphological changes of the pristine ZnO NWs regarding their shape and dimensions proceed after thermal annealing at 500 °C for 1 h under an O_2 atmosphere, as shown in **Figure II.2-1(f-j).**

II.2.3 Physicochemical adsorption process of Cu (II)-related species

To understand the physicochemical and adsorption processes of the Zn(II) and Cu(II) species occurring throughout the growth of ZnO NWs by CBD, the corresponding speciation diagrams are respectively plotted in **Figure II.2-3(a-b)** using Visual MINTEQ software. A [Cu]/[Zn]$_{bath}$ ratio of 1% was considered for the thermodynamic computations, by fixing the initial concentration of Zn^{2+} and Cu^{2+} ions at 30 mM and 0.3 mM, respectively. The pH was further set by varying the concentration of NH_4^+ ions from 0 to 2500 mM at 85 °C. At the thermodynamic equilibrium reached at 85 °C, the main Zn(II) species in the chemical bath are Zn^{2+} ions and $Zn(NH_3)_4^{2+}$ complexes in the pH regions below ~7 (low pH-region) and above ~7.7 (high pH-region), respectively. Interestingly, similar behavior is revealed for Cu(II) species, which form Cu^{2+} ions and $Cu(NH_3)_4^{2+}$ complexes in the low-pH and high-pH regions, respectively. The characteristics of the speciation diagrams along with the similar ionic radii of Zn(II) and Cu(II) ions strongly suggest the occurrence of identical adsorption processes during the growth of ZnO NWs by CBD.[2] It is worth mentioning that the speciation diagrams

of the Zn(II) and Cu(II) species for the $[Cu]/[Zn]_{bath}$ ratios of 1, 3, 5, and 10% reveal the same formation of Zn- and Cu-related species as a function of pH. The only difference among the present speciation diagrams is related to the degrees of supersaturation of Cu(II) and Zn(II) species, as illustrated in **Figure II.2-3(c-d)**. The supersaturation of metallic species, namely as M(X), refers to the difference between the initial concentration of M^{X+} ions ($[M(X)]_{initial}$) and the concentration at the thermodynamic equilibrium of soluble M(X) species ($[M(X)]_{eq}$)[6,8,9]. By adding a higher concentration of $Cu(NO_3)_2$ in the chemical bath, the supersaturation of Cu(II) species slightly increases, while the supersaturation of Zn(II) species decreases. Therefore, a competitive process of adsorption between the Zn(II) and Cu(II) species and thus incorporation of Zn and Cu occurs throughout the growth of ZnO NWs. This affects the morphology of ZnO NWs, which switches from larger to shorter NWs as the $[Cu]/[Zn]_{bath}$ ratio is increased, as summarized in **Figure II.2-2**.

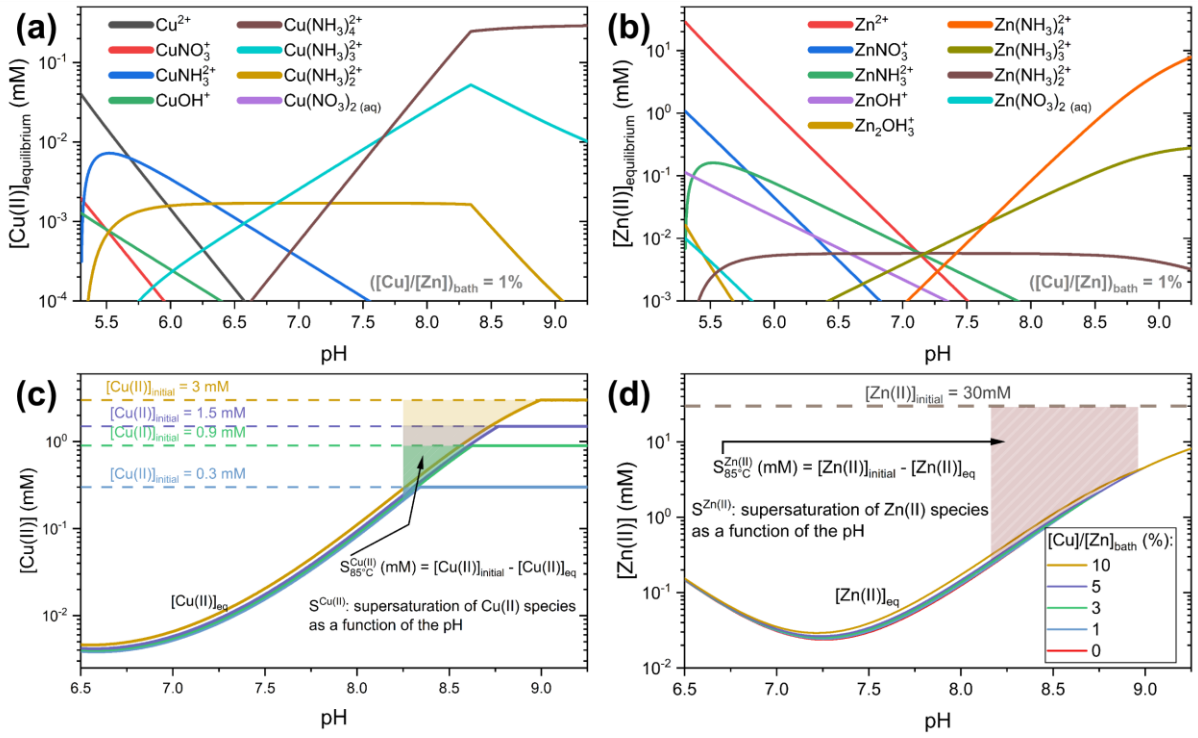

***Figure II.2-3**. Theoretical solubility plots of **(a)** Cu(II) and **(b)** Zn(II) species at 85°C according to Visual MINTEQ software, using the initial concentrations of Zn^{2+} and Cu^{2+} ions corresponding to 30 mM and 0.3 mM, respectively. Theoretical supersaturation of **(c)** Cu(II) and **(d)** Zn(II) species in the chemical bath mixing 0, 0.3, 0.9, 1.5, and 3 mM of Cu-solution with 30 mM of Zn-solution.*

It should be noted that the polar *c*-plane top facet and non-polar *m*-plane sidewalls of ZnO NWs are positively or negatively charged, owing to the formation of $–OH_2^+$ and $–O^-$ groups at the surface, respectively.[15] The electrical transition from positively to negatively charged surface occurs for a given pH value called the point-of-zero-charge (PZC), located at 8.7 ± 0.2

and 10.2 ± 0.2 for the polar *c*-plane and non-polar *m*-planes of ZnO NWs, respectively.[16,17] Since the electrical behavior of the surfaces of ZnO NW is crucial for the physicochemical adsorption of Cu(II) species, *in situ* pH measurements were performed to estimate the electrical charge of the ZnO NW surfaces during the CBD process. Thus, **Figure II.2-4(a)** confirms the growth of ZnO NWs by CBD in the high-pH region after thermalization of the chemical bath at 85 °C, in which the $Zn(NH_3)_4^{2+}$ and $Cu(NH_3)_4^{2+}$ complexes are the main expected Zn(II) and Cu(II) species, respectively. Therefore, the electrostatic forces between the positively-charged $Cu(NH_3)_4^{2+}$ complexes and the negatively-charged polar *c*-plane of ZnO NWs assist the adsorption process of Cu(II) species. The Coulomb interactions lead to favorable changes in the electrostatic free energy. The latter combined with the chemical free energy (involving surface hydrogen bonding and short-range dispersion forces) results in a cumulative energy that overcomes the solvation-free energy barrier (defined as the solvation energy change of an ion moving from the bulk to the interfacial region). This results in the establishment of advantageous thermodynamic conditions for the adsorption process of Cu(II) species on the outside Stern plane of solid ZnO NW faces.[7,10,11] Consequently, a progressive increase in the amount of Cu(II) species adsorbed on the surfaces of ZnO NWs, and thus of Cu incorporated on the surfaces of ZnO NWs and in their bulk, denoted as $[Cu]/[Zn]_{NW}$, is expected as the $[Cu]/[Zn]_{bath}$ ratio is increased. This is successfully shown using ICP-MS measurements, as presented in **Figure II.2-4(b)**, where the atomic $[Cu]/[Zn]_{NW}$ ratio increases from 2 to 80 ppm as the $[Cu]/[Zn]_{bath}$ ratio was increased from 0 to 10%. Interestingly, the atomic $[Cu]/[Zn]_{NW}$ ratios roughly keep the same values after thermal annealing at 500 °C for 1h under an O_2 atmosphere. Accordingly, considering six atoms of Zn in one crystallographic unit cell (i.e. 4.2×10^{22} at/cm^3 of Zn), the amount of Cu is around $4.5 \pm 0.5 \times 10^{16}$, $6.71 \pm 1.11 \times 10^{17}$, $1.03 \pm 0.36 \times 10^{18}$, $1.59 \pm 0.51 \times 10^{18}$, and $3.58 \pm 0.56 \times 10^{18}$ at/cm^3 in ZnO NWs grown by CBD before and after thermal annealing for the given $[Cu]/[Zn]_{bath}$ ratio of 0, 1, 3, 5 and 10%, respectively. It is worth mentioning that the lowest amount of Cu in ZnO NWs when grown with the $[Cu]/[Zn]_{bath}$ ratio of 0%, i.e. no Cu-dopant solution added in the chemical bath, is due to the significant amount of Cu residual impurities in the chemical precursors used as zinc nitrate, HMTA and ammonia. In addition, the quantification of Cu by ICP-MS involves the Cu dopants located both on the surfaces of ZnO NWs and in their bulk.

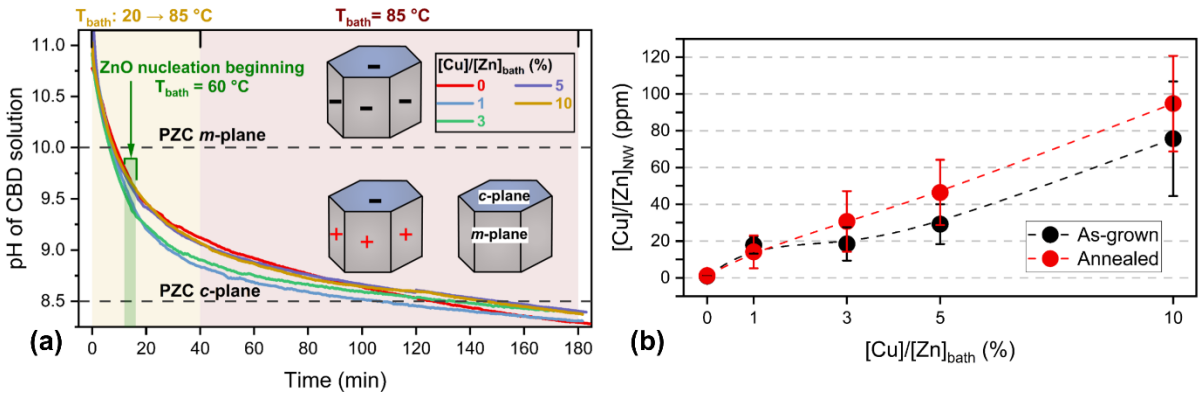

Figure II.2-4. (a) *In situ pH measurements of the chemical bath during the growth of ZnO NWs at different [Cu]/[Zn]bath ratios. The insets represent the expected surface electrical charge of the different crystallographic planes of ZnO NWs according to the PZC values reported in REFs [15–17].* ***(b)*** *Atomic [Cu]/[Zn]NW ratio inferred from ICP-MS of ZnO NWs grown by CBD at different [Cu]/[Zn]bath ratios. The annealed series corresponds to ZnO NWs thermally annealed at 500 °C for 1h under an O_2 atmosphere.*

II.2.4 Structural properties

The effect of the Cu(II) incorporation on the structural arrangement of ZnO NWs is assessed by XRD in the Bragg-Brentano configuration, in the narrow range from 30° to 100° with an acquisition time of 2.5 s for each 0.015° step, as presented in **Figure II.2-5(a)**. The instrumental shift was corrected by aligning the Si (400) diffraction peak to its theoretical value of 69.132°. The ZnO diffraction peaks were assigned according to the ICDD 00-036-1451 file. The wurtzite structure of ZnO NWs is revealed through its XRD peaks, exhibiting a preferential orientation along the *c*-axis based on the highest (002) diffraction peak at 34.4°. The presence of small diffraction peaks, which correspond to various orientations of the ZnO structure, and their varying intensity across different samples, suggest variations in the vertical arrangement of ZnO NWs and the amount of material deposited in each sample. As expected, no diffraction peaks related to any CuO, Cu_2O, or $Cu(OH)_2$ phases are observed. Therefore, no Cu-related solid phases precipitate in the chemical bath in the high-pH region, owing to the unfavorable thermodynamic conditions as suggested by the theoretical solubility plots of Cu(II) species in **Figure II.2-3(a),(c)**. The crystallographic constants *a* and *c* were subsequently calculated with the TOPAS program♣ by considering all the ZnO-related XRD peaks, as shown in **Figure II.2-5(b)**. The as-grown ZnO NWs exhibit *a* and *c* parameters higher than their bulk values of 3.24982 Å and 5.20661 Å, respectively, indicating that the NWs are under tensile stress relative to bulk ZnO. As the $[Cu]/[Zn]_{bath}$ ratio increases, there is a

♣ TOPAS program from BRUKER has numerous applications in crystallography field for quantitative phase analysis, analyzing microstructures, and analyzing crystal structures

negligible decrease in the *a* and *c* parameters, suggesting a slight but steady compressive stress in the wurtzite crystallographic structure. This apparent compression appears to be more pronounced after thermal annealing. However, given the minimal changes in these crystallographic parameters, it would be more consistent to conclude that Cu-doping does not affect the crystallographic quality of ZnO NWs. It is important to note that owing to the elasticity of the structure, a decrease in the *a* parameter would typically result in an increase in the *c* parameter. In addition, the detection limit of the XRD equipment could be not sufficient to accurately detect the effects of low concentrations of Cu atoms on the structural changes of ZnO NWs.

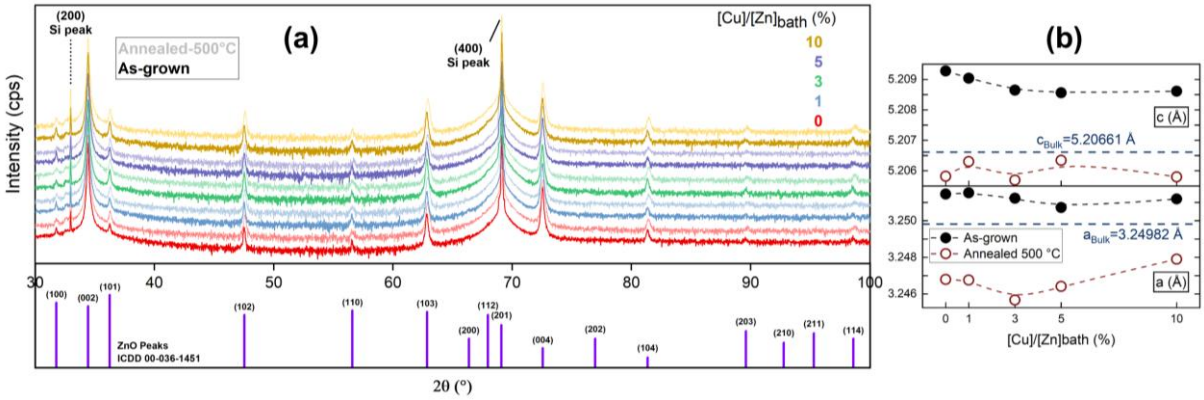

Figure II.2-5. (a) *XRD spectra in the Bragg-Brentano configuration of pristine and annealed ZnO NWs grown by CBD at 85 °C for 3h with [Cu)]/[Zn]$_{bath}$ ratios of 0, 1, 3, 5, and 10%, along with their* ***(b)*** *corresponding crystallographic constants. The latter were calculated with the TOPAS program by considering all the ZnO-related XRD peaks.*

The verticality of ZnO NWs grown with different [Cu]/[Zn]$_{bath}$ ratios is investigated through X-ray Pole Figures, as schematized in **Figure II.2-6(a)**. The X-ray Pole Figure patterns were recorded on the (002), (112), and (101) diffraction peaks at different *φ* positions ranging from 0° to 360°, along with χ varying from 0° to +90°. The pattern was subsequently plotted as a function of the χ angle from 0 to 90° by integrating the corresponding *φ* intensity in the range of 0 to 180°. **Figure II.2-6(b)-(d)** depicts the Pole Figures of ZnO NWs in the polar-(002) and semipolar (112) and (101) diffraction positions, respectively. The χ value refers to the angle difference between the normal to the substrate and the normal to the crystallographic plane (hkl). The Pole Figure peak on the (002), (112), and (101) diffraction position is centered at χ angles of 0.3°, 56.0°, and 59.2°, respectively, which is consistent with the theoretical χ. Given the broadening of the Pole Figure with the [Cu]/[Zn]$_{bath}$ ratio, its FWHM according to the χ position was considered to quantitatively measure the average tilt angle of ZnO NWs, as presented in **Figure II.2-6(e)**. The (002), (101) and (112) ZnO diffraction peaks show a

progressive tilting increase from 9.1 to 13.3° with the increase in the $[Cu]/[Zn]_{bath}$ ratio from 0 to 10%. This suggests that the addition of a higher concentration of $Cu(NO_3)_2$ in the chemical bath also influences the nucleation process of ZnO NWs,[18] which has also been reported using HMTA and PEI molecules.[14,19] As previously discussed in **Section II.2.3**, there is a direct competition of Zn(II) and Cu(II) species at the very beginning of the nucleation step of the ZnO NWs, occurring on the semipolar and polar *c*-planes of ZnO grains in the polycrystalline seed layer.[20]

In conclusion, Cu-doping affects the morphological properties and verticality of ZnO NWs, but it does not significantly disrupt the crystallographic quality of ZnO NWs.

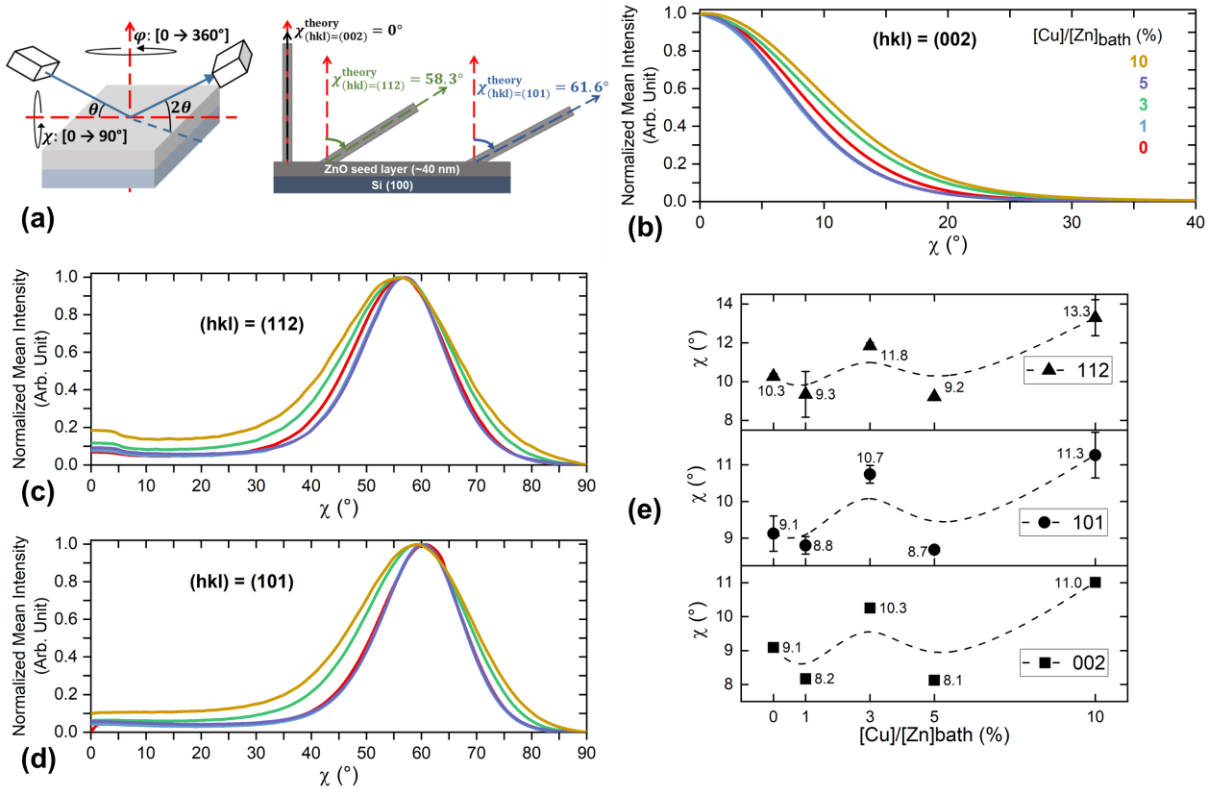

Figure II.2-6. (a) *Schema of X-ray pole acquisition and theoretical angle between the normal to the substrate and the (002), (112), and (101) ZnO diffraction peaks. Normalized mean intensity of X-ray pole figures recorded on the* ***(b)*** *(002),* ***(c)*** *(112), and* ***(d)*** *(101) diffraction peaks of ZnO NWs grown by CBD at 85 °C for 3h with* $[Cu]/[Zn]_{bath}$ *ratios of 0, 1, 3, 5, and 10%.* ***(e)*** *Resulting mean angle tilt from the theoretical angle between the normal to the substrate and the (002), (112), and (101) diffraction peak of the ZnO NW series.*

II.2.5 Raman spectroscopy

The effect of Cu-doping on the phonon modes of ZnO NWs was investigated by Raman spectroscopy in the scattering configuration at room temperature. A 532 nm excitation line of an Ar^+ laser probed the ZnO NW array from the top with a 100× objective and a power of ~2.5

mW on the sample surface. The spectral calibration was achieved using the theoretical Si Raman line set to 520.7 cm^{-1}.

The Raman scattering spectra of as-grown and thermally annealed ZnO NWs with a $[Cu]/[Zn]_{bath}$ ratio varying in the range of 0 to 10% were recorded in the low- and high-wavenumber regions, as presented in **Figure II.2-7(a-b)**, respectively. In the low-wavenumber region of 80-920 cm^{-1}, the typical phonon modes assigned to the wurtzite structure of ZnO NWs occur: the main Raman lines are located at 99 (E_2^{low}), 380 (A_1(TO)), 434 (E_2^{high}) and 581 (A_1(LO)) cm^{-1}, along with the second order Raman lines at 204 (2TA/2 E_2^{low}) and 333 (E_2^{high} - E_2^{low}) cm^{-1}. In the high-wavenumber region of 2600-3750 cm^{-1}, the Raman lines attributed to carbon-, nitrogen- and hydrogen-related defects occur. The broad Raman band lying from 2850 to 2990 cm^{-1} is assigned to phonon modes induced by the symmetric and anti-symmetric stretching bonds of $C\text{-}H_X$ (x=1, 2, 3),[21] as a result of an adsorption process of carbon on the *m*-plane sidewalls of ZnO NWs coming from the HMTA molecules.[14] Then, a weak Raman line is detected at 3073 cm^{-1} and related to V_{Zn}-N_O-H complexes,[22] followed by the occurrence of N_O-H-related phonons in the wavenumber region of 3100-3200 cm^{-1}.[23,24] Moreover, the V_{Zn}-*n*H (*n*=1, 2, 3) defect complexes lead to the broad Raman band observed from 3300 to 3450 cm^{-1}.[25–27] The asymmetric Raman shoulder lying between 3300 and 3650 cm^{-1} involves the contribution of O-H bonds[28] on the surfaces of ZnO NWs and H_{BC}[29] in their bulk.

By performing the thermal annealing of ZnO NWs at 500 °C under an O_2 atmosphere, several significant changes in the Raman scattering spectra arise, including the appearance of additional modes (AMs) in the low-wavenumber region and the apparent vanishing of Raman lines in the high-wavenumber region. Regardless of the $[Cu]/[Zn]_{bath}$ ratio of 0 to 10%, the occurrence of typical AMs after thermal annealing of ZnO NWs is depicted in the low-wavenumber region at 276 (B_1^{low}), 581 (B_1^{high}), 644 (TA+B_1^{high}), 668 (TA+LO), and 856 (B_1^{low} + B_1^{high}) cm^{-1}.[30,31] These AMs are due to the presence of silent Raman modes related to Al, Ga, Sb, and Fe as extrinsic impurities in ZnO NWs following the addition of ammonia in the chemical bath,[30] whose activation proceeds through the breakdown of the translational crystal symmetry upon thermal annealing.[32] A massive migration process of hydrogen in the form of H_{BC} further occurs towards the surfaces of ZnO NWs upon thermal annealing, where they recombine to form H_2 molecules leading to the vanishing of the different Raman lines attributed to hydrogen-related defects in the high-wavenumber region.[21,22] Moreover, no

Raman lines related to any Cu_2O, CuO, or $Cu(OH)_2$ phases are detected,[33] which is in agreement with XRD patterns.

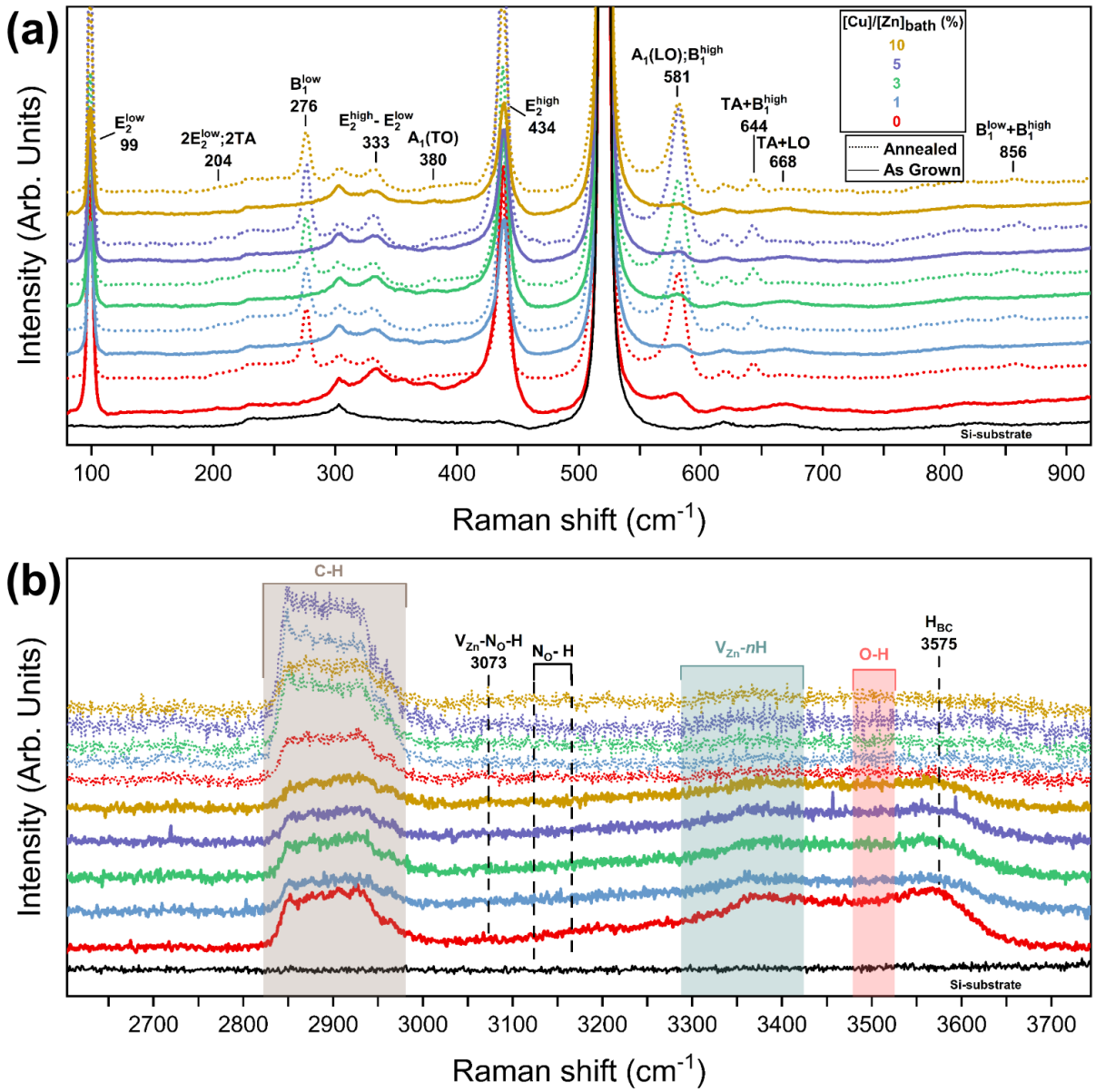

Figure II.2-7. *Raman scattering spectra of ZnO NWs grown by CBD at 85 °C for 3h for different $[Cu]/[Zn]_{bath}$ ratios, before and after thermal annealing at 500 °C for 1 h under an O_2 atmosphere, recorded in the* ***(a)*** *low- and* ***(b)*** *high-wavenumber regions.*

It is worth mentioning that the crystallographic properties of ZnO NWs can be correlated with their Raman line features. By focusing on the two intense and narrow E_2^{low} and E_2^{high} Raman lines of ZnO NWs, an increase in their intensity as well as a significant reduction of their full-width-at-half-maximum (FWHM) occurs after thermal annealing, regardless of the $[Cu]/[Zn]_{bath}$ ratio of 0 to 10%, as shown **Figure II.2-8(a-b)**. This reveals a strong improvement in the crystallinity of unintentionally n- and Cu-doped ZnO NWs following thermal annealing. In addition, as the $[Cu]/[Zn]_{bath}$ ratio increases, the noticeable shift of both E_2^{low} and E_2^{high}

Raman lines towards the higher wavenumbers could suggest the generation of a small compressive stress within the ZnO NWs. This would be in agreement with the nearly negligible decrease in the lattice parameters *a* and *c* observed in the XRD patterns. After thermal annealing, the E_2^{high} Raman line shifts to lower wavenumbers, likely indicating a residual tensile stress along the *c*-axis through the reduction of the lattice parameter *a*.[34] A similar shift of the E_2^{low} Raman line to lower wavenumbers would also be expected post-annealing; however, its opposite tendency suggests its unique behavior under pressure in wurtzite ZnO, as reported in REF [35]. The apparent lattice distortion of ZnO NWs when doped with Cu and after thermal annealing can induce structural potential fluctuations and finite-size effects, resulting in a change of the phonon contribution and subsequently in a modification of the shapes of the E_2^{low} and E_2^{high} Raman line.[36] Therefore, the unveiled changes in the shapes of the Raman lines along with the slight lattice parameter modification of ZnO NWs suggest the progressive incorporation of Cu atoms substituting for Zn sites (Cu_{Zn}) as the $[Cu]/[Zn]_{bath}$ ratio was increased. In addition, the absence of any AMs related to the Cu doping of ZnO NWs is consistent with the literature and does not imply the absence of Cu in the crystallographic structure of ZnO NWs.

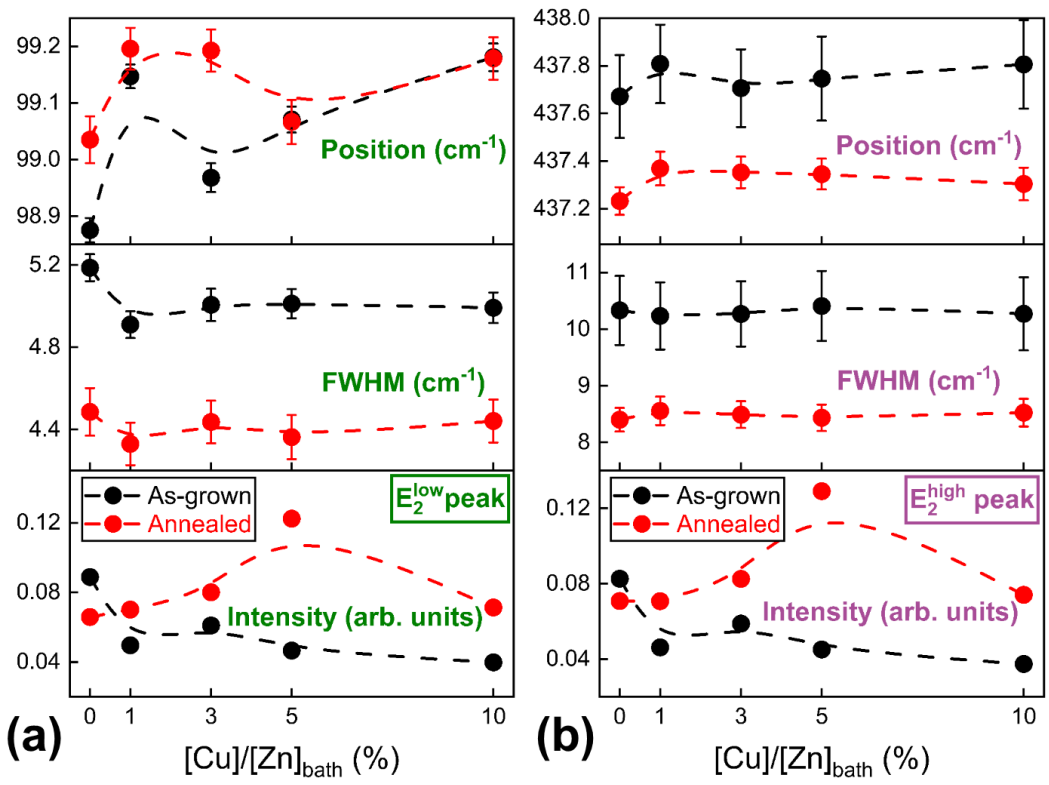

Figure II.2-8. *Evolution of the corresponding characteristics of the* ***(a)*** E_2^{low} *and* ***(b)*** E_2^{high} *Raman lines.*

II.2.6 Cathodoluminescence at 5 K

The 5K cathodoluminescence spectra of as-grown and thermally annealed ZnO NWs with a $[Cu]/[Zn]_{bath}$ ratio varying in the range of 0 to 10% are depicted in **Figure II.2-9** and **Figure II.2-10**, respectively. The typical near-band edge (NBE) emission of as-grown and annealed ZnO NWs involves the contribution of different radiative transitions, which are mainly related to neutral acceptor- and donor-bound excitons (A°X and D°X, respectively),[37] and free-A-excitons (FX),[37] as well as to donor-acceptor pair (DAP),[38–40] free electron-to-acceptor (FA),[40,41] and two-electron satellites (TES),[42,43] along with longitudinal optical (LO) phonon replicas with an energy separation of 72 meV.[43]

The NBE emission of as-grown ZnO NWs, as shown in the inset of **Figure II.2-9**, is centered at ~3.342 eV when the $[Cu]/[Zn]_{bath}$ ratio is 0%, and relatively broad with a full-width-at-half-maximum (FWHM) of 0.133 meV. It is composed of the main H-related D°X lines at 3.3601 (H_{BC}), 3.3614 (V_{Zn}-3H – I_5 line), and 3.3628 (H_O – I_4 line) eV,[44,45] as well as the associated TES lines in the range of 3.316 to 3.333 eV. In addition, radiative transitions involving extended defects resulting from the coalescence of grains in polycrystalline ZnO seed layers are also expected.[46] It should further be noted that the visible emission band is centered at ~2.0 eV, as shown in **Figure II.2-9**, and intense. It involves the emissions of transition levels (ε) related to V_{Zn}-related defect complexes. The red-orange emission band (1.6-2 eV) originates from deep acceptors such as $[V_{Zn}\text{-}H]^{\varepsilon(0/-1)}$ and $[V_{Zn}\text{-}N_O\text{-}H]^{\varepsilon(0/-1)}$ defect complexes, whose share an emission energy of 1.82 eV, as well as $[V_{Zn}]^{\varepsilon(-1/-2)}$ defects with an emission energy of 1.6 eV.[22,44] The yellow emission band (2-2.3 eV) results from $[V_{Zn}\text{-}2H]^{\varepsilon(+1/0)}$ and $[V_{Zn}\text{-}N_O\text{-}H]^{\varepsilon(0/-1)}$ defect complexes with an emission energy at 2.29 and 2.27 eV, respectively.[22,44] Finally, the green emission band (2.3-2.5 eV) is assigned to surface-related effects.[44,47] Interestingly, as the $[Cu]/[Zn]_{bath}$ ratio is increased from 0 to 10%, the intensity of the corresponding NBE emission is severely reduced and centered at ~3.311 eV, resulting in a redshift of about 31 meV. Concomitantly, the intensity of the visible emission band is significantly increased, which may be related to the change of the concentration of V_{Zn}-related defect complexes both in the bulk and on the surfaces of as-grown Cu-doped ZnO NWs.[44]

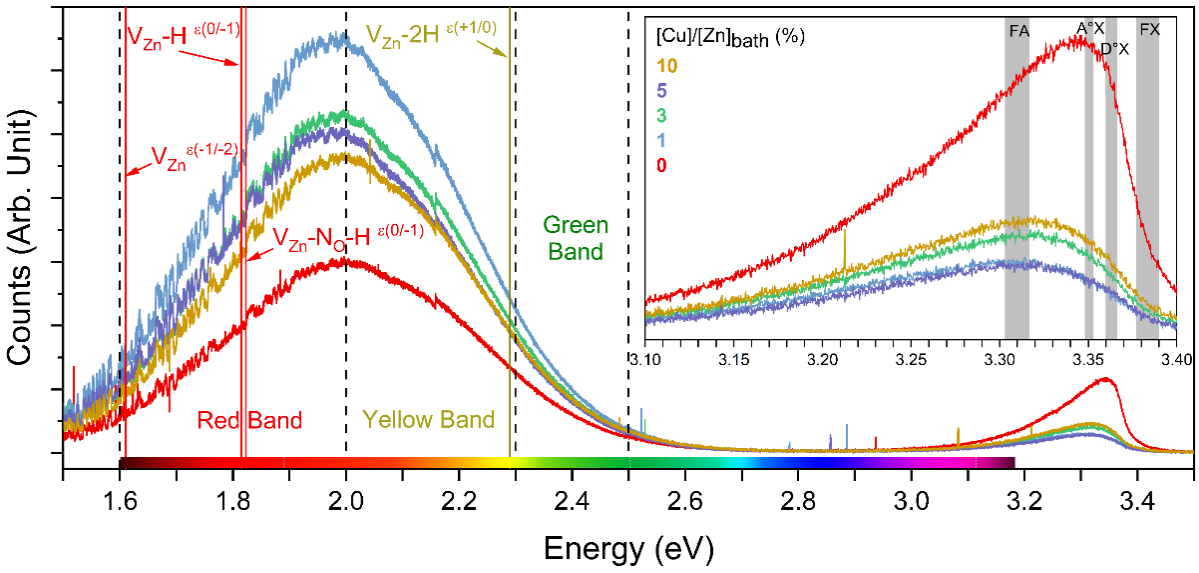

***Figure II.2-9**. 5K cathodoluminescence spectra of ZnO NWs grown by CBD with [Cu]/[Zn]$_{bath}$ ratios of 0, 1, 3, 5, and 10%, along with their respective NBE emission as an inset.*

Following a thermal annealing of unintentionally n- and Cu-doped ZnO NWs at 500 °C under O_2 atmosphere, a noteworthy change of their cathodoluminescence spectra is depicted. The NBE emission of thermally annealed ZnO NWs, as shown in the inset of **Figure II.2-10**, reveals a sharp line located at ~3.362 eV (denoted as Peak-1) within the region where the H_O (I_4 line) contribution is expected, specifically as the [Cu]/[Zn]$_{bath}$ ratio is above 0%.[44,45] In this same region, the D°X lines from Al- and Ga-related extrinsic donors occur at 3.3606 (Al_{Zn} – I_6 line) and 3.3598 (Ga_{Zn} – I_8 line) eV,[48] which is in agreement with their corresponding AMs observed in the Raman scattering spectra after thermal annealing. As a result, it is expected that the slight lattice distortion originating from the incorporation of Cu dopants as Cu_{Zn} likely favors the formation of Al_{Zn} and Ga_{Zn} extrinsic donors and hence the development of Peak-1. Accordingly, the intensity of Peak-1 steadily decreases as the [Cu]/[Zn]$_{bath}$ ratio is increased from 0 to 10%, resulting from a competitive process with the predominant formation of Cu_{Zn} defects with respect to Al_{Zn} and Ga_{Zn} extrinsic donors. Then, the broad shoulder centered at ~3.325 eV is assigned to the associated TES lines.[45] In contrast, the prominent line located at ~3.247 eV (denoted as Peak-2) dominates the NBE emission, with its first- and second-LO phonon replica at 3.171 and 3.097 eV, respectively. Peak-2 is mainly associated with DAP transitions related to a compensatory process of donor-acceptor pairs involving V_{Zn}, V_{Zn}-H and V_{Zn}-N_O-H defect complexes acting as deep acceptors.[31,40] It is worth mentioning that the slight redshift of Peak-2 as the [Cu]/[Zn]$_{bath}$ ratio is increased from 0 to 10% suggests a progressive increase in the concentration of acceptor defects contributing to DAP transitions. Importantly,

the visible emission band of unintentionally n- and Cu-doped ZnO NWs is the most affected following the thermal annealing, as presented in **Figure II.2-10**. Unintentionally n-doped ZnO NWs show a redshift from 2 to ~1.9 eV of the red-orange emission band after thermal annealing, which is in agreement with the expected massive formation of V_{Zn}-related defect complexes acting as deep acceptors.[31,40] Very interestingly, as the $[Cu]/[Zn]_{bath}$ ratio is increased from 1 to 10%, the visible band emission is strongly altered with a prominent peak at 2.428 eV corresponding to the 6°-LO phonon replica of the zero phonon line (ZPL) located at E_{ZPL}~2.856 eV and involving $[Cu_{Zn}^{2+}]^{\varepsilon(-1/-2)}$ acceptor defects.[49,50] The complete set of LO phonon replica of the ZPL are separated by ~70 meV, and are located at 2.785, 2.711, 2.642, 2.570, 2.495, 2.428, 2.362, 2.934 and 2.226 eV corresponding to the (1° – 9°)-LO phonon replica, respectively. The strong phonon coupling was assessed through the determination of the Huang-Rhys constant *S*, for which the values were found to be (6.61 ± 0.11), (6.45 ± 0.08), (6.40 ± 0.07) and (6.36 ± 0.06) in the case of ZnO NWs grown with $[Cu]/[Zn]_{bath}$ ratios of 1, 3, 5, and 10%, respectively. The ZPL emission peak is assigned to the radiative transitions from a (Cu^{+},h) short excited state to the Cu^{2+} ($^2T_2$) ground state.[51] When a neighboring O atom transfers one electron to the neutral acceptor Cu^{2+}, the negatively charged acceptor Cu^{1+} is created, which undergoes a transition to the (Cu^{+},h) excited state by capturing the free hole from a created free exciton under electron beam illumination. The (Cu^{+},h) excited state, located at ~0.4 eV above the valence band maximum, thus leads to the emission of a photon when the free hole is captured by the potential created by the tenth electron of the *d*-orbital of Cu^{+}, resulting in the Cu^{2+} ($^2T_2$) ground state located at ~0.2 eV below the conduction band minimum.[51,52] Therefore, the greatly enhanced green emission band as the $[Cu]/[Zn]_{bath}$ ratio is increased from 1 to 10% and following the thermal annealing involves: i) a surface-to-bulk migration process of Cu_{Zn} acceptor defects through the massive creation of V_{Zn} defects in ZnO NWs under O_2 atmosphere,[53] as well as ii) a change of the local environment of Cu_{Zn} acceptors through the likely formation of complexes involving V_{Zn} defects. Additionally, a redshifted secondary line constantly separated by ~30 meV from $[Cu_{Zn}]^{\varepsilon(-1/-2)}$-related transitions occurs, for which its origin is still unclear. West et al. suggest the appearance of a second series of radiative transitions separated by ~225 cm^{-1} (~28 meV) involving the spin-orbit splitting in the ground state of Cu^{2+}.[54] This hypothesis could strongly be correlated to the spin splitting of the valence (conduction) band maximum (minimum) owing the strong (weak) spin-orbit

coupling between the Cu *d*-orbital and O *p*-orbital (Zn *s*-orbital).[55,56] Moreover, Dingle et al. reported two Cu^{2+}-related peaks separated by 0.11 meV at the energy of ~2.8590 eV, whose two emission lines were assigned to an identical electronic process taking place at similar but separate sites involving ^{63}Cu and ^{65}Cu isotopes.[49] In the present work, the discussed two peaks are largely separated by 0.11 meV. It is worth mentioning that a transition between the (Cu^{+},h) excited state and the Cu^{2+} (E_2) ground state, located at 1 eV below the conduction band minimum, could occur as well under polarized light excitation.[57] However, the cathodoluminescence spectra were recorded under un-polarized electron beam. The 5K cathodoluminescence spectra eventually reveal unambiguously the incorporation of Cu dopants into ZnO NWs as the $[Cu]/[Zn]_{bath}$ ratio is above 0%.

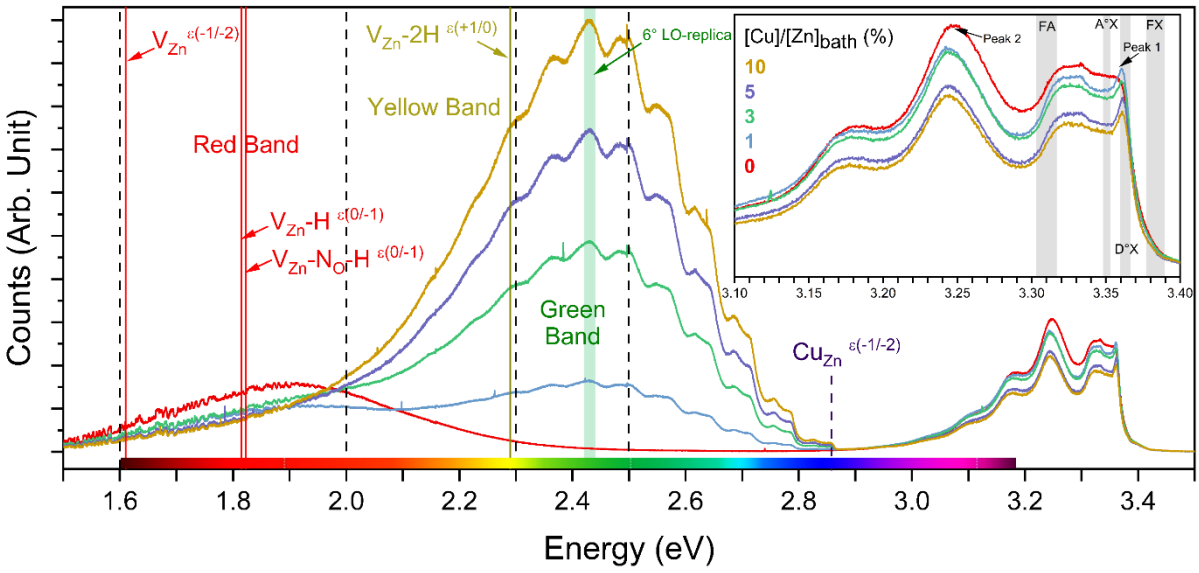

***Figure II.2-10**. 5K cathodoluminescence spectra of ZnO NWs grown by CBD with $[Cu]/[Zn]_{bath}$ ratios of 0, 1, 3, 5, and 10% after thermal annealing at 500 °C for 1 h under O_2 atmosphere, along with their respective NBE emission as an inset.*

II.2.7 XANES and XLD spectroscopy

To investigate the local environment around Cu and Zn atoms in Cu-doped ZnO NWs before and after thermal annealing, XANES and XLD spectra were recorded at the ESRF ID12 beamline. The experimental Zn K-edge XANES spectra, recorded with the polar *c*-axis oriented perpendicular (E⊥*c*) and parallel (E//*c*) to the electric field of the linearly polarized X-ray beam, along with their difference as the XLD spectrum, of Cu-doped ZnO NWs with a $[Cu]/[Zn]_{bath}$ ratio of 5%, are shown in **Figure II.2-11(a-b)**, respectively. The XANES and XLD spectral shape depicts the typical Zn atoms with an oxidation state of 2+ structured in a wurtzite configuration, i.e. Zn^{2+} cations surrounded by O^{2-} anions in a tetrahedral coordination.[58,59] It

should be mentioned that the spectral shape along with the intensity (amplitude of 1.15) of the Zn K-edge XLD spectra of Cu-doped ZnO NWs were found to be similar regardless of the $[Cu]/[Zn]_{bath}$ ratio. These XLD spectra are comparable to those of both-high quality Co-doped ZnO films and Ga-doped ZnO NWs.[60,61] This indicates that i) the Cu-doped ZnO NWs exhibit a high degree of vertical alignment along the *c*-axis (no XLD signal was detected in the substrate plane, i.e. absence of ZnO NWs parallel to the substrate), and that ii) the incorporation of Cu dopants does not disturb the local wurtzite crystalline quality of ZnO NWs, which is consistent with the Raman scattering spectra and XRD patterns). It is worth mentioning that the atomic ratio between the Cu and Zn atoms into the ZnO NWs (denoted as $[Cu]/[Zn]_{NW}$) can quantitatively be determined by comparing directly the edge jump intensity at the Cu K-edge and Zn K-edge. For instance, in the case of Cu-doped ZnO NWs grown with a $[Cu]/[Zn]_{bath}$ ratio of 5%, an atomic $[Cu]/[Zn]_{NW}$ ratio as low as ~0.01% was found. Despite the sizeable concentration of Cu-dopants present in the chemical bath, only a very small amount of Cu-dopant is incorporated into the ZnO NWs during the CBD process. This agrees with ICP-MS measurements, where a low atomic $[Cu]/[Zn]_{NW}$ ratio in the ZnO NWs increasing from 2 (~0.0002%) to 80 (~0.008%) ppm is achieved through the increase in the $[Cu]/[Zn]_{bath}$ ratio from 0 to 10%. The normalized isotropic Cu K-edge XANES and corresponding XLD spectra of ZnO NWs grown at different $[Cu]/[Zn]_{bath}$ ratios are presented in **Figure II.2-11(c-d)**, respectively. The isotropic XANES spectra show a similar spectral shape regardless of the $[Cu]/[Zn]_{bath}$ ratio, exhibiting a peak at the leading edge followed by a prominent one located ~11 eV above. In addition, no pre-edge peak occurs within the noise-level in the recorded XANES spectra. Interestingly, the present isotropic XANES spectra at the Cu K-edge of Cu-doped ZnO NWs resemble the XANES spectrum recorded for 20% Cu-doped ZnO films grown by reactive magnetron sputtering (RMS) under optimum growth conditions,[62] but significantly differ from the XANES spectrum measured on low-concentrated Cu-doped ZnO polycrystalline pellets.[63,64] It should be noted that the XLD spectra at the Cu K-edge are found to exhibit a similar spectral shape that those at the Zn K-edge, which is nearly independent of the $[Cu]/[Zn]_{bath}$ ratio. This strongly suggests that few Cu atoms are arranged in a wurtzite structure by substituting for Zn sites. For instance, in the case of Cu-doped ZnO NWs grown with a $[Cu]/[Zn]_{bath}$ ratio of 5%, a maximum amplitude of ~0.09 is reached for the XLD signal at the Cu K-edge, which is much lower as compared to the XLD signal recorded at the Zn K-

edge (amplitude of 1.15). As a comparison, an amplitude of about 0.5 of the XLD spectrum at the Cu K-edge is expected when substituting one Zn atom by one Cu^{2+} ion in a ZnO supercell using the bulk lattice constants, according to FDMNES simulations.[62] Hence, by comparing the XLD intensities measured at the Cu K-edge and Zn K-edge for ZnO NWs grown with a $[Cu]/[Zn]_{bath}$ ratio of 5%, only 15 ± 5% of the total amount of Cu dopants into ZnO NWs are incorporated as Cu_{Zn} . By considering 4.2×10^{22} at/cm^3 of Zn in one ZnO hexagonal crystallographic cell, the Cu_{Zn} amount here can thus be calculated by multiplying the intensity ratio of XANES and XLD spectra recorded at the Cu K-edge and Zn K-edge, i.e. $(0.01\%)\times(15\%)\times(4.2\times10^{22}$ at.cm$^{-3})=6.3\times10^{17}$ at/cm^3 of Cu_{Zn}. Following the present approach, the amount of Cu_{Zn} acceptor defects in ZnO NWs grown with $[Cu]/[Zn]_{bath}$ ratios of 1, 3, and 10% are expected to be 1.3, 3.8, and 12.7 $\times10^{17}$ at/cm^3, respectively. The majority amount of Cu (~85%) in ZnO NWs grown with a $[Cu]/[Zn]_{bath}$ ratio of 5% is likely in a Cu_2O-like environment when comparing its isotropic XANES spectrum with that of Cu-reference samples.[62] Vachhani et al. reported a similar conclusion in the case of Cu-doped ZnO films prepared by pulsed-laser deposition, in which most of the Cu atoms are not incorporated into the wurtzite structure, but exhibit a CuO-like coordination.[65]

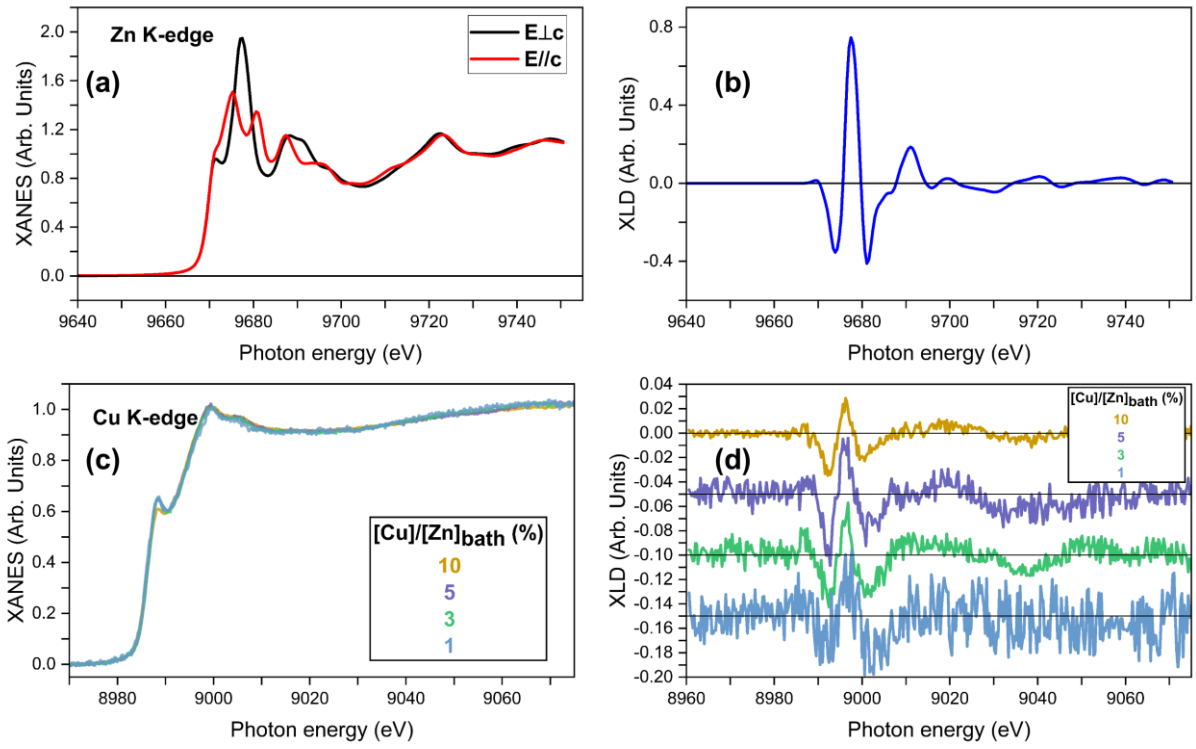

Figure II.2-11. *Zn K-edge* ***(a)*** *XANES and corresponding* ***(b)*** *XLD spectra of Cu-doped ZnO NWs grown by CBD with* $[Cu]/[Zn]_{bath}$ *ratio of 5%. Normalized* ***(c)*** *XANES and corresponding* ***(d)*** *XLD spectra of ZnO NWs grown by CBD with* $[Cu]/[Zn]_{bath}$ *ratios of 1, 3, 5, and 10% recorded at the Cu K-edge.*

Before thermal annealing, the minority CuZn dopants are likely incorporated in the bulk of ZnO NWs, while the majority amount of Cu is located on their surfaces. After thermal annealing of Cu-doped ZnO NWs grown with a $[Cu]/[Zn]_{bath}$ ratio of 5% at 500 °C under O_2 atmosphere, a noteworthy change of the isotropic XANES and XLD spectra recorded at Cu K-edge occurs, as depicted in **Figure II.2-12(a-b)**, respectively. The isotropic XANES spectra exhibit the disappearance of the sharp peak at the leading edge along with the widening of the following prominent peak. The XLD spectra also reveal a moderate peak around 9890 eV and a slight shift (~2 eV) to higher energies of the highest peak at ~9000 eV. The modifications of the XANES and XLD spectra observed in the case of thermally annealed Cu-doped ZnO NWs suggest a change in the electronic structure of the Cu dopants due to a more oxidizing local environment. This may indicate the formation of V_{Zn} defects in the vicinity of Cu dopants after thermal annealing, possibly forming Cu_{Zn}-related defect complexes as in the cases of Ga-doped ZnO NWs and Sb-doped ZnO NWs.[8,60,66–68]

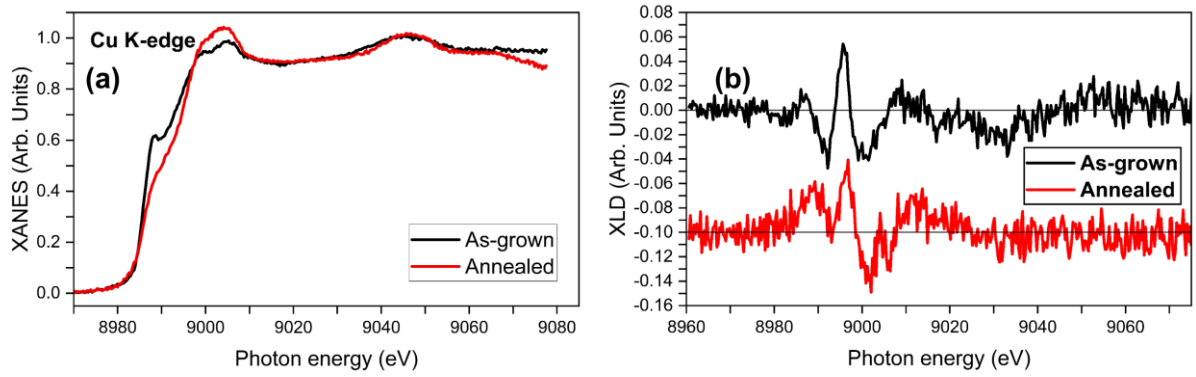

Figure II.2-12. *Normalized* ***(a)*** *XANES and corresponding* ***(b)*** *XLD spectra of ZnO NWs grown by CBD with a* $[Cu]/[Zn]_{bath}$ *ratio of 5%, before and after thermal annealing at 500 °C for 1 h under* O_2 *atmosphere.*

II.2.8 Electrical properties assessed by two-point probe measurements on single NW

Given the effective incorporation of Cu atoms within ZnO NWs, two-point probe measurements were performed to investigate their electrical properties before and after thermal annealing. The two-point probe resistivity measurements♣ were done on single NW-based channel bottom transistor devices, whose whole process flow of fabrication is schematized in **Figure II.2-13(a)**. A fragment of the substrate on which the ZnO NWs were

♣ Due to the resolution limitations of the photolithography equipment, only two metallic electrodes can be achieved to contact a single NW. Consequently, the two-point probe method was utilized to characterize the electrical properties of the NWs.

grown was immerged in isopropyl alcohol solution during a sonication process under ultrasound (1), allowing the NWs to be separated from the substrate. The isopropyl alcohol solution containing the dispersed ZnO NWs was subsequently put by drop casting on p++ Si (100) substrates coated with a Si_3N_4 insulating layer (2). The present substrate was placed on a heated plate to evaporate the isopropyl alcohol, leaving solely the ZnO NWs in contact with the Si_3N_4 insulating layer (3). A single and random ZnO NW was then selected to contact its edges with two metallic electrodes separated by ~4 µm through an optical lithography process. After the development of the photoresist, the contacts acting as the two metallic electrodes consisting of the stack of 100 nm thick Ti layer and 250 nm Au layer were achieved by vacuum evaporation followed by a lift-off process, resulting in an operating bottom transistor (4). The electrical characterizations of single ZnO NWs were performed in an ambient atmosphere by measuring the current *I* when sweeping an applied voltage *V* from -1 to +1 V with a step of 0.1 V between the two electrodes of the device. Therefore, the resistance *R* of each ZnO NW was determined as the slope of its corresponding linear *I-V* curve, according to Ohm's Law, as shown in **Figure II.2-13(b)**.

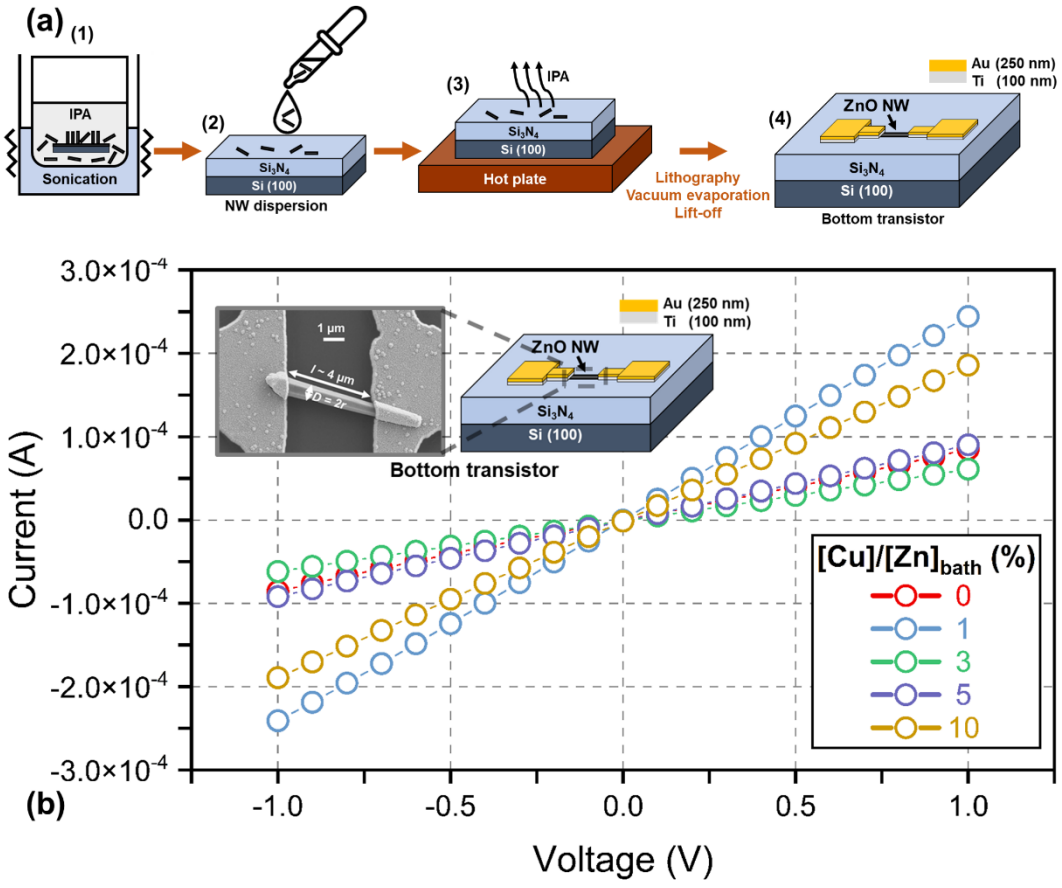

***Figure II.2-13**. **(a)** Fabrication steps of a single NW-based channel bottom transistor device. **(b)** Typical I-V curves for pristine ZnO NWs grown by CBD at 85 °C for 3h with different $[Cu]/[Zn]_{bath}$ ratios of 0, 1, 3, 5, and 10%.*

For clarification purposes, the R depends on the dimensions of the NW, while the electrical resistivity is determined by its intrinsic properties. Therefore, it is crucial to consider the NW dimensions to accurately evaluate its electrical properties. In addition, it should be noted that the establishment of a contact resistance may occur during the two-point probe measurements, such that the measured electrical resistance values can likely be overestimated. Therefore, the statistical analysis of the *R/l* values of distinct ZnO NWs, where *l* is the distance between the two metallic electrodes, was performed as a function of their radius *r*, as presented in **Figure II.2-14**. These *R/l* values are compared with experimental data from four-point probe measurements on ZnO NWs synthesized by different methods.[44,69] It should be mentioned that the *R/l* values depend on the *r*, regardless of the chemical synthesis. Indeed, the electrical conduction in ZnO NWs can be driven by two different mechanisms. When *r* is smaller than 25 nm,[69,70] a surface electron depletion region forms due to the chemisorption of O_2^- and OH^- ions,[47,70–72] leading to higher *R/l* values. In contrast, when *r* is above 25 nm, bulk-like electrical conduction in a flat-band regime becomes dominant, where electrons flow through the core of the ZnO NW.

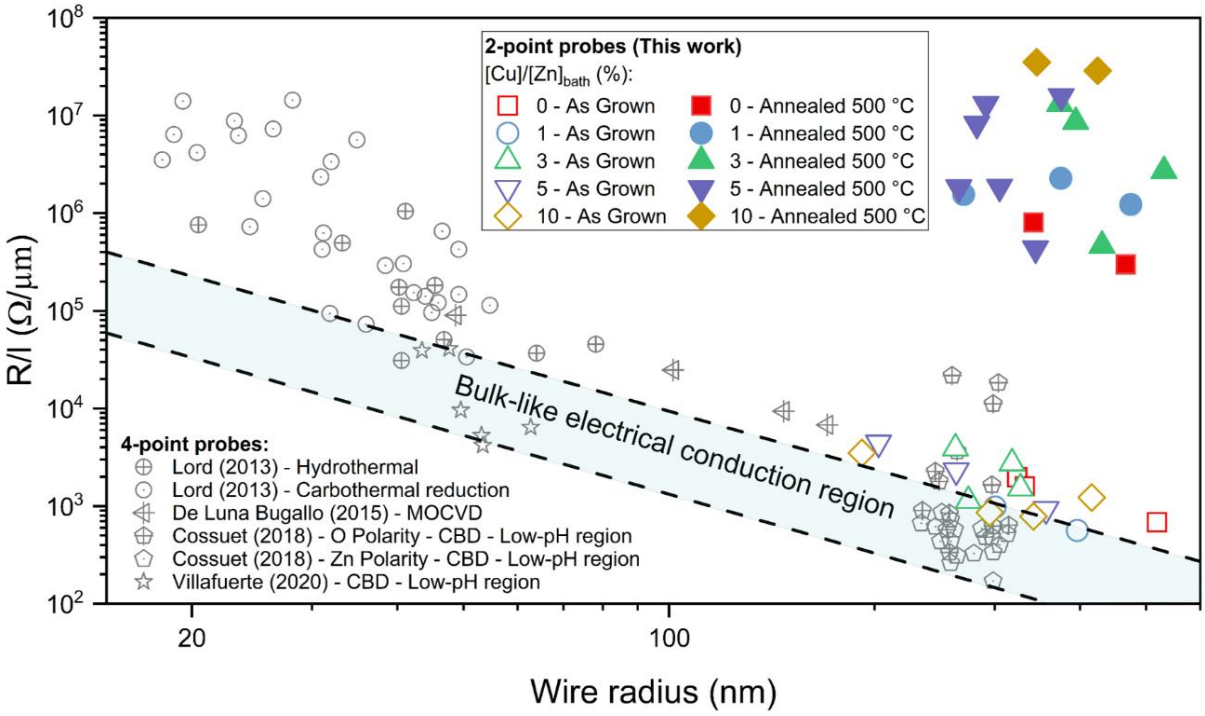

Figure II.2-14. *R/l values vs r of ZnO NWs for the present work assessed by the 2-point probe method, along with those reported on ZnO NWs grown by hydrothermal process,[73] carbothermal reduction,[73] MOCVD,[71] and CBD in the low-pH region.[44,69] Axis of R/l values is presented in the logarithmic scale. (Image inspired from REF [44]).*

The dashed lines in **Figure II.2-14**, representing isoresistivity values of 4.1 and 28.4 mΩ.cm (typical resistivity range for Zn-polar ZnO NWs), delimit this bulk-like electrical

conduction region in ZnO NWs, where surface effects are negligible, and electrons are expected to flow across the entire core of the ZnO NWs resulting in *R/l* values proportional to $1/r^2$.[44] The higher *R/l* values observed in as-grown ZnO NWs with a radius similar to those of REF [69] suggest an apparent overestimation due to contact resistance. However, it is important to note that the addition of ammonia to the chemical bath leads to oxygen-rich conditions, which could promote the formation of V_{Zn} defects which potentially dissociate shallow V_{Zn}-3H donor complexes, leading to increased electrical resistance.[31,66] Therefore, the rise in pH of the chemical solution could also account for the higher *R/l* values, as further discussed in **Section II.3.6**. Given that the 2-point probe method cannot separate the effects of pH from contact resistance, further studies on this topic are required. However, as the ZnO NWs differ only in their $[Cu]/[Zn]_{bath}$ ratio, it can be assumed that the pH and contact resistance effects remain identical across the samples, and consequently, any differences in electrical behavior among these NWs can be attributed to factors beyond these influences.

The electrical resistivity ρ was later estimated according to the following equation: $\rho \cong RS/l$, where *S* refers to the effective electrical conduction section of the ZnO NW, i.e. $S=\pi r^2$, considering a bulk-like electrical conduction in a flat-band regime.[71] The resulting ρ values of as-grown and thermally annealed ZnO NWs with a $[Cu]/[Zn]_{bath}$ ratio varying in the range of 0 to 10% are shown in **Figure II.2-15**. It should be mentioned that each point represents the mean resistivity value of an individual NW, each corresponding to a specific doping and thermal treatment, with measurements taken at least twice at different times during the academic year. The as-grown ZnO NWs present low ρ values lying in the range of 0.024 – 0.087 Ω.cm, regardless of the $[Cu]/[Zn]_{bath}$ ratio. In contrast, the thermally annealed ZnO NWs exhibit higher mean values of ρ, progressively increasing from 12.9 to 1479.4 Ω.cm as the $[Cu]/[Zn]_{bath}$ ratio was increased from 0 to 10%. The compensatory process with Cu dopants in as-grown ZnO NWs regardless of the $[Cu]/[Zn]_{bath}$ ratio is thus fairly poor. Concerning the thermally annealed ZnO NWs, their higher electrical resistivity values, regardless of the $[Cu]/[Zn]_{bath}$ ratio, is understandable beyond the influence of a contact resistance as the sign of an efficient compensatory process involving Cu dopants after thermal annealing. The electrical resistivity involving the intrinsic semiconducting properties can be defined as $\rho = \frac{1}{nq\mu}$, where *n*, *q* and μ refers to the mean charge carrier density (cm^{-3}), the absolute value of the electron charge (1.6×10^{-19} C), and the electron mobility ($cm^2V^{-1}s^{-1}$), respectively. If a

compensatory process occurs in Cu-doped ZnO NWs, a decrease in the free electron density and mobility would be expected as reported in thin Cu-doped ZnO films in Refs. [74,75]. The condition satisfying this hypothesis could thus be expressed as $n^{ZnO} \times \mu^{ZnO} > n^{Cu:ZnO} \times \mu^{Cu:ZnO}$, where n^i and μ^i are the free electron density and mobility of unintentionally n-doped (*i=ZnO*) and Cu-doped (*i=Cu:ZnO*) ZnO NWs, respectively. The present condition would unambiguously lead to higher electrical resistivity values of ZnO NWs when doped with Cu dopants (i.e. $\rho^{ZnO} < \rho^{Cu:ZnO}$). In the present work, a progressive increase in the values of ρ of ZnO NWs is achieved after thermal annealing and as the $[Cu]/[Zn]_{bath}$ ratio was increased from 0 to 10%. The evolution of the electrical resistivity involves the engineering of H- and N-related defects in the ZnO NWs,[22] as well as the migration process of Cu dopants in their center, as well as the change of the oxidation state of Cu_{Zn} acceptor defects.

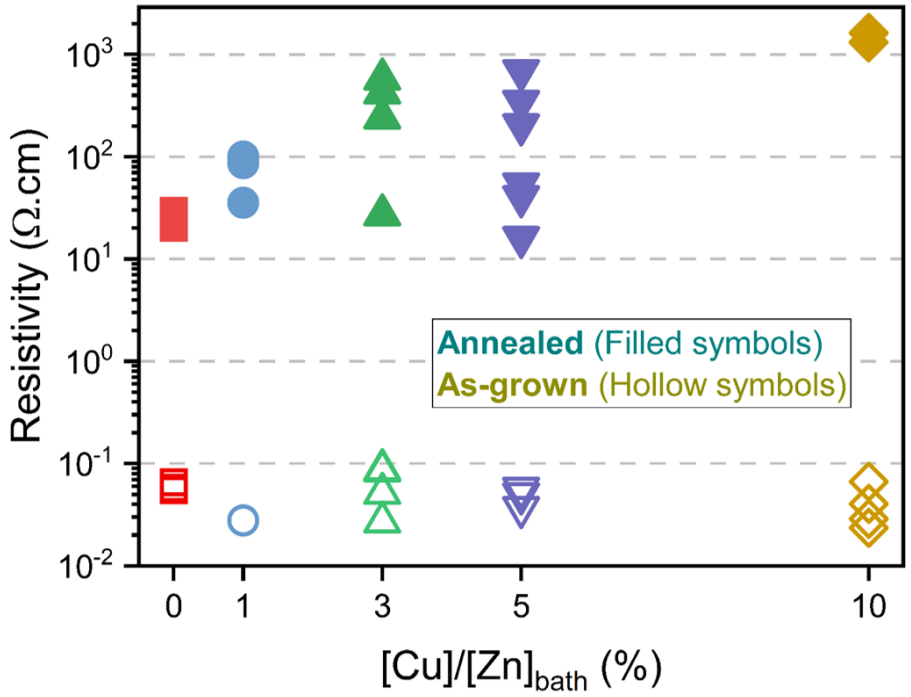

Figure II.2-15. *Electrical resistivity assessed by two-point probe measurements of ZnO NWs grown by CBD with [Cu]/[Zn]bath ratios of 0, 1, 3, 5 et 10%, before and after thermal annealing at 500 °C under O_2 atmosphere. Axis of resistivity is presented in the logarithmic scale.*

II.3 Effect of thermal annealing treatment in Cu-doped ZnO nanowires

Cu atoms were successfully incorporated by the CBD process in a high pH region within ZnO NWs. The formation of Cu_{Zn} acceptor defects was also demonstrated. However, the need for their thermal activation was highlighted. This section will consequently explore the effect of different thermal annealing on the physicochemical and electrical properties of a Cu-doped ZnO NW.

The results presented in section II.3 and II.5 have been published in: Manrique, Manuel, et al. "Enhancing the Output Voltage of Piezoelectric Nanogenerators Based on ZnO Nanowires Grown by Chemical Bath Deposition Using Compensatory Cu Doping." *Energy Technology* 12.5 (2024): 2301381.

II.3.1 Experimental procedure: thermal annealing of Cu-doped ZnO nanowires grown at fixed Cu-dopant level

For this experiment, ZnO NWs were grown via the CBD method with $[Cu]/[Zn]_{bath}$ ratios of 0 and 5%, as described in **Section II.2.1** and summarized in **Table II.3-1**. The initial pH of the chemical solution was set to 10.6 by adding 600 mM of ammonia. The ZnO NW growth was achieved at 85 °C for 21h in sealed reactors containing a 150 ml chemical solution. It should be mentioned that the growth time and volume of chemical solution were chosen to synthesize NWs long enough to facilitate their contact in bottom transistor devices for further electrical measurements. After the synthesis, the samples were divided into four parts, each of which followed a distinct thermal annealing in an O_2 atmosphere at 300, 500, and 800 °C for 1h.

***Table II.3-1**. Growth conditions of ZnO NWs synthesized via CBD with $[Cu]/[Zn]_{bath}$ ratios of 0 and 5%.*

$[Cu]/[Zn]_{bath}$ (%)	$[Zn(NO_3)_2]_{bath}=[HMTA]_{bath}$ (mM)	$[Cu(NO_3)_2]_{bath}$ (mM)	$[NH_3]_{bath}$ (mM)	Comments
0	30	0	600	Total volume of solution: 150 ml Growth time: 21h Temperature: 85 °C
5		1.5		

II.3.2 Morphological properties

The morphological properties of both unintentionally *n*-doped and Cu-doped ZnO NWs grown by CBD with a $[Cu]/[Zn]_{bath}$ ratio of 0 and 5%, respectively, are shown in **Figure II.3-1** using FESEM images. An epitaxial vertical growth on the preferentially *c*-axis oriented

polycrystalline ZnO seed layer is observed.[13] Concerning their morphological properties, the unintentionally *n*-doped ZnO NWs have a mean length of 6.7 ± 0.2 µm with tapered shape top faces (**Figure II.3-1(a)**), while Cu-doped ZnO NWs reach a mean length of 7.3 ± 0.1 µm with flat hexagonal shape top faces (**Figure II.3-1(b)**). The tapered shape top face results from a high axial growth rate along the polar *c*-axis, which occurs at the expense of the radial growth along the non-polar *m*-axis.[7] On the contrary, the hexagonal flat shape is consecutive to a possible obstruction of the axial growth[76] by the adsorption process of $Cu(NH_3)_4^{2+}$ complexes on the polar *c*-plane of ZnO NWs[7,16].

In addition, it is well-known that the coexistence of heterogeneous and homogeneous growth processes occurs during the growth of ZnO NWs by CBD (*i.e.*, on the substrate and into the bulk solution, respectively). The dominance of each growth process depends on the solubility of Zn(II) species, which can be modified by the presence of chemical additives. In the present study, since ZnO NWs were grown using a chemical bath with a large volume for an extended length of time, the presence of NH_3 and $Cu(NO_3)_2$ might have a major impact on the depletion of chemical reactants contributing to the heterogeneous growth. Accordingly, the amount of chemical reactants available for the formation of unintentionally *n*-doped ZnO NWs is expected to be smaller than that of Cu-doped ZnO NWs. This may also account for the different morphologies of *n*-doped and Cu-doped ZnO NWs resulting from the different depletion rates of chemical reactants.

Furthermore, neither Cu_2O nor CuO nanocrystals are detected when growing Cu-doped ZnO NWs in the present high-pH region.

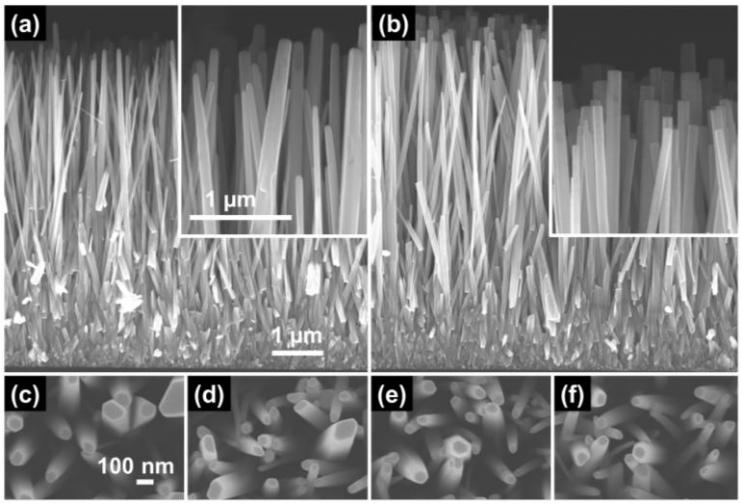

Figure II.3-1. *Cross-sectional FESEM images of ZnO NWs with a $[Cu]/[Zn]_{bath}$ ratio of **(a)** 0 and **(b)** 5%. Top view FESEM images of annealed Cu-doped ZnO NWs at: **(c)** as-grown, **(d)** 300 °C, **(e)** 500 °C, and **(f)** 800 °C under an O_2 atmosphere for 1h.*

It is worth mentioning that no morphological changes were observed in ZnO NWs after the distinct thermal annealing, as depicted in **Figure II.3-1(c-f)**. In addition, ICP-MS analysis were performed to quantify the amount of Cu in ZnO NWs, which reveals that the atomic [Cu]/[Zn] ratio lies in the range of 50 - 65 ppm and hence remains stable before and after annealing, as depicted in **Figure II.3-2**. As seen before, the residual Cu amount in unintentionally n-doped ZnO NWs (labeled as Reference in **Figure II.3-2**) could come from the ammonia added in the chemical bath. The atomic [Cu]/[Zn] ratio quantified by ICP-MS will help to understand the migration processes of Cu atoms into the bulk of ZnO NWs, as suggested later by XPS spectra in **Section II.3.4**. It should be noted that ICP-MS analysis does not distinguish the chemical environment of Cu atoms within ZnO NWs. XANES and XLD spectroscopy will further discuss this topic in **Section II.3.5**.

Sample	Dilution factor	[Cu] (mg/l)	Dilution factor	[Zn] (mg/l)
Bare ZnO as-grown	1	0.001	500	0.617
ZnO:Cu as-grown	1	0.016	500	0.521
ZnO:Cu – 300°C	1	0.018	500	0.622
ZnO:Cu – 500°C	1	0.011	500	0.431
ZnO:Cu – 800°C	1	0.018	500	0.547

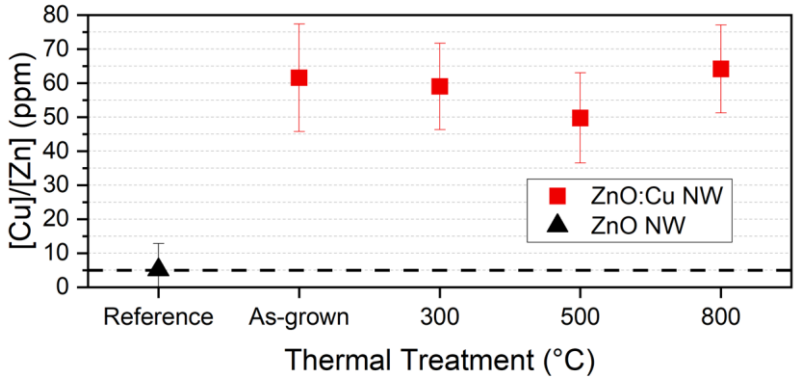

Figure II.3-2. *ICP-MS results from Cu-doped ZnO NWs grown by CBD ($[Cu]/[Zn]_{bath}$ ratio of 5%) after different thermal annealing under an O_2 atmosphere. The dashed horizontal line defines the reference of [Cu]/[Zn] content from unintentionally n-doped ZnO NW.*

II.3.3 Raman spectroscopy

After different thermal annealing of both unintentionally *n*-doped and Cu-doped ZnO NWs, no evolution of their morphological properties occurs. The Raman scattering spectra of as-grown and annealed unintentionally *n*-doped and Cu-doped ZnO NWs were recorded in the low wavenumber range from 70 to 800 cm^{-1} and calibrated from the Si line at 520.7 cm^{-1}, as

shown in **Figure II.3-3**. The indicative optical phonon modes of the wurtzite structure of ZnO NWs are observed at 99 (E_2^{low}), 380 (A_1(TO)), ~438 (E_2^{high}) and 574 (A_1(LO)) cm^{-1}.[77] The second-order modes are located at 203 (2TA/2 E_2^{low}), 333 (E_2^{high} - E_2^{low}) and 483 (2LA) cm^{-1}. Concerning Cu-doped ZnO NWs, no Cu_2O, CuO or $Cu(OH)_2$ related Raman peaks are detected,[33] regardless of the thermal annealing used. Furthermore, for both unintentionally *n*-doped and Cu-doped ZnO NWs, additional modes (AMs) attributed to dopant-induced defects appear after thermal annealing. They are related to the presence of extrinsic impurities including Al, Ga, N, Sb, and Fe,[30] probably coming from the ammonia added in the chemical bath. Villafuerte et al. assigned these AMs to ZnO B_1 silent modes located at 275 (B_1^{low}), 581 (B_1^{high}), and 643 (TA+ B_1^{high}) cm^{-1},[31] which become Raman active due to the breakdown of the translational crystal symmetry after thermal annealing.[32] Particularly, the increase of the Raman peak around 580 cm^{-1} for thermal annealing at 300 and 500 °C is the result of the coupling of the two B_1^{high} and A_1(LO) modes owing to their wavenumber proximity.

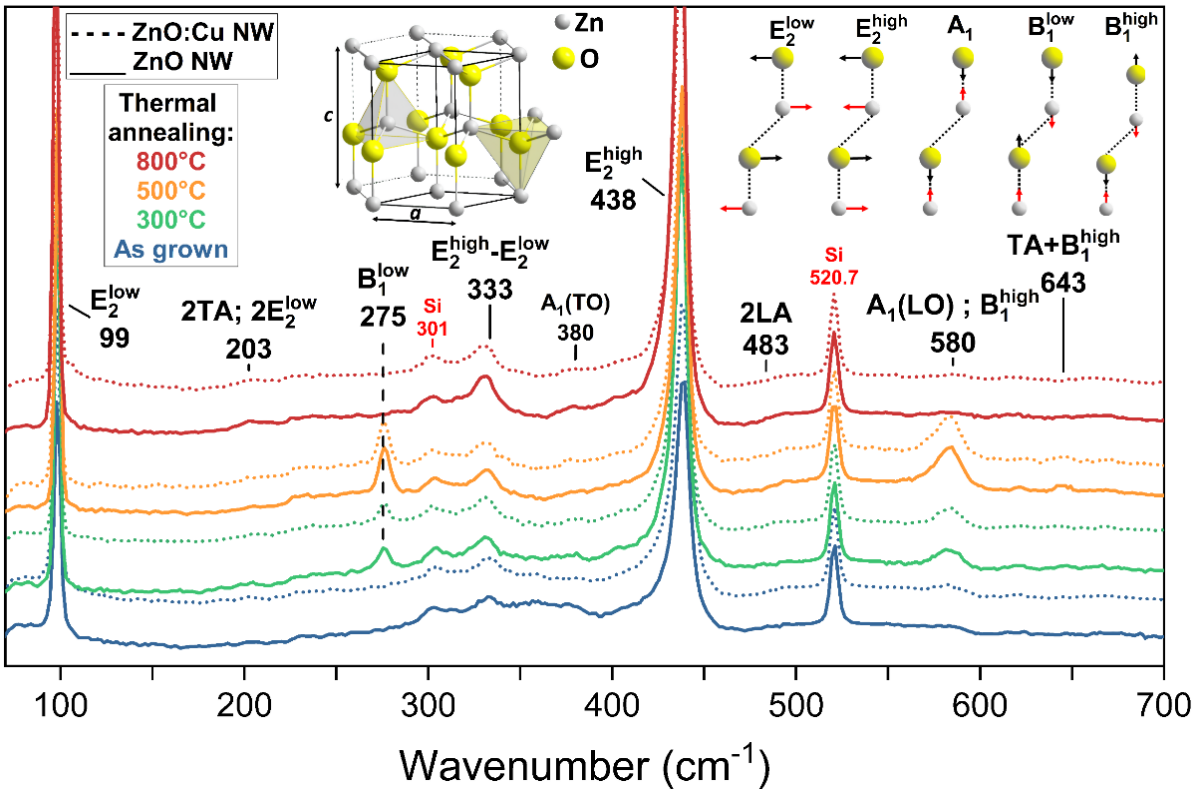

***Figure II.3-3**. Raman spectra of unintentionally n-doped and Cu-doped ZnO NWs after thermal annealing at different temperatures in an O_2 atmosphere.*

Interestingly, the increase in the area of the E_2^{low} and E_2^{high} peaks along with the decrease of their full-width half maximum (FWHM) as the annealing temperature is increased

reveals an improvement of the crystallinity of unintentionally *n*-doped and Cu-doped ZnO NWs after thermal annealing, as depicted in **Figure II.3-4(a-b)**.

Additionally, the position of both E_2^{low} and E_2^{high} Raman lines shifts to lower wavenumbers as the annealing temperature is increased, indicating a possible relaxation of the residual stress along the *c*-axis of the wurtzite structure of ZnO NWs.[78,79] For unintentionally *n*-doped ZnO NWs, the E_2^{high} peak significantly shifts from 437.1 cm^{-1} (as-grown) to 435.6 cm^{-1} (800 °C), which probably originates from the redistribution of hydrogen- and nitrogen-related defects through the thermal annealing.[31] For Cu-doped ZnO NWs, the E_2^{high} peak shifts from 437.1 cm^{-1} (as-grown) to 435.8 cm^{-1} (800 °C). The E_2^{low} peak also follows a similar shift to lower wavenumbers as the thermal annealing increases, shifting from 98.3 (as-grown) to 97.5 cm^{-1} (800 °C) for unintentionally *n*-doped ZnO NWs, and from 98.0 (as-grown) to 97.9 cm^{-1} (800 °C) for Cu-doped ZnO NWs. Interestingly, Cu is expected to preferentially occupy Zn sites to form Cu_{Zn} owing to its similar ionic radius of 74 pm (Zn^{2+}), 77 pm (Cu^{1+}) and 73 pm (Cu^{2+}).[76,80] This leads to a distortion of the lattice of ZnO NWs,[78] and consequently a possible modification of the Raman line shape induced by a change of phonon contribution, as explained by Samanta et al. through the alloy potential fluctuation (APF) within a phonon confinement model.[36]

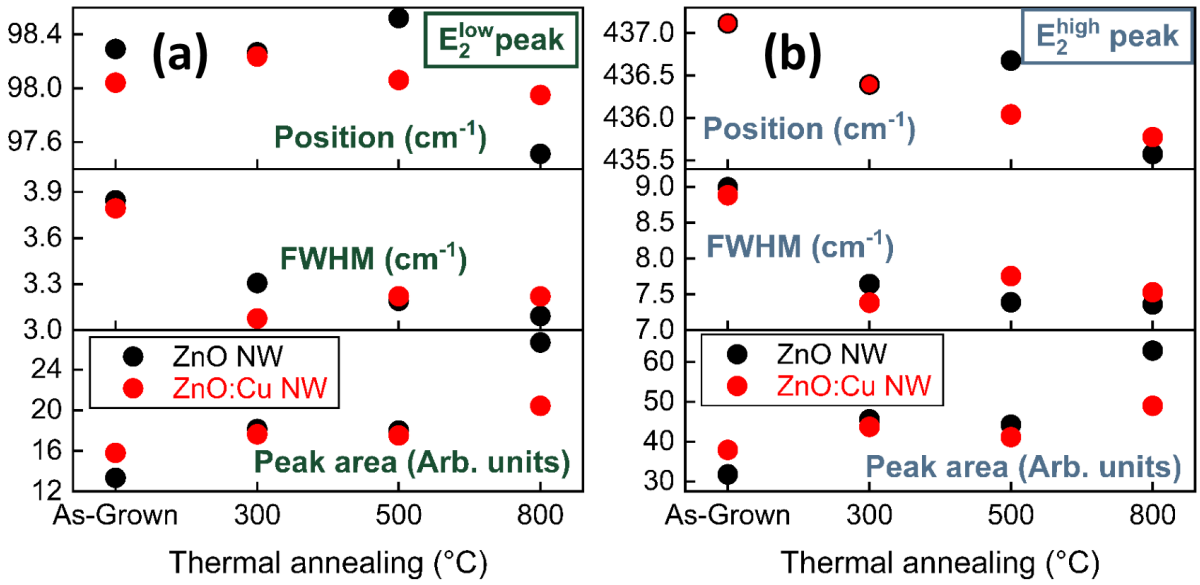

Figure II.3-4. (a) *E_2^{low} and* ***(b)*** *E_2^{high} Raman peak evolution of unintentionally* n*-doped and Cu-doped ZnO NWs after thermal annealing at different temperatures in an O_2 atmosphere.*

II.3.4 X-ray photoelectron spectroscopy

X-ray photoelectron spectroscopy (XPS) was performed on a customized Thermo Fisher Scientific Theta 300 system with a monochromatized Al Kα source. The recorded data was analyzed with the Thermofisher Avantage software, and the XPS spectra were referenced with the 1s neutral carbon peak at 284.8 eV.

XPS spectra centered on the Cu 2p core level, as presented in **Figure II.3-5(a)**, reveal the Cu $2p_{1/2}$ and Cu $2p_{3/2}$ peaks pointed at 952.5 and 932.7 eV, respectively, of Cu-doped ZnO NWs after thermal annealing. The XPS spectra confirm that neither Cu_2O nor CuO residual phases are formed since no prominent satellite peaks in the range of 940 – 944 eV are detected,[81] which is in agreement with Lausecker et al.[7] Concerning the Cu $2p_{3/2}$ peak, owing its weak intensity, it is difficult to accurately evaluate the Cu oxidation state. Indeed, the Cu $2p_{3/2}$ peak could be the contribution of Cu(0), Cu(I) or Cu(II) centered at 932.63, 932.18 and 933.11, respectively. [81] Moreover, the contribution of each Cu oxidation state can depend on the thermal annealing. For instance, Sultana et al. studied the structural properties of CuO thin films after different annealing at 250, 550 and 850 °C for 10 minutes under Ar atmosphere, and showed that the $Cu2p_{3/2}$ peak intensity is mainly related to an evolution of the Cu(II) contribution.[82] The latter is high for as-deposited films, then severely decreases until 550 °C and finally increases at 880 °C, while the Cu(0)/Cu(I) contribution remains almost constant regardless the thermal annealing. Another work conducted by Garces et al. confirmed a change of the oxidation state from Cu(I) to Cu(II) after a thermal annealing for 1h at 900 °C in ZnO crystal with trace of Cu.[83] From these studies, aiming to evaluate the possibility of a modification of the oxidation state of Cu, the O 1s and Zn $2p_{3/2}$ core levels were fitted for both unintentionally *n*-doped and Cu-doped ZnO NWs after thermal annealing, as shown in **Figure II.3-5(b-c)**, respectively. A clear shift of the O 1s (530.3 eV) as well as the Zn $2p_{3/2}$ (1021.6 eV) peaks towards higher energies is observed as a function of the thermal annealing. This could be the result of an enrichment of hydroxyl groups in the surface of ZnO NWs, resulting from an *exo*-difussion process of hydrogen,[22] as explained by Gaffuri et al.[84] In this context, bonding in the form of $Cu(OH)_2$ (Cu(II)) with two peaks at 933.1 and 934.5 eV in the Cu $2p_{3/2}$ range could be expected in our samples.[81] Then, given the fact that the present XPS measurements are recorded from data provided up to about 5 nm below the surface of Cu-doped ZnO NWs, the decrease in the intensity of the $Cu2p_{3/2}$ peak highlights a reduction of

the amount of Cu at their surfaces after thermal annealing. This indicates a migration process of Cu atoms from the surface into the bulk of ZnO NWs, since the atomic [Cu]/[Zn] ratio remains constant, according to the ICP-MS analysis.

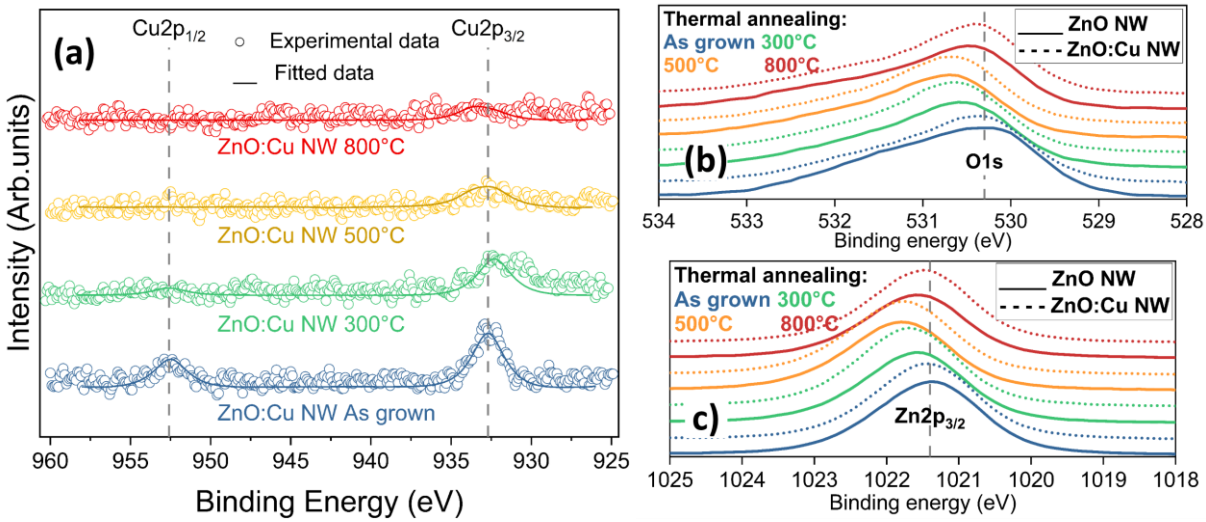

Figure II.3-5. *XPS spectra centered on the* ***(a)*** *Cu 2p,* ***(b)*** *O 1s, and* ***(c)*** *Zn 2p core levels of unintentionally n-doped and Cu-doped ZnO NWs after thermal annealing at different temperatures under O_2 atmosphere.*

II.3.5 XANES and XLD spectroscopy

The chemical environment of Cu atoms within ZnO NWs was assessed by XANES and XLD spectroscopy recorded at the ESRF ID12 beamline. The typical XANES and XLD spectra of wurtzite ZnO NWs at the Zn K-edge are shown in **Figure II.3-7**, registered with the polar *c*-axis oriented perpendicular (E⊥*c*) and parallel (E//*c*) to the linearly-polarized X-ray beam electric field. As discussed in **Section II.2.7**, the Zn K-edge XLD spectra indicate a high vertical alignment along the *c*-axis and a high crystalline quality of Cu-doped ZnO NWs, as compared to those XLD spectra reported on high-quality ZnO films and NWs.[60,61]

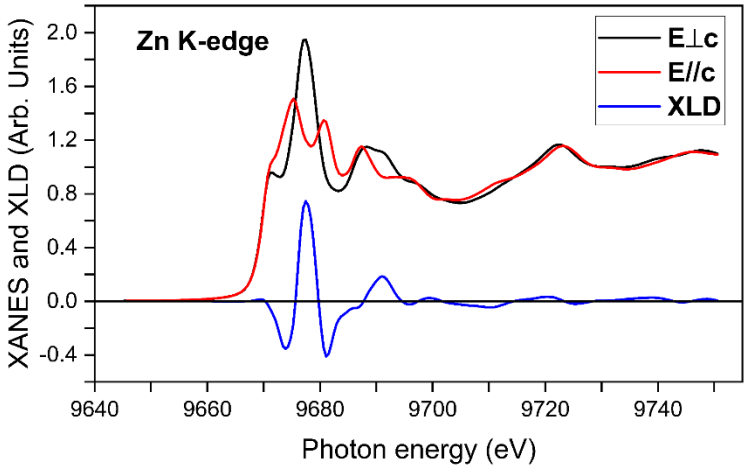

Figure II.3-6. *XANES and XLD spectroscopy of Cu-doped ZnO NWs grown with $[Cu]/[Zn]_{bath}$ ratio of 5%.*

Figure II.3-7(a-b) depicts the normalized XANES and XLD spectra of Cu-doped ZnO NWs after the different thermal treatments at the Cu K-edge. By comparing the edge jump intensities at the Cu and Zn K-edges, an atomic $[Cu]/[Zn]_{NW}$ ratio of around 0.01% was found within the ZnO NWs, consistent with the ~65 ppm (0.0065%) obtained through ICP-MS measurements. This value is similar to that reported in Cu-doped ZnO NWs grown with a $[Cu]/[Zn]_{bath}$ ratio of 5% in **Section II.2.7**. This strongly suggest that the amount of Cu in ZnO NWs depends on the $[Cu]/[Zn]_{bath}$ ratio. In addition, the XANES and XLD spectra of as-grown Cu-doped ZnO NWs at the Cu K-edge does not exhibit changes compared to those previously presented in **Section II.2.7**: the peak at ~8985 eV, followed by a prominent one ~11 eV higher, remains consistent. The substitution of Cu atoms for Zn in the wurtzite structure is also confirmed, as the XLD spectra at the Zn and Cu K-edge are similar. Then, approximately 18 ± 5 % of the total Cu dopants are incorporated as Cu_{Zn}, resulting in a density of $(7.6 \pm 2.1) \times 10^{17}$ at/cm^3 of Cu_{Zn}.

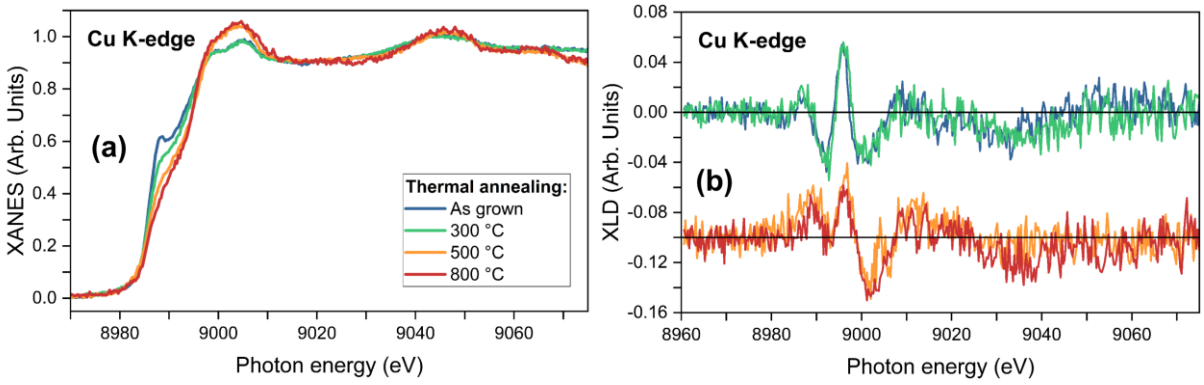

***Figure II.3-7**. Normalized **(a)** XANES and corresponding **(b)** XLD spectra of Cu-doped ZnO NWs grown by CBD with a $[Cu]/[Zn]_{bath}$ ratio of 5%, before and after thermal annealing at 300, 500, and 800 °C for 1 h under an O_2 atmosphere.*

After thermal annealing, a noteworthy change in the Cu K-edge XANES and XLD spectra of Cu-doped ZnO NWs is observed. The isotropic XANES spectra exhibit the steady disappearance of the sharp peak at the leading edge as the temperature of thermal annealing increases until 800 °C. The prominent shoulder located around 9000 eV increases in intensity and wide after thermal annealing at 500 and 800 °C. This strongly suggests a change in the electronic structure of the Cu dopants due to a more oxidizing local environment through thermal annealing. Interestingly, the XLD spectra reveal the occurrence of a moderate peak around 8985 eV for thermal annealing higher than 500 °C. In addition, the highest XLD peak located at ~8995 eV exhibits a slight shift of ~1 eV to higher energies as the thermal annealing increases in temperature. Given that the intensity of the XLD signal does not significantly

change following different thermal annealing, the density of Cu_{Zn} defects in ZnO NWs seems to be identical after thermal annealing. By combining XANES and XLD spectra after different thermal annealing, the more oxidizing environment could indicate the formation of V_{Zn} defects in the vicinity of Cu dopants after thermal annealing. This would be in agreement with the massive expected formation of V_{Zn} defects in O-rich conditions.[66]

II.3.6 Electrical properties assessed by 2-point probes measurements on single NW

The electrical properties of unintentionally *n*-doped and Cu-doped ZnO NWs after thermal annealing were assessed using a two-point probe electrical resistivity measurement through the bottom transistor devices, using the same protocol explained in **Section II.2.8**.

Figure II.3-8(a) compares the deduced *R*/*l* values of each NW with experimental data reported in the literature, using a four-point probe resistivity measurements on ZnO NWs grown by metal-organic chemical vapor deposition (MOCVD), carbothermal reduction, hydrothermal process, and CBD in the low-pH region, as already presented in **Section II.2.8**. It is worth mentioning that the dashed lines delimited the bulk-like electrical conduction region for ZnO NWs grown by CBD, where surface effects are negligible and the *R/l* values are proportional to $1/r^2$.[44] For the present work, the as-grown unintentionally *n*-doped and Cu-doped ZnO NWs exhibit *R/l* values inside this region. Then, a clear variation of *R/l* values is observed as a function of the annealing temperature. For unintentionally *n*-doped ZnO NWs, the *R/l* values progressively increase from 2.0×10^2 to 1.3×10^6 Ω/µm as the annealing temperature reaches 800 °C. The same trend is noticed for Cu-doped ZnO NWs, but the *R/l* values ranging from 1.2×10^3 to 8.9×10^8 Ω/µm are systematically higher for each annealing temperature.

It is important to note that the *R/l* values can be influenced by changes in the pH of the chemical bath, which is suggested when comparing the present *R/l* values of as grown n- and Cu-doped ZnO NWs with those reported in **Figure II.2-14** of **Section II.2.8**. The ZnO NWs grown in a chemical bath with a pH_0 of 11 ($[NH_3]_{bath}$ = 800 mM) exhibited *R/l* values higher than 10^3 Ω/µm. In contrast, the present ZnO NWs grown with a pH_0 of 10.6 ($[NH_3]_{bath}$ = 600 mM) show lower *R/l* values. This difference could be attributed to an increased formation of V_{Zn} defects as the pH of the chemical bath rises. This increase in pH creates oxygen-rich conditions, which

can lead to the dissociation of shallow V_{Zn}-3H donor complexes, resulting in neutral V_{Zn}-2H and deep V_{Zn}-H acceptor complexes.[31] This process should decrease the free carrier density in ZnO NWs and leads to higher *R/l* values. The dimensions of the NW could also lead to changes in *R/l*, but this is unlikely in the present case as all the characterized NWs have radius within the range of 200 – 400 nm. This hypothesis, however, deserves further investigation.

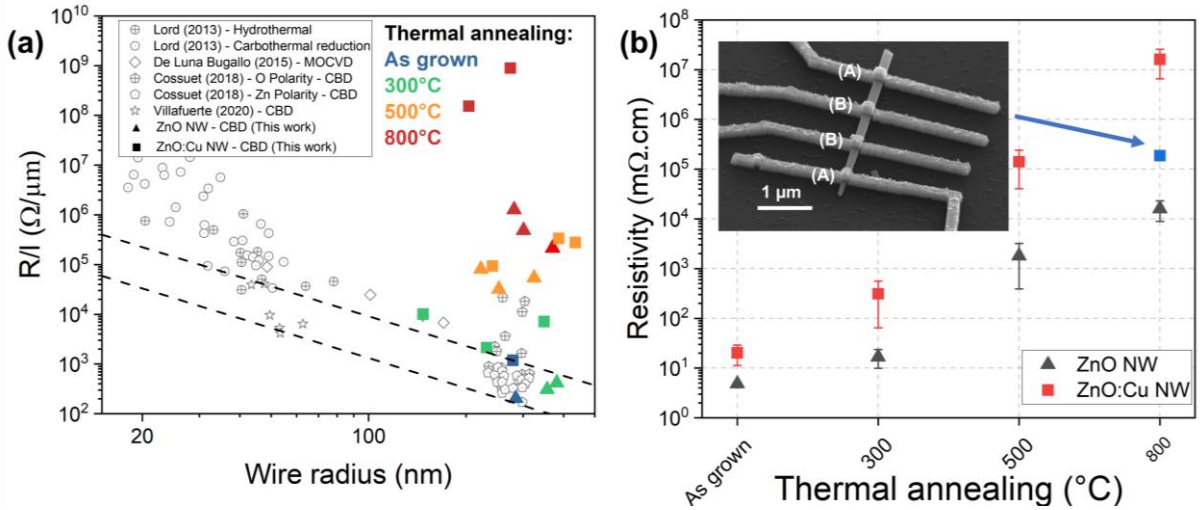

Figure II.3-8. *R/l values versus r for the present work along with experimental data reported on ZnO NWs grown by chemical synthesis: hydrothermal process[85], carbothermal reduction[85], MOCVD[71] and CBD[44,69] in the low-pH region. (Image inspired from REF [44]).* ***(b)*** *Electrical resistivity of unintentionally n-doped and Cu-doped ZnO NWs for different annealing in an O_2 atmosphere during 1h assessed by the 2-point probe method. The blue point refers to the resistivity of an 800 °C thermally annealed Cu-doped ZnO NW measured by the 4-point probe method.*

The electrical resistivity ρ was estimated through the equation $\rho \cong R\frac{S}{l}$; where *S* is the effective electrical conduction section of the NW. The last parameter can be written as $S = \pi r^2$. As expected from the plot of *R/l* values as a function of *r*, the electrical resistivity of ZnO NWs increases with the thermal annealing, as presented in **Figure II.3-8(b)**. The *ρ* mean value for unintentionally *n*-doped ZnO NWs is 4.8 mΩ.cm, and continuously increases from 1.7×10^1 mΩ.cm through 1.8×10^3 mΩ.cm to 1.6×10^4 mΩ.cm for annealing temperatures of 300, 500, and 800 °C, respectively. As for Cu-doped ZnO NWs, the ρ mean value is higher and of 20.2 mΩ.cm, and continuously increases from 3.1×10^2 mΩ.cm, through 1.4×10^5 mΩ.cm to 1.7×10^7 mΩ.cm for annealing temperature of 300, 500, and 800 °C, respectively.

It is well-known that the two-point probe method could induce an apparent higher electrical resistivity as a result of the occurrence of a significant contact resistance. In the present study, we assume a lower contact resistance for as-grown ZnO NWs, since their obtained *R/l* values lie in the same region as those reported using the four-point probe method on ZnO NWs grown by CBD in REF [69]. Then, a progressive increase in the contact resistance

following the thermal annealing is expected, reaching its largest influence on the electrical characterizations of Cu-doped ZnO NWs annealed at 800 °C, which present the highest ρ values. Following this hypothesis, only these NWs were measured using a four-point probe method, revealing a decrease in the ρ value by a 100 factor, as depicted by the blue point in **Figure II.3-8(b)**. It is worth noticing that, after the thermal annealing at 800 °C, the four-point probe measured electrical resistivity of Cu-doped ZnO NWs is still higher than the initially overestimated electrical resistivity of unintentionally *n*-doped ZnO NWs assessed by the two-point probe method. The present observation implies that the evolution of electrical resistivity involves an additional factor beyond the influence of contact resistance.

II.4 In-depth discussion of Cu-doping and thermal annealing effects on the optical and electrical properties of ZnO nanowires

The studies discussed in both **Section II.2** and **Section II.3** highlight the compensatory doping process at work by using the incorporation of Cu atoms in ZnO NWs grown by CBD, as schematized in **Figure II.3.6** During the nucleation and growth of ZnO NWs by CBD, the unintentional incorporation of shallow donors as H_{BC}, H_O, and V_{Zn}-3H defect complex results in a high free electron density lying in the range of 5×10^{17} to 1.1×10^{19} cm^{-3}.[44,69,86] Moreover, through the addition of ammonia in the chemical bath to tune the pH in the region where the electrostatic interactions are favorable for the incorporation of Cu atoms into ZnO NWs, a significant amount of deep acceptors as V_{Zn}-N_O-H defect complex is expected as well.[22] Therefore, the electrical resistivity of ZnO NWs is conducted by the concentration of these defects and defect complexes acting as shallow donors and deep acceptors. In the scenario where an additional Cu-solution is added to the chemical bath for inducing the compensatory doping and hence reducing the screening effect of the piezoelectric potential for PNGs,[87] the incorporation of Cu_{Zn} as acceptors in ZnO NWs is thermodynamically favorable through its low formation energy.[88] The incorporation process of Cu atoms is assisted by electrostatic forces between the positively charged $Cu(NH_3)_4^{2+}$ ion complexes and the negatively charged *c*-polar top face of ZnO NWs. Nevertheless, the as-grown Cu-doped ZnO NWs synthesized at two distinct pH_0 levels of 10.6 and 11.0 exhibit different electrical behavior. Those with $[Cu]/[Zn]_{bath}$ ratio of 1, 3, 5, and 10%, grown at the higher pH_0 of 11.0, exhibit an electrical resistivity in the same order of magnitude as the as-grown unintentionally n-doped ZnO NWs ($[Cu]/[Zn]_{bath}$ ratio of 0%). In contrast, those with a $[Cu]/[Zn]_{bath}$ ratio of 5%, grown at pH_0 of 10.6, display higher electrical resistivity than unintentionally n-doped ZnO NWs, regardless of thermal treatment.

This unexpected behavior could be attributed to a reduction in the density of V_{Zn}-3H defect complexes as the pH of the chemical bath increases, which favors the formation of V_{Zn},[31,66] as well as the additional formation of other Cu-related defects with unknown electronic properties, which should be distinguished from Cu_{Zn}. This latter hypothesis is strongly supported by XLD measurements performed on ZnO NWs grown with the $[Cu]/[Zn]_{bath}$ ratio of 5% presented in **Section II.2** and **Section II.3**, which reveal that only 15 - 18% of the total amount of Cu atoms incorporated is found to substitute for Zn sites. In

contrast, the remaining 82-85% of the total amount of Cu atoms appears to be in a Cu_2O or CuO-like environment. Moreover, the significant presence of electrically inactive Cu-related defects located at the surfaces of ZnO NWs is also strongly expected from XPS measurements (**Figure II.3-5**), which does contribute to the compensatory doping and hence does affect the electrical resistivity. Given the expected intermediate formation energy of V_{Zn}-N_O-H defect complex acting as deep acceptor in the ZnO NWs grown in a high pH region,[22] the presence of Cu_{Zn} could further lead to the formation of Cu_{Zn}-N_O-H defect complex with unknown electronic properties.

After thermal annealing under an O_2 atmosphere at 300, 500, and 800 °C, the notable and progressive increase in the electrical resistivity of Cu-doped ZnO NWs mainly originates from the three following phenomena: i) the reduction of the concentration of shallow donors as H_{BC} and V_{Zn}-3H defect complex are unstable at that high annealing temperature,[22] ii) the active formation of V_{Zn}-N_O-H defect complexes as deep acceptors,[31,89] and iii) the formation of electrically active Cu-related acceptors, all of them leading to a decrease in the free electron density and consequently to the higher electrical resistivity.

It should be noted that while the density of Cu_{Zn} defects in the Cu-doped ZnO NWs do not show several changes after thermal annealing, their local environment becomes more oxidizing, as revealed by XLD and XANES spectra, respectively. This suggests that the highest electrical resistivity reported in thermally annealed Cu-doped ZnO NWs is driven by additional Cu-related effects, as supported by 5K cathodoluminescence spectroscopy (**Figure II.2-10**), which showed an enhanced structured DLE band only after thermal annealing. This indicates the potential formation of complexes involving Cu_{Zn} and V_{Zn} following the thermal annealing process, which could be explained by both the increased resistivity and the enhanced visible band emission in Cu-doped ZnO NWs. For instance, under oxygen-rich conditions, the formation of impurity complexes involving P, As, Sb or Ga atoms along with V_{Zn} defects in ZnO is highly expected, which can form, with low formation energy, deep acceptors, such as M_{Zn}-xV_{Zn} (M=P, As, Sb, Ga; x=1, 2, 3),[8,60,68,90] or shallow donors in proximity to H atoms, like V_{Zn}-Ga_{Zn}-3H and V_{Zn}-Al_{Zn}-2H.[60,91] The formation of complexes involving Cu_{Zn} and V_{Zn} could arise from the migration of Cu_{Zn} defects, which should be promoted by the high formation and easy migration of V_{Zn} defects according to the thermal annealing temperature in an O_2 atmosphere. Indeed, it is well-known that, under oxygen-rich conditions, the V_{Zn} defects are efficiently

formed in ZnO NWs owing their low formation energy and can further migrate in an isotropic manner by benefiting from the relatively low migration barrier of 1.4 eV.[66] As a consequence, by performing the thermal annealing under an O_2 atmosphere at temperatures higher than 300 °C for 1h, the V_{Zn} defects are strongly mobile, which should favor the migration of Cu_{Zn} defects and the formation of Cu_{Zn}-related complexes. This could account for the changes in the electronic structure of Cu_{Zn} defects, which can act as efficient (Cu_{Zn}^{2+}) or poor (Cu_{Zn}^{1+}) acceptors.[50] When combining the formation and migration processes of Cu_{Zn}-related species above described, a strong reduction in the free electron density in the ZnO NWs occurs through enhanced electron-hole pair recombination, i.e. a compensatory process involving Cu_{Zn}-related acceptors and intrinsic or extrinsic donor species in the ZnO NWs. For instance, negatively ionized $[Cu_{Zn}^{1+}(3d^{10})]^-$ acceptors may associate with singly positive ionized $Zn_i^+(4s^1)$ donors to form neutral $\{[Cu^{2+}(3d^{10})]Zn_i^+\}^0$ complex defects.[50,54] In addition, the steady increase in the electrical resistivity of annealed Cu-doped ZnO NWs is in excellent agreement with the progressive formation process of Cu_{Zn} acceptors as the [Cu]/[Zn] ratio was increased from 1 to 10% in **Section II.2**, as confirmed by XANES and XLD measurements. The present findings highlight the advantages of combining Cu-doping with thermal annealing in ZnO NWs, effectively tuning their optical and electrical properties, and potentially enhancing the performance of the related devices. Thus, based on these studies, PNGs are fabricated to evaluate the piezoelectric properties of the resistive ZnO NWs.

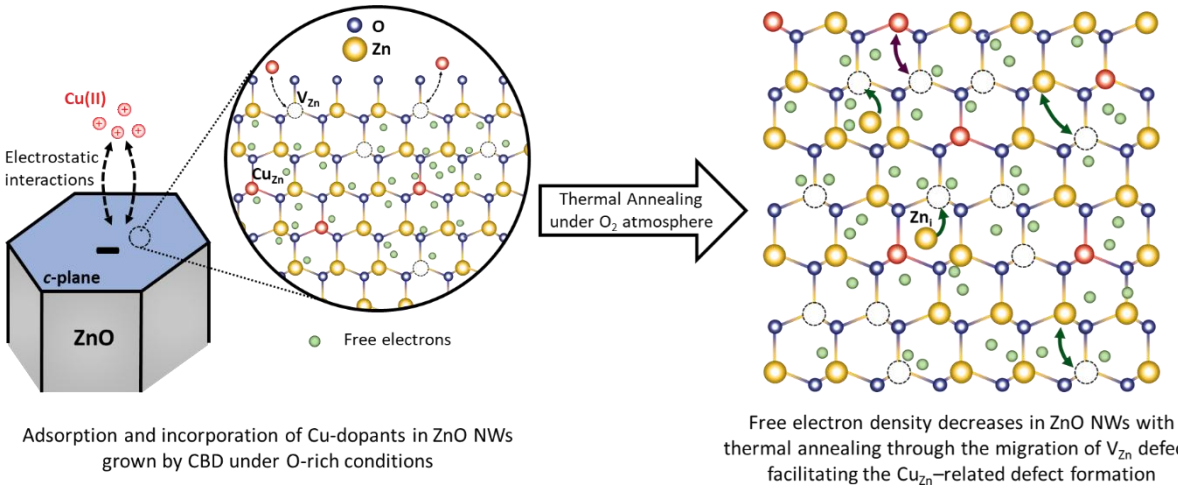

Figure II.3.6 *Adsorption and incorporation process of Cu atoms in ZnO NWs grown by CBD in the high pH region, along with the migration processes of Cu_{Zn} as acceptors assisted by the massive formation and migration processes of V_{Zn} using thermal annealing under an O_2 atmosphere at 300, 500, and 800 °C.*

II.5 Enhancing the output voltage of piezoelectric nanogenerators based on ZnO nanowire matrix through Cu-doping and thermal annealing

Resistive ZnO NWs were achieved through compensatory Cu-doping and thermal annealing. To evaluate their piezoelectric properties, PNGs based on these nanostructures were fabricated. Piezoelectric characterizations of the devices were subsequently performed using the test bench available at the Cameleon platform – LTM.

II.5.1 Piezoelectric characterizations on the LTM's test bench

The test bench for the piezoelectric characterizations of PNGs available at the LTM was initially developed by Dr. Clement LAUSECKER, and modified/complemented during the present thesis, as presented in **Figure II.5-1(a)**. This test bench involves a SmartShaker K2007E01 (PCB Piezotronics) acting as a mechanical excitation source. A Keysight 33210A function generator supplies the shaker with an alternating electrical signal, which in turn is converted into a mechanical vibration. The latter is transmitted to a mechanical arm attached to the shaker. Thus, the mechanical stress could reach values from 0.5 N to 30 N applied over an area of 0.2 cm^2 (*i.e.* from 25 kPa to 1.5 MPa) at different frequencies between $0.1 - 9000$ Hz. This mechanical stress is measured in real-time by an ICP 208C02 (PCB Piezotronics) force sensor placed between the shaker and the mechanical arm with a sensitivity of 11.24 mV/N. Then, this sensor is connected to an ICP 480C02 (PCB Piezotronics) signal conditioner to optimize the transmitted signal. The piezoelectric signal generated by the PNG is gathered by a Stanford Research Systems SR560 amplifier♣ in order to amplify it and/or filter the external noise signals. Finally, a Teledyne LeCroy T3DSO2304 oscilloscope display in real time the electrical signals coming from the PNG and the force conditioner♦, as shown in **Figure II.5-1(b)**.

All the piezoelectric characterizations are performed keeping constant the distance between the PNG and the shaker, and controlling the mechanical compression cycle via the frequency and magnitude of a sinus-mode power supplier of the mechanical shaker.

♣ The internal impedance of the Stanford Research Systems is 100 MΩ

♦ To estimate the applied force on the PNG, the root mean square (RMS) of the force sensor's electrical signal is calculated and divided by its sensitivity of 11.24 mV/N.

Concerning the piezoelectric signal, three different regimes are observed, as described in **Figure I.3-1** in **Section I.3**.[92] Initially, the beginning of the mechanical compression leads to a fast polarization of the ZnO NW matrix of the PNG, resulting in an appearance of external charges in the electrodes and thus a positive voltage peak♣ is achieved. Subsequently, a screening effect caused by the free charge carriers inside the ZnO NWs occurs, reducing the polarization as long as the mechanical deformation time decreases (in other words when the mechanical compression reaches its highest magnitude), and hence reducing in this way the external charges in the electrodes until the total neutralization of the piezoelectric polarization, for which no charges are generated and the voltage plummet as consequence. Eventually, at the end of the compression cycle (release), the same charge creation and transfer occurs in the other way, inducing a symmetrical opposite voltage.

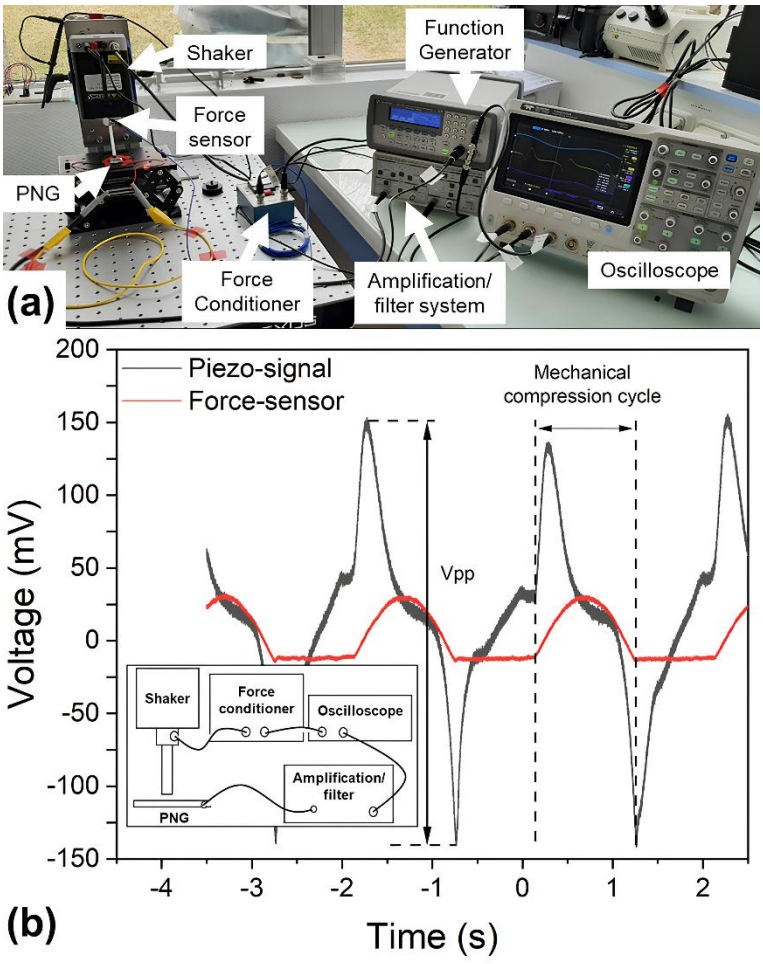

Figure II.5-1. (a) *Test bench available at the LTM for characterizations of PNG under vertically applied sinusoidal forces.* ***(b)*** *Piezoelectric characterization of a PNG (commercial PZT) along with the test bench schematic (inset). Both the piezoelectric signal and the force sensor signal share the same vertical axis in mV.*

♣ The sign of the peak depend on the how the PNG electrodes are connected to the measurement system cables, i.e. forward or reverse connection.

II.5.2 Output voltage of piezoelectric nanogenerators based on a Cu-doped ZnO nanowire matrix

Given the incorporation of Cu atoms, which result in resistive ZnO NWs, this section investigates their effect on the piezoelectric response of a related PNG.

II.5.2.1 Fabrication of piezoelectric nanogenerators based on Cu-doped ZnO nanowires

The PNG fabrication process is described in **Figure II.5-2(a)**. First, on a Si substrate covered by the bottom electrode (50 nm-thick Au layer over 10 nm-thick Ti layer) deposited by e-beam evaporation, a ZnO seed layer was deposited by dip-coating process, whose crystallization was obtained by keeping the sample at 300°C for 2 h 30 min♣ in an oven under air (ZnO/Metal/Si). This ZnO seed layer increases the density of ZnO NWs compared to an Au-seed layer, as discussed further in **Chapter IV**. ZnO NWs were grown on ZnO/Metal/Si substrates by using 50 ml of chemical solution mixing 50 mM of $Zn(NO_3)_2$ and HMTA in equimolar ratio. Ammonia was also added in the chemical bath ($[NH_3]_{bath}$ = 600 mM) to set its pH_0 to 10.6, along with 0 and 2.5 mM of $Cu(NO_3)_2$ to grow ZnO NWs with $[Cu]/[Zn]_{bath}$ ratio of 0 and 5%, respectively, as studied in **Section II.3.1**. The ZnO NW growth was achieved at 85 °C for 3 h. After the synthesis of ZnO NWs (1), they were encapsulated by a Parylene-C layer, which was deposited by vacuum deposition and polymerization process (VPD) according to the Gorham method (2).[93] The 1×1 cm^2 top electrode assisted by a mask was obtained by the stack of 3 metallic layers: 20 nm-thick of Ti layer, 250 nm-thick of Al layer, and 100 nm-thick of Au layer using an e-beam evaporator (3). Finally, both the bottom and top electrodes were contacted by two Cu wires using a conductive resin (4). As a comparison, some PNGs were encapsulated with PDMS to protect them from external natural factors.

Two different PNGs were fabricated according to the $[Cu]/[Zn]_{bath}$ ratio of 0% and 5% in the chemical bath for the CBD of unintentionally *n*-doped and Cu-doped ZnO NW matrix (*PNG-A* and *PNG-B*, respectively). Furthermore, it is worth mentioning that a reference-PNG (without ZnO NW) was also manufactured in order to reveal a possible piezoelectric contribution from the Parylene-C layer.

♣ The ZnO seed layer's crystallization was performed at 300 °C for 2h 30 min to prevent damage to the Au layer of the bottom electrode. Typically, this crystallization process is conventionally performed at 500 °C - 1 h.

The morphological properties of the vertically integrated ZnO NW matrix are shown and summarized in **Figure II.5-2(b)**. The *PNG-A* has an integrated unintentionally *n*-doped ZnO NW matrix with the higher mean density (122 NWs per µm^2 – NW/µm^2), larger aspect ratio (defined as the ratio between the length divided by the diameter; in this case 54) and higher deposited volume (0.9 µm^3). The *PNG-B* has an integrated Cu-doped ZnO NW matrix, for which the mean density, aspect ratio, and deposited volume are of 118 NW/µm^2, 47 and 0.78 µm^3, respectively. In addition, the conformity of the Parylene-C layer deposited on these devices, *i.e.* a good isolation of the NW matrix along with a top dielectric layer allowing a capacitive contact between the top of the NW and the top electrode, was verified as shown in **Figure II.5-2(c)**. Furthermore, no short-circuit was detected on any final device (**Figure II.5-2(d)**), by measuring an internal impedance value higher than 10 MΩ for both *PNG-A* and *PNG-B*.

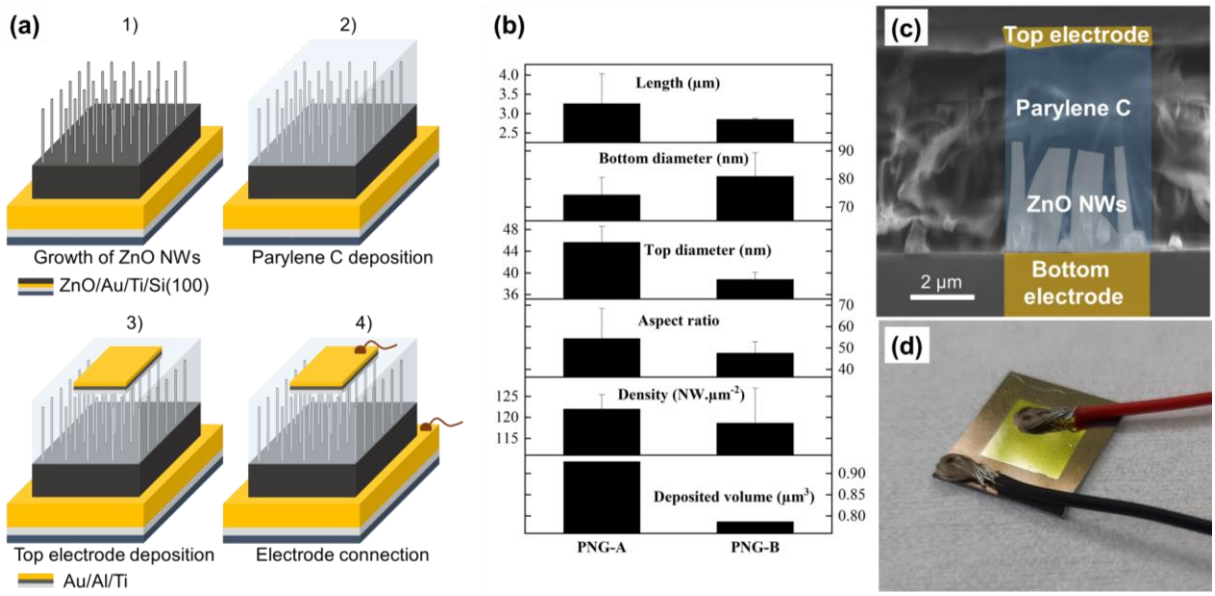

Figure II.5-2. (a) *Fabrication steps of a PNG based on vertically integrated ZnO NWs,* ***(b)*** *morphological properties of the integrated ZnO NW matrix with [Cu]/[Zn]$_{bath}$ ratio of 0% (PNG-A) and 5% (PNG-B),* ***(c)*** *cross-sectional FESEM image, and* ***(d)*** *photo of a final ZnO NW based PNG device.*

II.5.2.2 Characterization of piezoelectric nanogenerators based on Cu-doped ZnO nanowires

The applied vertical force over the PNG was determined from the force-sensor signal by calculating its RMS (integration of the force sensor signal divided by the compression cycle duration) divided by its sensitivity of 11.24 mV/N. In addition, the PNGs were tested in both forward and reverse connection to confirm a real piezoelectric signal from the signal inversion achieved by reversing the connection polarity. Ideally, the piezoelectric signal must be symmetric when changing the polarity connection of the PNGs; however, the test bench used

was not equipped to characterize PNGs in open-circuit conditions, leading to lower piezoelectric signals in reverse connection, as shown in **Figure II.5-3**. As a result, only the forward-connection data are shown in the present work. From reference-PNG characterizations, we confirm that the obtained output voltage is due to the piezoelectric phenomenon from ZnO NWs.

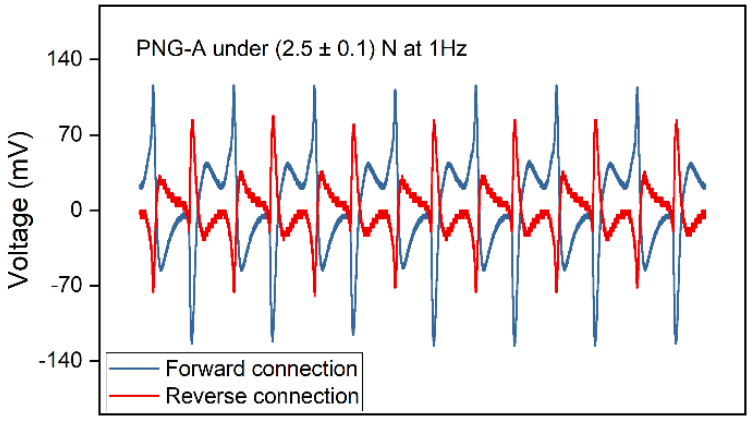

Figure II.5-3. *Output voltage of the PNG-A (ZnO NWs without Cu-doping) when the polarity connection is changed.*

Thus, *PNG-A* and *PNG-B* were characterized under low forces (0.5 - 5 N) and low frequency (0.5 - 5 Hz) as they are the typical mechanical and frequency ranges present in daily life (people walking,[94] human breathing and heart beating,[95] soft finger tapping,[96] etc.), i.e. lower mechanical stress and frequencies. As expected, according to the mathematical description of the piezoelectric effect (coupling between Hooke and electric displacement field equations), a progressive increment of the piezoelectric signal is obtained as long as the mechanical stress increases (i.e. the compressing force), as shown in **Figure II.5-4(a)**. Furthermore, the piezoelectric signal exhibits a direct correlation with the working frequency, as revealed in **Figure II.5-4(b)**. Indeed, a current (*I*) will be generated according to the equation: $I = \frac{\Delta Q}{\Delta t} = d_{33} \times A \times \frac{\Delta \sigma}{\Delta t}$, where ΔQ is the charge generated under a mechanical stress (Δσ) applied over an area (A) of a material with a piezoelectric coefficient (d_{33}).[91] It is worth noticing here that Q only varies with σ. By increasing the working frequency (i.e. by decreasing Δt), the strain rate ($\frac{\Delta \sigma}{\Delta t}$) of the ZnO NW matrix increases along with the generated current *I* flowing in the external load (R_{load}), i.e. in the amplifier/filter system of the test bench. Subsequently, according to the Ohmic law $I=R_{load}V$, an increase in the piezoelectric voltage (*V*) occurs.[97,98]

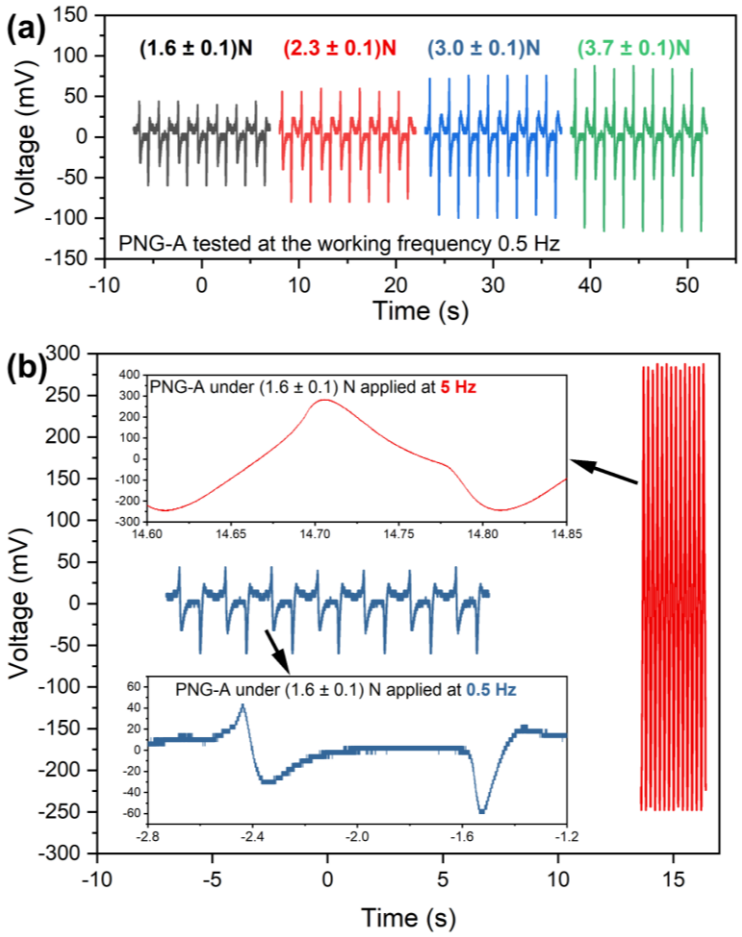

Figure II.5-4. (a) *Output voltage of the PNG-A (ZnO NWs without Cu-doping) as a function of the applied sinusoidal force at 0.5 Hz, and* ***(b)*** *as a function of the working frequency at constant applied force of 1.6 N.*

Interestingly, *PNG-B* provides higher piezoelectric signals than *PNG-A*, whose output signal is stable over time, as shown in **Figure II.5-5(a-b)**, respectively.

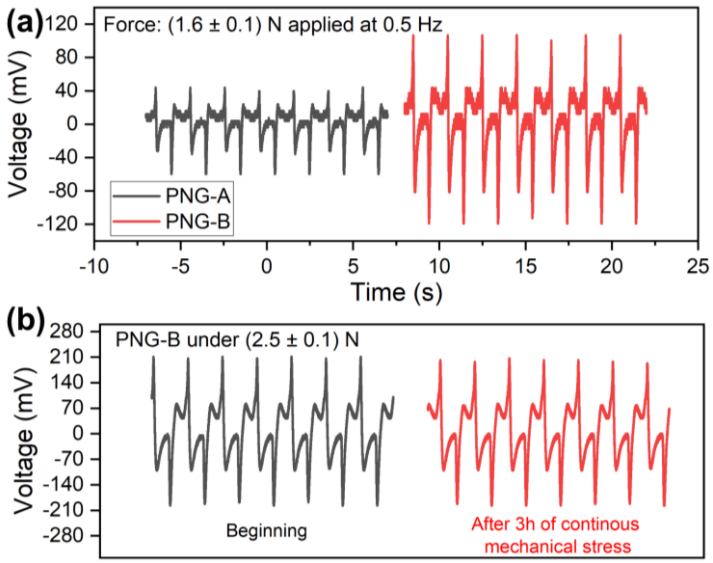

Figure II.5-5. (a) *Output voltage comparison between both PNG-A and PNG-B (ZnO NWs with 0 and 5% of Cu-doping, respectively) under the same applied force condition.* ***(b)*** *Durability of the PNG-B under 2.5 N applied at 1 Hz for 180 min.*

Therefore, the output voltage obtained for different applied forces at different working frequencies of the *PNG-A* and *PNG-B*, before and after encapsulation with PDMS, are summarized in **Figure II.5-6(a-b)**, respectively.

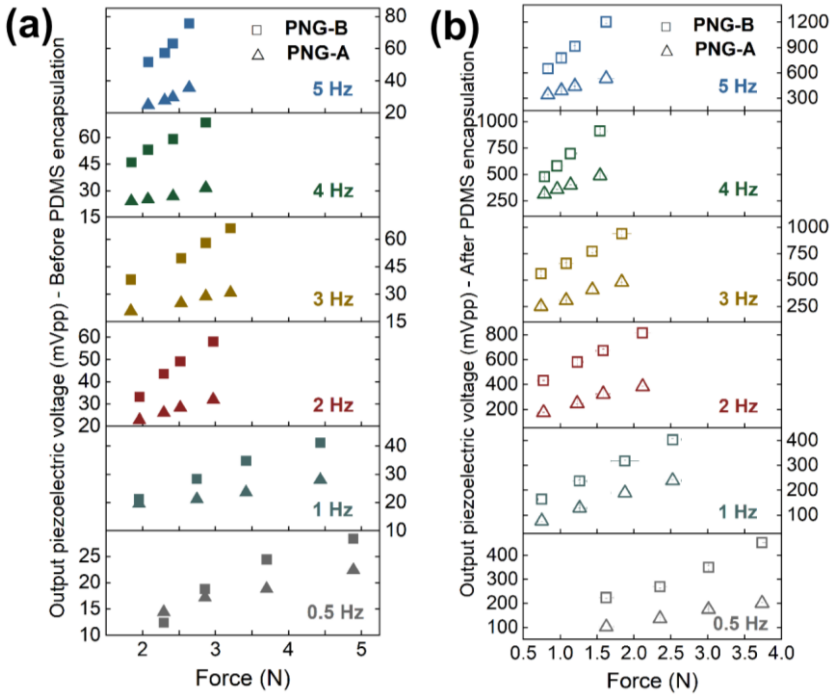

Figure II.5-6. *Summary of the output voltages of both PNG-A and PNG-B (ZnO NWs with 0 and 5% of Cu-doping, respectively)* ***(a)*** *before and* ***(b)*** *after PDMS encapsulation, under different applied forces and working frequencies.*

Interestingly, the PNGs exhibit higher piezoelectric signals after a PDMS encapsulation, displaying minimum values of about 100 mVpp and maximum values of more than 1 Vpp, regarding the highest signal of about 80 mVpp without encapsulation. The improvement of the output voltage could be attributed to a coupling between piezoelectric and triboelectric effects, the latter induced by the friction between the PDMS layer and metallic top electrode of the PNG. However, it is worth mentioning that the mechanical shaker arm was carefully isolated with a 5 mm-thick cardboard piece to minimize a possible triboelectric effect when applying the mechanical stress. A reference-PNG (i.e. without ZnO NWs, containing only Parylene-C between the two electrodes) encapsulated with PDMS was also characterized, giving a maximum electrical signal of ~20 mVpp. This response, absent before encapsulation, remains lower than the piezoelectric signal values of *PNG-A* and *PNG-B*. These results suggest that the PDMS could induce a triboelectric effect during the piezoelectric characterization. In addition, mechanical effects could also arise from the PDMS encapsulation, which could promote a more uniform distribution of mechanical stress across the sample, improving consequently the output signal.

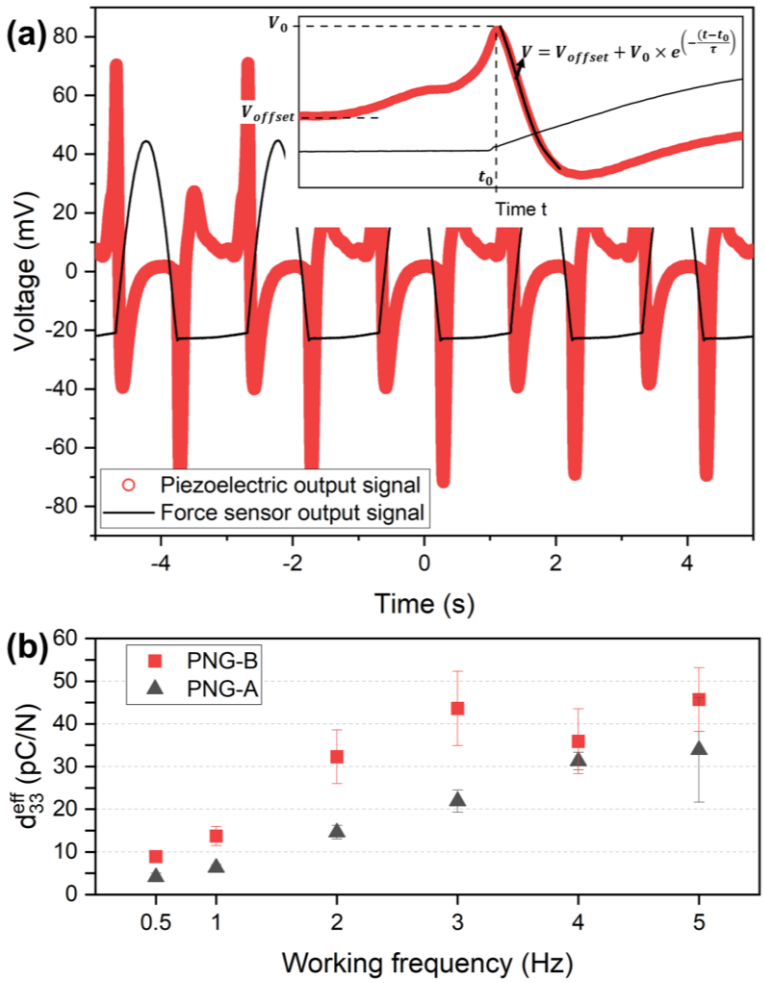

***Figure II.5-7**. **(a)** Graphical method to calculate the effective piezoelectric coefficient d_{33}^{eff} from the output piezoelectric signal as a function of mechanical stress and working frequency[♣]. **(b)** Effective piezoelectric coefficient d_{33}^{eff} calculated from the piezoelectric signal of PNG-A and PNG-B (ZnO NWs with 0 and 5% of Cu-doping, respectively) as a function of the working frequency.*

Furthermore, regardless of the test condition and PDMS encapsulation, although *PNG-A* presents a better ZnO NW matrix morphology for piezoelectric effect (i.e. slightly higher aspect ratio and density), *PNG-B* provides higher piezoelectric signals, and the gap becomes greater as a function of working frequency. These findings thus indicate an additional beneficial effect involving Cu-doping. To elucidate this effect, the effective piezoelectric coefficient d_{33}^{eff} of the device was calculated by using the approach developed by Lopez Garcia et al.[99] This considers the PNG as a capacitor (C_0) discharging over a resistive external load R_{load} (corresponding to the input impedance of the amplifier/filter equipment connected to

[♣] The formula given in **Figure II.5-7(a)** provides an approximation for estimating the time constant (τ) of the PNG's output voltage (V) when $V_0 \leq V \leq V_{offset}$. However, this formula should be implemented considering factors such as the generated piezoelectric charge (Q) and its coupling with the mechanical excitation mode.[108][109] Thus, the formula can be expressed as $V = V_{offset} + V_0 \times e^{\left(-\frac{t-t_0}{\tau}\right)} \times f(t-t_0)$, where $f(t-t_0)$ takes into account different factors.

the PNG – 100 MΩ), allowing us to write d_{33}^{eff} as C_0*V**/**$F_{applied}$**,** where V and $F_{applied}$ are the generated voltage and applied force, respectively. In the present work, C_0 was calculated from the time constant τ (τ = C_0*R_{load}) determined by fitting the exponential decay piezoelectric voltage, as shown in **Figure II.5-7(a)**. Therefore, the d_{33}^{eff} coefficients of *PNG-A* and *PNG-B* are shown in **Figure II.5-7(b)** as a function of working frequency, which values at 0.5 and 1 Hz are in the same range as the values reported in the literature.[100,101]

Given the fact that d_{33}^{eff} does not depend on the applied force and the output voltage,[99] the observed increase of these values with the working frequency could be the result of a progressive accumulation of external charges during the mechanical compression cycle, leading to higher output voltages.[97,98] Interestingly, *PNG-B* exhibits higher d_{33}^{eff} values than *PNG-A*, regardless of the working frequency.

The reported output voltage increase is in agreement with Raman spectroscopy, XPS, ICP-MS and resistivity measurements: Cu dopants are incorporated into ZnO NWs and decrease their density of free electrons,[7,80] resulting in an increase of the electrical resistivity and thus a strong reduction of the screening effect.[102–104] Then, more external charges are generated during the mechanical stress cycle, leading to an improvement of the output voltage.

II.5.3 Output voltage of piezoelectric nanogenerators based on thermally annealed ZnO nanowire matrix

As previously discussed in **Section II.3**, thermal annealing in oxygen-rich conditions form resistive ZnO NWs. In **Section II.5.2**, the output voltage of PNGs was increased through the integration of Cu-doped ZnO NWs, which are more resistive than unintentionally n-doped ZnO NWs. Based on these findings, the integration of thermally annealed ZnO NWs could potentially lead to higher output voltage in related PNGs. This topic is investigated in the present section.

II.5.3.1 Fabrication of piezoelectric nanogenerators based on thermally annealed ZnO nanowires

This study investigates three different PNGs, each based on ZnO NWs subjected to distinct thermal treatments. The architecture of these PNGs is presented in **Figure II.5-8**. First, n-type highly doped (100) Si substrates (0.01 – 0.02 Ω.cm) were coated with a ZnO seed layer

by a dip-coating process. The ZnO seed layer was crystallized by heating the sample (ZnO/Si) in an oven at 500 °C for 1 h in air. Subsequently, 2.5 × 2 cm² samples containing the ZnO seed layer on the Si substrate were used to grow ZnO NWs by CBD following the same protocol presented in **Section II.5.2.1**. After the ZnO NW synthesis, the samples were subjected to thermal annealing in an O_2 atmosphere for 1h at temperatures of 300 and 500 °C. Following annealing treatments, the parylene-C was deposited by vacuum evaporation processes to encapsulate the ZnO NW matrix, resulting in a 2 µm-thick parylene-C layer over the NWs. A more detailed discussion about this parylene-C thickness control will be discussed in **Chapter 3**. Finally, the 1 × 1 cm² top electrode (20 nm of titanium (Ti) – 250 nm of aluminum (Al) – 150 nm of gold (Au)) was achieved by vacuum evaporation deposition with a mask. Cu-wires were then used to contact both the bottom (Si substrate) and the top electrode of the device.

It is important to note that the metallic bottom electrode (Ti/Au) used in the PNGs of **Section II.5.2** was replaced with the highly n-doped Si substrate to allow the thermal treatment of ZnO NWs.

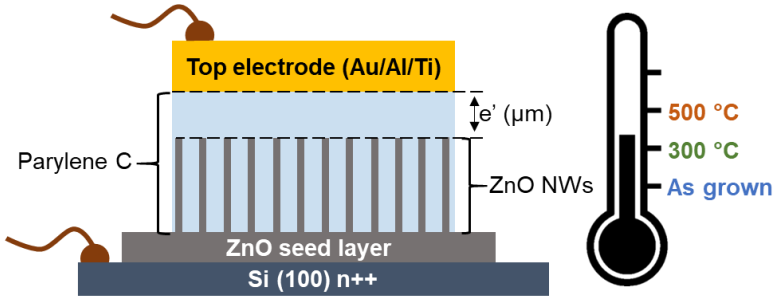

Figure II.5-8. *Schematic of a PNG based on thermally annealed ZnO NWs.*

Vertical ZnO NWs are grown on the preferentially c-axis oriented polycrystalline ZnO seed layer,[105,106] as shown by FESEM images in **Figure II.5-9**. These nanostructures exhibit a mean length, diameter, and density of 6.1 ± 0.8 µm, 69 ± 35 nm, and 42.9 ± 5.7 NW/µm², respectively. It is worth mentioning that the synthesized ZnO NWs of the present section have different morphological features than those obtained in **Section II.5.2.1**, although the chemical bath conditions were identical. This indicates that the change in properties of the ZnO seed layer, likely induced by the different crystallization steps used in the present experiment, affects directly the properties of ZnO NWs.[105] In addition, to investigate potential morphological changes in ZnO NWs after thermal annealing, a sample was divided into three pieces, each subjected to different annealing conditions. Thus, no morphological changes are observed after thermal annealing, as depicted in **Figure II.5-9**. It is important to

note that the length of the NWs can vary depending on the observation area within the sample, such as the edge or the center.

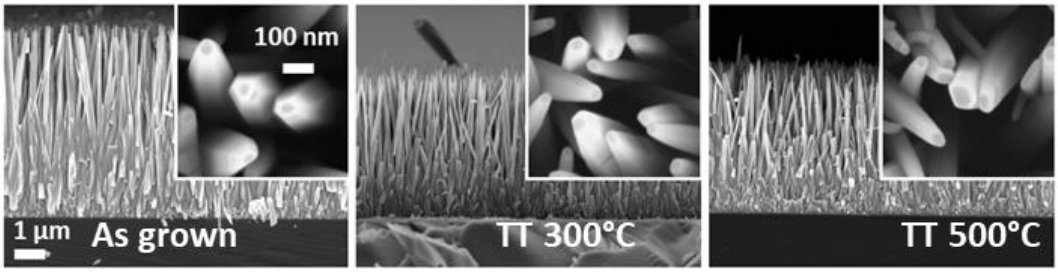

Figure II.5-9. *Cross-section and top-view (inset) FESEM images of ZnO NWs after thermal annealing at* ***(a)*** *As-grown,* ***(b)*** *300 °C, and* ***(c)*** *500 °C under an O_2 atmosphere before parylene-C encapsulation.*

After the deposition of parylene-C and the top electrode over all the samples, a random PNG was selected to verify the uniformity of the parylene-C deposition, which showed a thickness of 2 µm over the NWs, as illustrated in **Figure II.5-10(a)**. Thus, the fabrication of PNGs based on ZnO NWs annealed at different temperatures is achieved, whose features are summarized in **Table II.5-1**.

Table II.5-1. *Features of PNGs based on ZnO NWs with different thermal treatments.*

PNG	Integrated ZnO NW features	Thermal annealing		Parylene-C over NW matrix
		T (°C)	Comments	
PNG – REF	Length: 6.1 ± 0.8 µm	As-Grown	Annealing in an O_2 atmosphere for 1 h	Thickness of around 2 µm
PNG – TT300°C	Diameter: 69 ± 35 nm	300		
PNG – TT500°C	Density: 42.9 ± 5.7 NW/µm²	500		

In addition, the isolation of each NW from its neighbor with the parylene-C was investigated through FESEM-EDS♣ mapping of the PNG's cross-section, as shown in **Figure II.5-10(b)**. The parylene-C (blue-sky region), positioned between the bottom and top electrodes of the PNG, appears to infiltrate between the ZnO NWs (blue and green region for O and Zn, respectively). This should isolate the ZnO NWs and prevent free electron tunneling between them, inducing screening effects in the device.[107] However, the parylene-C seems more concentrated at the top of the NWs, as suggested by the dense blue-sky region. Regarding the top electrode, the 20 nm-thick Ti layer appears to extend across the device, as evoked by the purple region. The 250 nm-thick Al layer adheres effectively to the Ti layer, as indicated by the highly concentrated yellow region. Interestingly, the orange region shows the

♣ EDS: energy dispersive X-ray spectroscopy

presence of the 150 nm-thick Au layer over the Al and Ti layers, and suggest a non-negligible amount of Au within the ZnO NW matrix. This apparent Au contamination could originate from the reactants used in the chemical bath such as $Zn(NO_3)_2$ (98% purity), HMTA (99.5% purity), and ammonia (28 – 30% purity). The potential presence of Au in the ZnO NWs could cause a short circuit of the device. To verify this, the two electrodes were connected to an ohmmeter, and the device's impedance was measured. Since the impedances were greater than 2 MΩ, it suggests that the devices remain functional and are suitable for further characterization. Further details concerning the apparent inhomogeneous density of parylene-C across the PNG and the presence of an Au signal detected from the ZnO NWs will be discussed in **Section III.2.2**, which investigates PNGs with different thickness of parylene-C top layers.

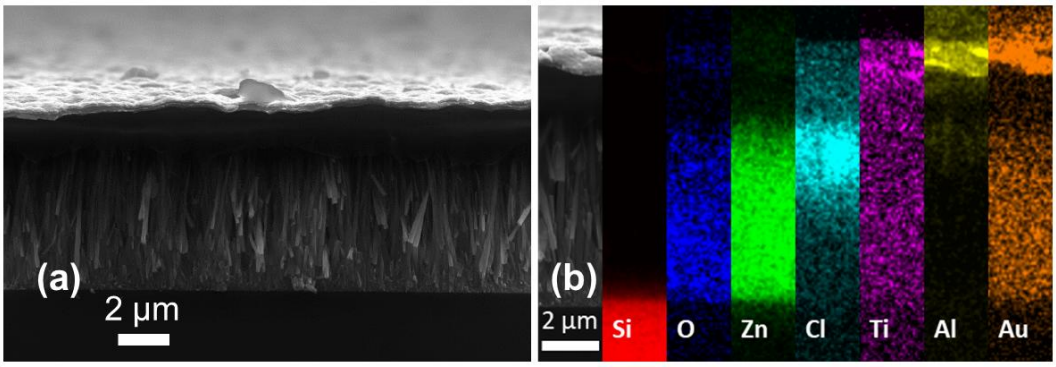

Figure II.5-10. (a) *Cross-section FESEM image of a PNG.* ***(b)*** *FESEM-EDS mapping of the PNG's cross-section depicting the bottom electrode (Si-red), ZnO NW matrix (Zn-green and O-blue), parylene-C layer (Cl-blue-sky), and the top electrode (Ti-purple, Al-yellow and Au-orange).*

II.5.3.2 Characterization of piezoelectric nanogenerators based on thermally annealed ZnO nanowires

The PNGs were tested under identical conditions to those characterized in **Section II.5.2.2** in the LTM's test bench. It should be mentioned that the output signal of the devices was amplified by a 10-factor using the Stanford Research Systems SR560 amplifier of the test bench to easily discern the piezoelectric signal from the electronic noise. In addition, piezoelectric signal of the PNGs was confirmed through its inversion with the connection polarity reverse. However, the highest piezoelectric signal achieved in the forward connection of the device will be presented in this section. As expected, the output voltage of the PNG gradually increases as the temperature of thermal annealing was increased until 500 °C, as illustrated in **Figure II.5-11(a)**. Then, regardless of the mechanical test condition, the device integrating a 500 °C thermally annealed ZnO NW matrix (PNG_TT500°C) exhibits the highest output voltage, as summarized in **Figure II.5-11(b)**. This agrees with the dependency of the

resistivity of ZnO NWs on the thermal temperature, as discussed in **Section II.3.6**. Thus, by increasing the temperature of the thermal annealing in an O_2 atmosphere, a decrease in free carrier density occurs in ZnO NWs, improving their piezoelectric properties and the performance of the PNG.[89] It appears, however, that the PNGs with thermally annealed ZnO NWs need to be tested with working frequencies over 2 Hz to display significant improvement as compared to the PNG-REF. This could potentially innvolve probable changes in the mechanical properties of ZnO NWs with thermal annealing. Indeed, as revealed by Raman spectroscopy in **Section II.2.5** and **Section II.3.3**, the shift towards lower wavenumber of the E_2^{high} Raman line indicates tensile stress along the *c*-axis in ZnO NWs after thermal annealing.[34] A mechanical effect of the parylene-C layer with inhomogeneous density across the PNG should also account for the piezoelectric behavior of the device, which require additional FEM calculations.

The reported improvement in the output voltage of PNGs integrating annealed ZnO NWs is in agreement with the previous results in **Section II.3**: thermal annealing engineer H- and N-related defects, resulting in increased electrical resistivity and thus a strong reduction of the screening effect in ZnO NWs.[22] Then, more external charges are generated during the mechanical stress cycle, leading to an improvement in the output voltage of the device.

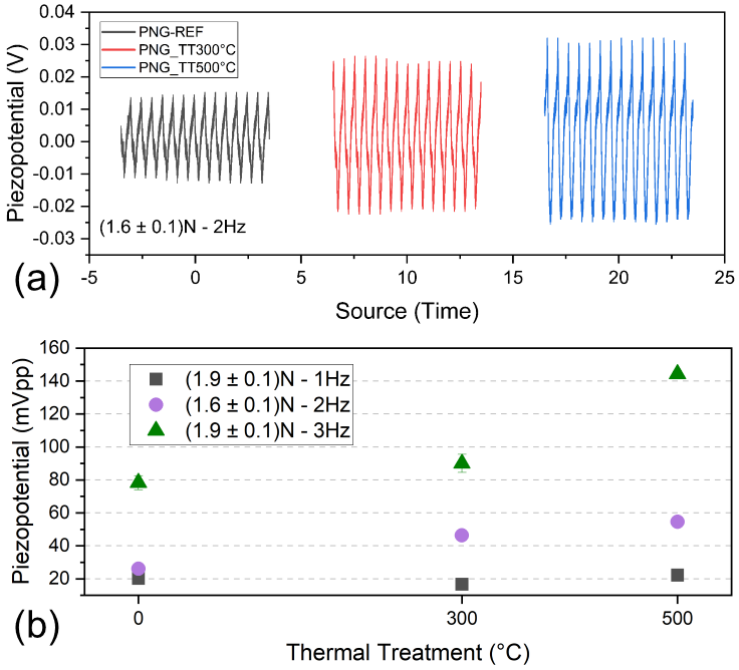

Figure II.5-11. (a) *Output voltage comparison between PNGs with thermally annealed ZnO NWs under the same applied force condition.* ***(b)*** *Output voltage values of PNGs based on as-grown, 300 °C, and 500 °C-thermally annealed ZnO NWs measured under different mechanical stress conditions. This figure displays the piezoelectric signals and the output voltage values amplified by a 10-factor using the Stanford Research Systems SR560 amplifier of the LTM's test bench for better readability.*

II.6 Conclusion

In conclusion, Cu-doped ZnO NWs have been grown by CBD in a high pH region using $Cu(NO_3)_2$ and NH_3 as chemical additives. The pH_0 of the chemical bath was set above 10.6 to promote electrostatic interactions between the *c*-polar faces of ZnO NWs and Cu(II) species in the solution. Under these favorable thermodynamic conditions, ICP-MS analysis has confirmed the incorporation of Cu in ZnO NWs, with atomic $[Cu]/[Zn]_{NW}$ ratio around 20 – 100 ppm according to the $[Cu]/[Zn]_{bath}$ ratio. However, only 15-18% of the total amount of Cu in ZnO NWs was found to form Cu_{Zn} acceptor defects, as XANES and XLD spectroscopy have evidenced. Interestingly, the density of Cu_{Zn} acceptor defects can be easily tuned by adjusting the concentration of the Cu-dopant in the bath.

Electrical measurements on single nanowires have revealed the acceptor behavior of Cu in ZnO NWs, resulting in increased electrical resistivity. However, the extent of resistivity enhancement induced Cu atoms appeared to be influenced by the pH_0 used for the growth of ZnO NWs. Thermal annealing further increased the resistivity of Cu-doped ZnO NWs, making them the most resistive nanostructures studied. This resistivity rise was attributed to the migration of Cu atoms and the likely formation of Cu-related complexes in ZnO NWs, as XPS, 5 K cathodoluminescence, XANES, and XLD spectroscopy have suggested.

Based on the resistive properties of Cu-doped and thermally annealed ZnO NWs, PNGs were fabricated to evaluate their piezoelectric properties. Thus, PNGs based on Cu-doped or thermally annealed ZnO NWs exhibited a significant increase in output voltage compared to PNGs using unintentionally n-doped ZnO NWs (reference) under soft mechanical conditions. These findings present promising pathways for enhancing PNG performance via the reduction of screening effects in ZnO NWs.

Bibliography

[1] M. D. McCluskey, S. J. Jokela, *J. Appl. Phys.* 2009, *106*, 1–13.

[2] R. D. Shannon, *Acta Crystallogr. Sect. A* 1976, *32*, 751–767.

[3] E. Kaminska, I. Pasternak, P. Boguslawski, A. Jezierski, E. Dynowska, R. Jakiela, E. Przezdziecka, A. Piotrowska, J. Kossut, *AIP Conf. Proc.* 2009, *1199*, 120–121.

[4] J. Joo, B. Y. Chow, M. Prakash, E. S. Boyden, J. M. Jacobson, *Nat. Mater.* 2011, *10*, 596–601.

[5] C. Verrier, E. Appert, O. Chaix-Pluchery, L. Rapenne, Q. Rafhay, A. Kaminski-Cachopo, V. Consonni, *Inorg. Chem.* 2017, *56*, 13111–13122.

[6] P. Gaffuri, E. Appert, O. Chaix-Pluchery, L. Rapenne, M. Salaün, V. Consonni, *Inorg. Chem.* 2019, *58*, 10269–10279.

[7] C. Lausecker, B. Salem, X. Baillin, O. Chaix-Pluchery, H. Roussel, S. Labau, B. Pelissier, E. Appert, V. Consonni, *Inorg. Chem.* 2021, *60*, 1612–1623.

[8] J. Villafuerte, X. Zhang, E. Sarigiannidou, F. Donatini, O. Chaix-Pluchery, L. Rapenne, M.-Q. Le, L. Petit, J. Pernot, V. Consonni, *Nano Energy* 2023, *114*, 108599.

[9] A. Baillard, E. Appert, M. Weber, V. Jacob, H. Roussel, L. Rapenne, O. Chaix-Pluchery, V. Consonni, *J. Phys. Chem. C* 2023, *127*, 8306–8319.

[10] R. O. James, T. W. Healy, *J. Colloid Interface Sci.* 1972, *40*, 65–81.

[11] D. W. Fuerstenau, K. Osseo-Asare, *J. Colloid Interface Sci.* 1987, *118*, 524–542.

[12] D. Huang, Y. J. Zhao, D. H. Chen, Y. Z. Shao, *Appl. Phys. Lett.* 2008, *92*, 90–93.

[13] S. Guillemin, V. Consonni, E. Appert, E. Puyoo, L. Rapenne, H. Roussel, *J. Phys. Chem. C* 2012, *116*, 25106–25111.

[14] R. Parize, J. Garnier, O. Chaix-Pluchery, C. Verrier, E. Appert, V. Consonni, *J. Phys. Chem. C* 2016, *120*, 5242–5250.

[15] A. Degen, M. Kosec, *J. Eur. Ceram. Soc.* 2000, *20*, 667–673.

[16] M. Valtiner, S. Borodin, G. Grundmeier, *Langmuir* 2008, *24*, 5350–5358.

[17] C. Kunze, M. Valtiner, R. Michels, K. Huber, G. Grundmeier, *Phys. Chem. Chem. Phys.* 2011, *13*, 12959.

[18] M. Raja, N. Muthukumarasamy, D. Velauthapillai, R. Balasundaraprabhu, *Superlattices Microstruct.* 2014, *72*, 102–110.

[19] R. Parize, J. D. Garnier, E. Appert, O. Chaix-Pluchery, V. Consonni, *ACS Omega* 2018, *3*, 12457–12464.

[20] T. Cossuet, H. Roussel, J. M. Chauveau, O. Chaix-Pluchery, J. L. Thomassin, E. Appert, V. Consonni, *Nanotechnology* 2018, *29*, DOI 10.1088/1361-6528/aadf62.

[21] N. H. Nickel, K. Fleischer, *Phys. Rev. Lett.* 2003, *90*, 4.

[22] J. Villafuerte, O. Chaix-Pluchery, J. Kioseoglou, F. Donatini, E. Sarigiannidou, J. Pernot, V. Consonni, *Phys. Rev. Mater.* 2021, *5*, 1–15.

[23] X. Li, B. Keyes, S. Asher, S. B. Zhang, S. H. Wei, T. J. Coutts, S. Limpijumnong, C. G. Van De Walle, *Appl. Phys. Lett.* 2005, *86*, 1–3.

[24] S. J. Jokela, M. D. McCluskey, *Phys. Rev. B - Condens. Matter Mater. Phys.* 2007, *76*, 6–9.

[25] E. V. Lavrov, J. Weber, F. Börrnert, C. G. Van de Walle, R. Helbig, *Phys. Rev. B - Condens. Matter Mater. Phys.* 2002, *66*, 1–7.

[26] F. Herklotz, A. Hupfer, K. M. Johansen, B. G. Svensson, S. G. Koch, E. V. Lavrov, *Phys. Rev. B - Condens. Matter Mater. Phys.* 2015, *92*, 1–10.

[27] J. L. Lyons, J. B. Varley, D. Steiauf, A. Janotti, C. G. Van De Walle, *J. Appl. Phys.* 2017, *122*, DOI 10.1063/1.4992128.

[28] E. . Lavrov, *Phys. B Condens. Matter* 2003, *340–342*, 195–200.

[29] E. V Lavrov, F. Börrnert, J. Weber, *Phys. Rev. B* 2005, *71*, 035205.

[30] C. Bundesmann, N. Ashkenov, M. Schubert, D. Spemann, T. Butz, E. M. Kaidashev, M. Lorenz, M. Grundmann, *Appl. Phys. Lett.* 2003, *83*, 1974–1976.

[31] J. Villafuerte, E. Sarigiannidou, F. Donatini, J. Kioseoglou, O. Chaix-Pluchery, J. Pernot, V. Consonni, *Nanoscale Adv.* 2022, *4*, 1793–1807.

[32] P. Sundara Venkatesh, V. Ramakrishnan, K. Jeganathan, *Phys. B Condens. Matter* 2016, *481*, 204–208.

[33] Y. Deng, A. D. Handoko, Y. Du, S. Xi, B. S. Yeo, *ACS Catal.* 2016, *6*, 2473–2481.

[34] T. Gruber, G. M. Prinz, C. Kirchner, R. Kling, F. Reuss, W. Limmer, A. Waag, *J. Appl. Phys.* 2004, *96*, 289–293.

[35] F. Decremps, J. Pellicer-Porres, A. M. Saitta, J.-C. Chervin, A. Polian, *Phys. Rev. B* 2002, *65*, 092101.

[36] K. Samanta, P. Bhattacharya, R. S. Katiyar, W. Iwamoto, P. G. Pagliuso, C. Rettori, *Phys. Rev. B - Condens. Matter Mater. Phys.* 2006, *73*, 1–5.

[37] A. Teke, Ü. Özgür, S. Doğan, X. Gu, H. Morkoç, B. Nemeth, J. Nause, H. O. Everitt, *Phys. Rev. B - Condens. Matter Mater. Phys.* 2004, *70*, 1–10.

[38] J. F. Rommeluère, L. Svob, F. Jomard, J. Mimila-Arroyo, A. Lusson, V. Sallet, Y. Marfaing, *Appl. Phys. Lett.* 2003, *83*, 287–289.

[39] D. Pfisterer, J. Sann, D. M. Hofmann, M. Plana, A. Neumann, M. Lerch, B. K. Meyer, *Phys. Status Solidi Basic Res.* 2006, *243*, 2–4.

[40] J. W. Sun, Y. M. Lu, Y. C. Liu, D. Z. Shen, Z. Z. Zhang, B. Yao, B. H. Li, J. Y. Zhang, D. X. Zhao, X. W. Fan, *J. Appl. Phys.* 2007, *102*, DOI 10.1063/1.2772581.

[41] J. G. Reynolds, C. L. Reynolds, A. Mohanta, J. F. Muth, J. E. Rowe, H. O. Everitt, D. E. Aspnes, *Appl. Phys. Lett.* 2013, *102*, DOI 10.1063/1.4802753.

[42] D. C. Look, D. C. Reynolds, C. W. Litton, R. L. Jones, D. B. Eason, G. Cantwell, *Appl. Phys. Lett.* 2002, *81*, 1830–1832.

[43] B. K. Meyer, H. Alves, D. M. Hofmann, W. Kriegseis, D. Forster, F. Bertram, J. Christen, A. Hoffmann, M. Straßburg, M. Dworzak, U. Haboeck, A. V. Rodina, *Phys. Status Solidi Basic Res.* 2004, *241*, 231–260.

[44] J. Villafuerte, F. Donatini, J. Kioseoglou, E. Sarigiannidou, O. Chaix-Pluchery, J. Pernot, V. Consonni, *J. Phys. Chem. C* 2020, *124*, 16652–16662.

[45] E. V. Lavrov, F. Herklotz, J. Weber, *Phys. Rev. B - Condens. Matter Mater. Phys.* 2009, *79*, 1–13.

[46] S. Guillemin, V. Consonni, L. Rapenne, E. Sarigiannidou, F. Donatini, G. Bremond, *RSC Adv.* 2016, *6*, 44987–44992.

[47] C. Soci, A. Zhang, B. Xiang, S. A. Dayeh, D. P. R. Aplin, J. Park, X. Y. Bao, Y. H. Lo, D. Wang, *Nano Lett.* **2007**, *7*, 1003–1009.

[48] R. Heinhold, A. Neiman, J. V. Kennedy, A. Markwitz, R. J. Reeves, M. W. Allen, *Phys. Rev. B* **2017**, *95*, 1–13.

[49] R. Dingle, *Phys. Rev. Lett.* **1969**, *23*, 579–581.

[50] H. Qiu, F. Gallino, C. Di Valentin, Y. Wang, *Phys. Rev. Lett.* **2011**, *106*, 1–4.

[51] P. Dahan, V. Fleurov, P. Thurian, R. Heitz, A. Hoffmann, I. Broser, *J. Phys. Condens. Matter* **1998**, *10*, 2007–2019.

[52] M. A. Reshchikov, V. Avrutin, N. Izyumskaya, R. Shimada, H. Morkoç, S. W. Novak, *J. Vac. Sci. Technol. B Microelectron. Nanom. Struct. Process. Meas. Phenom.* **2009**, *27*, 1749–1754.

[53] X. H. Huang, C. Zhang, C. B. Tay, T. Venkatesan, S. J. Chua, *Appl. Phys. Lett.* **2013**, *102*, DOI 10.1063/1.4798240.

[54] C. West, D. J. Robbins, P. J. Dean, W. Hayes, *Phys. B+C* **1983**, *116*, 492–499.

[55] M. Ferhat, A. Zaoui, R. Ahuja, *Appl. Phys. Lett.* **2009**, *94*, 1–4.

[56] A. Ciechan, P. Bogusławski, *Sci. Rep.* **2021**, *11*, 1–11.

[57] P. Dahan, V. Fleurov, P. Thurian, R. Heitz, A. Hoffmann, I. Broser, *J. Phys. Condens. Matter* **1998**, *10*, 2007–2019.

[58] A. Ney, K. Ollefs, S. Ye, T. Kammermeier, V. Ney, T. C. Kaspar, S. A. Chambers, F. Wilhelm, A. Rogalev, *Phys. Rev. Lett.* **2008**, *100*, 157201.

[59] K. M. McPeak, M. A. Becker, N. G. Britton, H. Majidi, B. A. Bunker, J. B. Baxter, *Chem. Mater.* **2010**, *22*, 6162–6170.

[60] E. Sarigiannidou, P. Gaffuri, F. Wilhelm, J. Kioseoglou, A. Rogalev, E. Nikidis, E. Appert, V. Consonni, *Phys. Rev. Mater.* **2023**, *7*, 076001.

[61] V. Ney, B. Henne, J. Lumetzberger, F. Wilhelm, K. Ollefs, A. Rogalev, A. Kovacs, M. Kieschnick, A. Ney, *Phys. Rev. B* **2016**, *94*, 1–9.

[62] V. Ney, V. Venkataraman, F. Wilhelm, A. Rogalev, A. Ney, *J. Appl. Phys.* **2019**, *126*, DOI 10.1063/1.5124352.

[63] P. S. Vachhani, G. Dalba, R. K. Ramamoorthy, F. Rocca, O. Šipr, A. K. Bhatnagar, *J. Phys. Condens. Matter* **2012**, *24*, 506001.

[64] O. Šipr, J. Vackář, P. S. Vachhani, R. K. Ramamoorthy, G. Dalba, A. K. Bhatnagar, F. Rocca, *J. Phys. Conf. Ser.* **2013**, *430*, 012128.

[65] P. S. Vachhani, O. Šipr, A. K. Bhatnagar, R. K. Ramamoorthy, R. J. Choudhary, D. M. Phase, G. Dalba, A. Kuzmin, F. Rocca, *J. Alloys Compd.* **2016**, *678*, 304–311.

[66] A. Janotti, C. G. Van de Walle, *Phys. Rev. B* **2007**, *76*, 165202.

[67] D. O. Demchenko, B. Earles, H. Y. Liu, V. Avrutin, N. Izyumskaya, Ü. Özgür, H. Morkoç, *Phys. Rev. B - Condens. Matter Mater. Phys.* **2011**, *84*, 1–5.

[68] S. Limpijumnong, S. B. Zhang, S. H. Wei, C. H. Park, *Phys. Rev. Lett.* **2004**, *92*, 1–4.

[69] T. Cossuet, F. Donatini, A. M. Lord, E. Appert, J. Pernot, V. Consonni, *J. Phys. Chem. C* **2018**, *122*, 22767–22775.

[70] A. Soudi, C. H. Hsu, Y. Gu, *Nano Lett.* **2012**, *12*, 5111–5116.

[71] A. De Luna Bugallo, F. Donatini, C. Sartel, V. Sallet, J. Pernot, *Appl. Phys. Express* 2015, *8*, 025001.

[72] A. M. Lord, T. G. Maffeis, M. W. Allen, D. Morgan, P. R. Davies, D. R. Jones, J. E. Evans, N. A. Smith, S. P. Wilks, *Appl. Surf. Sci.* 2014, *320*, 664–669.

[73] A. M. Lord, T. G. Maffeis, A. S. Walton, D. M. Kepaptsoglou, Q. M. Ramasse, M. B. Ward, J. Köble, S. P. Wilks, *Nanotechnology* 2013, *24*, DOI 10.1088/0957-4484/24/43/435706.

[74] H. L. Pan, B. Yao, T. Yang, Y. Xu, B. Y. Zhang, W. W. Liu, D. Z. Shen, *Appl. Phys. Lett.* 2010, *97*, 2–5.

[75] M. Suja, S. B. Bashar, M. M. Morshed, J. Liu, *ACS Appl. Mater. Interfaces* 2015, *7*, 8894–8899.

[76] W. Dai, X. Pan, C. Chen, S. Chen, W. Chen, H. Zhang, Z. Ye, *RSC Adv.* 2014, *4*, 31969–31972.

[77] R. Cuscó, E. Alarcón-Lladó, J. Ibáñez, L. Artús, J. Jiménez, B. Wang, M. J. Callahan, *Phys. Rev. B* 2007, *75*, 165202.

[78] O. Lupan, T. Pauporté, T. Le Bahers, B. Viana, I. Ciofini, *Adv. Funct. Mater.* 2011, *21*, 3564–3572.

[79] S. Sahoo, G. L. Sharma, R. S. Katiyar, *J. Raman Spectrosc.* 2012, *43*, 72–75.

[80] C. L. Hsu, Y. D. Gao, Y. S. Chen, T. J. Hsueh, *ACS Appl. Mater. Interfaces* 2014, *6*, 4277–4285.

[81] M. C. Biesinger, *Surf. Interface Anal.* 2017, *49*, 1325–1334.

[82] J. Sultana, S. Paul, A. Karmakar, G. K. Dalapati, S. Chattopadhyay, *J. Mater. Sci. Mater. Electron.* 2018, *29*, 12878–12887.

[83] N. Y. Garces, L. Wang, L. Bai, N. C. Giles, L. E. Halliburton, G. Cantwell, *Appl. Phys. Lett.* 2002, *81*, 622–624.

[84] P. Gaffuri, T. Dedova, E. Appert, M. Danilson, A. Baillard, O. Chaix-Pluchery, F. Güell, I. Oja-Acik, V. Consonni, *Appl. Surf. Sci.* 2022, *582*, 152323.

[85] A. M. Lord, T. G. Maffeis, A. S. Walton, D. M. Kepaptsoglou, Q. M. Ramasse, M. B. Ward, J. Köble, S. P. Wilks, *Nanotechnology* 2013, *24*, DOI 10.1088/0957-4484/24/43/435706.

[86] L. Wang, S. Guillemin, J. M. Chauveau, V. Sallet, F. Jomard, R. Brenier, V. Consonni, G. Brémond, *Phys. Status Solidi Curr. Top. Solid State Phys.* 2016, *13*, 576–580.

[87] M. Manrique, V. Consonni, S. Boubenia, H. Roussel, M. Zeghouane, S. Labau, S. Cavalaglio, C. Pudda, V. Jacob, G. Le Rhun, B. Salem, *Energy Technol.* 2024, *2301381*, DOI 10.1002/ente.202301381.

[88] Y. Yan, M. M. Al-Jassim, S. H. Wei, *Appl. Phys. Lett.* 2006, *89*, 87–90.

[89] C. Opoku, A. S. Dahiya, F. Cayrel, G. Poulin-Vittrant, D. Alquier, N. Camara, *RSC Adv.* 2015, *5*, 69925–69931.

[90] B. Puchala, D. Morgan, *Phys. Rev. B - Condens. Matter Mater. Phys.* 2012, *85*, 1–5.

[91] Y. K. Frodason, K. M. Johansen, T. S. Bjørheim, B. G. Svensson, A. Alkauskas, *Phys. Rev. B* 2018, *97*, 104109.

[92] O. Graton, G. Poulin-Vittrant, A. S. Dahiya, N. Camara, L. P. T. H. Hue, M. Lethiecq, *Phys. Status Solidi - Rapid Res. Lett.* 2013, *7*, 915–918.

[93] W. F. Gorham, *J. Polym. Sci. Part A-1 Polym. Chem.* 1966, *4*, 3027–3039.

[94] A. Pachi, T. Ji, *Struct. Eng.* 2005, *83*, 36–40.

[95] A. S. Bugaev, V. V. Chapursky, S. I. Ivashov, V. V. Razevig, A. P. Sheyko, I. A. Vasilyev, *Proc. Tenth Int. Conf. Gr. Penetrating Radar, GPR 2004* 2004, *1*, 291–294.

[96] C. B. Irwin, M. E. Sesto, *Appl. Ergon.* 2012, *43*, 1038–1043.

[97] R. Yang, Y. Qin, L. Dai, Z. L. Wang, *Nat. Nanotechnol.* 2009, *4*, 34–39.

[98] K. Il Park, S. Bin Bae, S. H. Yang, H. I. Lee, K. Lee, S. J. Lee, *Nanoscale* 2014, *6*, 8962–8968.

[99] A. J. Lopez Garcia, R. Tao, M. Mouis, G. Ardila, *21st Int. Conf. Solid-State Sensors, Actuators Microsystems, TRANSDUCERS 2021* 2021, 1056–1059.

[100] E. Broitman, M. Y. Soomro, J. Lu, M. Willander, L. Hultman, *Phys. Chem. Chem. Phys.* 2013, *15*, 11113–11118.

[101] D. A. Scrymgeour, J. W. P. Hsu, *Nano Lett.* 2008, *8*, 2204–2209.

[102] G. Romano, G. Mantini, A. Di Carlo, A. D'Amico, C. Falconi, Z. L. Wang, *Nanotechnology* 2011, *22*, DOI 10.1088/0957-4484/22/46/465401.

[103] R. Hinchet, S. Lee, G. Ardila, L. Montès, M. Mouis, Z. L. Wang, *Adv. Funct. Mater.* 2014, *24*, 971–977.

[104] A. J. Lopez Garcia, M. Mouis, V. Consonni, G. Ardila, *Nanomaterials* 2021, *11*, DOI 10.3390/nano11040941.

[105] S. Guillemin, V. Consonni, E. Appert, E. Puyoo, L. Rapenne, H. Roussel, *J. Phys. Chem. C* 2012, *116*, 25106–25111.

[106] S. Guillemin, L. Rapenne, H. Roussel, E. Sarigiannidou, G. Brémond, V. Consonni, *J. Phys. Chem. C* 2013, *117*, 20738–20745.

[107] D. Yang, Y. Qiu, Q. Jiang, Z. Guo, W. Song, J. Xu, Y. Zong, Q. Feng, X. Sun, *Appl. Phys. Lett.* 2017, *110*, DOI 10.1063/1.4975477.

[108] N. Buatip, T. Auzelle, P. John, S. Rauwerdink, M. Sodhi, M. Salaün, B. Fernandez, E. Monroy, D. Mornex, C. R. Bowen, R. Songmuang, *ACS Appl. Nano Mater.* 2024, *7*, 15798–15807.

[109] K. Nadaud, G. Poulin-Vittrant, D. Alquier, *Mech. Syst. Signal Process.* 2019, *133*, 106278.

The page was intentionally left blank.

The page was intentionally left blank.

Chapter III – Investigation of nanocomposites based on ZnO nanowire/Parylene-C/Al_2O_3 to enhance the performance of piezoelectric nanogenerators

Content

III.1 State-of-the-art: impact of polymer thickness and surface passivation on the performance of ZnO nanowire-based piezoelectric nanogenerators 130
III.1.1 Thickness of the polymer layer 130
III.1.2 Surface Fermi level pinning effect 131
III.1.3 Surface passivation of ZnO nanowires with polymer layers 132
III.2 Influence of parylene-C top layer thickness on the output voltage of piezoelectric nanogenerators 134
III.2.1 Fabrication of piezoelectric nanogenerators with different thicknesses of Parylene-C top layer 134
III.2.2 Measuring parylene-C thickness in piezoelectric nanogenerators using electronic microscopy 135
III.2.3 Raman spectroscopy of a parylene-C layer on ZnO nanowires 138
III.2.4 Internal impedance of piezoelectric nanogenerators with different thicknesses of parylene-C top layer 140
III.2.5 Output voltage of piezoelectric nanogenerators with different thicknesses of parylene-C top layer 142
III.3 Effect of Al_2O_3 shell layers on the surface defects of ZnO nanowires grown by chemical bath deposition 145
III.3.1 Experimental procedure: ZnO/Al_2O_3 core-shell heterostructures elaboration 145
III.3.2 Morphological properties of ZnO/Al_2O_3 core-shell heterostructures assessed by electronic microscopy 146
III.3.3 Structural properties of ZnO/Al_2O_3 core-shell heterostructures evaluated by θ-2θ and Grazing X-ray diffraction 147
III.3.4 Raman spectroscopy of ZnO/Al_2O_3 core-shell heterostructures 149
III.3.5 Cathodoluminescence spectroscopy at 5 K of ZnO/Al_2O_3 core-shell heterostructures 151
III.4 Enhancing the performance of piezoelectric nanogenerators based on ZnO nanowire matrix with Al_2O_3 shell passivation layers 154
III.4.1 Fabrication of piezoelectric nanogenerators based on ZnO/Al_2O_3 core-shell heterostructures 154
III.4.2 First piezoelectric characterizations of ZnO/Al_2O_3 heterostructures-based piezoelectric nanogenerators on the LTM's test bench 155
III.4.3 Piezoelectric characterizations of ZnO/Al_2O_3 heterostructures-based piezoelectric nanogenerators on the CROMA's test bench 157
III.4.3.1 Description of the CROMA's test bench 158
III.4.3.2 Choice of the force load configuration 159
III.4.3.3 Removing the 50 Hz noising signals from the recorded piezoelectric signals 161
III.4.4 Performance characterizations of piezoelectric nanogenerators based on ZnO/A_2O_3 core-shell heterostructures 162
III.4.4.1 Piezoelectric signal as a function of the vertically applied force and external load 162
III.4.4.2 Performance comparison of piezoelectric nanogenerators integrating ZnO NWs coated with different thicknesses of Al_2O_3 layers 164
III.5 Conclusion 169
Bibliography 170

The occurrence of inconvenient screening effects originating from a high density of free carriers in piezoelectric ZnO NWs has prompted researchers to explore potential solutions to enhance the performance of ZnO NW-based PNGs. Different approaches were thus developed involving doping processes, increase of areal density of ZnO NWs, surface treatment, and interfacial modification, as described in **Section I.3.3**. It should be noted that each strategy enhances the performance of the PNG through its own unique mechanism, which can either compete with/or complement other strategies. For instance, the piezoelectric properties of ZnO NWs can be enhanced through doping and thermal annealing processes. However, when they are integrated into a PNG, other factors beyond that intrinsic properties of individual NWs can significantly impact the overall device performance, as the features of the polymer layer embedding the NWs.

This chapter will consequently present the effect of the electromechanical properties and surface passivation of ZnO NW/parylene-C/alumina (Al_2O_3) on the piezoelectric behavior of PNGs.

III.1 State-of-the-art: impact of polymer thickness and surface passivation on the performance of ZnO nanowire-based piezoelectric nanogenerators

III.1.1 Thickness of the polymer layer

The PNG architecture developed in this thesis consists of a ZnO NW matrix embedded in a parylene-C layer, vertically integrated between two electrodes. Although the polymer layer prevents the short-circuiting of the device, the optimization of the electromechanical properties of the ZnO NW/parylene-C composite is crucial to enhance the piezoelectric response of the PNGs. For clarity, the polymer layer is divided into two sections: a bottom layer embedding the NWs (composite layer) and a top layer ensuring capacitive coupling with the top electrode, as illustrated in **Figure III.1-1(a)**.

Hinchet et al. used finite element method (FEM) simulations to establish optimization guidelines for PNGs based on ZnO NWs coated in PMMA, as summarized in **Figure III.1-1(b)**.[1] These guidelines suggest: i) reducing the equivalent Young's modulus of the composite layer (E_{2eq}) while increasing that of the top polymer layer (E_1), ii) lowering the equivalent dielectric constant of the composite layer (ε_{2eq}) while increasing that of the top polymer layer (ε_1), and iii) making the top polymer layer thinner than the composite layer ($d_1 << d_2$). This section will specifically focus on the engineering of the polymer layer integrated into a PNG.

Figure III.1-1(b) indicates that using a bottom polymer layer with a lower Young's modulus than the ZnO NWs and a rigid top polymer layer enhance the transfer of mechanical energy and its conversion into electrical energy in a PNG. While the integration of two distinct polymer layers could improve PNG's performance, as demonstrated with a soft PMMA bottom layer and a rigid Al_2O_3 top layer,[2] this approach could present challenges due to deposition technique incompatibilities. A practical alternative is to replace the two distinct polymers with a single and soft polymer, while carefully controlling its thickness over the NW matrix. Indeed, previous studies have demonstrated that using a single layer of PMMA[3,4] or PDMS[5] in PNGs results in output voltages that vary with the thickness of the top layer, highlighting a compromise between device leakage current, mechanical energy transfer, and electrical energy conversion. Thus, optimizing the thickness of the parylene-C layer in the PNGs fabricated in this work is crucial, following the same line of reasoning.

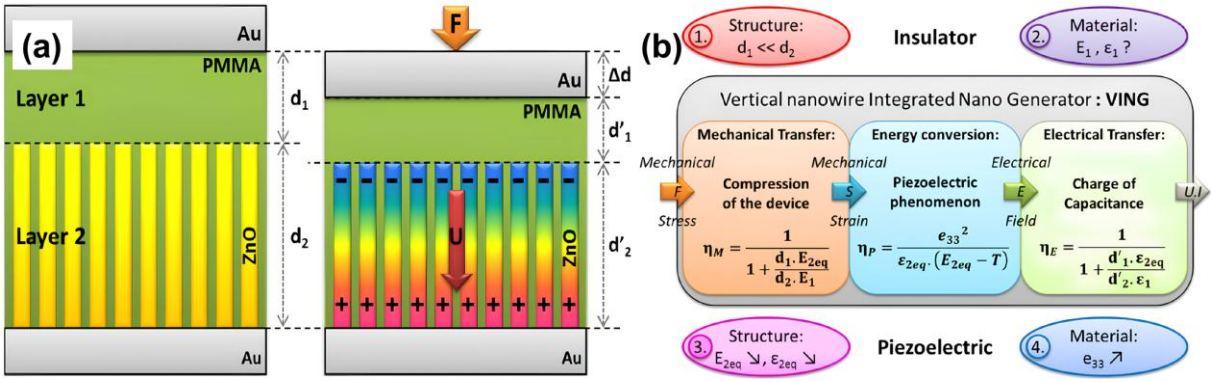

Figure III.1-1. (a) *Structure of a PNG before and after vertical compressive stress.* ***(b)*** *Diagram of the working principle of a PNG and the listed strategies to enhance its performance. Adapted from REF [1].*

III.1.2 Surface Fermi level pinning effect

FEM simulations have shown that high free carrier density in ZnO NWs reduce their piezoelectric properties through screening potential effects, which can entirely neutralize the piezoelectric potential at carrier densities higher than 1×10^{18} cm^{-3}.[6–8] However, studies using PFM and dual-frequency resonance tracking (DFRT) found that gallium-doped ZnO NWs with a higher carrier density (9.0×10^{19} cm^{-3}) still exhibit response amplitudes of around 40 pm.[9] The discrepancies between FEM simulations and experimental studies were assessed by R. Tao et al. by considering surface Fermi level pinning (SFLP) in ZnO NWs,[10] where fixed (or pinned) energy levels at the surface create a carrier depletion region near the NW surface due to the presence of surface states.[11] As the NW radius decreases, this depletion region can reach the core of the NW, reducing the density of free carriers that contribute to screening effects and enhancing the piezoelectric properties, as schematized in **Figure III.1-2(a)**. Complete depletions in ZnO NWs depend on both the NW radius and free carrier density, as depicted in **Figure III.1-2(b)**. When the free carrier density increases, the maximum radius required for a full depletion of the NW decreases. For instance, ZnO NWs with a free carrier density of 10^{19} cm^{-3} require a radius smaller than 15 nm to fully deplete their core and significantly reduce screening effects. Thus, ZnO NWs with small diameters and high surface defects are expected to enhance the performance of related PNGs.

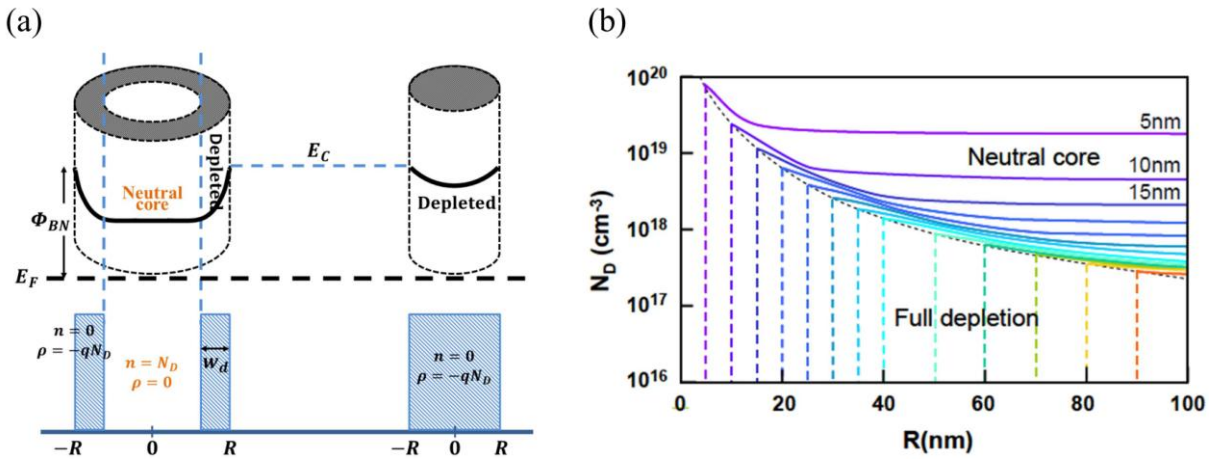

Figure III.1-2. (a) *Depletion region with its corresponding band diagram.* ***(b)*** *Depletion width as a function of the radius of ZnO NWs along with their free carrier density. Adapted from REFs [A-1]♦ and [A-2],♣ respectively.*

III.1.3 Surface passivation of ZnO nanowires with polymer layers

As previously discussed, the piezoelectric properties of ZnO NWs are enhanced through SFLP effects originating from surface defects, whose density is estimated to be around 10^{13} $eV^{-1}.cm^{-2}$ in ZnO NWs grown by CBD.[12] However, when these nanostructures are embedded in polymer materials, a crucial step in the fabrication of PNGs, surface passivation occurs at the ZnO-polymer interface. This passivation decreases surface defects, increases the density of near-surface excitons, and enhances the near band-edge (NBE) emission of ZnO NWs, as observed when coated with polymers such as polymethyl methacrylate (PMMA), Al_2O_3, polystyrene, polyacrylic acid, and polyvinylpyrrolidone (PVP).[13–17] However, this surface passivation can degrade the piezoelectric properties of the NWs. For instance, T. Sodhi et al. demonstrated that coating GaN NWs with 10 nm-thick amorphous Al_2O_3 layers degrades their piezoelectric properties by reducing surface trap density and increasing screening effects.[18] Interestingly, the surface passivation of ZnO NWs depends on the balling abilities of the coating polymer, as confirmed by the NBE/DLE (DLE: deep-level emission) ratio in photoluminescence spectra.[16] For instance, PMMA provides stronger passivation of ZnO NWs than Al_2O_3, as indicated by their NBE/DLE ratios of 10 and 4, respectively.[16,17] This strongly suggests that incorporating an Al_2O_3 layer at the interface between ZnO NWs and

♦ [A-1]: Ran Tao. Piezoelectric generators based on semiconducting nanowires: simulation and experiments. Micro and nanotechnologies/Microelectronics. Université Grenoble Alpes, 2017. English. NNT: 2017GREAT094. Tel-01774910

♣ [A-2]: Mouis, M., Hinchet, R., Tao, R., Ardila, G., & Montès, L. (2014, April). Nanowire-based piezoelectric transducers. In *2014 MRS Spring Meeting, Symposium R: Materials Challenges and Integration Strategies foor Flexible Energy Devices ans Systems*.

PMMA could enhance the PNG performance. Similarly, using Al_2O_3 at the interface between ZnO NWs and parylene-C could also be beneficial. Al_2O_3 shells have demonstrated stable passivation properties over time when coating ZnO NWs.[19] While Al_2O_3 shells are known to enhance responsivity and reduce leakage currents in solar cells[20] and UV photodetectors[21] based on ZnO NWs, their effect on PNG remains unexplored, leaving this question open for further investigations.

Objectives

This chapter will present the effect of different thicknesses of a parylene-C top layer and Al_2O_3 shell layers on the performance of PNGs based on ZnO NWs. The objectives are the following:

1- Optimize the thickness of the parylene-C over the ZnO NW matrix to enhance the output voltage of a PNG and prevent short circuits. This knowledge was used to fabricate and characterize the PNGs integrating thermally annealed ZnO NWs at 300 and 500 °C (Chapter II).

2- Investigate the properties of ZnO/Al_2O_3 core-shell heterostructures and their effect on the PNG performance when integrated into this device.

III.2 Influence of parylene-C top layer thickness on the output voltage of piezoelectric nanogenerators

The results presented in section III.2 been published in: Manrique, Manuel, et al. "Performance optimization of ZnO nanowire/parylene-C composite-based piezoelectric nanogenerators." *Nano Trends* 9 (2025): 100066.

III.2.1 Fabrication of piezoelectric nanogenerators with different thicknesses of Parylene-C top layer

In this study, four different PNGs were conceived according to the thickness of parylene-C over the ZnO NW matrix, whose fabrication is detailed in **Figure III.2-1**. N-type highly doped (100) Si substrates (0.01 – 0.02 Ω.cm) were coated with a ZnO seed layer by a dip-coating process (1). Subsequently, ZnO NWs were grown by CBD in an aqueous solution consisting of 50 mM of $Zn(NO_3)_2$, 50 mM of HMTA, and 600 – 640 mM of NH_3 to keep the bath in a high pH condition for 3h at 85 °C (2). To control the thickness of parylene-C, different masses of GALXYL* C were used to follow the Gorham process under vacuum, which involves sublimation of the dimmer around 120 °C, pyrolysis at 690 °C splitting the dimer into monomers, and condensation and polymerization processes of the gaseous monomer in the surface of the substrates at room temperature.[22] Then, the 1 × 1 cm² top electrode was achieved by vacuum evaporation with a mask. Finally, Cu-wires were used to contact both the bottom (Si substrate) and the top electrode of the device (3).

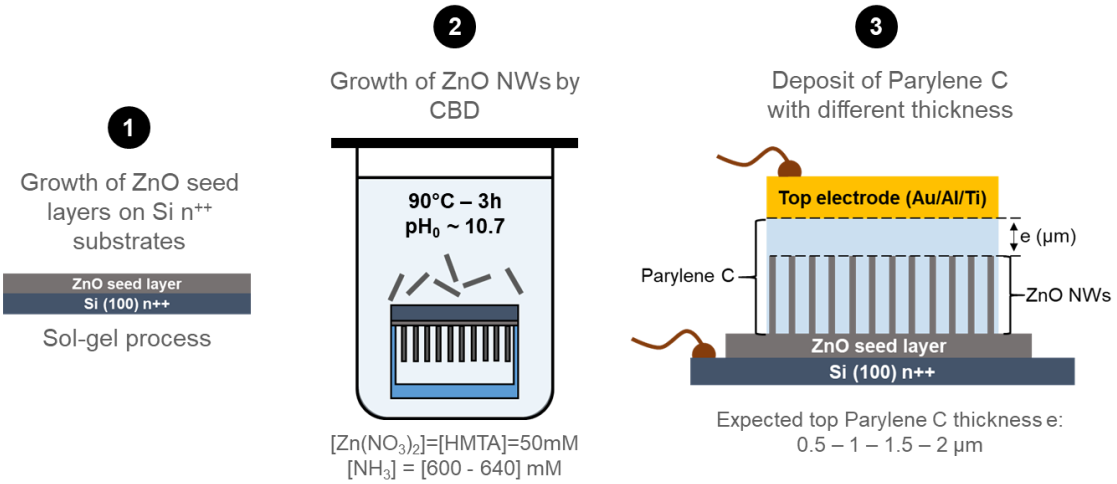

Figure III.2-1. *Fabrication steps of PNGs based on ZnO NWs with different thicknesses of parylene-C top layer.*

III.2.2 Measuring parylene-C thickness in piezoelectric nanogenerators using electronic microscopy

The morphological properties of the synthesized ZnO NWs and parylene-C layers integrated in the piezoelectric nanogenerators were assessed by FESEM images and EDS mappings.

The cross-section and top-view FESEM images of the ZnO NWs grown vertically on the ZnO seed layer are presented in **Figure III.2-2(a)**. The integrated NWs exhibit a mean length of 5.5 ± 0.4 µm with a number density of 43.3 ± 8.2 NW/µm^2. The diameter steadily decreases from their bottom to their top, resulting in a pencil-like shape, due to a faster axial growth rate along the polar *c*-axis compared to the radial growth rate along the non-polar *m*-axis.[23] The mean diameters are 42 ± 21 nm at the top and 166 ± 40 nm at the middle of the NW height. The final thickness of the parylene-C top layer was verified through FESEM images of the PNG's cross-section, as depicted in **Figure III.2-2(b-e)**. These images confirm the fabrication of four distinct PNGs as a function of the parylene-C top layer thickness increasing from 1.11 µm to 3.34 µm, whose features are summarized in **Table III.2-1**.

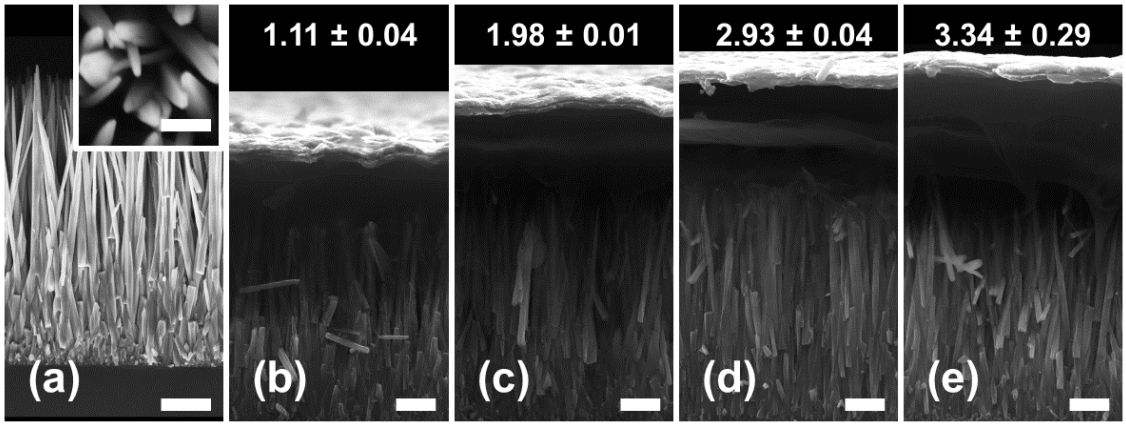

***Figure III.2-2**. FESEM images of the **(a)** cross-section and (inset) top view of the integrated ZnO NWs, and **(b)-(e)** the cross-section of the four fabricated PNGs with different thicknesses of the parylene-C top layer. The bar scale corresponds to 1 µm, except for the inset of **(a)** which corresponds to 200 nm.*

The "shadows" observed in the parylene-C top layer region are residual fragments of parylene-C that detached from the opposing section of the cut sample during cross-sectional imaging.

Table III.2-1. *Features of PNGs based on ZnO with different thicknesses of parylene-C top layer for piezoelectric characterizations in the LTM's test bench.*

PNG	Integrated ZnO NW features	Thickness of the parylene-C top layer	
		Expected	Final
PNG – A	Length: 5.5 ± 0.4 µm Top diameter: 42 ± 21 nm Middle diameter: 166 ± 40 nm Density: 43.3 ± 8.2	0.5	1.11 ± 0.04
PNG – B		1	1.98 ± 0.01
PNG – C		1.5	2.93 ± 0.04
PNG – D		2	3.34 ± 0.29

To ensure the mechanical stability and proper electrical isolation between ZnO NWs, the infiltration of parylene-C into the NW matrix was evaluated using cross-sectional FESEM-EDS mapping, as shown for the PNG with a 1.11 µm-thick parylene-C top layer in **Figure III.2-3(a)**. As previously discussed in **Section II.5.3.1**, the different components of the PNG are color-coded in these elemental maps. The ZnO NWs (blue and green regions for O and Zn, respectively) are vertically integrated on the bottom electrode (red region for Si substrate) and coated by the parylene-C layer (blue-sky region for Cl). This polymer successfully infiltrates the NW arrays, ensuring their effective mechanical robustness and electrical isolation. Parylene-C also establishes capacitive coupling between the ZnO NWs and top metallic electrode of the PNG, preventing leakage currents. Regarding the top metallic electrode of the PNG, the deposition of the Ti layer appears to induce a diffusion process of Ti atoms across the device, as suggested by the dispersed purple region. In contrast, the Ti layer prevents the diffusion process of Al atoms into the device, as shown by the localized yellow region. The Au layer (orange region) is well confined over the Al layer on the top electrode, although traces of Au were detected in the composite matrix. This apparent presence of Au in the ZnO NWs could originate from the chemical bath reagents, such as $Zn(NO_3)_2$ (98% purity), HMTA (99.5% purity), and ammonia (28 – 30% purity). In addition, contamination can have arisen from the beakers (sealed reactors) used in the CBD process, as they could have retained Au particles from previous experiments involving Au seed layers for the growth of ZnO NWs. Indeed, despite cleaning the beakers with HCl and deionized water after each synthesis, residual Au contamination in the ZnO NWs remains a possibility. Notably, the adhesion of Au particles on the surface of ZnO NWs could form Schottky junctions, potentially reducing screening effects and enhancing PNG performance.[24] To further investigate, ICP-MS analysis should be conducted to quantify the Au content in ZnO NWs, along with electrical characterizations to

study its impact. However, since this Au trace appears consistently across all the PNGs, and only the parylene-C top layer thickness varies, the parylene-C layer more probably influences the device performance than any surface property changes in ZnO NWs.

Moreover, cross-sectional FESEM-EDS maps of the PNGs with parylene-C top layer thicknesses of 1.11 and 3.34 µm, as shown in **Figure III.2-3(b-c)**, suggest a non-homogeneous density distribution of the parylene-C layer over the ZnO NW matrix, indicated by the denser blue-sky region at the top of the NW arrays. This non-uniformity could affect the mechanical and electrical behavior of the device. For instance, if parylene-C accumulates on the top of the NWs during early deposition, it could obstruct penetration into the NW matrix, resulting in poor isolation of the NWs and changes in the equivalent Young's modulus and dielectric constant of the composite layer (ZnO NW embedded in parylene-C). The penetration of parylene-C could be also influenced by the density of the NW matrix, with denser NWs reducing polymer infiltration. In addition, the uncontrolled deposition rate of parylene-C could contribute to its penetration. Despite the presentment statement, the parylene-C layer thickness is well-controlled across the ZnO NW arrays, confirming the reliability of the deposition process.

In the following sections, the effect of parylene-C thickness on the electrical properties of piezoelectric nanogenerators will be discussed as an "overall effect", without focusing on specific accumulation phenomena or surface property modifications.

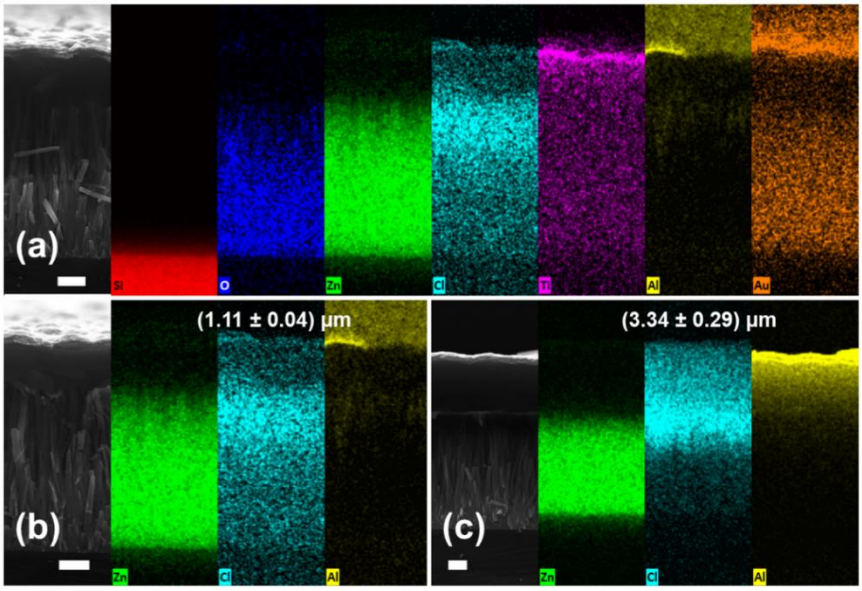

Figure III.2-3. (a) *FESEM-EDS mapping of a PNG's cross-section displaying the bottom electrode (Si-red), ZnO NW matrix (O-blue and Zn-green), parylene-C layer (Cl-blue-sky), and the top electrode (Ti-purple, Al-yellow and Au-orange). FESEM-EDS mapping of the PNG's cross-section with* ***(b)*** *1.11 µm and* ***(c)*** *3.34 µm-thick parylene-C top layer. The bar scale corresponds to 1 µm.*

III.2.3 Raman spectroscopy of a parylene-C layer on ZnO nanowires

It has been reported that ZnO can enhance its piezoelectric properties through a modification of its crystallographic parameters.[25,26] Thus, to thoroughly investigate the potential residual mechanical stress in ZnO NWs induced by the parylene-C coating layer, Raman scattering spectroscopy was performed thanks to the strong coupling between the phonon modes of ZnO NWs and their crystallographic properties. Then, backscattering Raman spectroscopy was performed with a 514.532 nm – Ar^+ laser probing the top of the sample with a power of 0.8 mW and a 50 × objective. To prevent a sublimation of the polymer layer, the total acquisition time was fixed to 600s (10 recordings of 60 seconds each) from 50 to 3750 cm^{-1}. The Raman spectra were calibrated and normalized according to the position (520.7 cm^{-1}) and the intensity of the Si Raman line, respectively. **Figure III.2-4** presents the Raman scattering spectra for ZnO NWs coated with a parylene-C layer (green), a parylene-C layer-coated Si substrate (yellow), ZnO NWs on a Si substrate (blue), and a reference Si substrate (dotted line).

In the low-wavenumber region of 50 - 1620 cm^{-1}, the ZnO NWs with the wurtzite structure exhibit first phonon modes at 99 (E_2^{low}), 380 (A_1(TO)), 438 (E_2^{high}) and 581 (A_1(LO)) cm^{-1}, as well as second phonon modes at 204 (2TA/2 E_2^{low}) and 333 (E_2^{high} - E_2^{low}) cm^{-1}.[27] The pronounced shoulder observed between 1048 and 1191 cm^{-1} is assigned to phonon modes related to ZnO. The Raman lines associated with the parylene-C layer, marked by yellow stars, are mainly assigned to carbon-related bonds.[28] In the wavenumber region of 50 – 700 cm^{-1}, the Raman lines at 164, 243, and 689 cm^{-1} correspond to translational and rotational lattice vibrations, C-C in-plane bending, and C-Cl stretching vibrations, respectively.[28,29] In the wavenumber region of 700 – 1620 cm^{-1}, the Raman lines at 870 and 912 cm^{-1} are attributed to CH out-of-plane deformations; those at 1003, 1050, and 1209 cm^{-1} are assigned to CH in-plane deformations, the line at 1339 cm^{-1} corresponds to CH_2 wagging and twisting vibrations; and the lines at 1404, 1443, and 1608 cm^{-1} are attributed to CH scissoring in CH_2 and/or C-C skeletal in-plane vibrations of the aromatic ring.[28]

In the high-wavenumber region of 2500 – 3750 cm^{-1}, as zoomed in the inset of **Figure III.2-4**, the Raman lines arising from carbon-, nitrogen-, and hydrogen-related defects occur. The broad Raman band observed from 2850 to 2990 cm^{-1} (brown area) proceeds from C-H_x

(x=1, 2, 3) bonds, as a result of molecular carbon-adsorption processes on the *m*-plane sidewalls of ZnO NWs coming from HMTA molecules.[30] The weak Raman line at 3075 cm^{-1} is assigned to V_{Zn}-N_O-H complexes in ZnO NWs.[31] The broad Raman region noticed between 3100 and 3200 cm^{-1} (turquoise area) derives from V_{Zn}-xH (x=1, 2, 3) defect complexes,[32–34] while the asymmetric Raman shoulder observed from 3480 to 3650 cm^{-1} includes the contribution of O-H bonds (red area)[35] on the surface of ZnO NWs and H_{BC}[36] in their bulk. Regarding the parylene-C layer, four Raman lines at 2860, 2890, 2928, and 3045 cm^{-1} occur, which are related to stretching vibrations of C-H bonds from the aromatic ring.[28,37]

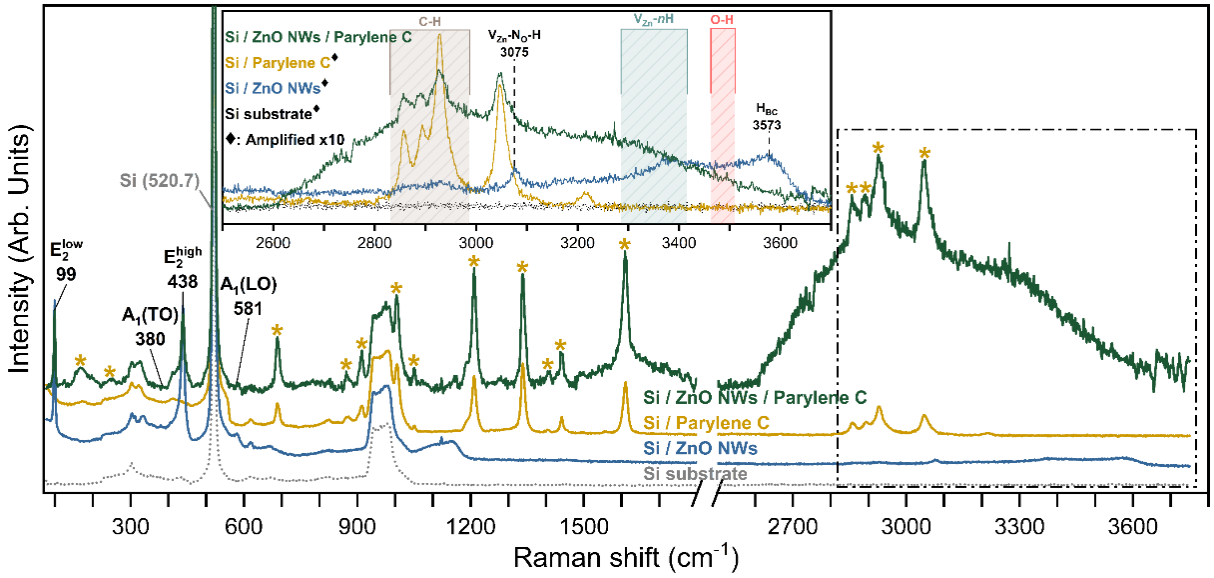

Figure III.2-4. *Raman spectroscopy of ZnO NWs coated with a 1.11 µm-thick parylene-C top layer. Zoom-in of the high wavenumber region (inset). The spectra of reference samples were amplified by a 10-factor for the sake of clarity.*

Furthermore, the position and intensity of both the E_2^{low} and E_2^{high} Raman lines of ZnO NWs remain unchanged when coated with the parylene-C layer, with no additional phonon modes observed. This suggests that the parylene-C coating layer does not alter the crystallographic properties of the ZnO NWs, hence it does not introduce any mechanical stress into the NWs.[38] Consequently, the parylene-C coating layer appears not to affect the spontaneous polarization field of ZnO NWs.[25,26] In contrast, the strong fluorescence observed in the polymer-embedded ZnO NWs at high wavenumbers could indicate a modification of the optical properties of ZnO NWs when coated with parylene-C.

III.2.4 Internal impedance of piezoelectric nanogenerators with different thicknesses of parylene-C top layer

It is worth mentioning that the fabricated PNGs integrate three distinct layers: i) a ZnO seed layer, ii) a bottom composite layer, which consists of the ZnO NW matrix embedded by the parylene-C layer, iii) and a top polymer layer, which refers to the parylene-C over the NW matrix with different thicknesses. Therefore, the equivalent electronic circuit of a PNG can be modeled as three impedances in series involving a resistance R_i in parallel with a capacitance C_i,[39] as schematized in **Figure III.2-5(a)**.

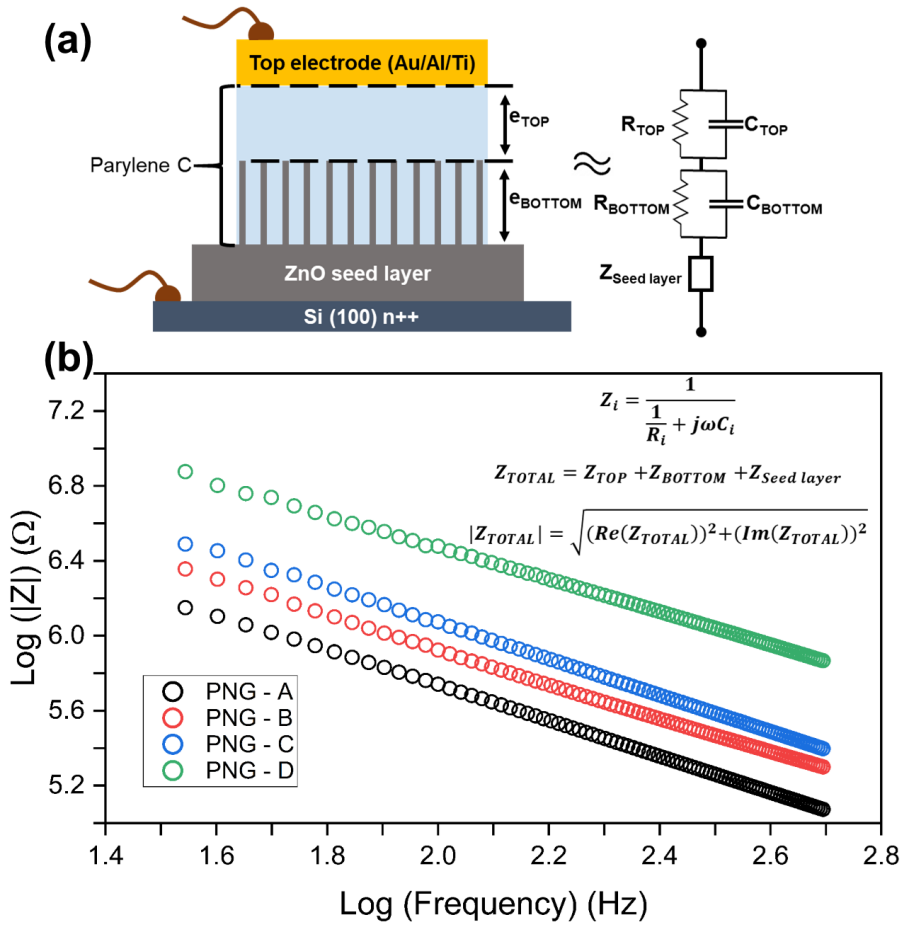

Figure III.2-5. (a) *Equivalent electronic circuit a PNG vertically integrating a ZnO NW matrix impregnated by a parylene-C layer.* ***(b)*** *Measurement of internal impedances of PNG with different thicknesses of parylene-C.*

The electrical resistance is calculated as $R_i = \rho_i \frac{L_i}{A_i}$, where ρ_i, L_i, A_i refer to the resistivity, thickness, and area of the studying layer. The capacitance is given by $C_i = \varepsilon_0 \varepsilon_i \frac{A_i}{L_i}$, where ε_0 and ε_i are, respectively, the dielectric permittivity of the vacuum and the analyzed layer. By considering the bottom composite layer as an effective homogeneous material, the mathematical expression of its impedance involves the volume fraction *V* of each material (i.e.

ZnO NWs and the parylene-C) along with their electrical and mechanical properties. This results in a complex mathematical expression of the bottom composite layer impedance.[39] For instance, the dielectric permittivity of the bottom composite layer can be expressed as:

$$\varepsilon_{Bottom} = V_{ZnO}\left(\varepsilon_{33}^{ZnO} - \frac{2V_{Par-C}(\varepsilon_{31}^{ZnO})^2}{V_{ZnO}(c_{11}^{Par-C} + c_{12}^{Par-C}) + V_{Par-C}(c_{11}^{ZnO} + c_{12}^{ZnO})}\right) + V_{Par-C}\varepsilon_{11}^{Par-C}$$

where V_{ZnO} and $V_{Par\text{-}C}$ are the volume fraction of ZnO NW and Parylene-C, respectively.

Given that the four manufactured PNGs differ only in the thickness of the polymer top layer, the variation in their corresponding internal impedance (Z_{PNG}) is mainly related to the properties of this parylene-C top layer.

Figure III.2-5(b) presents the impedance module ($/Z_{TOTAL}/ = Z_{PNG}$) of the four fabricated PNGs as a function of the working frequency. This module was measured with a Keysight E4980A/AL LCR meter over a frequency band from 20 to 495 Hz, by applying an AC voltage of 1 Vpp between their top and bottom electrode, and measuring the current. The devices are labeled as PNG-A, PNG-B, PNG-C, and PNG-D according to the thickness of the parylene-C top layer of 1.11 µm, 1.98 µm, 2.93 µm, and 3.34 µm, respectively. Then, increasing the thickness of the parylene-C top layer leads to an increase in Z_{PNG}, suggesting that a thicker polymer top layer leads to an increase in the electrical resistance while simultaneously reducing the capacitance of the device, resulting in higher Z_{PNG}. In addition, the frequency dependence of Z_{PNG} confirms that the devices exhibit capacitive behavior, indicating that they are not short-circuited and are available for piezoelectric characterizations. For operating frequencies below 1 Hz, the Z_{PNG} is expected to exceed 49.6, 56.6, 117.4, and 192.7 MΩ for PNG-A, PNG-B, PNG-C, and PNG-D, respectively, by fitting a linear regression in the graph *log(/Z/)-log(Frequency)*. In theory, connecting an external resistive load in parallel with the PNGs, with values within the range of Z_{PNG}, would enable PNGs to generate a maximum power density under mechanical stress.[40] Thus, it should be mentioned that the following results from piezoelectric characterizations in the LTM's test bench were obtained with the PNGs connected to a Stanford Research Systems SR560 amplifier, whose entrance impedance is 100 MΩ.

III.2.5 Output voltage of piezoelectric nanogenerators with different thicknesses of parylene-C top layer

The output voltage of the PNGs was measured on the test bench available at the Cameleon platform of the LTM, which was described in **Section II.5.1**. A vertical compressive force was applied with a sinus waveform over an area of 0.2 cm^2 on the top electrode of the device with a mechanical arm. It is worth mentioning that, to avoid/reduce triboelectric effects, a piece of cardboard was fixed to the side of the mechanical arm that contacts the metallic electrode of the device during the tests. In addition, the output signal was amplified by a 10-factor through the Stanford Research Systems SR560 amplifier to easily discern the piezoelectric signal from the electronic noise. For illustrative purposes, the piezoelectric signals of the four fabricated PNGs under 3 N at 0.5 Hz are presented in **Figure III.2-6(a)**, where the highest output voltage is exhibited by the PNG-B with a 1.98 µm-thick top parylene-C layer. When comparing the output voltage of the PNGs for different force magnitudes applied at different working frequencies, the PNG-B displays the highest signals, as summarized in **Figure III.2-6(b)**. The PNG-A, in contrast, exhibits the lowest output voltage regardless of the test conditions, and after a short fatigue period, the device short-circuits. It is worth mentioning that, as discussed in **Section II.5.2.2**, increasing the working frequency♣ raises the strain rate ($\frac{\Delta\sigma}{\Delta t}$) applied on the device, thereby boosting the current generated by the PNG ($I = \frac{\Delta Q}{\Delta t} = d_{33} \times A \times \frac{\Delta\sigma}{\Delta t}$).[41] Consequently, the output voltage (*V*) increases according to the Ohm's law $I = Z_{load}V$, where Z_{load} refers to the internal impedance of the amplifier/filter system of the test bench.[42,43] This could explain the higher output voltage generated under 0.9 N applied at 3 Hz, which correspond to the highest working frequency used in the piezoelectric characterizations. For illustrative purposes, increasing the working frequency of the sinusoidal mechanical stress causes the waveform to progressively resemble a pulse, in which situation the piezoelectric characterizations are performed in a "tapping mode" regime, i.e. instantaneous mechanical excitation, presented further in **Section III.4.3**.

Moreover, it has been shown that reducing the thickness of the polymer top layer increases the mechanical deformation of ZnO NWs under compressive stress, which in turn boosts the output voltage of the PNG.[4,44] In the present work, a 1.98 µm-thick parylene-C

♣ It refers to the frequency of the applied sinusoidal force

layer over the ZnO NWs seems to yield the highest PNG output voltage. When the parylene-C top layer is thicker than 1.98 µm, both the transfer of mechanical deformation to the ZnO NWs and the capacitance of the PNG can be reduced, resulting in decreased PNG performance.[3,4,44] Conversely, when the parylene-C top layer is thinner than 1.98 µm, leakage current in the device could arise, which similarly compromises the PNG performance. Thus, an optimal balance between mechanical energy transfer and electrical energy storage is required, as experimentally reported in PNGs that enhanced their output voltage with an optimal thickness of a PMMA layer.[4,45]

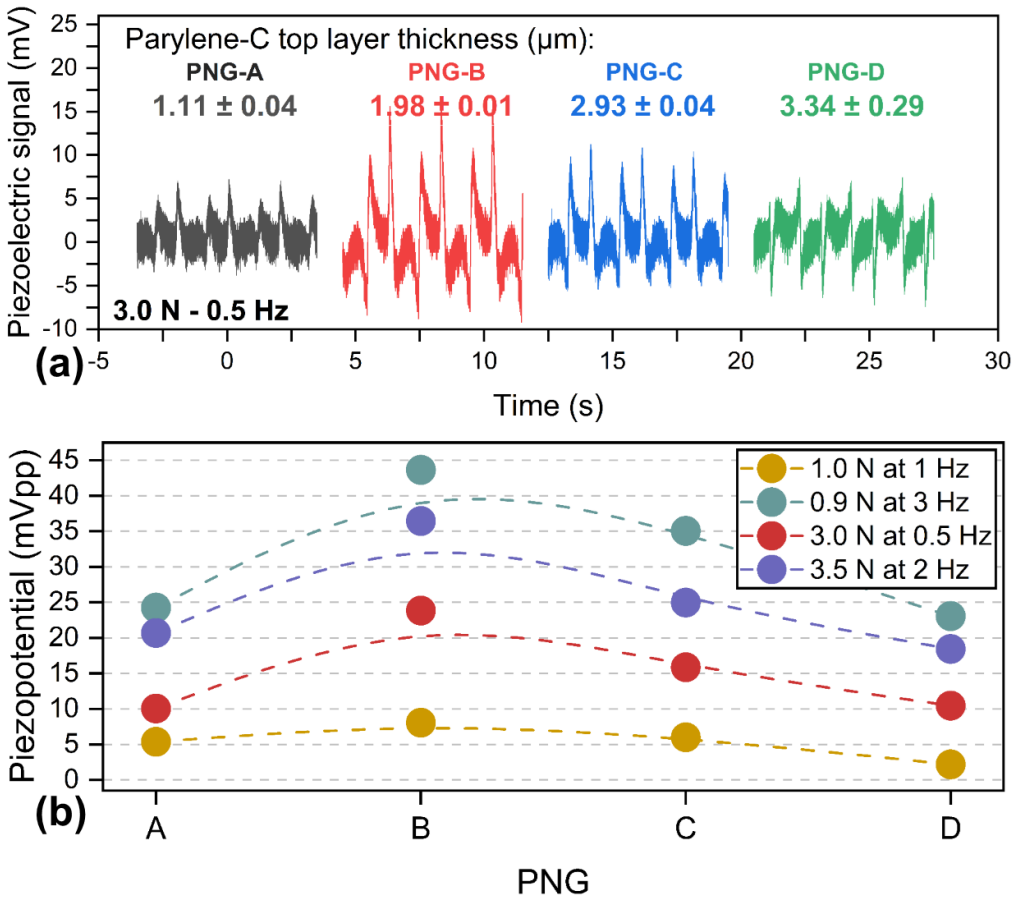

Figure III.2-6. (a) *Piezoelectric signal of the four fabricated PNGs according to the thickness of the parylene-C top layer tested under 3.0 N at 0.5 Hz.* ***(b)*** *Summary of their corresponding output voltages (peak-to-peak) under different sinusoidal force magnitudes applied at different frequencies. This figure displays the piezoelectric signals and the output voltage values amplified by a 10-factor using the Stanford Research Systems SR560 amplifier of the LTM's test bench for the sake of readability.*

In the present study, around 2 µm of parylene-C between the top of the ZnO NWs and the top electrode of the PNG maximized the output voltage of the device. In addition, this PNG was found to be reliable after some stress conditions. This finding will be implemented in the fabrication of PNGs integrating ZnO/Al_2O_3 core-shell heterostructures, discussed in **Section III.4**.

It is important to note that the presented data correspond to a single PNG with a specific parylene-C top layer thickness. To ensure reproducibility, additional characterizations with multiple samples should be conducted, along with DFT calculations. Moreover, the low-generated voltages of the tested devices can involve poor electrical contact between the natural oxide film of the Si substrate and the Cu wire, as well as a loss of mechanical energy transfer to the device induced by the soft cardboard that can absorb the mechanical stress.

III.3 Effect of Al_2O_3 shell layers on the surface defects of ZnO nanowires grown by chemical bath deposition

III.3.1 Experimental procedure: ZnO/Al_2O_3 core-shell heterostructures elaboration

The synthesis of ZnO/Al_2O_3 core-shell heterostructures is described in **Figure III.3-1** along with their features in **Table III.3-1**. (1) ZnO polycrystalline layers were deposited by sol-gel process on pre-cleaned (100) Si wafers. The latter is highly *n*-type doped (0.01 – 0.02 Ohm.cm) for future piezoelectric applications. (2) ZnO NWs were subsequently grown on these substrates *via* the CBD method. A 54 ml – aqueous solution mixing $Zn(NO_3)_2$ and HMTA in equimolar concentration of 50 mM was used. The initial pH of the chemical bath was fixed at 10.7 by adding ~620 mM of ammonia. The substrate was introduced face-down into a beaker containing the chemical solution. The growth of ZnO NWs was achieved by keeping the sealed system in a regular oven heated at 85 °C for 3 h. (3) Finally, Al_2O_3 layers were deposited on the ZnO NWs by thermal ALD method in a FlexAL reactor from Oxford Instruments.♣ The substrate temperature during the ALD was kept at 300 °C, and the number of ALD cycles was adjusted to grow 1, 2, 5, and 10 nm thick Al_2O_3 layers.

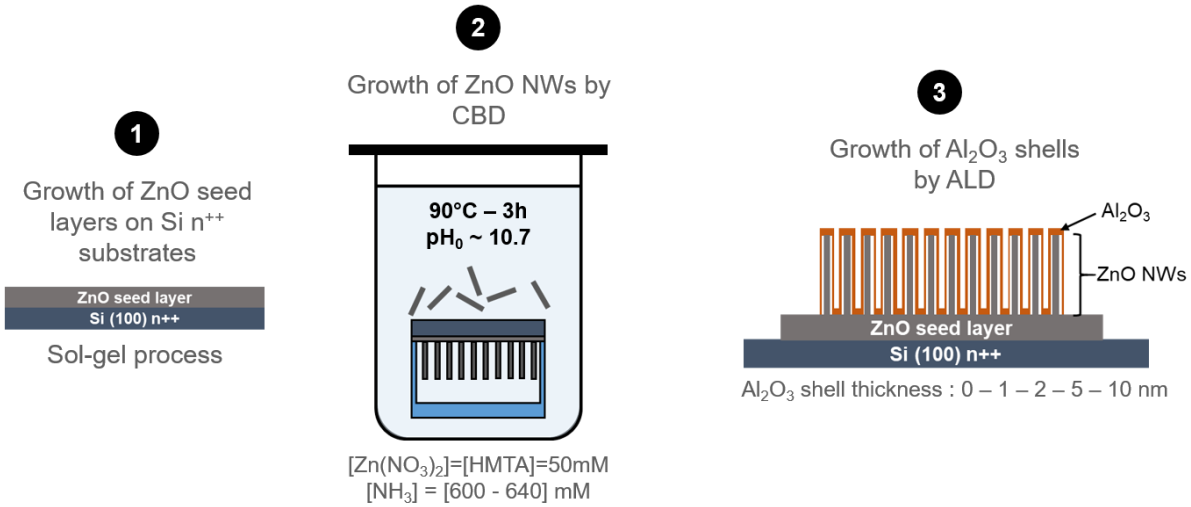

Figure III.3-1. *Fabrication steps of ZnO/Al_2O_3 core-shell heterostructures.*

♣ The growth of Al_2O_3 layers by ALD was done by Liliane ALRIFAI, PhD student at LTM.

Table III.3-1. *Features and specific denomination of samples with Al_2O_3 shell layers for physicochemical, structural, and luminescent studies.*

Sample	Al_2O_3 thickness (nm)	Observation
ZnO:Al_2O_3 0 nm	0	Sample of reference (No introduced in the ALD chamber)
ZnO:Al_2O_3 1 nm	1	Samples with Al_2O_3 shell layers grown by ALD at 300 °C
ZnO:Al_2O_3 2 nm	2	
ZnO:Al_2O_3 5 nm	5	
ZnO:Al_2O_3 10 nm	10	

III.3.2 Morphological properties of ZnO/Al_2O_3 core-shell heterostructures assessed by electronic microscopy

Once CBD is finished, FESEM images confirm the typical vertical growth of ZnO NWs on polycrystalline ZnO seed layers preferentially oriented in the *c*-axis direction,[46] as shown in **Figure III.3-2(a)**. ZnO NWs exhibit a diameter that decreases progressively from the bottom to the top of the structure. This well-known diameter profile observed in ZnO NWs grown in a high-pH region is attributed to the higher axial growth rate along the *c*-axis compared to the radial growth rate along the *m*-axis. Therefore, the resulting diameter at the top and the half along the length of ZnO NWs are 42 ± 25 and 166 ± 40 nm, respectively. In addition, ZnO NWs display an apparent density of 42.9 ± 5.7 NW/µm², a mean length of 6.1 ± 0.7 µm, and an aspect ratio of 36.7 ± 1.2 by dividing their length by their diameter.

HRTEM images depict the high crystal quality of the wurtzite-structured ZnO NWs. In addition, the coating of ZnO NWs with Al_2O_3 shell layers is also confirmed, whose Al_2O_3 films exhibit amorphous structure regardless of their thickness, as shown in **Figure III.3-2(b-e)**. The homogeneous thickness of Al_2O_3 layers over all the faces of ZnO NWs is evaluated through the deposit compliance rate n_{conf}, which is calculated as the ratio between the final thickness e_{real} over the target thickness e_{target} of Al_2O_3 shells, as illustrated in **Figure III.3-2(f)**. The conformal deposition of Al_2O_3 is thus verified, as expected, due to the self-limiting nature of the ALD method providing a high control over thickness and uniform coating of materials,[47] which is consistent with STEM EDS images shown in **Figure III.3-2(g-j)**. Therefore, ZnO/Al_2O_3 core-shell heterostructures were successfully achieved with Al_2O_3 shell thickness of 1, 2, 5 and 10 nm. X-ray based techniques will further discuss the structural properties of these heterostructures.

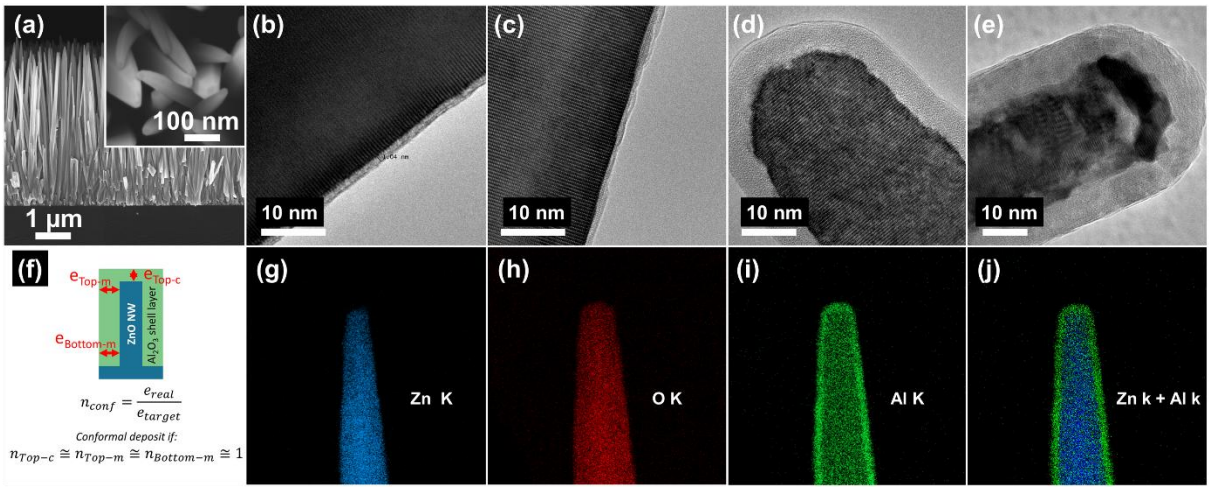

Figure III.3-2. (a) *Cross-section and (inset) top-view FESEM images of ZnO NWs grown by CBD for Al_2O_3 layer deposition. HRTEM images of ZnO coated with Al_2O_3 shells of* ***(b)*** *1,* ***(c)*** *2,* ***(d)*** *5, and* ***(e)*** *10 nm.* ***(f)*** *Schematic for deposition compliance rate calculations. STEM-EDS elemental maps of the* ***(g)*** *Zn,* ***(h)*** *O,* ***(i)*** *Al and simultaneously* ***(j)*** *Zn + Al of ZnO NWs with 10 nm-thick of Al_2O_3 layers.*

III.3.3 Structural properties of ZnO/Al_2O_3 core-shell heterostructures evaluated by θ-2θ and Grazing X-ray diffraction

To confirm the amorphous structure of Al_2O_3 layers coating ZnO NWs, XRD measurements were performed in the Bragg – Brentano configuration (θ - 2θ), as shown in **Figure III.3-3(a)**. The XRD patterns were corrected by aligning the Si (400) diffraction peak to its theoretical value of 69.132°. The ZnO diffraction peaks were indexed according to the ICDD 00-036-1451 file. Then, XRD spectra reveal that wurtzite ZnO NWs are highly textured along the *c*-axis as the highest diffraction intensity is noticed for the (002)-ZnO peak at ~34.4°. Interestingly, it appears that this diffraction peak slightly shifts from 34.40° to 34.42° as the thickness of Al_2O_3 is increased from 0 to 10 nm, as shown in the inset of **Figure III.3-3(a)**. It is worth noting that this shift of 0.02° is higher than the acquisition step of 0.0075° used for recording the XRD data. From XRD patterns, the crystallographic constants were calculated with the DIFFRAC.TOPAS software from Bruker by considering all the ZnO diffraction peaks. Thus, a slight and apparent progressive decrease of the crystallographic constant *c* in ZnO NWs is obtained as the thickness of Al_2O_3 increases, as depicted in the inset of **Figure III.3-3(a)**. This could suggest an apparent compression of the ZnO NWs with Al_2O_3 shell layers along the *c*-axis. Moreover, no diffraction peaks related to Al_2O_3 are detected, indicating the amorphous structure of these coating layers, consistent with HRTEM images. To accurately confirm the crystallographic nature of Al_2O_3 shell layers, XRD in the in-plane configuration was performed on ZnO NWs coated with 10 nm-thick Al_2O_3 layers, as presented in **Figure III.3-3(b)**. Then, ZnO

NWs exhibit the strongest intensity for the (103) diffraction peak, which is in agreement with the presence of semi-polar ZnO NWs that homoepitaxially grow on ZnO seed nanoparticles oriented in a semi-polar direction.[48] The both non-indexed peaks between 50 and 55° could be likely related to the multiple diffractions in the silicon substrate. Then, the absence of diffraction peaks related to Al_2O_3 strongly suggests that the crystallization could not occur for thicknesses lower than 10 nm.

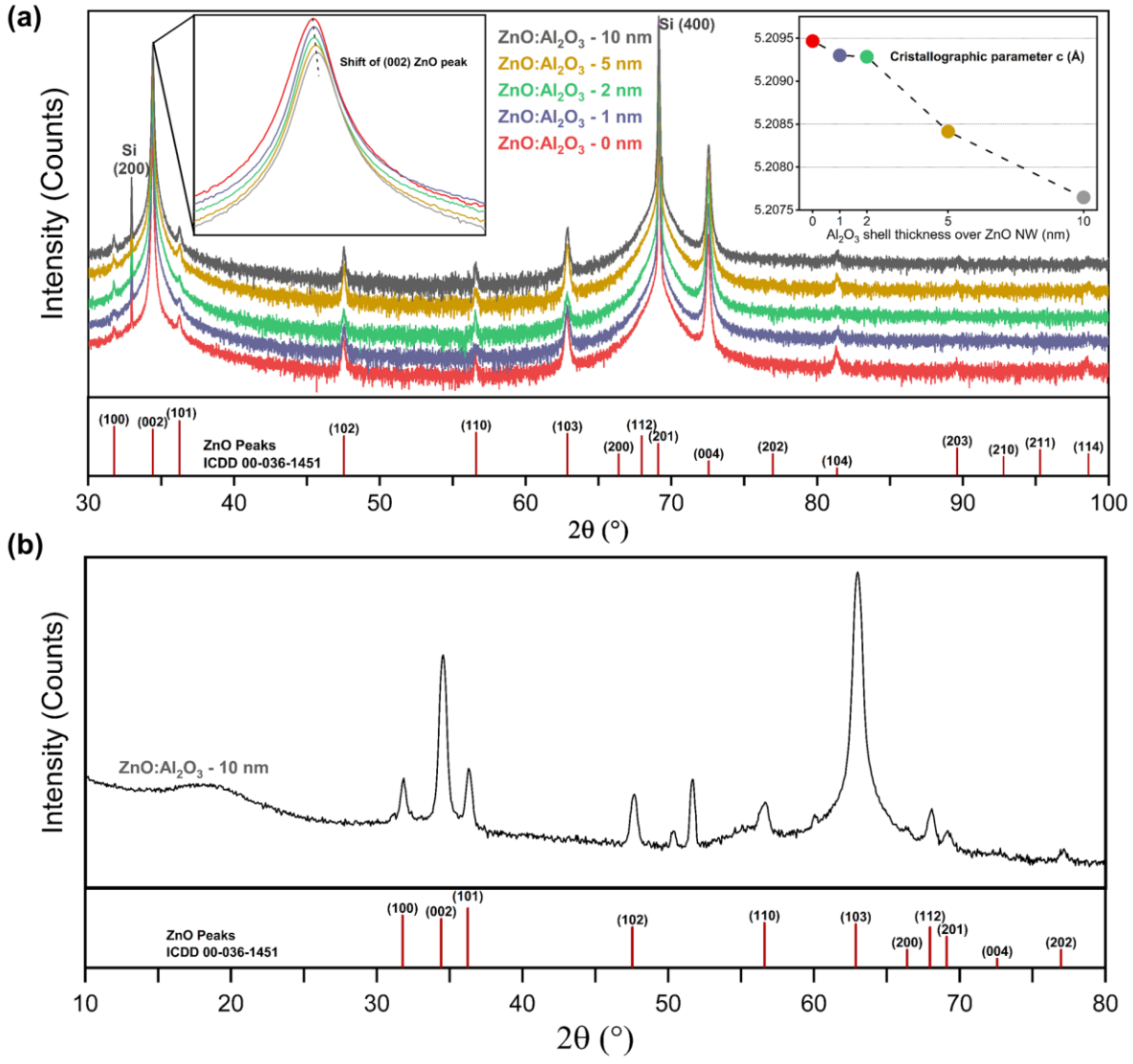

Figure III.3-3. (a) *XRD spectra in Bragg – Brentano configuration of ZnO NWs with different thickness of Al_2O_3 shells layers.* ***(b)*** *XRD spectrum in Grazing mode of ZnO NWs with 10 nm-thick Al_2O_3 shell layer.*

Therefore, the amorphous Al_2O_3 layers coated on ZnO NWs can exhibit a uniform mechanical behavior in all directions with Young's modulus lower than that of crystalline layers (330 – 400 GPa).[49,50] In addition, the heterostructures can display higher hardness and tensile strength as the thickness of Al_2O_3 increases.[51] It is important to note that, in materials science, hardness refers to the resistance to indentation, whereas tensile strength measures

the ability to resist stretching or pulling forces before breaking. Consequently, the mechanical properties of the ZnO/Al_2O_3 core-shell heterostructures could be modified, affecting their piezoelectric behavior when integrated into a PNG.

III.3.4 Raman spectroscopy of ZnO/Al_2O_3 core-shell heterostructures

Given the strong coupling between phonons and crystallographic properties, Raman spectroscopy is performed to provide more insights into possible changes in ZnO NW's crystallographic properties with Al_2O_3 shell layers, particularly the apparent compression suggested by XRD patterns. Thus, Raman scattering was collected on the ZnO/Al_2O_3 core-shell heterostructures in the wavenumber range of 75 to 1300 cm^{-1} at room temperature. For this, an Ar^+ laser (514.32 nm) was used to probe the top of the ZnO/Al_2O_3 core-shell heterostructures with a 100 × objective and a power of ~0.2 mW. Subsequently, Raman spectra were normalized and calibrated according to the intensity and the position of the Si peak at 520.7 cm^{-1}, respectively.

In the low-wavenumber region comprised between 75 and 1300 cm^{-1}, the typical phonon modes of wurtzite-structured ZnO NWs are observed,[27] as shown in **Figure III.3-4(a)**, exhibiting first phonon modes at 99 (E_2^{low}), 380 (A_1(TO)), 438 (E_2^{high}) and 581 (A_1(LO)) cm^{-1}, as well as second phonon modes at 204 (2TA/2 E_2^{low}) and 333 (E_2^{high} - E_2^{low}) cm^{-1}. The pronounced shoulder located between 1048 and 1191 cm^{-1} is attributed to vibration modes related to ZnO.

Interestingly, a Raman line at 276 cm^{-1} is solely observed in samples with Al_2O_3 shell layers. It is worth mentioning that this Raman line, assigned as B_1^{low}, along with additional modes at 581 (B_1^{high}), 644 (TA+B_1^{high}), 668 (TA+LO), and 856 (B_1^{low} + B_1^{high}) cm^{-1}, are commonly observed in ZnO NWs when they grow by CBD in a high pH region and are thermally annealed at temperatures higher than 300 °C.[23] The appearance of these additional modes (AMs) with the thermal annealing corresponds to the activation of B_1 silent Raman modes through a breakdown of the translational symmetry of the crystal lattice.[52] In addition, by adding ammonia in the chemical bath, the incorporation of extrinsic impurities such as Al, Ga, Sb, and Fe in ZnO NWs can also account for the presence of these AMs.[53] Indeed, this extrinsic incorporation create lattice distortions in ZnO, activating inactive defects as interstitial Zinc clusters involved in the B_1^{low} mode presence, and enhancing the TA and TO modes which

depend on the Zn-like and/or O-like vibrations. [53–56] It should be noted that the intensity of the A_1(LO) (581 cm^{-1}) Raman line is also increased in samples with Al_2O_3 shell layers, which could originate from an additional contribution of the B_1^{high} mode. Therefore, the presence of the B_1^{low} mode along with the increase of the A_1(LO) Raman line strongly suggest a thermal effect on the phonon density of state in ZnO NW with Al_2O_3 shell layers.

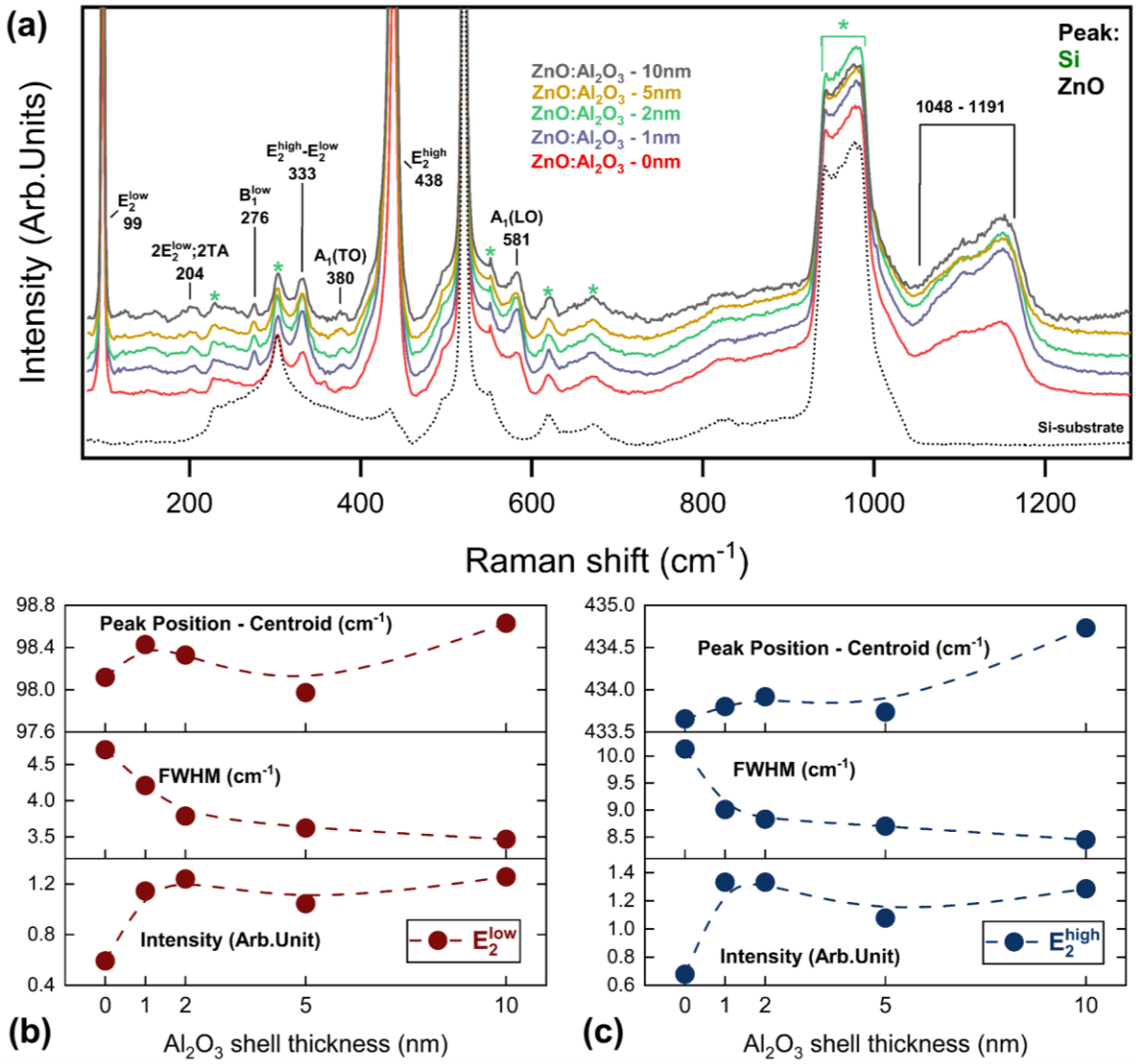

Figure III.3-4. (a) *Raman spectra of ZnO/Al_2O_3 core-shell heterostructures in the low-wavenumber region. Features of the associated* ***(b)*** *E_2^{low} and* ***(c)*** *E_2^{high} Raman peaks.*

The decoupling between a thermal effect and the presence of coating layers is assessed through the study of the two highest E_2^{low} and E_2^{high} Raman lines, whose features are presented in **Figure III.3-4(b-c)**, respectively. The decrease in FWHM along with the increase in intensity of both E_2^{low} and E_2^{high} lines suggest an enhancement of the crystallinity occurred during the growth of Al_2O_3 layers at 300 °C. Interestingly, the noticed shift towards higher wavenumbers of both E_2^{low} and E_2^{high} lines could suggest compressive stress of ZnO NWs with

Al_2O_3 shell layers,[38,57] which would be consistent with the apparent decrease of the *c*-parameter in XRD patterns. Thus, Raman spectra and XRD patterns suggest the structural modification of ZnO NWs with Al_2O_3 shell layers, which could influence the optical properties of these heterostructures, as discussed by cathodoluminescence spectroscopy in the following section.

III.3.5 Cathodoluminescence spectroscopy at 5 K of ZnO/Al_2O_3 core-shell heterostructures

Given the uniform coating of amorphous Al_2O_3 layers on all the surfaces of ZnO NWs, as confirmed by structure-morphological studies, 5 K cathodoluminescence spectroscopy was performed to investigate their optical properties. These spectra were obtained by scanning an area of 5 × 6 μm^2 of the sample with a 5 kV accelerated electron beam in a FEI Inspect F50 FESEM. The cathodoluminescence signal was collected with a 550 nm focal length monochromator, a nano-manipulating parabolic mirror, and a cooled silicon CCD detector, resulting in the spectra presented in **Figure III.3-5**.[♣] The Near Band Edge (NBE) emissions involve radiative transitions higher than 3.0 eV, where contributions of neutral acceptor- and donor-bound excitons (A^0X and D^0X, respectively),[58] free-A-excitons (FX),[58] donor-acceptor pair (DAP),[59–61] free electron-to acceptor (FA),[61,62] and two-electron satellites (TES)[63,64] are mainly expected. Conversely, the Deep Level Emission (DLE) region originates from emissions lower than 3.0 eV involving V_{Zn}-related defects and O-related surface states.[31]

A noteworthy NBE and DLE emission modification is observed in ZnO NWs when coated with Al_2O_3 shell layers. First, since ZnO NWs were grown in a high pH region (pH_0 ~10.7), a low NBE emission is expected due to a competition with radiative emissions in the visible region,[65] or the presence of dislocations, point defects, and surface states acting as non-radiative centers.[66] For instance, since a high formation of V_{Zn}-related surfaces is expected in ZnO NWs during the CBD process in oxygen-rich conditions (i.e. high pH-region), according to DFT calculations,[67] these surface defects can act as non-radiative centers, leading to a low NBE emission.[66] This is accordingly observed in ZnO NWs without coating layers. Then, an enhancement of the NBE region of ZnO NWs is observed according to the thickness of the

[♣] The 5 K cathodoluminescence were done at Institut Néel in Grenoble in collaboration with Emilien LEFEBVRE and Fabrice DONATINI

Al_2O_3 shell layer, as summarized in the inset of **Figure III.3-5**. This emission improvement could involve two mechanisms: a thermal effect occurred on ZnO NWs during the growth of Al_2O_3 films in the ALD chamber at 300 °C, and the effect of the coating layers themselves. Indeed, by keeping the samples at 300 °C in the ALD chamber, a thermal annealing of ZnO NWs can occur, as discussed in **Chapter II**, which can decrease the density of surface V_{Zn}-related defects, enhancing their NBE emission.[23] However, given the identical thermal treatment that could occur in ZnO NWs in the ALD chamber, the difference in NBE emission is further attributed to the effect of Al_2O_3 layers. Thus, the improvement of the NBE with Al_2O_3 shell layers could be strongly assigned to a density increase in free excitons through the reduction of surface traps (surface passivation), which can act as non-radiative recombination centers, or defects emitting in the visible region. Indeed, Richters et al. concluded that by passivating the surface defects of ZnO NWs with an amorphous Al_2O_3 shell layer, the density of near-surface excitons increases, resulting in the enhancement of the NBE emissions at the expense of DLE transitions.[65] Concerning the latter, the red band (1.6 – 2 eV), the yellow band (2 – 2.3 eV), and the green band (2.3 – 2.5 eV) are involved in the DLE emission. Since DLE emission is steadily centered around 1.9 eV but varies in intensity depending on the thickness of Al_2O_3 layers, as illustrated in the inset of **Figure III.3-5**, we can assume that Al_2O_3 shell layers do not promote the formation of defects that emit in a specific visible region, which would lead to a DLE shift. Based on this hypothesis, Al_2O_3 layers severely enhance the radiative emission of free excitons, potentially reducing the emission in the visible band. Therefore, the measured ratios of NBE over DLE are 0.06, 0.49, 0.34, 0.55, and 1.18 for ZnO NWs with 0, 1, 2, 5, and 10 nm-thick Al_2O_3 shell layers, respectively. This suggests progressive surface passivation as the thickness of Al_2O_3 increases. For comparison, Richters et al. showed a NBE/DLE ratio of 1.7 for pristine ZnO NWs and 4 for those with 10 nm-thick Al_2O_3 layers.[17] In other work, Richters et al. also demonstrated a NBE/DLE ratio of 0.46 for as-grown ZnO NWs and 10 for those coated with PMMA layers,[16] indicating a lower passivation with Al_2O_3 when compared to PMMA. In the present study, the surface passivation of ZnO NWs with Al_2O_3 shell layers is higher than in Richters' work. However, it could be possible that this passivation is lower than that obtained for parylene-C-coated ZnO NWs. It should be mentioned that this surface passivation will severely affect the piezoelectric behavior of ZnO NWs, as explained by SFLP effects.

Moreover, a blueshift of the NBE emission of ZnO NWs with Al_2O_3 layers is interestingly observed, which could be assigned to strain effects. Indeed, by compressing the structure of ZnO NWs with Al_2O_3 layers, as suggested by Raman and XRD studies, an increase of the bandgap could occur, leading to recombination of free excitons with higher energies, and subsequently a blueshift of the NBE.[57,68,69] Indeed, Jaffe et al. explained that compressing ZnO enhances the interaction between the O 2p and Zn 3d states, leading to increased repulsion between these states , broadening the bandgap in the Brillouin zone,[70] as discussed in **Section I.2.1.2.1**. The compression stress can also increase the overlap of the electron and hole wavefunctions of the free-excitons, enhancing the recombination rate and the NBE emission.[71] This suggested compression with the Al_2O_3 shell layer can also account for the piezoelectric response of ZnO NWs.

In conclusion, 5 K cathodoluminescence illustrates the high surface passivation and structural contraction of ZnO NW with Al_2O_3 shell layers. This can account for the piezoelectric response of a PNG, which will be investigated in the following section.

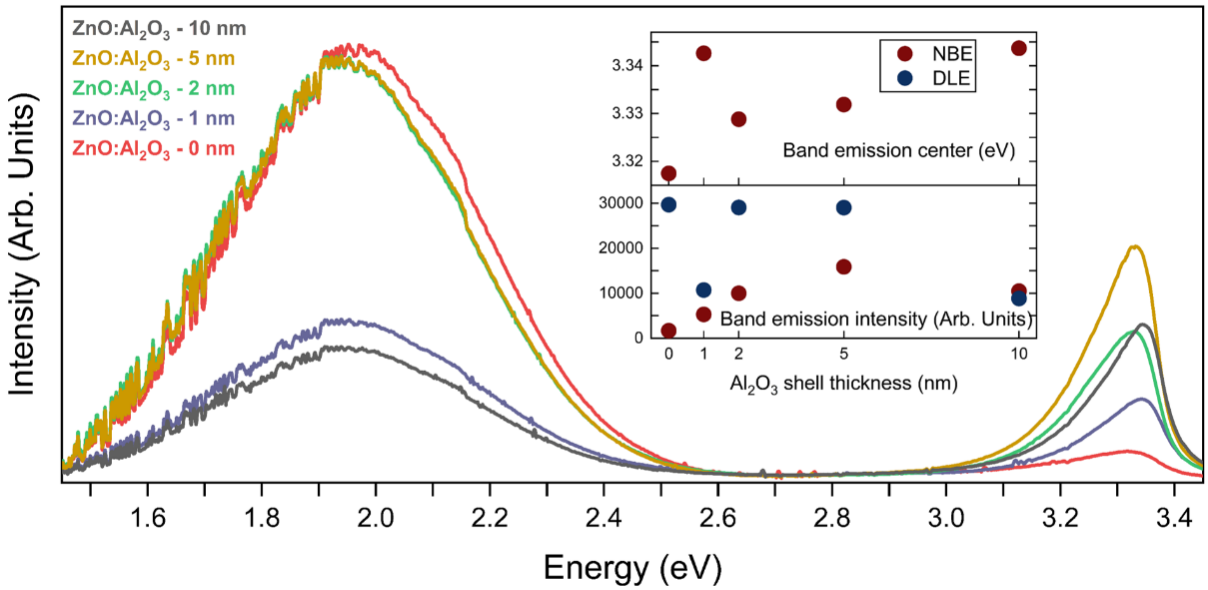

***Figure III.3-5**. Cathodoluminescence at 5 K of ZnO NWs coated with Al_2O_3 shell layers with different thicknesses. (Inset) Associated emission peaks of the Near Band Edge(NBE) and Deep Level Emission (DLE) bands along with their intensities. The DLE peak is centered around 1.9 eV regardless of the Al_2O_3 shell thickness.*

III.4 Enhancing the performance of piezoelectric nanogenerators based on ZnO nanowire matrix with Al_2O_3 shell passivation layers

III.4.1 Fabrication of piezoelectric nanogenerators based on ZnO/Al_2O_3 core-shell heterostructures

Following the physicochemical, structural, and optical studies performed on ZnO/Al_2O_3 heterostructures, the evaluation of their ability to convert mechanical energy into electrical energy is subsequently investigated. The integration of these heterostructures into a PNG is therefore crucial. The architecture of the fabricated PNGs is presented in **Figure III.4-1(a)**. On the substrates integrating the ZnO/Al_2O_3 core-shell heterostructures prepared in **Section III.3.1**, the deposition of parylene-C was achieved by vacuum evaporation and polymerization process, according to the Gorham process.[22] The 1×1 cm^2 top electrode was subsequently obtained by depositing through a mask the stack made of 20 nm-thick Ti layer, 250 nm-thick Al layer, and 100 nm-thick Au layer by vacuum evaporation. Finally, two Cu wires contact both the top (red) and bottom (black) electrodes by using conductive resin, resulting in the final devices shown in **Figure III.4-1(b)**. Thus, 5 different PNGs were fabricated according to the thickness of 0, 1, 2, 5, and 10 nm of Al_2O_3 shell layers, whose features are summarized in **Table III.4-1**. It is important to mention that Parylene C, in addition to providing robustness to the device, should ensure the isolation of NWs from their neighbors to reduce the screening effect, and create capacitive-like contact between the NWs and the top electrode. FESEM-EDS mapping of the cross-section of an arbitrary device is recorded, as depicted in **Figure III.4-1(c)**, confirming the deposit compliance of parylene-C (C_8H_7Cl) through the Cl-K signal (orange). Thus, parylene-C successfully penetrates the NW matrix and separates the top of the NW from the top electrode by 2 µm, consequently reducing the leakage current of the device.

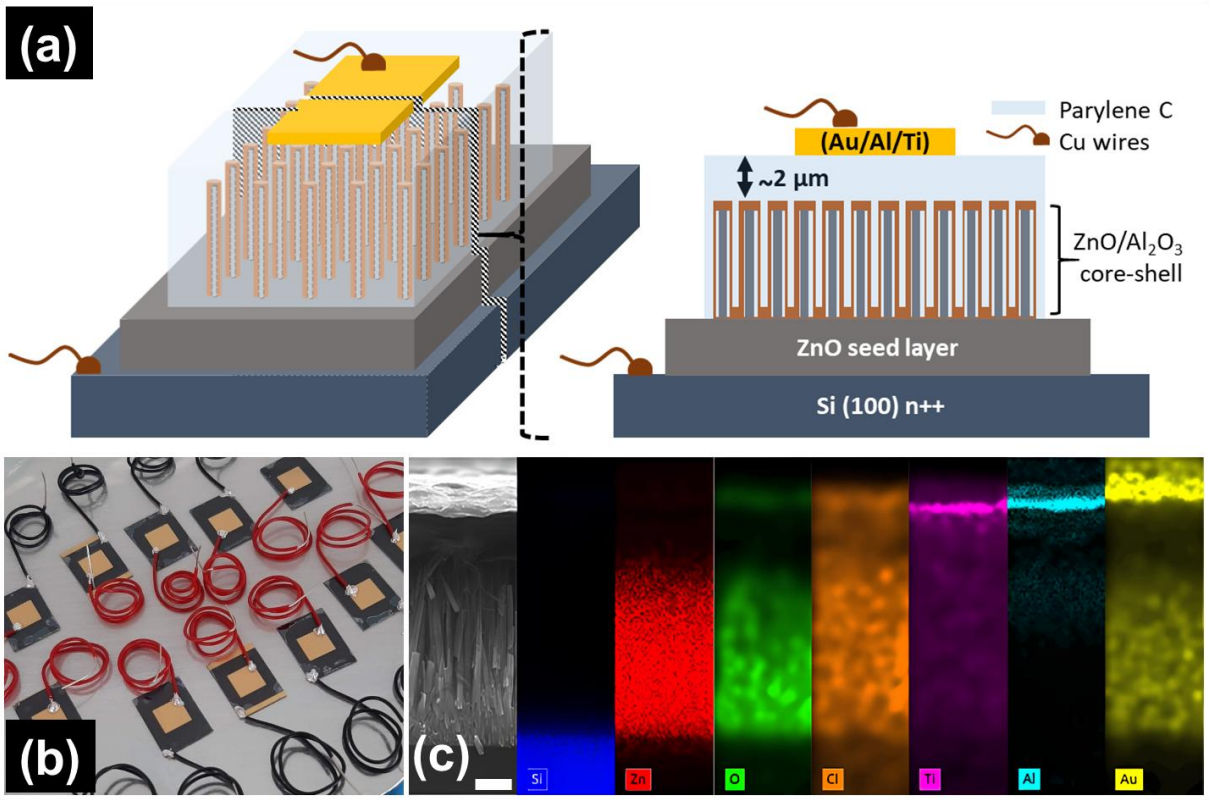

Figure III.4-1. (a) *Design of PNG based on ZnO/Al_2O_3 core-shell heterostructures.* ***(b)*** *Picture of final devices.* ***(c)*** *FESEM - EDS mapping image of the cross-section of a final device, depicting the bottom electrode (Si-blue), ZnO NW matrix (Zn-red and O-green), parylene-C layer (Cl-orange), and the top electrode (Ti-pink, Al-blue-sky and Au-yellow). The bar scale corresponds to 1 µm.*

Table III.4-1. *Features of PNGs integrating Al_2O_3 shell layers with different thicknesses for piezoelectric characterizations in the LTM's test bench.*

PNG	Al_2O_3 thickness (nm)	Integrated ZnO NWs	Parylene C
A	0	Density (NW/µm^2) 42.9 ± 5.7 Length (µm) 6.1 ± 0.7 Top diameter (nm) 42 ± 25 Middle diameter (nm) 166 ± 40 Aspect ratio 36.7 ± 1.2	Conformal deposition of 2 µm over the NWs
B	1		
C	2		
D	5		
E	10		

III.4.2 First piezoelectric characterizations of ZnO/Al_2O_3 heterostructures-based piezoelectric nanogenerators on the LTM's test bench

The output voltage of the fabricated PNGs was measured on the LTM's test bench under soft mechanical stress conditions. The working principle of the setup is described in **Section II.5.1**. Controlled by a sinusoidal signal from the function generator, vertical forces of 3.2, 6.6, and 9.6 N were applied on the top electrode of the PNGs at 1 Hz. **Figure III.4-2** illustrates the output voltage values of the PNGs with the different Al_2O_3 shell layers. These values were

amplified tenfold using the Stanford Research Systems SR560 amplifier to distinguish them from electronic noise signals. The unit mVpp refers to the total amplitude between the opposite peaks of the piezoelectric signal for the compression and release cycle. The PNG of reference, i.e. 0 nm of Al_2O_3, delivers the lowest output signal for the three different applied forces. This could be the result of a low charge accumulation at the bottom electrode. When mechanical stress is applied to the NWs, the piezoelectric polarization generated inside their structure should attract charges flowing from an external load to the electrodes of the PNG. However, it is reasonable to expect a loss of charge accumulation if the electrode is not a good conductor. Thus, although the Si substrate is highly n-type doped, its resistivity acts as a barrier to the flow of external electrons, so that fewer carriers are accumulated. Moreover, given the direct dependency of the external carrier flow on the strain rate of the PNG, the low output voltage could be also due to the slow mechanical deformation of the device in the test bench. This was discussed in **Section II.5.2.2** where the output voltage of the PNGs was increased as the frequency of the applied force was rised from 0.5 to 5 Hz.

Comparing the output voltage of the PNGs, which were characterized simultaneously in the same mechanical conditions, the PNG integrating an Al_2O_3 shell layer of 2 nm exhibits the highest values. Then, it appears that thicker Al_2O_3 layers than 2 nm lead to a loss of the output signal. Given that the conformal thicknesses and amorphous structure of these coating layers are confirmed, mechanical effects can arise and conduct the energy conversion in the device. Indeed, by increasing the thickness of Al_2O_3, a slight increase in the equivalent Young's modulus of the ZnO/Al_2O_3 heterostructure could be expected. This change would make the heterostructures less affected by mechanical deformations, resulting in reduced piezoelectric polarization. A modification in the internal impedance of the PNGs with Al_2O_3 can occur as well. For this, piezoelectric characterizations with different external loads are needed. However, this study cannot be performed on the LTM's test bench for the moment. This is how our collaboration with Gustavo Ardila's group from the CROMA♣ laboratory was established to characterize our PNGs connected to different external loads.

♣ Radiofrequency, Optics and Micro-nanoelectronics Center of the Alps, formerly called IMEP-LaHC

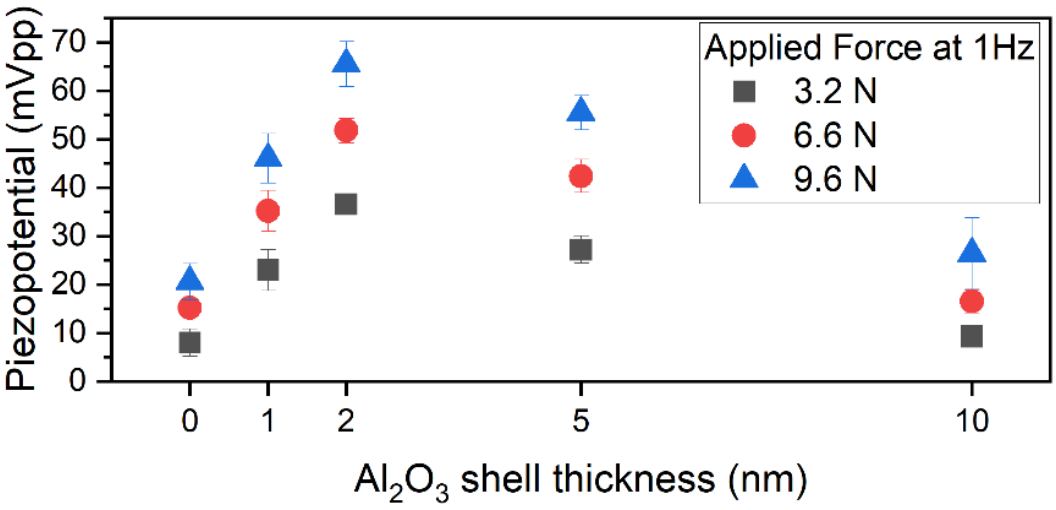

***Figure III.4-2**. Output voltage values (peak-to-peak) of PNGs integrating different thicknesses of Al_2O_3 shell layers characterized on the LTM's test bench. This figure displays the output voltage values amplified by a 10-factor using the Stanford Research Systems SR560 amplifier of the test bench for better readability.*

III.4.3 Piezoelectric characterizations of ZnO/Al_2O_3 heterostructures-based piezoelectric nanogenerators on the CROMA's test bench

This section presents the setup and operation mode of the CROMA's test bench for characterizing our PNGs based on ZnO/Al_2O_3 heterostructures. A key advantage of this test bench is the integration of a variable external impedance connected to a PNG, allowing the study of the electrical power generated by this device, whose study is not yet enabled on the LTM's test bench. However, the application of a vertical force to the device requires preliminary studies, as will be detailed in **Section III.4.3.2**. Indeed, on the LTM's test bench, the force is applied "slowly" following a sinusoidal function as power supply signal, whereas on the CROMA's system, the force is applied "rapidly" using a square function as power supply signal.

Moreover, it is crucial to emphasize that the devices tested on the CROMA's test bench correspond to a "second manufacturing batch". Unfortunately, some devices from the previous characterizations were short-circuited or broken during the experiments. One reason was, for instance, the abnormal behavior of the mechanical arm that unexpectedly applied excessive force to the device before suddenly stopping, resulting in irreparable damages.

The second batch of PNGs was manufactured using the same protocol as the first batch. In addition, two PNGs sharing the same characteristics were manufactured. Thus, the piezoelectric characterizations represent the average of these two devices. The morphological

properties of the integrated ZnO NWs are shown in **Table III.4-2**. They exhibit small changes compared to those integrated in the previous PNGs. The thickness of 2 µm of parylene-C over the NW matrix was also confirmed with FESEM-EDS mapping images. It is worth mentioning that the PNG-A corresponds to a device that was placed in the ALD chamber without depositing Al_2O_3. This will help to discern the effects of possible thermal annealing of ZnO NWs during the ALD process from the effect of the Al_2O_3 layers themselves on the PNG performance. The effect of thermal annealing of ZnO NWs on the piezoelectric response of a PNG was discussed in **Section II.5.3**

Table III.4-2. *Features of the second batch of PNGs integrating Al_2O_3 layers with different thicknesses.* ***PNG-REF*** *corresponds to devices that were not introduced in the ALD chamber, whereas* ***PNG-A*** *refers to devices introduced in the ALD chamber without deposit of Al_2O_3 layers.*

PNG	Al_2O_3 thickness (nm)	Integrated ZnO NWs	Parylene C
REF	0	Density (NW/µm^2) 60.0 ± 5.7 Length (µm) 4.7 ± 0.2 Top diameter (nm) 23 ± 7 Middle diameter (nm) 122 ± 48 Aspect ratio 38.1 ± 14.9	Conformal deposition of 2 µm over the NW matrix
A	0		
B	1		
C	2		
D	5		
E	10		

III.4.3.1 Description of the CROMA's test bench

The automatized set-up to characterize the fabricated PNGs under compressive stress is presented in **Figure III.4-3(a)**. The whole test bench consists of four main modules: an equipment to set the external load (10 k – 122 MΩ) and amplify the signal of the testing device, an oscilloscope to record the piezoelectric signal, an electromechanical set-up to apply mechanical stress to the PNG, and a PC unit to control the whole system with different software based on LabVIEW program. The electromechanical system, located within the Faraday cage, consists of different accessories as well, as shown in **Figure III.4-3(b)**. The PNG is taped to the sample holder, whose position can be manually adjusted in the planar (x, y) direction with two screws, and in the z-direction with the actuator controlled by the PC unit. Finally, the actuator moves the PNG upward until it contacts the fixed force load connected to a force sensor, applying consequently a vertical compressive force on the top electrode of the device.

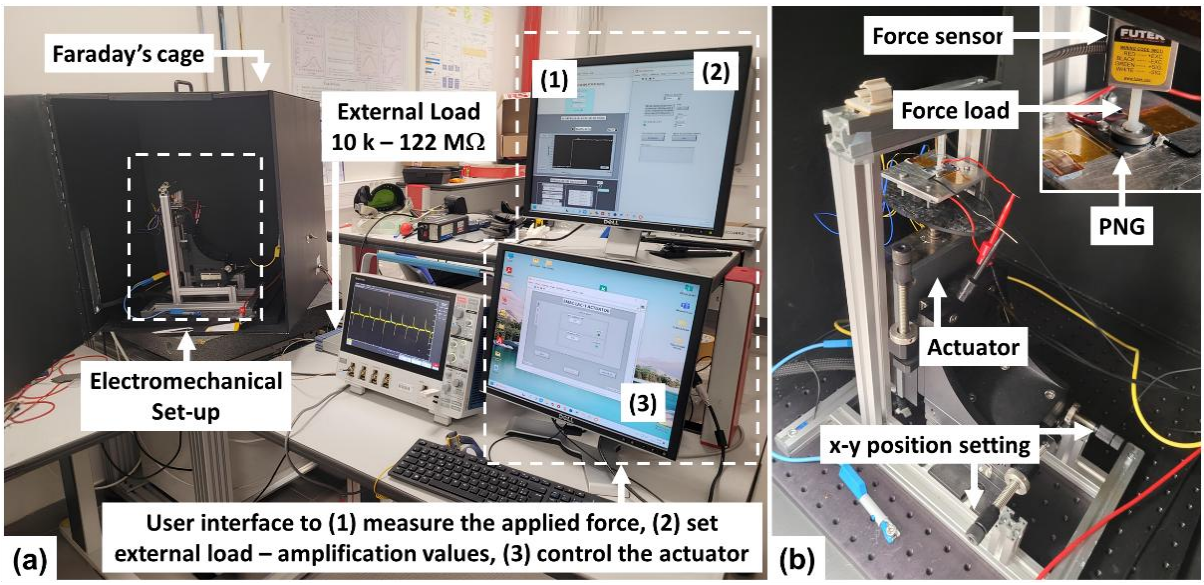

Figure III.4-3. (a) *Picture of all the modules integrating the test bench for PNG characterizations available at CROMA laboratory – Grenoble, France.* ***(b)*** *Picture of the electromechanical test bench within the Faraday's cage.*

III.4.3.2 Choice of the force load configuration

The devices were subjected to continuous mechanical compression cycles, where compression forces were applied by the force load. It is worth noting that the force load consists of a contact head and a screw fastened to the force sensor. It should be mentioned that the configuration of the force load system can affect the piezoelectric response of the PNG. For instance, a stiffer load system results in greater deformation of the device during mechanical compressions. Thus, a loading system made entirely of metal would be ideal. However, triboelectric effects can arise from friction between the metal force load system and the metal electrode of the device. This highlights the need for an appropriate configuration of the force load system to ensure accurate characterizations of PNGs. Therefore, four different structures were investigated based on the materials used for the screw and the contact head, as well as the dimension of the contact head. **Figure III.4-4** highlights the piezoelectric signals generated from a PNG connected to an external load of 90 MΩ when 1 N is applied using distinct force loads: **(a)** a plastic screw with an iron-based contact head, **(b)** both the screw and the contact-head made of iron, **(c)** a plastic screw with a copper-based contact head, and **(d)** both the screw and the contact head made of plastic. It is important to mention that, according to the triboelectric series, copper and iron are expected to be neutral or slightly positively charged materials. This suggests that when they come into contact with the Au layer of the PNG's top electrode, triboelectric effects can occur. In the present study, the

mechanical compression is achieved when the actuator rapidly ascends the sample holder, compressing the PNG against the force load. This impact can lead to higher applied forces than expected, which is immediately stabilized when the actuator slightly descends until the sensor force read the targeted force. Then, the actuator holds the sample at this position for ~2.5 s, and finally drops to release the device of the mechanical stress, thereby generating two symmetric piezoelectric peaks of opposite sign for the compression and releasing cycle. In **Figure III.4-4**, a strong relationship between the response of the device and the force load configuration is observed. Indeed, during the compression cycle, the load configuration "a" is the only one that leads to the apparition of a positive piezoelectric peak. Then, for the release cycle, a negative piezoelectric peak is generated by the load configurations "a", "b" and "c" which include a metal-based contact head, whereas the positive peak appears for the load configuration "d" entirely made of plastic. Therefore, these differences in polarity and intensity of the piezoelectric signal can involve mechanical and electrical effects. For instance, differences in force load, such as the contact head area and the stiffness of the screw, could induce different deformation of the Parylene C and the NWs within the device during the compression cycle. This mechanical deformation can be even more pronounced by the strong impact occurring between the device and the force load when the actuator ascends, as described before, resulting in a probable bouncing effect in the device and consequently generating a piezoelectric signal of unpredicted polarity and intensity. For the release cycle, when a "mechanical stabilization" of the device is already expected, the generated signal is assigned to a piezoelectric response under controlled mechanical excitation. Consequently, changes in peak intensity correspond to the contribution of NWs to the piezoelectric signal, which is directly correlated to the contact area of the force load, as observed in signals generated by load configurations "a" and "c". Given that load configurations "a" and "b" share the same contact area, the differences in signal amplitude could arise from generated electrical charges leaking through the metallic force load "b". In contrast, the load configuration "d" could induce triboelectric effects leading to a positive piezoelectric peak in the release cycle, i.e. electrostatic charges can be generated during the friction between the plastic head contact and the Au layer of the top electrode of the device, changing the polarity of the piezoelectric peak.

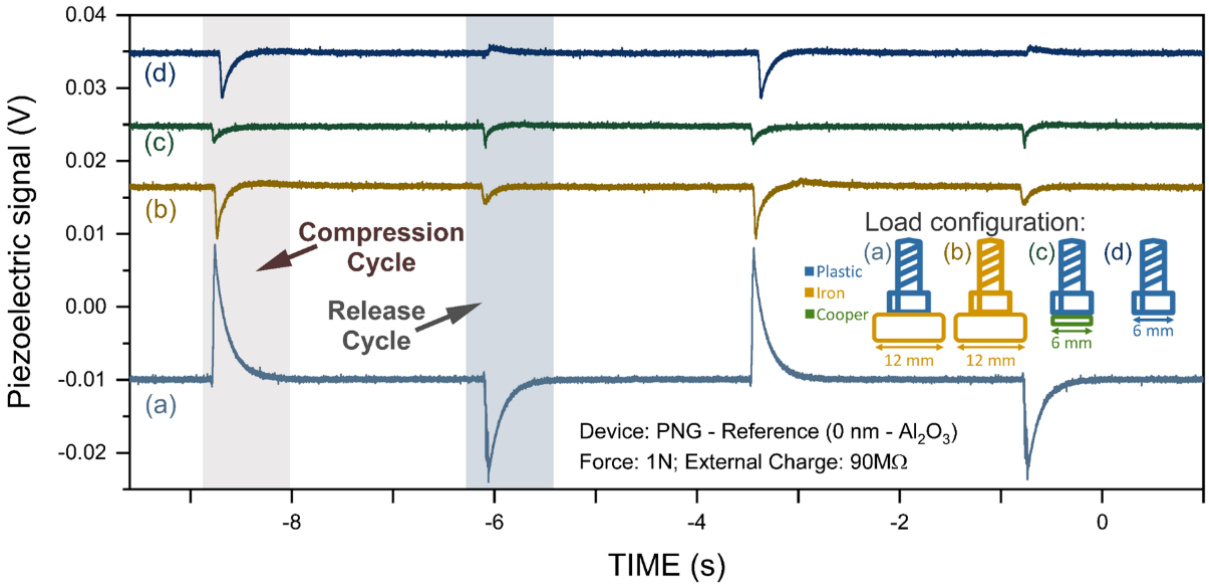

***Figure III.4-4**. Piezoelectric response of a PNG tested under 1 N at 0.2 Hz with different force load configurations on the CROMA's test bench. Note: The load configuration "a" was chosen for the piezoelectric characterizations of PNGs presented in the following sections.*

These findings highlight the need to perform studies focusing on the mechanical and electrical behavior of PNGs under different mechanical stress conditions. However, this question will remain open since we will focus on studying the effect of Al_2O_3 layers on the piezoelectric performance of PNGs. For this purpose, the piezoelectric characterization of these devices will be performed with the load configuration "a", i.e. the screw made in plastic with an iron-based contact head, which led to the strongest peaks with opposite polarity according to the compression and release cycle.

III.4.3.3 Removing the 50 Hz noising signals from the recorded piezoelectric signals

The generated piezoelectric signals were observed through the Oscilloscope and recorded in a USB key for ulterior treatment. Given the electronic noise of 50 Hz corresponding to the power alimentation of the system, a Notch-based filter is applied to remove this noise signal from the recorded piezoelectric signals by using a code based on Python programming language, resulting in the red signal presented in **Figure III.4-5(a)**. Consequently, all the recorded data are filtered by applying the same parameters and shown in the next sections of this chapter. Moreover, the piezoelectric behavior of all the devices is confirmed by changing the polarity connection of their electrodes and obtaining an inversion of the piezoelectric signal, as shown in **Figure III.4-5(b)**. The asymmetry in intensity observed in the generated peaks involves electronic effects related to the measuring circuit,[40] as well as mechanical

effects described above. In the following part, only the piezoelectric signals recorded in direct connection are shown.

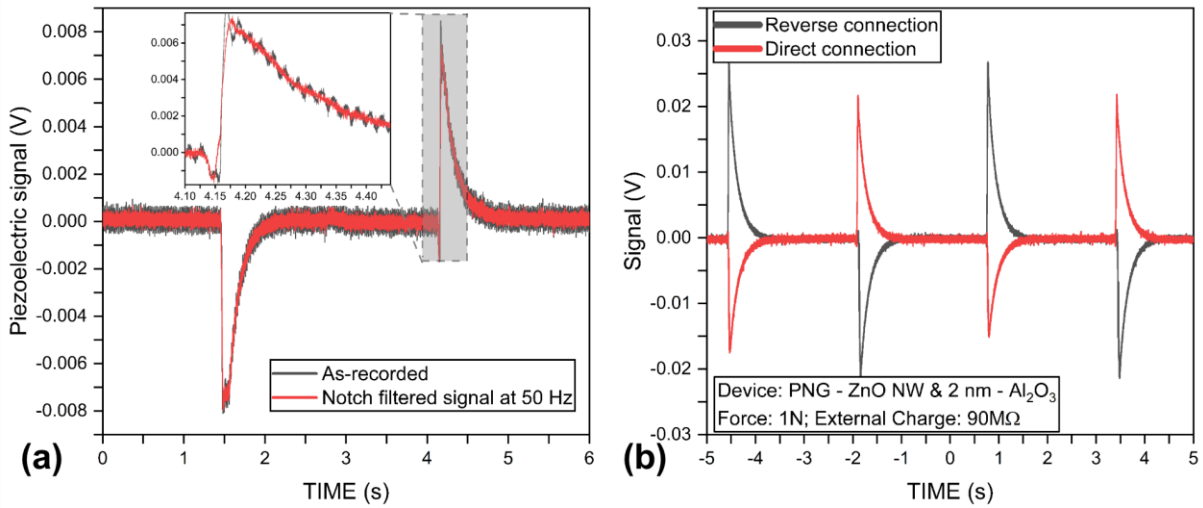

Figure III.4-5. (a) *Elimination of 50 Hz noise-signals from recorded piezoelectric signals on the CROMA's test bench by using a Notch filter coded in Python language.* ***(b)*** *Piezoelectric signal in the forward and direct connection.*

III.4.4 Performance characterizations of piezoelectric nanogenerators based on ZnO/A_2O_3 core-shell heterostructures

III.4.4.1 Piezoelectric signal as a function of the vertically applied force and external load

To establish conditions that allow an accurate characterization and comparison of devices without damaging their structures, two different PNGs were arbitrarily chosen for preliminary tests based on the applied force and the external load connection. It is worth mentioning that the devices are characterized by using a force load consisting of a screw made of plastic with an iron-based contact head, as explained in **Section III.4.3.2**. The positive and negative piezoelectric peaks appear for the compression and release cycle, respectively. In **Figure III.4-6(a)**, a PNG integrating ZnO NWs coated with a 10 nm-thick Al_2O_3 layer was tested, highlighting an increment of its piezoelectric signal's peak-to-peak as long as the applied force increases from 0.42 to 5.2 N. This behavior is consistent with the mathematical description of the piezoelectric effect, which couples Hooke and electric displacement field equations. While the homogeneous negative peaks progressively increase in magnitude with the applied force, the positive peaks exhibit different intensities when the force is higher than 2 N. This variation could be attributed to the strong impact on the device when the compression cycle starts, as explained in **Section III.4.3.2**. The impact becomes more pronounced with higher applied

forces, leading to a random piezoelectric signal highly affected by mechanical effects. This would explain why the signals are more homogeneous during the release cycle, where mechanical stabilization of the device is expected. Therefore, the peaks arising during the release cycle will be used as references to measure the generated piezoelectric signals of the devices. Accordingly, **Figure III.4-6(b)** summarizes the generated voltage in the testing device (i.e. PNG with ZnO NWs/Al_2O_3 10 nm) as a function of the applied force. Interestingly, a linear response of the device is depicted, whose signal amplitudes increase from 30 to 60 mV when forces are applied from 0.45 to 2.5 N. Then, a saturation region is reached for forces higher than 3.6 N, where the signal remains around 72 mV. It is worth mentioning that this saturation region can vary depending on the PNG features and the external load. However, for the next characterizations, PNGs will be characterized under 1 N to avoid a possible saturation regime and to limit the mechanical effects influencing their piezoelectric responses.

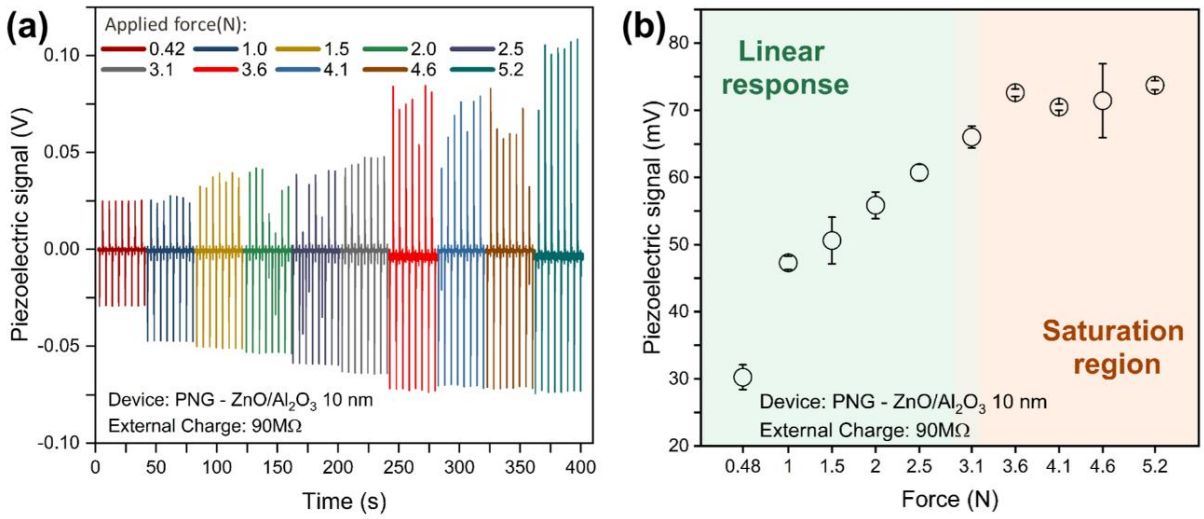

***Figure III.4-6**. **(a)** Piezoelectric signal of a PNG based on ZnO NWs coated with a 10 nm-thick Al_2O_3 layer as a function of the vertically applied force at 0.2 Hz. **(b)** Peak voltage generated by the same PNG when a vertically applied force is released. **Note**: The negative piezoelectric peak of the stress-release cycle should be considered instead of the compression cycle due to mechanical rebound effects caused by the load applied during compression. Measurements done on the CROMA's test bench.*

Figure III.4-7(c) presents the generated signal of a PNG integrating ZnO NWs without Al_2O_3 shell layers under 1 N as a function of the external load. The latter starts from 1 MΩ to obtain the smallest piezoelectric signal that can be measured. As expected, the generated signal increases with the increment of the external load. Indeed, according to the following equation: $V_m = \frac{Z_L}{Z_L + Z_{PNG}} V_{OC}$; the generated voltage V_m, which is lower than the open-circuit voltage V_{OC}, increases when the external load Z_L becomes higher than the internal impedance of the device Z_{PNG}.[40] Interestingly, the piezoelectric signal rapidly increases when the external

load rises until 20 MΩ, and then the signal slowly continues to increase for an external load larger than 20 MΩ. It suggests that the testing device possesses an internal impedance lower than 20 MΩ, and can work in open-circuit when the external load exceeds its internal impedance. This outcome anticipates the adaptability of the test bench to characterize our devices in open-circuit mode and to calculate their power transfer, as discussed in the following section.

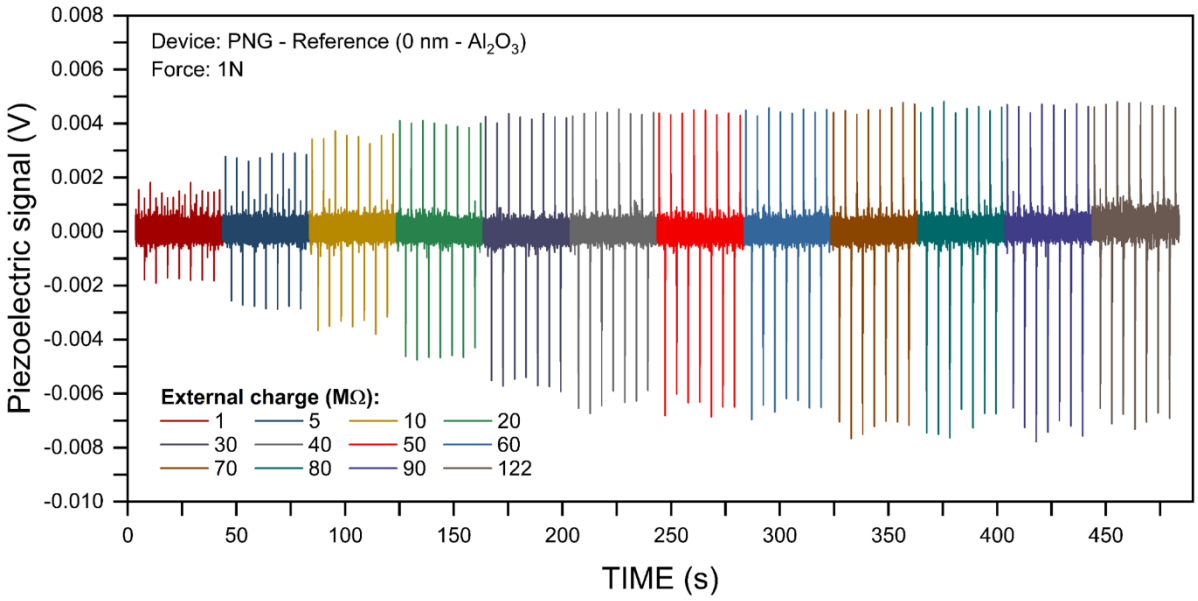

Figure III.4-7. *Piezoelectric signal of a PNG – reference (ZnO NWs without Al_2O_3 shell layer) under 1 N at 0.2 Hz as a function of the external resistive load magnitude on the CROMA's test bench.* ***Note****: The negative piezoelectric peak of the stress-release cycle should be considered instead of the compression cycle due to mechanical rebound effects caused by the load applied during compression.*

III.4.4.2 Performance comparison of piezoelectric nanogenerators integrating ZnO NWs coated with different thicknesses of Al_2O_3 layers

After the preliminary studies based on the effect of the force load configuration, device polarity connection, applied vertical force, and external load on the piezoelectric response of arbitrary devices, the performances of the different fabricated PNGs described in **Section III.4.3** were compared. For this purpose, PNGs were tested in direct connection (i.e. the positive and negative peaks correspond to the compression and release cycle, respectively), in which 1 N force was applied by a screw made in plastic with an iron-based contact head, resulting in the piezoelectric voltages shown in **Figure III.4-8(a)**. First, a thermal effect on the output voltage of the device is confirmed when comparing PNG-REF and PNG-A. Indeed, neither of them integrates the Al_2O_3 layer; however, PNG-A, which was introduced in the ALD

chamber on a 300 °C heated plate, exhibits a voltage of ~20 mV, 4 times higher than the PNG-REF's voltage, which integrates a pristine ZnO NW matrix (no introduced in the ALD chamber). This is consistent with experiments in **Section II.5.3**, which show that thermal treatment of the NWs reduces the free carrier density, leading to a decrease in screening effects and consequently improving the output signal of a PNG.

Considering this, the difference in performance among the PNG-X (X=A, B, C, D, E) devices arises from the effect of the Al_2O_3 layer. An increase of the piezoelectric signal of PNG is achieved as the thickness of integrated Al_2O_3 shell layers rises until 5 nm, whose device exhibits the highest signal of ~80 mV. Then, the signal drops to 50 mV when the PNG integrates 10 nm-thick Al_2O_3 layer. From these piezoelectric signals, the effective piezoelectric coefficient d_{33}^{eff} of each PNG is calculated by using the equation $d_{33}^{eff} = \frac{V \times C_0}{F_{applied}}$; where the device is equivalent to a capacitor C_0 discharging over an external load Z_L, V is the generated voltage of this PNG under a given applied force $F_{applied}$.[72] Then, by calculating the time constant τ ($\tau = C_0 \times Z_L$) from the exponential decay piezoelectric signals presented in **Figure III.4-8(a)**, the associated d_{33}^{eff} values are calculated and presented in **Figure III.4-8(b)**. It is worth mentioning that d_{33}^{eff} refers to the ability of the device to convert mechanical stress into electrical voltage, which should not be confused with the piezoelectric coefficient d_{33} of a single NW. The energy conversion of the device involves the piezoelectric behavior of the integrated ZnO NWs, the effectiveness of the electrodes, the mechanical properties of the polymer, etc.

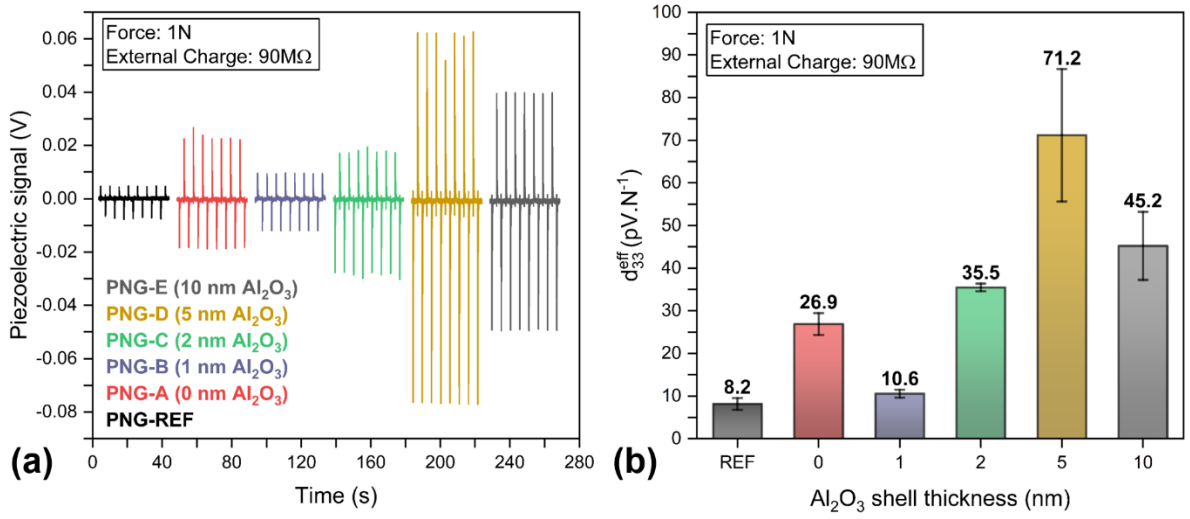

***Figure III.4-8**. **(a)** Piezoelectric signal comparison of PNGs based on ZnO NWs coated with 0, 1, 2, 5 and 10 nm-thick Al_2O_3 layers, and their corresponding **(b)** d_{33}^{eff} piezoelectric coefficient calculated with the approach of REF [72] when 1 N at 0.2 Hz is released and an external charge of 90 MΩ is connected. Measurements done on the CROMA's test bench.*

The mean d_{33}^{eff} of a typical PNG in this thesis could lie between 4 and 35 pV/N when a sinusoidal force is applied between 0.5 to 5 Hz, as presented in **Figure II.5-7** in **Section II.5.2.2**. In the present study, the PNG-REF exhibits a d_{33}^{eff} of 8.2 pV/N under a square force of 1 N. Then the d_{33}^{eff} increases to 26.9 pV/N for the PNG-A, whose improvement is related to thermal effects in the ALD chamber. Subsequently, 1 nm of an Al_2O_3 shell layer appears to degrade the performance of the PNG, which displays a d_{33}^{eff} of 10.6 pV/N. As long as the thickness of the Al_2O_3 layer increments from 1 to 5 nm, the PNG steadily enhances its d_{33}^{eff}, whose highest value is 71.2 pV/N. Finally, when the Al_2O_3 layer exceeds 5 nm, the d_{33}^{eff} severely reduces until 45.2 pV/N

The previous findings indicate that the use of ZnO/Al_2O_3 heterostructures embedded with a parylene-C layer enhance the performance of the PNG. This improvement could involve surface defect passivation along with structural modification of the ZnO NWs. Indeed, by compressing the structure of the NWs with the Al_2O_3 shell layers, as revealed by XRD, Raman, and 5 K cathodoluminescence analysis, the strain induced along the *c*-axis increases, which can affect the piezoelectric coefficient of ZnO NWs, and thereby the output voltage of the PNG.[73] However, with the increase in thickness of the Al_2O_3 layer, a slight increment of the effective Young's modulus of ZnO/Al_2O_3 heterostructures can occur, making them less flexible during the compression of the device, resulting in a loss of output voltage. In addition, Al_2O_3 effectively passivates the surface of ZnO NWs. The degree of passivation increases with the thickness of this coating layer, which leads to a decrease in SFLP and, consequently, could reduce the piezoelectric properties of ZnO NWs. However, the level of passivation achieved with Al_2O_3 layers could be lower than that obtained with a parylene-C layer. This suggests that using Al_2O_3 shell layers at the interface of ZnO NW with parylene-C would be advantageous. Therefore, it is essential to find a balance between the level of passivation and the mechanical properties of the ZnO/Al_2O_3 heterostructures to improve the overall performance of a PNG.

Additional characterizations of the PNGs under 1 N were performed as a function of the external load, revealing the strongest piezoelectric voltages for the PNG integrating 5 nm-thick Al_2O_3 shell layers, regardless of the external load, as presented in **Figure III.4-9(a)**. Then, the generated voltage steadily decreases for the PNGs with Al_2O_3 layer thicknesses of 10, 2, 1, and 0 nm, respectively. The lowest voltage is generated by the PNG-REF. It is important to mention that when comparing the piezoelectric voltages generated by the PNGs, a correlation with

their d_{33}^{eff} coefficient is observed, i.e. the devices generate a voltage consistent with their respective d_{33}^{eff} coefficients. Interestingly, all the devices reach a saturation of their generated voltage for external charges larger than 20 MΩ.

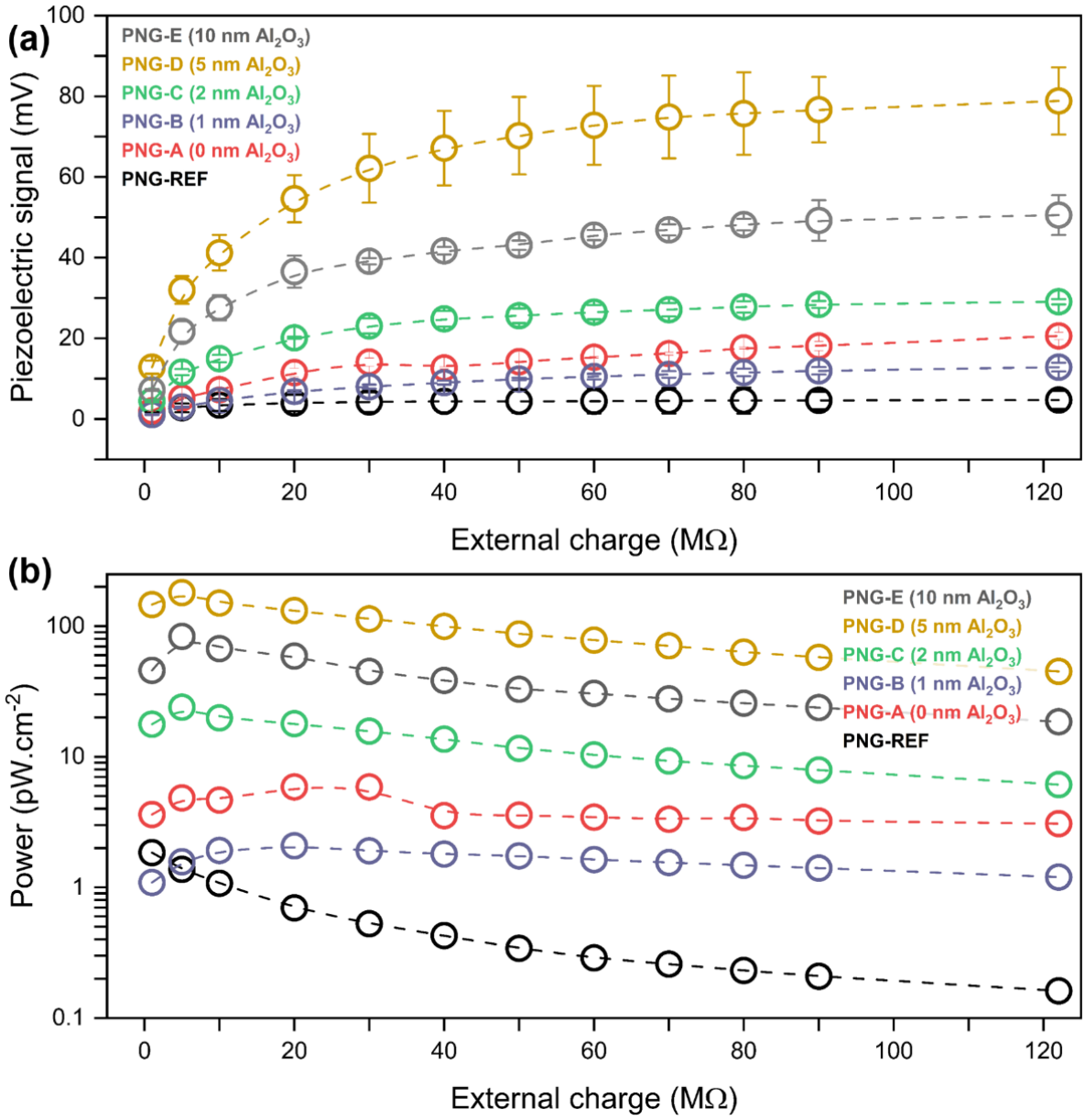

***Figure III.4-9**. **(a)** Piezoelectric peak and **(b)** instantaneous power density (logarithmic scale) generated by PNGs based on ZnO NWs coated with 0, 1, 2, 5 and 10 nm-thick Al_2O_3 layers as a function of the external load under the release of 1 N at 0.2 Hz. The piezoelectric peak and power density values shown in this figure represent the mean values obtained from two PNGs with identical properties for each Al_2O_3 shell layer thickness. Measurements done on the CROMA's test bench.*

The instantaneous power density *P* produced by these devices was calculated according to the equation $P = \frac{V^2}{Z_L} \times \frac{1}{A}$, where *V*, Z_L and *A* are the generated voltage peak, external load, and active area of the device, respectively. The PNG-X (X=A, B, C, D, E) devices exhibit a maximum instantaneous power density when connected to external loads between 5 and 20

MΩ, after which the instantaneous power steadily decreases as the external load increases. In contrast, the PNG-REF shows a constant decrease in generated power density across the entire range of the external loads, suggesting that its peak power could occur at resistive loads lower than 1 MΩ. However, due to the very low output voltage of PNG-REF at external loads below 1 MΩ, the signal is hidden by electronic noise from the oscilloscope, making it impossible to determine its maximum power. The variation in power density between the PNG-REF and the devices introduced in the ALD chamber could suggest a change of internal impedance of the PNG due to thermal effects. Indeed, the devices introduced in the ALD chamber could have higher internal impedance compared to the reference device. This would be in agreement with a reduction of free carrier in ZnO NWs due to thermal annealing, which results in more resistive NWs that should increase the internal impedance of the PNG that integrates them. Then, as expected, the PNG with the 5 nm-thick Al_2O_3 layer provides the largest power density values regardless of the external load, reaching its highest value of 180 $pW.cm^{-2}$ for 5 MΩ, as shown in **Figure III.4-9(b)**. This power density is 120 times higher than that generated by the PNG of reference for the same external charge. Then, the power density produced by the PNGs with 0, 1, 2, and 10 nm-thick Al_2O_3 shell layers for 5 MΩ are 1.5, 2.0, 24, and 83.5 $pW.cm^{-2}$, respectively. Thus, the present findings suggest that an Al_2O_3 shell layer of approximately 5 nm provides an optimal balance between passivation and the mechanical deformation of the ZnO/Al_2O_3 heterostructures, enhancing the overall performance of a PNG.

III.5 Conclusion

The performance optimization of PNGs through surface modification of ZnO NWs was investigated. Initially, the thickness of the parylene-C layer integrated into the PNG was engineered. FESEM and EDS images have confirmed the fabrication of four different PNGs with parylene-C layers of 1.11, 1.98, 2.93, and 3.34 µm over the ZnO NW matrix. The parylene-C successfully impregnates the ZnO NW arrays, but its density distribution over the NW arrays appears non-homogeneous, as FESEM-EDS maps have revealed. Raman spectroscopy has identified the phonon modes of parylene-C, mainly associated with carbon-related bonds, and suggested that the parylene-C layer does not induce any mechanical stress in ZnO NWs. This indicate that parylene-C coating layer is unlikely to affect the spontaneous polarization of the ZnO NWs. Moreover, an increase in internal impedance of the PNGs with thicker parylene-C layers have been observed, suggesting an adaptation of external loads to characterize the device in open-circuit. Piezoelectric measurements have revealed that the PNG with 1.98 µm of parylene-C top layer produced the highest signal, indicating that ~2 µm would be an optimal balance mechanical energy transfer and energy conversion efficiency.

In addition, amorphous Al_2O_3 shell layers with thicknesses of 1, 2, 5, and 10 nm were grown by ALD to coat a ZnO NW matrix for piezoelectric applications. XRD, Raman spectroscopy, and 5K cathodoluminescence spectroscopy have revealed that these Al_2O_3 shell layers induce compression along the *c*-axis on the ZnO NWs. The Al_2O_3 layers also passivate the surface of ZnO NWs, as evidenced by a steady increase in the NBE/DLE ratio with increasing Al_2O_3 thickness, as 5 K cathodoluminescence have revealed.

PNGs incorporating ZnO/Al_2O_3 core-shell heterostructures were subsequently fabricated and characterized under soft mechanical conditions. Given that a thermal treatment during the Al_2O_3 shell deposition on ZnO NWs can occur, a reference PNG was prepared by placing a ZnO NW matrix in the ALD chamber without Al_2O_3 deposition to isolate the effects of Al_2O_3 from potential thermal treatment. Piezoelectric characterizations have indicated that a 5 nm-thick Al_2O_3 shell layer leads to the best performances of a PNG, likely due to a good balance between surface passivation and the ZnO/Al_2O_3 heterostructure's ability to deform under mechanical stress.

In conclusion, this chapter have demonstrated that introducing an interfacial layer such as Al_2O_3 between the ZnO NW and parylene-C is beneficial for PNG performance.

Bibliography

[1] R. Hinchet, S. Lee, G. Ardila, L. Montes, M. Mouis, Z. L. Wang, *Proc. PowerMEMS* **2013**, *7*, 4.

[2] R. Hinchet, S. Lee, G. Ardila, L. Montès, M. Mouis, Z. L. Wang, *Adv. Funct. Mater.* **2014**, *24*, 971–977.

[3] R. Tao, M. Parmar, G. Ardila, P. Oliveira, D. Marques, L. Montès, M. Mouis, *Semicond. Sci. Technol.* **2017**, *32*, DOI 10.1088/1361-6641/aa691f.

[4] X. Zhang, J. Villafuerte, V. Consonni, J.-F. Capsal, P.-J. Cottinet, L. Petit, M.-Q. Le, *Nanomaterials* **2021**, *11*, 1712.

[5] H. G. Kim, E. H. Kim, S. S. Kim, *Materials (Basel).* **2021**, *14*, 1461.

[6] G. Romano, G. Mantini, A. Di Carlo, A. D'Amico, C. Falconi, Z. L. Wang, *Nanotechnology* **2011**, *22*, DOI 10.1088/0957-4484/22/46/465401.

[7] Y. Gao, Z. L. Wang, *Nano Lett.* **2009**, *9*, 1103–1110.

[8] G. Mantini, Y. Gao, A. D'Amico, C. Falconi, Z. L. Wang, *Nano Res.* **2009**, *2*, 624–629.

[9] O. Synhaivskyi, D. Albertini, P. Gaffuri, J. M. Chauveau, V. Consonni, B. Gautier, G. Bremond, *J. Phys. Chem. C* **2021**, *125*, 15373–15383.

[10] R. Tao, M. Mouis, G. Ardila, *Adv. Electron. Mater.* **2018**, *4*, 1–9.

[11] A. J. Bard, A. B. Bocarsly, F. R. F. Fan, E. G. Walton, M. S. Wrighton, *J. Am. Chem. Soc.* **1980**, *102*, 3671–3677.

[12] Q. X. Zhao, L. L. Yang, M. Willander, B. E. Sernelius, P. O. Holtz, *J. Appl. Phys.* **2008**, *104*, DOI 10.1063/1.2991151.

[13] W.-C. Sun, Y.-C. Yeh, C.-T. Ko, J.-H. He, M.-J. Chen, *Nanoscale Res. Lett.* **2011**, *6*, 556.

[14] K. W. Liu, R. Chen, G. Z. Xing, T. Wu, H. D. Sun, *Appl. Phys. Lett.* **2010**, *96*, 1–4.

[15] C. Y. Chen, C. A. Lin, M. J. Chen, G. R. Lin, J. H. He, *Nanotechnology* **2009**, *20*, 185605.

[16] J.-P. Richters, T. Voss, L. Wischmeier, I. Rückmann, J. Gutowski, *Appl. Phys. Lett.* **2008**, *92*, DOI 10.1063/1.2829598.

[17] J.-P. Richters, T. Voss, D. S. Kim, R. Scholz, M. Zacharias, *Nanotechnology* **2008**, *19*, 305202.

[18] T. K. Sodhi, P. Chrétien, Q. C. Bui, A. Chevillard, L. Travers, M. Morassi, M. Tchernycheva, F. Houzé, N. Gogneau, *Nanoenergy Adv.* **2024**, *4*, 133–146.

[19] C. Chen, H. He, Y. Lu, K. Wu, Z. Ye, *ACS Appl. Mater. Interfaces* **2013**, *5*, 6354–6359.

[20] M. Law, L. E. Greene, A. Radenovic, T. Kuykendall, J. Liphardt, P. Yang, *J. Phys. Chem. B* **2006**, *110*, 22652–22663.

[21] Z. Chen, B. Li, X. Mo, S. Li, J. Wen, H. Lei, Z. Zhu, G. Yang, P. Gui, F. Yao, G. Fang, *Appl. Phys. Lett.* **2017**, *110*, 1–6.

[22] W. F. Gorham, *J. Polym. Sci. Part A-1 Polym. Chem.* **1966**, *4*, 3027–3039.

[23] J. Villafuerte, E. Sarigiannidou, F. Donatini, J. Kioseoglou, O. Chaix-Pluchery, J. Pernot, V. Consonni, *Nanoscale Adv.* **2022**, *4*, 1793–1807.

[24] S. Lu, Q. Liao, J. Qi, S. Liu, Y. Liu, Q. Liang, G. Zhang, Y. Zhang, *Nano Res.* **2016**, *9*, 372–379.

[25] F. Bernardini, V. Fiorentini, D. Vanderbilt, *Phys. Rev. B* **1997**, *56*, R10024–R10027.

[26] C. Noguera, F. Finocchi, J. Goniakowski, *J. Phys. Condens. Matter* **2004**, *16*, S2509–S2537.

[27] R. Cuscó, E. Alarcón-Lladó, J. Ibáñez, L. Artús, J. Jiménez, B. Wang, M. J. Callahan, *Phys. Rev. B* 2007, *75*, 165202.

[28] M. S. Mathur, N. A. Weir, *J. Mol. Struct.* 1973, *15*, 459–463.

[29] M. H. Yang, S. W. Jeong, S. J. Chang, K. H. Kim, M. Jang, C. H. Kim, N. H. Bae, G. S. Sim, T. Kang, S. J. Lee, B. G. Choi, K. G. Lee, *ACS Appl. Mater. Interfaces* 2016, *8*, 34978–34984.

[30] R. Parize, J. Garnier, O. Chaix-Pluchery, C. Verrier, E. Appert, V. Consonni, *J. Phys. Chem. C* 2016, *120*, 5242–5250.

[31] J. Villafuerte, O. Chaix-Pluchery, J. Kioseoglou, F. Donatini, E. Sarigiannidou, J. Pernot, V. Consonni, *Phys. Rev. Mater.* 2021, *5*, 1–15.

[32] J. L. Lyons, J. B. Varley, D. Steiauf, A. Janotti, C. G. Van De Walle, *J. Appl. Phys.* 2017, *122*, DOI 10.1063/1.4992128.

[33] F. Herklotz, A. Hupfer, K. M. Johansen, B. G. Svensson, S. G. Koch, E. V. Lavrov, *Phys. Rev. B - Condens. Matter Mater. Phys.* 2015, *92*, 1–10.

[34] E. V. Lavrov, J. Weber, F. Börrnert, C. G. Van de Walle, R. Helbig, *Phys. Rev. B - Condens. Matter Mater. Phys.* 2002, *66*, 1–7.

[35] E. . Lavrov, *Phys. B Condens. Matter* 2003, *340–342*, 195–200.

[36] E. V Lavrov, F. Börrnert, J. Weber, *Phys. Rev. B* 2005, *71*, 035205.

[37] K. M. Balss, G. Llanos, G. Papandreou, C. A. Maryanoff, *J. Biomed. Mater. Res. - Part A* 2008, *85*, 258–270.

[38] F. Decremps, J. Pellicer-Porres, A. M. Saitta, J.-C. Chervin, A. Polian, *Phys. Rev. B* 2002, *65*, 092101.

[39] X. Zhang, Characterization and Structuration of Piezoelectric ZnO-Based Composites : Toward Medical Applications, 2022.

[40] K. Nadaud, F. Morini, A. S. Dahiya, C. Justeau, S. Boubenia, K. P. Rajeev, D. Alquier, G. Poulin-Vittrant, *Appl. Phys. Lett.* 2018, *112*, 1–6.

[41] C. Wan, C. R. Bowen, *J. Mater. Chem. A* 2017, *5*, 3091–3128.

[42] R. Yang, Y. Qin, L. Dai, Z. L. Wang, *Nat. Nanotechnol.* 2009, *4*, 34–39.

[43] K. Il Park, S. Bin Bae, S. H. Yang, H. I. Lee, K. Lee, S. J. Lee, *Nanoscale* 2014, *6*, 8962–8968.

[44] R. Hinchet, S. Lee, G. Ardila, L. Montes, M. Mouis, Z. L. Wang, *Proc. PowerMEMS* 2013, *7*, 4.

[45] R. Tao, M. Parmar, G. Ardila, P. Oliveira, D. Marques, L. Montès, M. Mouis, *Semicond. Sci. Technol.* 2017, *32*, DOI 10.1088/1361-6641/aa691f.

[46] S. Guillemin, V. Consonni, E. Appert, E. Puyoo, L. Rapenne, H. Roussel, *J. Phys. Chem. C* 2012, *116*, 25106–25111.

[47] N. E. Richey, C. De Paula, S. F. Bent, *J. Chem. Phys.* 2020, *152*, DOI 10.1063/1.5133390.

[48] T. Cossuet, H. Roussel, J. M. Chauveau, O. Chaix-Pluchery, J. L. Thomassin, E. Appert, V. Consonni, *Nanotechnology* 2018, *29*, 475601.

[49] C. Pashartis, M. J. van Setten, M. Houssa, G. Pourtois, *Comput. Mater. Sci.* 2024, *242*, 113042.

[50] S. Davis, G. Gutiérrez, *J. Phys. Condens. Matter* 2011, *23*, DOI 10.1088/0953-8984/23/49/495401.

[51] R. Raghavan, M. Bechelany, M. Parlinska, D. Frey, W. M. Mook, A. Beyer, J. Michler, I. Utke, *Appl. Phys. Lett.* 2012, *100*, DOI 10.1063/1.4711767.

[52] F. J. Manjón, B. Marí, J. Serrano, A. H. Romero, *J. Appl. Phys.* 2005, *97*, DOI 10.1063/1.1856222.

[53] C. Bundesmann, N. Ashkenov, M. Schubert, D. Spemann, T. Butz, E. M. Kaidashev, M. Lorenz, M. Grundmann, *Appl. Phys. Lett.* **2003**, *83*, 1974–1976.

[54] A. Momot, M. N. Amini, G. Reekmans, D. Lamoen, B. Partoens, D. R. Slocombe, K. Elen, P. Adriaensens, A. Hardy, M. K. Van Bael, *Phys. Chem. Chem. Phys.* **2017**, *19*, 27866–27877.

[55] P. Sundara Venkatesh, V. Ramakrishnan, K. Jeganathan, *Phys. B Condens. Matter* **2016**, *481*, 204–208.

[56] J. Serrano, A. H. Romero, F. J. Manjón, R. Lauck, M. Cardona, A. Rubio, *Phys. Rev. B - Condens. Matter Mater. Phys.* **2004**, *69*, 1–14.

[57] S. Sahoo, G. L. Sharma, R. S. Katiyar, *J. Raman Spectrosc.* **2012**, *43*, 72–75.

[58] A. Teke, Ü. Özgür, S. Doğan, X. Gu, H. Morkoç, B. Nemeth, J. Nause, H. O. Everitt, *Phys. Rev. B - Condens. Matter Mater. Phys.* **2004**, *70*, 1–10.

[59] J. F. Rommeluère, L. Svob, F. Jomard, J. Mimila-Arroyo, A. Lusson, V. Sallet, Y. Marfaing, *Appl. Phys. Lett.* **2003**, *83*, 287–289.

[60] D. Pfisterer, J. Sann, D. M. Hofmann, M. Plana, A. Neumann, M. Lerch, B. K. Meyer, *Phys. Status Solidi Basic Res.* **2006**, *243*, 2–4.

[61] J. W. Sun, Y. M. Lu, Y. C. Liu, D. Z. Shen, Z. Z. Zhang, B. Yao, B. H. Li, J. Y. Zhang, D. X. Zhao, X. W. Fan, *J. Appl. Phys.* **2007**, *102*, DOI 10.1063/1.2772581.

[62] J. G. Reynolds, C. L. Reynolds, A. Mohanta, J. F. Muth, J. E. Rowe, H. O. Everitt, D. E. Aspnes, *Appl. Phys. Lett.* **2013**, *102*, DOI 10.1063/1.4802753.

[63] D. C. Look, D. C. Reynolds, C. W. Litton, R. L. Jones, D. B. Eason, G. Cantwell, *Appl. Phys. Lett.* **2002**, *81*, 1830–1832.

[64] B. K. Meyer, H. Alves, D. M. Hofmann, W. Kriegseis, D. Forster, F. Bertram, J. Christen, A. Hoffmann, M. Straßburg, M. Dworzak, U. Haboeck, A. V. Rodina, *Phys. Status Solidi Basic Res.* **2004**, *241*, 231–260.

[65] J. P. Richters, T. Voss, D. S. Kim, R. Scholz, M. Zacharias, *Nanotechnology* **2008**, *19*, DOI 10.1088/0957-4484/19/30/305202.

[66] Y. G. Wang, S. P. Lau, X. H. Zhang, H. H. Hng, H. W. Lee, S. F. Yu, B. K. Tay, *J. Cryst. Growth* **2003**, *259*, 335–342.

[67] J. Villafuerte, F. Donatini, J. Kioseoglou, E. Sarigiannidou, O. Chaix-Pluchery, J. Pernot, V. Consonni, *J. Phys. Chem. C* **2020**, *124*, 16652–16662.

[68] Ü. Özgür, Y. I. Alivov, C. Liu, A. Teke, M. A. Reshchikov, S. Doğan, V. Avrutin, S.-J. Cho, H. Morkoç, *J. Appl. Phys.* **2005**, *98*, 1–103.

[69] H. Xue, N. Pan, M. Li, Y. Wu, X. Wang, J. G. Hou, *Nanotechnology* **2010**, *21*, 215701.

[70] J. E. Jaffe, J. A. Snyder, Z. Lin, A. C. Hess, *Phys. Rev. B* **2000**, *62*, 1660–1665.

[71] L. Schmidt-Mende, J. L. MacManus-Driscoll, *Mater. Today* **2007**, *10*, 40–48.

[72] A. J. Lopez Garcia, R. Tao, M. Mouis, G. Ardila, *21st Int. Conf. Solid-State Sensors, Actuators Microsystems, TRANSDUCERS 2021* **2021**, 1056–1059.

[73] D. Hu, M. Yao, Y. Fan, C. Ma, M. Fan, M. Liu, *Nano Energy* **2019**, *55*, 288–304.

The page was intentionally left blank.

The page was intentionally left blank.

Chapter IV – Synthesis of ZnO nanowires on Au and AZO seed layers for piezoelectric applications

Content

IV.1 State-of-the-art: electrical interface and morphology of ZnO nanowires for piezoelectric nanogenerators 177
IV.1.1 Electrical interface between piezoelectric nanogenerator electrodes and ZnO nanowires 177
IV.1.2 Impact of the ZnO nanowire morphology on piezoelectric nanogenerator performance .. 179
IV.2 Effect of AZO seed layers on the morphological properties of ZnO nanowires for piezoelectric applications 182
IV.2.1 Morphological, structural, and optical properties of AZO layers grown by sputtering process 183
IV.2.1.1 Morphological properties 183
IV.2.1.2 Optical properties 184
IV.2.1.3 Electrical properties 186
IV.2.2 Morphological properties of ZnO nanowires grown spontaneously on 200 nm-thick AZO layers 189
IV.2.3 Selective Area Growth of ZnO NWs on patterned AZO layers 191
IV.3 Effect of Au seed layers on the morphological and structural properties of ZnO nanowires for piezoelectric applications 196
IV.3.1 Structural and morphological properties of Au layers grown by vacuum evaporation 197
IV.3.2 Structural and morphological properties of ZnO nanowires grown on Au layers 198
IV.3.2.1 FESEM Images and XRD 199
IV.3.2.2 X-ray Pole Figure 200
IV.3.3 Output voltage of a PNG based on ZnO NWs grown on Au layer 202
IV.4 Conclusion 205
Bibliography 206
IV.5 Supporting information 208
IV.5.1 XRD pattern of annealed 200 nm-thick AZO layer annealed in an O_2 atmosphere at different temperatures 208
IV.5.2 XRD pattern of ZnO nanowires grown on 200 nm-thick AZO layers 208
IV.5.3 Morphology of ZnO NWs grown on annealed 200 nm-thick AZO layers 209

The present chapter explores the influence of Gold and Aluminum-doped ZnO seed layers on the morphological properties of ZnO NWs for their integration into PNGs. In **Chapter II**, Au layers were used solely as the bottom and top electrodes of a PNG. Here, the Au film is expected to play a dual role, acting as both nucleation layer for ZnO NWs and the bottom electrode of a PNG. Furthermore, the chapter examines the potential use of Aluminum-doped ZnO layers for piezoelectric applications, which should play the same role as the Au-layers, opening perspectives for the development of transparent PNGs.

IV.1 State-of-the-art: electrical interface and morphology of ZnO nanowires for piezoelectric nanogenerators

IV.1.1 Electrical interface between piezoelectric nanogenerator electrodes and ZnO nanowires

In solid-state device physics, the electrical interfaces between semiconductors, metals, and dielectrics have been largely discussed, identifying four electrical contacts: p-n junctions, Schottky barriers, Ohmic contacts, or capacitive barriers, based on material properties. This thesis focuses on PNGs based on unintentionally n-doped ZnO NWs integrated between two metallic electrodes, hence three potential electrical contacts can form within the device: Ohmic, Schottky, or capacitive. It should be mentioned that the p-n junctions, formed at the interface between p-type materials and n-doped ZnO NWs, are not explored in this thesis, as no p-type materials are integrated into our PNGs. In addition, ZnO NWs-based PNGs typically use capacitive contacts to prevent electron flow between the metallic top electrode and the ZnO NWs by placing a dielectric such as PMMA,[1,2] PDMS,[3] and parylene-C,[4] discussed in **Section III.2**. This section will focus only on Ohmic contacts and Schottky barriers.

When a semiconductor contacts a metal, the system reaches thermodynamic equilibrium by aligning the Fermi levels of both materials in the absence of any applied external bias. This alignment leads to the bending of the conduction and valence band of the semiconductor at the interface with the metal, forming either an Ohmic contact or a Schottky barrier based on the work functions (ϕ) of the two materials.

The Ohmic contact is created when the work function of the metal is lower than that of the semiconductor ($\phi^M < \phi^{SC}$), causing electrons to flow from the metal into the semiconductor, creating an electron accumulation layer. This results in a downward bending of the conduction and valence band of the semiconductor, which facilitates the flow of external electrons into its structure, as illustrated in **Figure IV.1-1(a)**. Ohmic contacts have been reported at the interface between ZnO and metals such as Al, Ti, and In.[5] It is important to note that highly n-doped semiconductors behave as metals if their free carrier density exceeds the Mott transition, about 4.2×10^{18} cm^{-3} for ZnO NWs.[6] As discussed before, ZnO NWs grown by CBD have free carrier density ranging from 5×10^{17} to 1.1×10^{19} cm^{-3},[7–9] which would lead to Ohmic contact with highly n-doped semiconductors such as Indium Tin Oxide

(ITO),[10] and Aluminium-doped ZnO (AZO). However, this electrical contact could reduce the PNG performance due to the easy external electron migration contributing to screening effects.

The Schottky barrier forms when $\phi^M > \phi^{SC}$, resulting in the upward bending of the conduction and valence band of the semiconductor that prevents the flow of electrons from the metal to the semiconductor, as shown in **Figure IV.1-1(b)**. This barrier can occur between ZnO and metals such as Pd, Pt, Au, and Au, with barrier heights ranging from 0.54 to 0.80 eV.[11] Nevertheless, the presence of interface defects in ZnO introduces localized states in its band gap, increasing the tunneling probability for carriers through the Schottky barrier, and reducing its effectiveness.[5] Schottky barriers are ideal for PNG as they prevent screening effects by avoiding the flow of external electrons into the device. For instance, previous work has reported that a PNG incorporating ZnO NWs on an Au seed layer with a Schottky barrier top electrode produced twice the output voltage compared to a PNG with ZnO NWs on a ZnO seed layer under the same electrode configuration.[12] In this thesis, a Schottky barrier with a height of 0.37 to 0.44 eV could be expected at the interface between CBD-grown ZnO NWs and Au layers,[13] which is promising for the fabrication of our PNGs.

Finally, previous work compared the performance of PNGs using AZO or Au films as nucleation layers for ZnO NWs and the bottom electrode of the device.[4] The PNG with the Au layer generated a low voltage (under 4 mV) due to short-circuiting, indicating the challenging fabrication of such a device. In contrast, the PNG with the AZO layer generated a higher voltage of 36 mV, showing the feasibility of using AZO as both the seed layer and bottom electrode in PNG fabrication. These findings highlighted the need for more research to explore the potential of each material.

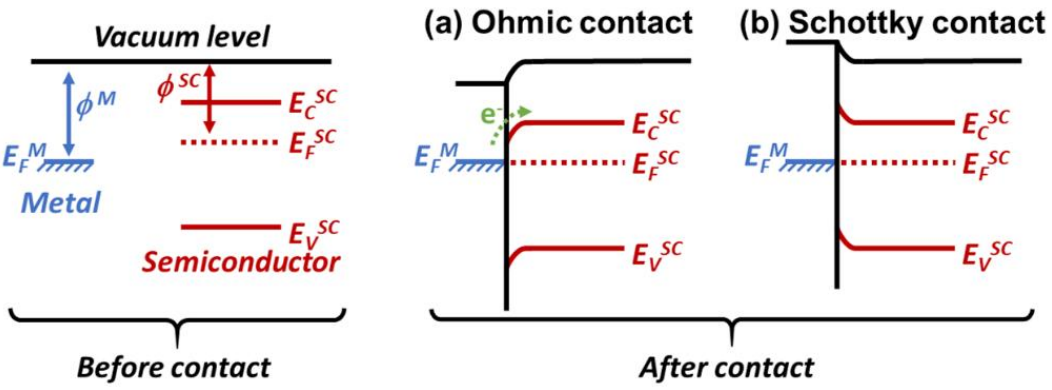

***Figure IV.1-1**. Band diagrams of a n-type semiconductor and a metal before and after contact forming an **(a)** Ohmic and **(b)** Schottky contact by aligning their Fermi levels (E_F).*

IV.1.2 Impact of the ZnO nanowire morphology on piezoelectric nanogenerator performance

The performance of a PNG can be improved by tuning the morphological properties of the integrated ZnO NWs, notably their diameter, length, and density.

Research has shown that reducing the diameter of ZnO NWs increases surface Fermi level pinning (SFLP) effects, which enhance their piezoelectric properties,[14] as discussed in **Section III.1.2**. This SFLP phenomenon is due to surface defects in the NWs, which creates a depletion layer of electrons at the NW surface and reduces screening effects. Therefore, SFLP effects depend on the diameter and free electron density of ZnO NWs, affecting the performance of PNGs. According to FEM simulations, ZnO NWs grown by CBD exhibit enhanced piezoresponses based on their radius, free carrier density, and polarity, as shown in **Figure IV.1-2(a-b)**.[15] For O-polar ZnO NWs, the radius should be lower than 55 nm and 15 nm for low (5×10^{17} cm^{-3}) and high (5×10^{18} cm^{-3}) free carrier density, respectively. In contrast, Zn-polar ZnO NWs exhibit a narrow window for enhancing their piezoresponse, whose radius should be lower than 18 nm and 12 nm for, respectively, low (5×10^{18} cm^{-3}) and high (1×10^{19} cm^{-3}) free carrier density.

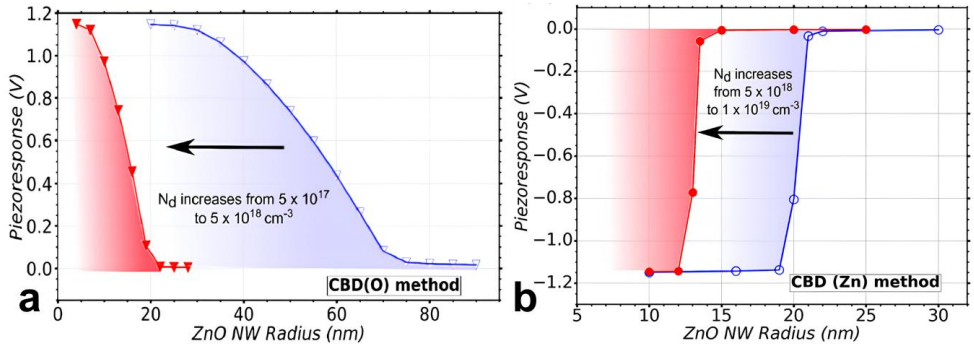

Figure IV.1-2. *Piezoresponse of a PNG as a function of the radius of vertically integrated ZnO NWs grown by CBD presenting* ***(a)*** *Oxygen- and* ***(b)*** *Zinc-polarity with different doping levels. Adapted from REF [15].*

The piezoresponse of a PNG based on O-polar ZnO NWs grown by CBD was found to increase linearly with the NW length up to 3 µm, after which it reach saturation, according to FEM simulations shown in **Figure IV.1-3**.[15] This initial linear increase is due to the generation of more electrical dipoles in longer NWs, a direct result of the piezoelectric effect, which enhances the piezoresponse of the PNG.[14,15] However, beyond a certain length, the efficiency of strain transfer within the NWs decreases. Since the NWs are coated with a polymer layer in the PNG, increasing their length also increases the thickness of the polymer layer, which

absorbs more of the mechanical stress applied to the PNG. This absorption reduces the effective strain transferred to the NWs, leading to a plateau in piezoresponse. Therefore, NWs longer than 3 µm would not improve the PNG performance, as mechanical factors limit their energy conversion efficiency.[16]

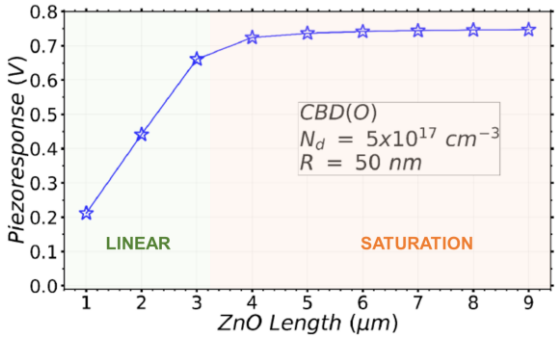

***Figure IV.1-3**. Piezoresponse of a PNG as a function of the length of O-polar ZnO NWs grown by CBD. Adapted from REF [15].*

The density of ZnO NWs also affects the electrical properties of a PNG, as shown in **Figure IV.1-4**. According to FEM simulations using various materials and densities of NWs in a PNG (**Figure IV.1-4(a)**) reveal that low NW density enhances the storage of mechanical energy in the device (**Figure IV.1-4(b)**). In contrast, high NW density improves the electrical potential (**Figure IV.1-4(c)**) and power density (**Figure IV.1-4(d)**) generated by the PNG. Thus, an optimal number density between 64 and 81 NW/µm^2, respectively corresponding to a D/W ratio of 0.4 and 0.45, should maximize the electrical energy storage of the PNG.[16,17] A different work, conversely, concluded that the optimal ZnO NW density is 25 NW/µm^2 for improving the output voltage of a device, according to FEM simulations.[2]

It is also important to mention that the vertical alignment of ZnO NWs influences the piezoelectric response of a PNG. Indeed, when NWs are in contact to each other, screening effects can occur, particularly in cases of high NW density or when the NWs are tilted. FEM simulations suggest that to prevent significant degradation of the PNG performance, the inclination angle of NWs should remain below 5° relative to the normal of the substrate where they were grown.[18] For ZnO NWs grown by CBD, their vertical alignment is strongly influenced by the properties of the nucleation layers.[19,20] A more detailed discussion of this topic will be provided in **Section IV.2**.

In summary, the previously presented works highlight a direct effect of the NW morphology on the performance of a PNG, where longer and thinner NWs with a correct density are strongly suitable.

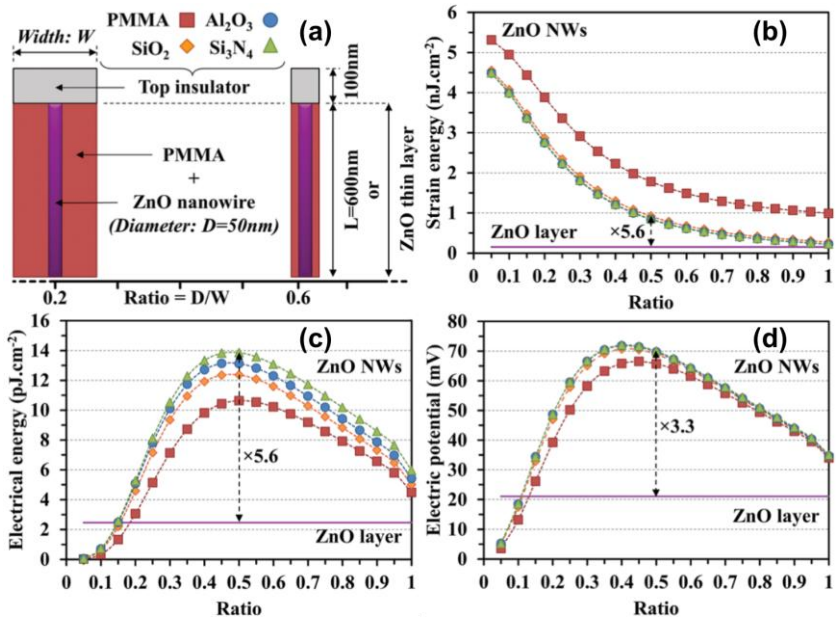

***Figure IV.1-4**. **(a)** Schematic of a PNG structure based on different top dielectric layers and NW densities. **(b)** Mechanical energy, **(c)** electrical potential, and **(d)** electrical energy of such PNG structures. Adapted from REF [16].*

Objectives

In **Chapters II and III**, PNGs were fabricated using two distinct bottom electrode structures: either i) Si substrate/Ti/Au/ZnO seed layer stack, or a simpler structure with a ii) highly n-doped Si substrate coated with a ZnO seed layer. However, in this work, dip-coated ZnO seed layers need long annealing at high temperature and have poor conductivity. Thus, alternative methods should be explored for fabricating efficient and low-cost bottom electrodes for PNGs. These electrodes should also allow controlling the morphology of ZnO NWs. This chapter explores the integration of ZnO NWs on two distinct nucleation layers, aiming to create different electrical interfaces between ZnO NWs and the bottom electrode of a PNG. The objectives are as follows:

1- To develop a more transparent Aluminum-doped Zinc Oxide (AZO) layer with low electrical resistance, and to tune the morphological properties of ZnO NWs grown on this layer by varying the chemical bath conditions or using the Selective Area Growth (SAG) method. The AZO layer should serve as bottom electrode of a PNG, where an Ohmic contact is expected at the interface with the NWs.

2- To synthesize ZnO NWs with optimal morphological properties for piezoelectric applications using an Au-nucleation layer. This layer should also function as the bottom electrode of a PNG, where a Schottky barrier is expected at the interface with the NWs.

IV.2 Effect of AZO seed layers on the morphological properties of ZnO nanowires for piezoelectric applications

State-of-the-art

AZO is a non-toxic, transparent, and conductive material composed of low-cost and abundant elements.[21] This material exhibits low electrical resistivity and high optical transmittance in the visible and infrared regions, which is ideal for enhancing the efficiency of solar cell devices.[22–24] Its crystallographic structure is compatible with growing ZnO NWs by hydrothermal method, positioning AZO as suitable material for both a nucleation layer for ZnO NWs and a bottom electrode in PNG, offering interesting properties.[4] AZO layers allow also thermal annealing of ZnO NWs at temperatures up to 800°C, which enhances their piezoelectric properties. In addition, AZO layers are expected to provide better electrical contact with ZnO NWs than highly n-doped Si substrates in PNGs. Furthermore, the transparency of AZO layers favors the development of transparent PNGs, opening up a wide range of potential applications.

In this context, it is crucial to control both the electrical and optical properties of AZO layers, as well as the morphology of ZnO NWs grown on them. The conductivity and transparency of AZO layers can be adjusted by manipulating deposition parameters such as the aluminum or oxygen concentration,[22,25,26] substrate temperature,[22,27,28] layer thickness,[23,26] and deposition pulse frequency.[29] Moreover, the morphology of ZnO NWs grown by CBD depends on the structural properties of AZO layers and the chemical bath conditions.[24,30,31] Sekar et al. investigated the effect of precursor concentration and growing time on the morphology of ZnO NWs grown by hydrothermal method on AZO layers for solar cell applications.[24] They found that longer growing time and equimolar concentration in $Zn(NO_3)_2$ and HMTA in the solution leads to ZnO NWs with higher aspect ratios and relatively high density, features that are favorable for piezoelectric applications.

Therefore, this study investigates the morphological, structural, optical, and electrical properties of AZO films grown by Physical Vapor Deposition (PVD) and their influence on the morphological properties of ZnO NWs grown by CBD.

IV.2.1 Morphological, structural, and optical properties of AZO layers grown by sputtering process

AZO layers were grown by the sputtering PVD method with thicknesses of 100, 200, 300, and 400 nm on Glass substrates in the equipment CT200 from Alliance Concept. A 200 nm-thick AZO layer was also grown on Si substrate as a reference.♣ Subsequently, AZO layers are thermally annealed in a controlled O_2 atmosphere for 1 h at 100, 200, 300, and 400 °C.

IV.2.1.1 Morphological properties

The top-view FESEM images of AZO layers grown on glass substrates are shown in **Figure IV.2-1(a)**. These continuous layers exhibit a steady increase in grain size, whose values are found to be 20.2 ± 4.7, 27.4 ± 6.2, 33.1 ± 9.4, and 41.6 ± 6.1 nm according to the AZO thickness incrementing from 100 to 400 nm. Then, according to AFM images presented in **Figure IV.2-1(b)**, AZO layers reveal relatively smooth surfaces, with roughness values of 1.76, 3.63, 3.7, and 3.52 nm for 100, 200, 300, and 400 nm thickness, respectively. Given that AFM measurements were done in tapping mode with a 20-nm diameter contact tip, the smoothest surface highlighted in the 100-nm thick AZO layer could be influenced by the resolution of the experimental setup, since its grain size shares an identical magnitude that the contact tip dimension. It is worth mentioning that after thermal treatment at 100, 200, 300, and 400 °C in an O_2 atmosphere, the AZO layers appear not exhibit several morphological changes.

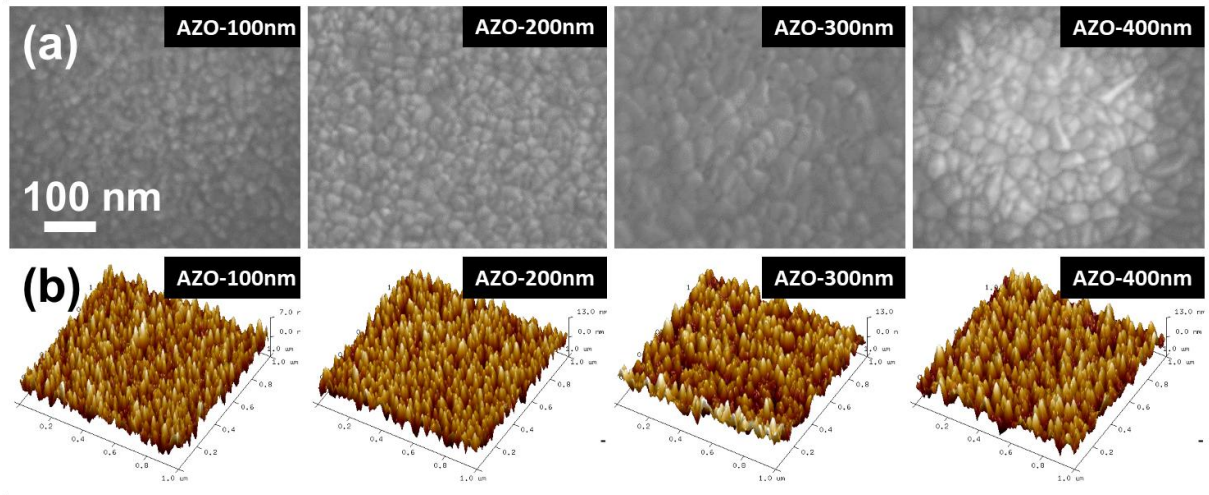

Figure IV.2-1. (a) *Top-view FESEM images and* ***(b)*** *AFM images of AZO layers grown by sputtering PVD on glass substrates with thicknesses of 100, 200, 300, and 400 nm.*

♣ The depositions by PVD were done by FARJOT Thierry and PERRIN Fabrice from DRT/LETI/DPFT/SDEP/LDE2 - CEA

IV.2.1.2 Optical properties

Transmittance measurements of AZO layers in the wavelength range of 200 – 800 nm were performed with a PerkinElmer Lambda 950 UV-vis-NIR spectrophotometer equipped with an integrating sphere. The transmittance of the air, fused quartz, and glass substrate was also measured as references. The optical transmittance spectra of AZO films with different thicknesses are present in **Figure IV.2-2(a)**, and their mean transmittance over the wavelength range of 400 to 800 nm is summarized in **Figure IV.2-2(c)**. The transmittance steadily decreases from around 85% to 82% as the thickness of the as-grown AZO layers is increased from 100 to 400 nm. Fluctuations in the transmittance spectra are also observed, which are more pronounced in thicker AZO layers. These "optical transmittance oscillations" could involve interference effects between the top and the bottom surfaces of the films, as well as the contribution of the surface roughness.[32,33] Interestingly, a change in the near transmittance edge is noticed according to the thickness of the AZO layers, suggesting a modification of their optical bandgap. Therefore, the optical bandgap energy was also determined from transmittance spectra using the Tauc plot approach. For this, the absorption coefficient (α) was estimated following the Beer-Lambert law given as:[34]

$$\alpha = \frac{1}{d}\ln\left(\frac{1 - R_{AZO}}{T_{AZO}}\right)$$

where d, R_{AZO}, and T_{AZO} are the thickness, reflectance, and transmittance of the AZO layer, respectively. In the present study, (1 - R_{AZO}) was approximated as 1, and T_{AZO} was calculated using:

$$T_{AZO} = \frac{T_S}{T_E \times T_G}$$

where T_S, T_E, and T_G are the transmittance of the sample (AZO layer on glass substrate), air, and glass substrate, respectively. The optical bandgap was finally extracted from the intercept of the linear region of the $(\alpha h\upsilon)^2$ vs $(h\upsilon)$ graph with the $(h\upsilon)$-axis.[35] Thus, the bandgaps for as-grown AZO layers with thicknesses of 100, 200, 300, and 400 nm were found to be 3.483, 3.605, 3.585, and 3.583 eV, respectively, which are consistent with values reported of 3.41 – 3.69 eV in sputter-grown AZO layers.[36] After thermal annealing in an O_2 atmosphere at temperatures of 100, 200, 300, and 400°C for 1h, several changes are observed in the transmittance spectra of the 200 nm-thick AZO layer, as shown in **Figure IV.2-2(b)**. Transmittance slightly increases from 84% to 86% as the annealing temperature rises to 200°C,

but then decreases to 85% when the annealing temperature exceeds 200 °C. The optical bandgap of the 200 nm-thick AZO film follows a similar trend: it increases from 3.605 to 3.728 eV as the annealing temperature reaches 200 °C, and then steadily decreases to 3.356 eV at 400 °C. It is important to mention that the other AZO layers exhibit similar behavior as a function of the annealing temperature. The increment in optical bandgap can be attributed to the Burstein-Moss phenomenon, where a high density of carriers fills the lower energy states in the conduction band of the semiconductor, leading to transitions with higher energy between the valence band and the first unfilled energy state of the conduction band.[37] In contrast, the decrease in optical bandgap could originate from non-active states that appear with thermal annealing, leading to optical transitions with lower energies. In addition, bandgap renormalization can also account for the decrease in optical bandgap energy. This phenomenon occurs when a high density of free carriers reduces electrostatic interactions between electrons and holes, altering their energy states and consequently lowering the bandgap energy.[38] It should be mentioned that the density of free carriers in AZO layers can increase when Al atoms substitutes for Zn sites, forming shallow Al_{Zn} donor defects, whose process can be favored by increasing the Al concentration in the layer or by thermal annealing in oxygen-rich conditions.[25,39] Moreover, the total transmittance of pristine and annealed AZO layers in the visible region was calculated as the total area below the transmittance spectra, summarized in **Figure IV.2-2(d)**. As expected, a decrease in total transmittance in the visible region occurs as the AZO film thickness increases. Interestingly, thermal annealing enhances the transmittance of AZO layers, which reach their highest transparency after annealing at 200 °C. The improved transmittance could be associated with a good crystallinity of the layers, as suggested by XRD spectra shown in **Supporting Information IV.5.1**, where an increase in intensity of the (002)-ZnO diffraction peak and the narrowing of its FWHM is noticed with thermal annealing. Thus, due to the interesting optical properties of AZO layers annealed at 200 °C, further electrical characterizations are performed on these layers.

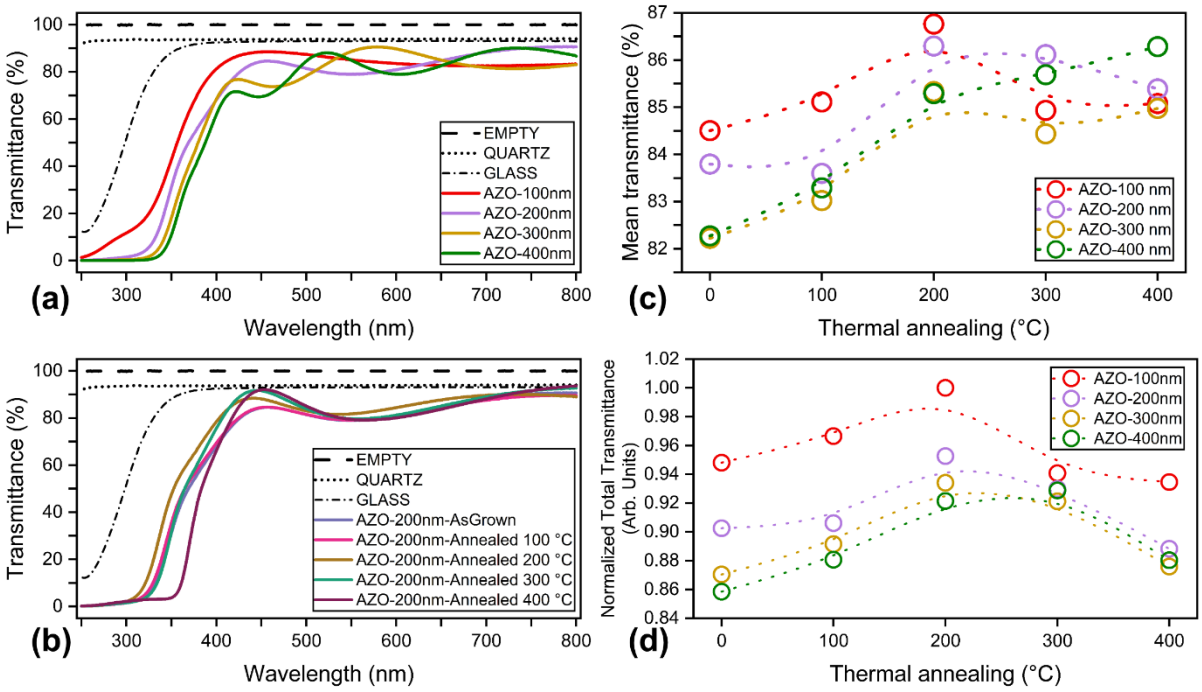

Figure IV.2-2. (a) *Transmittance spectra of AZO layers grown by sputtering PVD on glass substrates with different thicknesses.* ***(b)*** *Transmittance spectra of the 200 nm-thick AZO layer after thermal annealing in an O_2 atmosphere at different temperatures.* ***(c)*** *Mean and* ***(d)*** *total transmittance of AZO layers with different thicknesses as a function of the annealing temperature in an O_2 atmosphere.*

IV.2.1.3 Electrical properties

The electrical resistance of the pristine and 200 °C-annealed AZO layers was assessed through Transmission Line Method (TLM) measurements, whose structure is schematized in **Figure IV.2-3(a)**.[40] This TLM method consists of performing *I-V* measurements between adjacent metallic electrodes of width "*W*" and length "*a*" separated at different distances "L_i". The resistance "R_T" is determined from the slope of each *I-V* measurement, and plotted as a function of the distance electrode. From this curve, the contact resistance "R_C" and the sheet resistance "R_{SH}" are deduced from the intersection with the vertical axis and the slope, respectively.

Seven metallic contacts of width of 195.8 µm and length of 94.9 µm with varying spacing ranging from 15.9 µm to 55.8 µm were achieved on the AZO layers through a photolithographic process, as shown in **Figure IV.2-3(b)**.[♣] The electrical characterizations were performed with a Keithley 4200A-SCS parametric analyzer, where the voltage between adjacent electrodes was measured as a function of the current applied from -10 mA to 10 mA

[♣] The electrodes on AZO films for TLM were prepared through photolithographic process by Riadh BEN ABBES - LTM

by a step of 2 mA, resulting in the *I-V* curves shown in **Figure IV.2-3(c)**. From the slope of these linear *I-V* curves, the resistance R_T is calculated as a function of the electrode distance for each sample, whose values are reported in **Figure IV.2-3(d)**. As expected, R_T linearly evolves with the increment of the electrode spacing. Then, by multiplying the slope of these curves with the electrode width of 195.8 µm, the sheet resistance R_{SH} of the AZO layers is calculated, as summarized in **Table IV.2-1**.

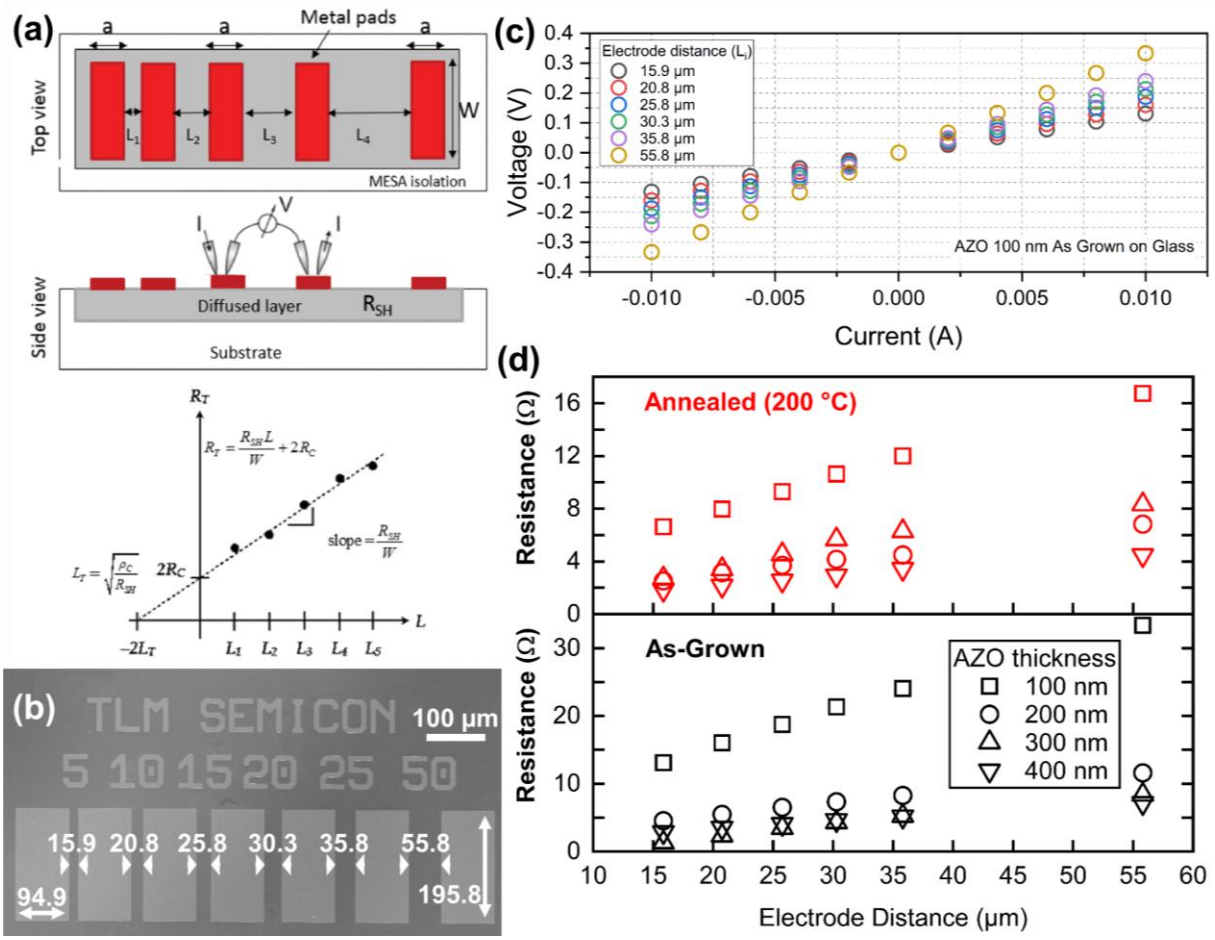

Figure IV.2-3. (a) *Schematic of TLM measurements on thin films. Adapted from REF [40].* ***(b)*** *Top view FESEM image of a prepared sample for TLM electrical characterizations.* ***(c)*** *I-V curves of the pristine 100 nm-thick AZO layer according to the electrode distance.* ***(d)*** *R_T values from I-V curves as a function of the distance electrode of pristine and annealed AZO layers.*

The resistivity of AZO layers was further calculated by multiplying the R_{SH} with the thickness of the film. Thus, a decrease in resistivity is noticed after thermal annealing at 200 °C in the AZO layers, regardless of their thickness, as shown in **Table IV.2-1**. It should be noted that the 200 nm-thick AZO layer exhibits the lowest resistivity before and after annealing, suggesting that this layer could have the best crystallinity compared to the other AZO films. Indeed, it has been reported an enhancement of the carrier mobility through the improvement of the AZO layer crystallinity by increasing the thickness and the deposition

temperature, leading to reduced resistivity.[27,36] However, when Al atoms segregate into the grain boundaries during the improvement in crystallinity of the film, a decrease in conductivity occurs, increasing the resistivity.[27] Consequently, 200 nm-thick AZO layers annealed at 200 °C possess interesting optical and electrical properties as bottom electrodes in a transparent PNG.

For comparison reasons, a figure-of-merit (FoM) involving the visible light transmittance (T_S) and the sheet resistance (R_{SH}) of AZO layers was used to quantitatively evaluate their performance. The FoM was calculated according to the equation:[25]

$$FoM = \frac{{T_S}^{10}}{R_{SH}}$$

Therefore, the as-grown AZO layers in this study exhibit a high FoM, which is further enhanced with thermal annealing at 200 °C, as depicted in **Table IV.2-1**. These values are comparable to those for AZO layers with thicknesses between 305 and 484 nm, deposited by DC magnetron sputtering at pulse frequencies ranging from 50 to 100 kHz, which have a FoM between (4 – 19.9) × 10^{-3} Ω^{-1}.[29] In addition, our FoM values are slightly higher than those of AZO layers grown by ALD with thicknesses between 176 and 187 nm, whose FoM values lies in the range of (0.41 – 6.40) × 10^{-3} Ω^{-1}.[25]

Table IV.2-1. *Resistivity, sheet resistance, mean optical transmittance, and figure-of-merit values of AZO layers grown by sputtering PVD on glass substrates with different thicknesses.*

	Resistivity (10^{-4} Ω.cm)		**R_{SH} (Ω/□)**		**Transmittance (%)**		**FoM (10^{-3} Ω^{-1})**	
Thickness (nm)	As-Grown	Annealed 200 °C	As-Grown	Annealed 200 °C	As-Grown	Annealed 200 °C	As-Grown	Annealed 200 °C
100	9.86	4.94	98,55	49,43	84,50	86,76	1,88	4,89
200	6.88	4.12	34,39	20,59	83,79	86,30	4,96	11,12
300	10.29	8.33	34,32	27,78	82,22	85,33	4,11	7,37
400	8.34	5.24	20,85	13,12	82,27	85,29	6,81	15,52

In conclusion, 200 nm-thick AZO layers exhibit optimal performance as a transparent conductive material, which can be enhanced with a thermal annealing at relatively low temperature of 200 °C. Thus, in the following sections, the synthesis of ZnO NWs by CBD will be performed on pristine 200 nm-thick AZO layers.

IV.2.2 Morphological properties of ZnO nanowires grown spontaneously on 200 nm-thick AZO layers

Having shown interesting electrical and optical properties, pristine 200 nm-thick AZO layers are used as nucleation layers to synthesize ZnO NWs via CBD to explore the most interesting morphological properties for piezoelectric applications. Thus, ZnO NWs were grown in different solutions in equimolar concentrations of $Zn(NO_3)_2$ and HMTA along with ammonia as an additive, as detailed in **Table IV.2-2**.

***Table IV.2-2**. Precursor concentrations used for the CBD of ZnO NWs on 200 nm-thick AZO layers.*

$[Zn(NO_3)_2]=[HMTA]_{bath}$ (mM)	$[NH_3]$ added (mM)	Growth Temperature	Growth time
10 30 50	0	90 °C	1 h 30 min
10 30 50	600		

ZnO NWs grew vertically to the substrate, indicating preferential nucleation on the grains oriented along the *c*-axis of AZO layers, as observed on ZnO seed layers.[19] The morphological properties of ZnO NWs grown with different chemical bath conditions are shown in **Figure IV.2-4(a-f)**. In the absence of ammonia in the chemical bath, i.e. low pH region, the NWs exhibit flat hexagonal top faces with regular diameters (**Figure IV.2-4(a-c)**). In contrast, when ammonia is added to the solution, i.e. high pH region, the NWs display tapered top faces (**Figure IV.2-4(d-f)**), resulting from the highest growth rate along the *c*-axis, as well as erosion processes on the top polar faces of ZnO NWs induced by OH^- ions.[41] From FESEM images, the resulting mean diameter at half of the height of the NWs, mean length, aspect ratio, and number density of the ZnO NWs grown with different concentrations of $Zn(NO_3)_2$ in a low and high pH region are measured and summarized in **Figure IV.2-4(g-h)**, respectively. The NWs grown in a low-pH region exhibit an increase in diameter from 45 to 57 nm and length from 0.2 to 0.8 µm as the concentration of $Zn(NO_3)_2$ is increased in the bath from 10 to 50 mM. Their corresponding aspect ratio follows the same tendency as a function of the $Zn(NO_3)_2$ concentration, whose values increment from 3.5 to 13.2. Surprisingly, the number density of ZnO NWs grown on the AZO layer, which decreases from 651.7 to 386.0 NW/µm^2, exceeds the typical values of ZnO NWs grown on ZnO seed layers ranging between 120 – 40

NW/µm^2. This strongly suggests that AZO layers grown by PVD offer higher nucleation sites than ZnO layers grown by a dip-coating process. An identical trend of morphological properties is observed in ZnO NWs grown in a high-pH region as a function of the bath concentration in $Zn(NO_3)_2$. The diameter, length, and aspect ratio increment as the $Zn(NO_3)_2$ is increased, whose values vary between 91 – 96 nm, 2.2 – 3.3 µm, and 24.3 – 27.1, respectively. The number density, in contrast, severely decreases with the addition of ammonia in the bath, whose values lie between 183.1 and 137.5 NW/µm^2. It is worth mentioning that the increase in length of ZnO NWs enhances the (002)-ZnO XRD peak, as shown in **Supporting Information IV.5.2**, which could suggest an enhancement of the related piezoelectric properties.

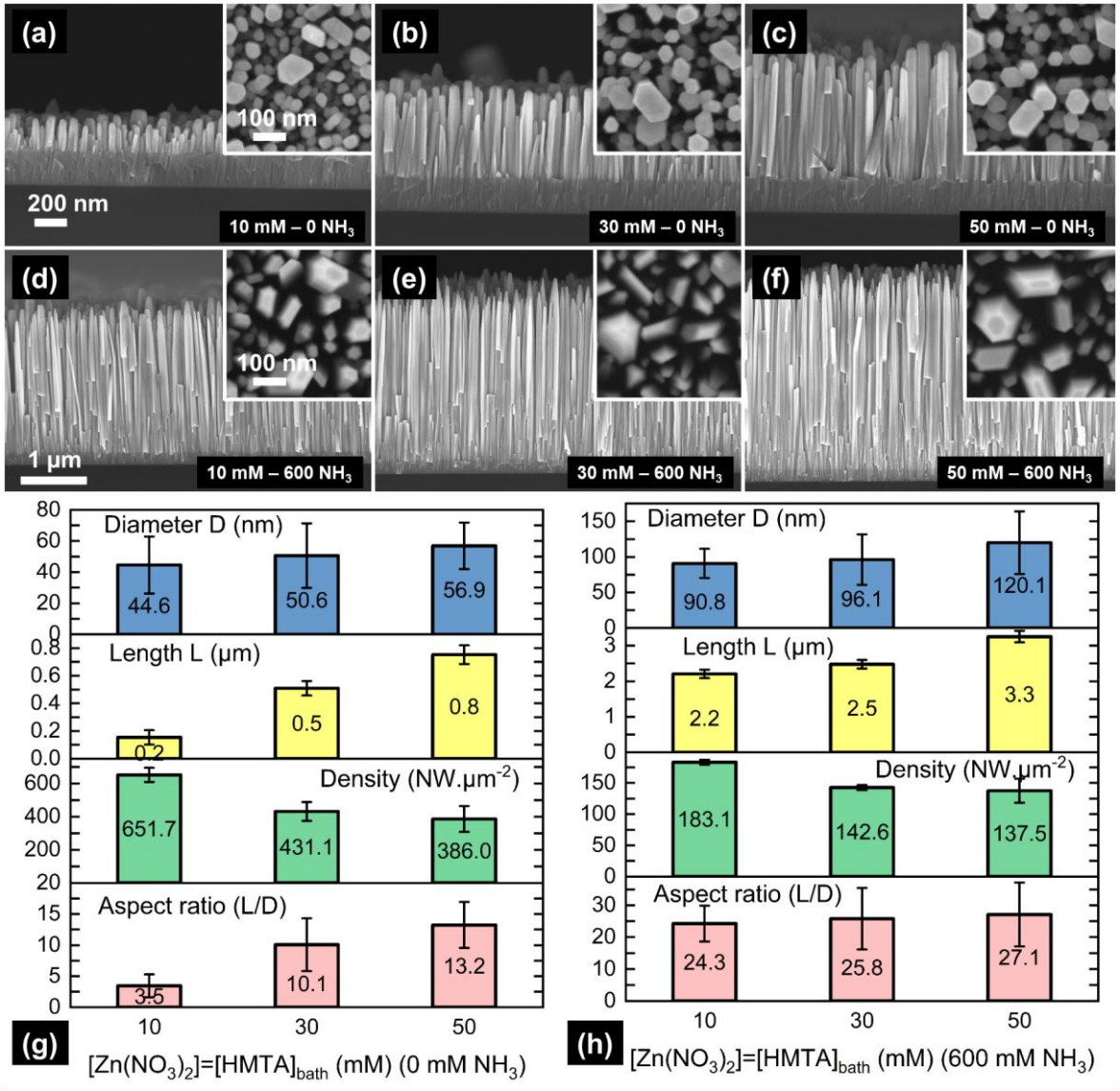

Figure IV.2-4. *Cross-section and (inset) top view FESEM images of ZnO NWs grown on 200 nm-tick AZO layers via CBD with $Zn(NO_3)_2$ and HMTA concentrations of 10, 30, and 50 mM, in a* ***(a-c)*** *low and* ***(d-f)*** *high pH region for 1h 30 min.* ***(g-h)*** *Corresponding morphological properties.*

It should be mentioned that ZnO NWs were grown on 200 nm-thick AZO layers annealed in an O_2 atmosphere for 1 h at 100, 200, 300, and 400°C, where no morphological changes were obtained, as shown in **Supporting Information IV.5.3**.

In conclusion, the morphological properties of ZnO NWs can be enhanced for piezoelectric characterizations by adding ammonia in the bath and increasing the concentration of $Zn(NO_3)_2$ and HMTA. Interestingly, the 200 nm-thick AZO layers exhibited high nucleation sites that led to a high density of NWs. However, it has been shown that in a PNG based on ZnO NWs, a high density of NWs decreases the performance of such a device, where the suitable density ranges between 158 – 25 NW/µm^2, according to FEM simulations.[2,17,42] Therefore, the control of the nucleation sites is essential, along with the reduction in diameter and elongation of the NWs.

IV.2.3 Selective Area Growth of ZnO NWs on patterned AZO layers

As seen in the precedent section, although the ZnO NWs grown on 200 nm-thick AZO layers improve their aspect ratio with the addition of ammonia along with the increase of $Zn(NO_3)_2$ and HMTA concentration in the chemical bath, there is still significant potential for improving their morphological properties for piezoelectric applications. It has been shown that the diameter, length, and density of ZnO NWs cannot be controlled independently, as these properties depend on the chemical bath condition involving the concentration of $Zn(NO_3)_2$ and HMTA,[31,43] polyethylenimine,[44] and ammonia, as well as the bath temperature,[31] growth time, and total solution volume. In addition, the tuning of the morphology of ZnO NWs through the adjustment of the chemical bath has limitations, which are directly related to the number of nucleation sites.[43] Therefore, effective control over the nucleation of ZnO NWs is crucial to accurately tune their morphological properties, which would enhance the performance of related PNG devices. In this context, the selective growth area (SAG) approach emerges as a promising solution. For instance, D. Yang et al. demonstrated that by tuning the density of ZnO NWs into a PNG through the SAG method, the device's output current increased six times compared to a device without SAG.[45]

In the present work, ZnO NWs were grown on 200 nm-thick AZO layers assisted by the SAG method. For this purpose, through lithographic processes assisted by an electron beam,[♣] five blocks consisting of 25 patterned domains with hole periods between 50 – 400 nm and hole diameters from 20 to 180 nm were prepared on resin-coated AZO layers, as schematized in **Figure IV.2-5**. These dimensions were chosen with future piezoelectric applications in mind. In addition, distinct resins were used such as 2% PMMA, 4% PMMA, and UV5.

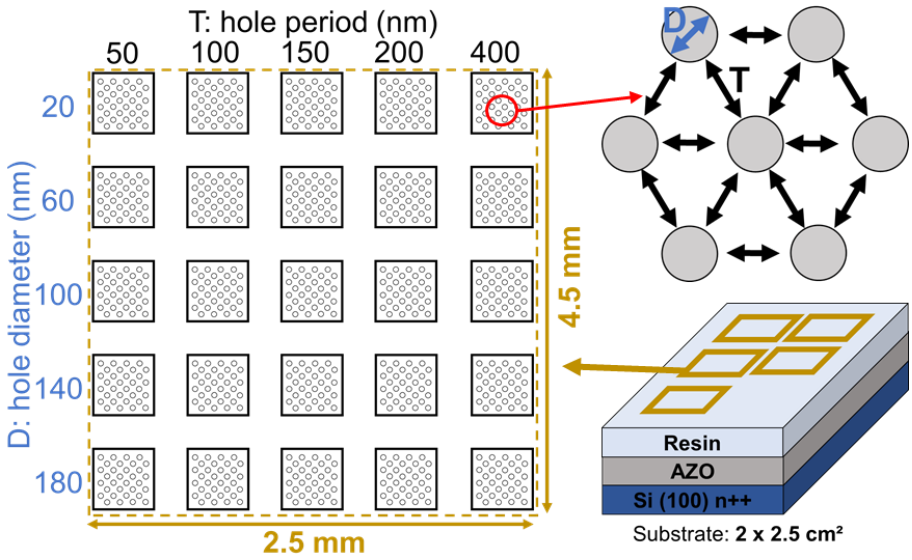

Figure IV.2-5. *Schematic representation of a block consisting of 25 patterned domains (yellow square) with different hole period/diameter combinations for the pattering of AZO layers by electron-beam lithographic process.*

ZnO NWs were subsequently grown on the patterned 200 nm-thick AZO films coated with the resin. These patterned substrates were introduced in sealed reactors containing a solution mixing $Zn(NO_3)_2$ and HMTA in an equimolar concentration of 50 mM. In addition, given the interesting properties of ZnO NWs grown in a high-pH region for piezoelectric applications, 600 mM of ammonia was added to the chemical bath. Finally, after the growth of ZnO NWs during 40 min at 90 °C, a lift-off process is softly performed in acetone and isopropyl to remove the resin, followed by cleaning the substrate with deionized water and drying with dry air.

The patterned AZO layers with ZnO NWs grown in a low and high-pH region on a random domain are shown in **Figure IV.2-6** for each resin. At low pH, traces of localized NW growth are observed in all three resins. Interestingly, the UV5 resin seems to outperform the other resins, as numerous domains indicate the presence of localized NWs. However, the latter

[♣] Lithographic process done by Sébastien LABAU – Cameleon Platform – LTM

seems to grow on holes exceeding 60 nm in diameter with periods larger than 100 nm. When the hole diameter is higher than 140 nm, more than 2 NWs were grown in the same site. Conversely, at high pH, no localized NWs are observed, indicating that the resins dissolve under alkaline conditions. It is worth mentioning that the lift-off process was carefully performed, keeping the sample face down on a support inside a beaker with acetone. This allows the resin to precipitate slowly. The subsequent cleaning with isopropyl and deionized water was also done delicately. However, it seems that the meticulous lift-off process "pulls out" NWs from the layer.

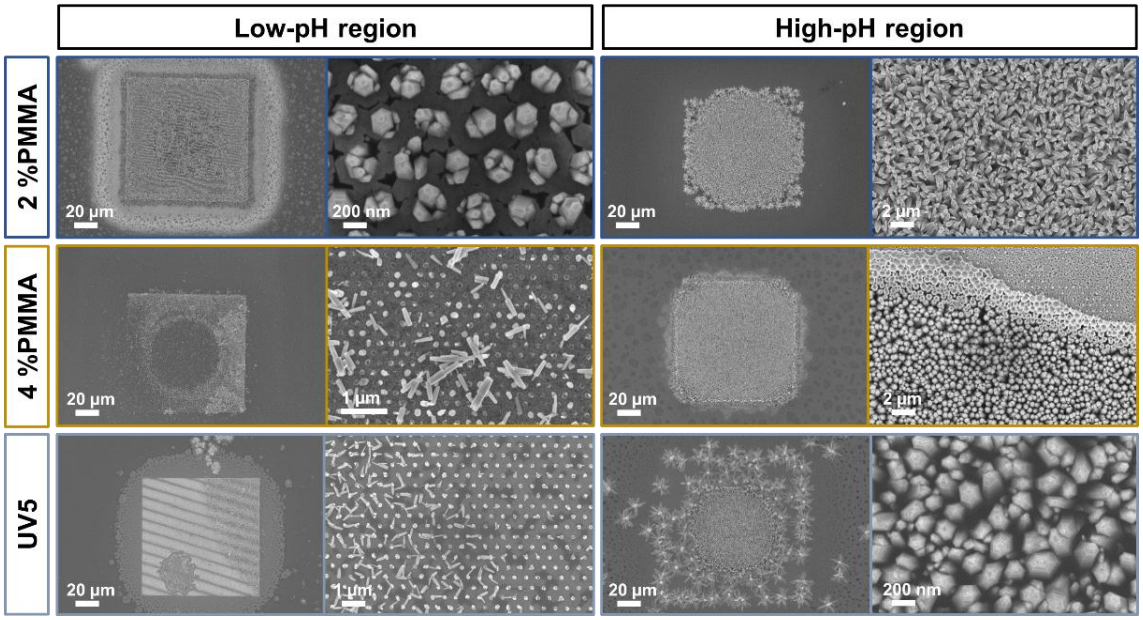

Figure IV.2-6. *FESEM images of ZnO NWs grown by CBD in a low- and high-pH region on random domains of patterned AZO layers coated with different resins.*

Given the promising results with the UV5 in the low pH region, a growth of ZnO NWs in two steps was planned. This process involves growing ZnO NWs in a low-pH region to promote their nucleation on the AZO layer without damaging the resin, and subsequently a second growth in a high-pH region to favor the NW enlargement as the resin gradually degrades. Consequently, at the end of the process, clean AZO surfaces with localized ZnO NWs are expected without a lift-off. According to this, ZnO NWs were grown on AZO layers coated with UV5 resin in a low- and subsequently in a high-pH region for 40 min for each step, whose final result is shown in **Figure IV.2-7**. A strong precipitation of ZnO NWs grown in the solution occurs at high pH, which adheres to the surface of the substrate and potentially hides the patterned domains, as observed in **Figure IV.2-7(a)**. These precipitates appear to adhere strongly to the surface, as even cleaning with deionized water could not remove them. In

addition, the zoomed region of a corner of this domain (dotted red circle) reveals that the localized NWs are still being pulled out, as depicted in **Figure IV.2-7(b)**. Indeed, different domains exhibit traces of localized NWs that unfortunately were broken or removed, as illustrated in **Figure IV.2-7(c-d)**. This suggests that resin detachment damages the localized grown NWs. The use of a hard resin arises thus as a possible solution.

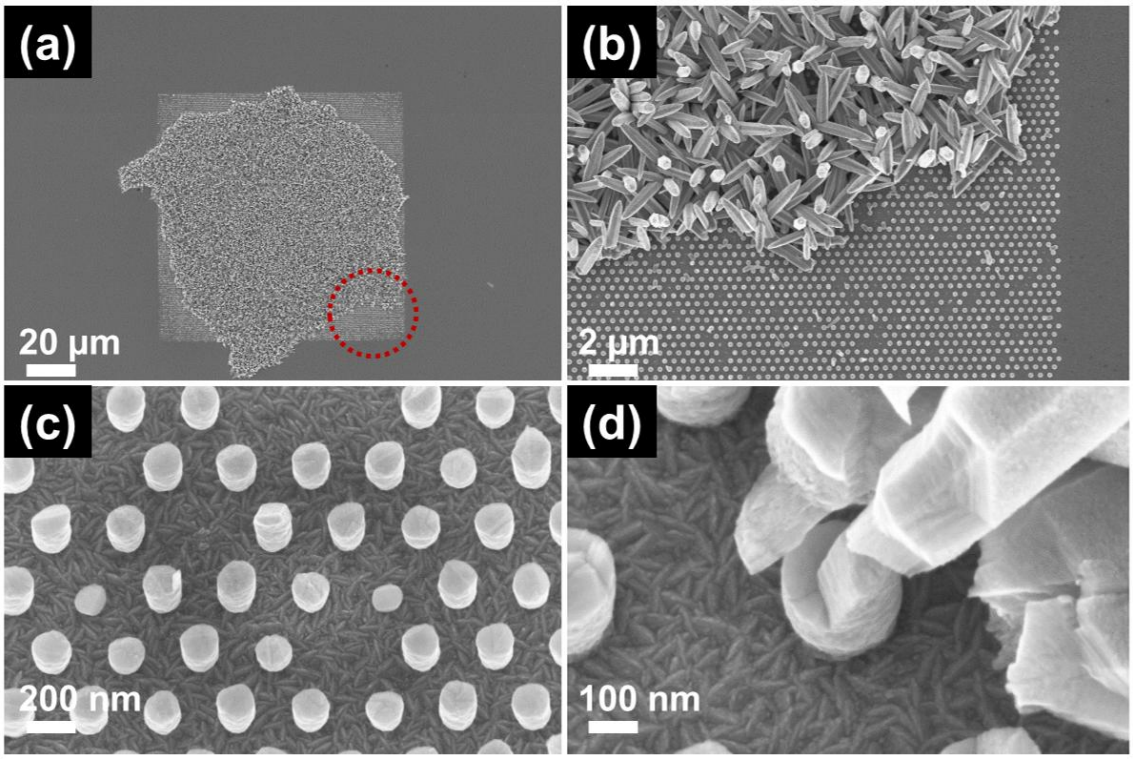

Figure IV.2-7. (a-d) *FESEM images of ZnO NWs grown by CBD in two steps on random domains of patterned AZO layers coated with a UV5 resin.*

By considering the transparent optical properties, a SiO_2 hard resin was used for SAG of ZnO NWs on AZO layers. The homogeneous 30 nm-thick SiO_2 layer was deposited by PVD on AZO layers.[♣] Then, the substrate followed an e-beam lithographic process as described before, resulting in the structure schematized in the inset of **Figure IV.2-8**. ZnO NWs were subsequently grown on the substrate in two steps as previously described. Thus, ZnO NWs grown on AZO layers coated with transparent SiO_2 layers are exclusively expected to remain at the end of the process. However, owing to the high adsorption of precipitated ZnO, a lift-off process was needed to clean the surface of the substrate. Surprisingly, the SiO_2 resin exhibited signs of damage, suggesting that this film is also soluble in alkaline conditions. In addition, the lift-off seems to unfavorably affect the NWs grown on the AZO layer. The

[♣] The SiO_2 deposition by PVD was done by Valentine BOLCATO at the CIME – PTA platform

substrate reveals traces of some patterned domains without NWs, as shown in **Figure IV.2-8(a)**. In contrast to the previous results with other resins, the density of NWs in each domain severely decreases, as presented in **Figure IV.2-8(b)**, which could suggest an enhancement in localized growth when using SiO_2. Indeed, long NWs nucleating at specific sites are observed, which were detached from the substrate or tilted, as depicted in **Figure IV.2-8(c-d)**. Therefore, the use of hard resin seems to be an interesting option for SAG of ZnO NWs grown *via* CBD. However, additional studies focused on the behavior of lithographic resin layers in a bath solution are strongly recommended. These primary findings open thus perspectives on the precise control of morphological properties of ZnO NWs in different seed layers and growth conditions.

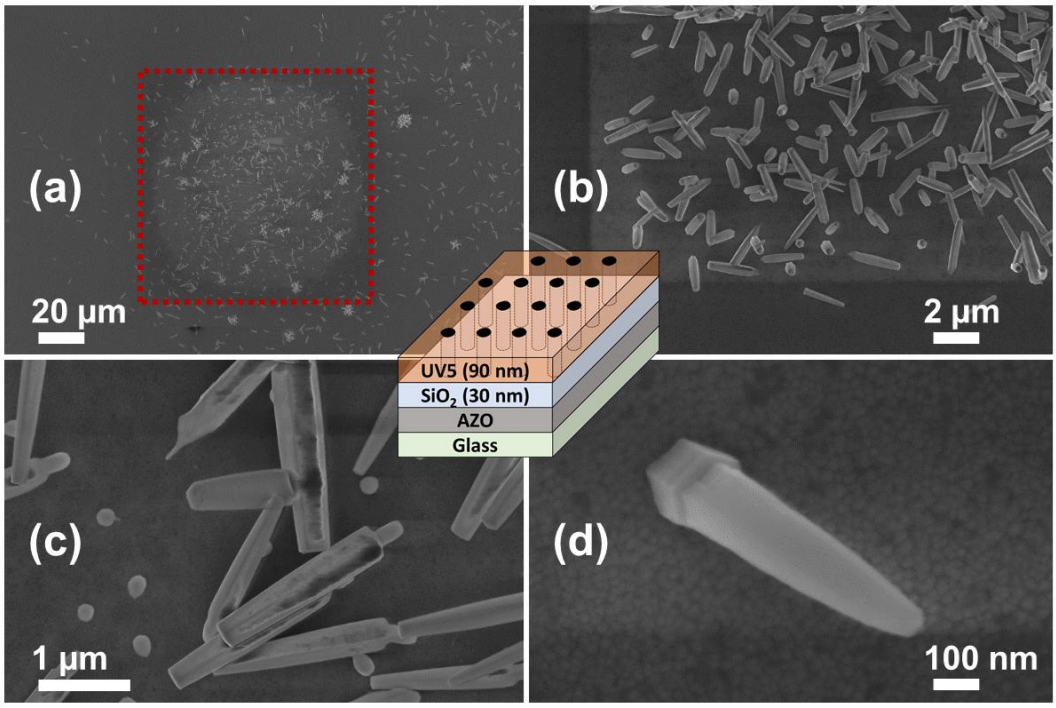

Figure IV.2-8. (a-d) *FESEM images of ZnO NWs grown by CBD in two steps on random domains of patterned AZO layers coated with a SiO_2 resin.*

In conclusion, previous results encourage further the fabrication of transparent PNGs based on AZO layers as bottom electrodes that also allows the growth of ZnO NWs.

IV.3 Effect of Au seed layers on the morphological and structural properties of ZnO nanowires for piezoelectric applications

State-of-the-art

Previous research by Lausecker et al. demonstrated the successful growth of ZnO NWs via CBD on Au layers, showing that the morphological and structural properties of ZnO NWs depend on both the structural properties of the Au seed layers[20] and the concentration of $Zn(NO_3)_2$ and HMTA in the chemical bath.[46]

The studies indicated that as the Au layer thickness increases from 5 to 100 nm, the diameter and length of the NWs also increase, but their density decreases. Thicker Au layers improve the verticality of ZnO NWs growing on the (111) facets of Au grains; however, a secondary population of ZnO NWs grows at an approximately 20° tilt angle on the (211) facets, as depicted in **Figure IV.3-1(a)**.

Moreover, for a given Au layer thickness, the concentration of $Zn(NO_3)_2$ and HMTA in the chemical bath directly affects its pH, which controls the supersaturation of Zn(II) species. This leads to three distinct growth regimes, each resulting in ZnO NW arrays with unique morphological properties such as length, diameter, density, and orientation, as schematized in **Figure IV.3-1(a)**. Related research by Boubenia et al. found that increasing the pH of the chemical bath by adding NH_4OH from 0 mM to 40 mM results in an excess of Zn(II) complexes, leading to more nucleation sites and a significant increase in NW density.[47] However, a higher pH also raises the free carrier density in ZnO NWs, with values ranging from 4.3×10^{16} to 2.0×10^{17} cm^{-3} as the NH_4OH is added. This increase in free carrier density contributes to screening effects that degrade the performance of PNGs.

These findings provided valuable insights for synthetizing ZnO NWs with optimal properties for piezoelectric applications when growing on Au seed layers. Lausecker's study recommended using i) an Au seed layer of about 50 nm thick and ii) a chemical bath mixing 50 mM of $Zn(NO_3)_2$ with 50 mM of HMTA. Under these growth conditions, ZnO NWs exhibited the best verticality (with an angle lower than 3° between the *c*-axis of ZnO NWs and the normal to the substrate), a high density of 17.4 NW/μm^2, and a moderate aspect ratio of 13.4 (ratio of NW length to diameter).

At the beginning of the present thesis work, the use of an Au film as a nucleation layer for the NWs and as the bottom electrode of a PNG was proposed. However, during experiments, an unexpected change in the morphological properties of ZnO NWs was observed, which could have been a consequence of changes in the deposition by vacuum evaporation of Au layers.

In this context, the current concise section studies how the deposition rate during vacuum evaporation influences the morphological and structural properties of Au layers and ZnO NWs grown on these films.

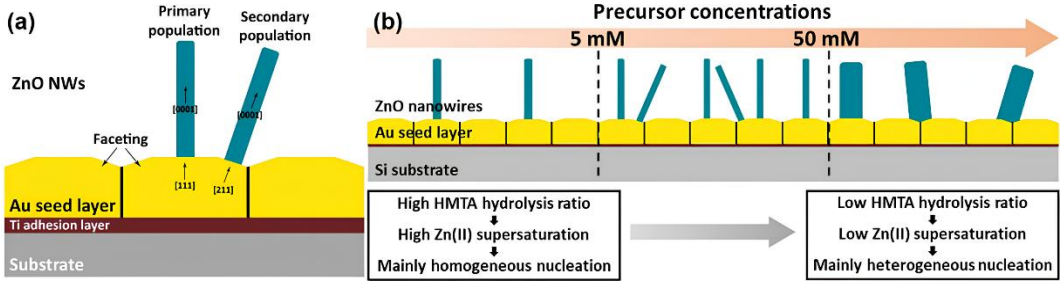

Figure IV.3-1. *Schematic diagram illustrating* ***(a)*** *how the primary and secondary population of ZnO NWs form on Au seed layers, and* ***(b)*** *how their morphology and structure change with varying concentrations of $Zn(NO_3)_2$ and HMTA in the chemical bath. Adapted from REFs [20] and [46], respectively.*

IV.3.1 Structural and morphological properties of Au layers grown by vacuum evaporation

Pre-cleaned (100) Si substrates in dry air were used to grow 20 nm-thick Ti layer by vacuum evaporation, and subsequently, 35 nm-thick Au layers were grown at different growth rates (V_{Au}) of 0.05, 0.1, 0.15, 0.25, and 0.5 nm/s. After confirming the uniform thickness of both 20 nm-thick Ti and 35 nm-thick Au layers by FESEM images, as shown in **Figure IV.3-2(a)**, AFM measurements were performed, exhibiting a decrease of roughness from 0.99 to 0.73 as the V_{Au} was increased from 0.05 to 0.5 nm/s, as presented in **Figure IV.3-2(b)**. In addition, the XRD pattern, displayed in **Figure IV.3-2(c)**, reveals a high orientation along the [111] direction of Au layers regardless of V_{Au}. From the previous analysis, the main structural features of Au layers are evaluated and summarized in **Figure IV.3-2(d)**. A decrease in the grain size from 40 to 34 nm is obtained by increasing the V_{Au}, according to FESEM and AFM images. From XRD data, the crystallite size (L) of the Au layers was calculated using the Scherrer Equation: $L = \frac{K\lambda}{\beta \cos\theta}$; where K is the shape factor (0.9), λ is the XRD radiation wavelength (0.15406 nm), β represents the full width at half maximum (FWHM) in radians, and 2θ indicates the position of the XRD peak. Thus, by focusing on the strongest Au (111) peak, the Au layer's crystallite

size increases from 32 to 33.2 nm as V_{Au} increments from 0.05 to 0.1 nm/s, and reaches a plateau around 33.2 nm for V_{Au} higher than 0.1 nm/s. This indicates that the Au layers consist of a single layer of Au grains, as the crystallite size corresponds to the thickness of these films. In addition, Rocking curves (also known as omega scans) were performed, revealing a high crystal quality of Au layers through the low mosaicity of Au (111) planes, which was calculated as the half of the FWHM of the peak located at the ω-position.

According to REF [48], the formation of thin films *via* evaporation-based techniques involves the adsorption of atoms and their diffusion over the surface until they reach equilibrium positions in the lattice through bulk diffusive motion. Therefore, as the deposition rate increases, the adsorbed atoms have less time to migrate and find energetically favorable sites, resulting in smaller and disordered grains. This is in agreement with FESEM, AFM, XRD, and Rocking curves analysis. Moreover, an increase in grain size can reduce the coordination of deformation between neighboring grains during the deposition process, leading to irregular deformations of the thin film and, consequently, an increase in its roughness,[49] which is also observed in the present study.

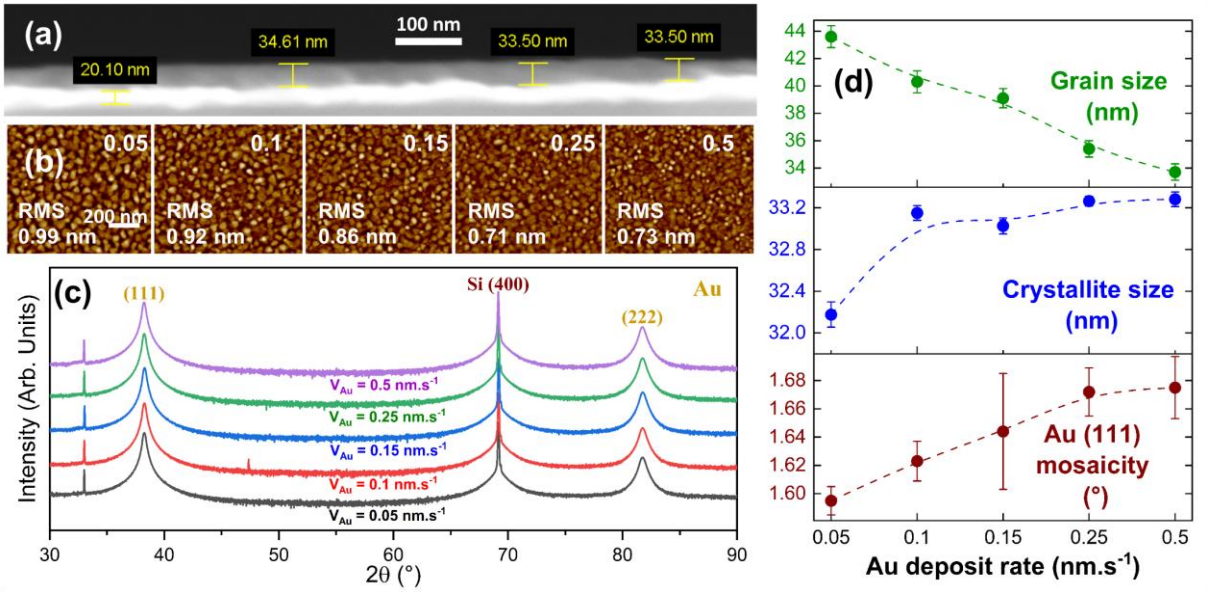

Figure IV.3-2. (a) *FESEM cross-section image of the 35 nm-thick deposited Au layer.* ***(b)*** *AFM images,* ***(c)*** *XRD spectra, and* ***(d)*** *Au-grain features of Au layers grown with deposition rates of 0.05, 0.1, 0.15, 0.25, and 0.5 nm/s.*

IV.3.2 Structural and morphological properties of ZnO nanowires grown on Au layers

Given the slight modification in the physical properties of the Au layers with V_{Au}, a question arises concerning their potential effects on the growth of ZnO NWs. For this purpose,

ZnO NWs were grown on the Au layers by CBD for 3 h at 90 °C using an aqueous solution mixing 50 mM of $Zn(NO_3)_2$ and 50 mM of HMTA. It is important to note that ammonia was not added to the chemical bath.

IV.3.2.1 FESEM Images and XRD

After the CBD process, ZnO NWs are found to grow by hetero epitaxy on the top face of (111)-oriented Au grains,[20] resulting in vertically integrated nanostructures, as shown in **Figure IV.3-3(a)**. The ZnO NWs exhibit hexagonal flat-top faces characteristic of the wurtzite atomic arrangement, and their diameter decreases from bottom to top. From FESEM images, the morphological properties of the NWs are assessed and summarized in **Figure IV.3-3(b)**. These properties do not exhibit a clear trend relative to V_{Au}. The length decreases from 1.7 to 1.5 µm as V_{Au} increases from 0.05 to 0.15 nm/s, then increases to 1.7 µm for a V_{Au} of 0.25 nm/s, and decreases again to 1.6 µm for a V_{Au} of 0.5 nm/s. The bottom diameter remains around 290 nm regardless of the V_{Au}. In contrast, the top diameter progressively increments from 148 to 162 nm as V_{Au} rises from 0.05 to 0.15 nm/s, and then decreases to 128 nm as V_{Au} reaches 0.5 nm/s. The aspect ratio, defined as the ratio between the length over the diameter of the NW, exhibits the highest values of 7.75, 7.71, and 7.58 for V_{Au} of 0.25, 0.5, and 0.05 nm/s, respectively. Moreover, the density of ZnO NWs is higher in Au layers grown with V_{Au} of 0.25 and 0.5 nm/s, displaying values of 14.3 NW/µm^2.

The High-Resolution XRD patterns of ZnO NWs grown on the Au layers reveal stronger (002) – ZnO and (111) – Au peaks, along with moderate (100), (101) (102), (110), (103), and (200) – ZnO peaks, as illustrated in **Figure IV.3-3(c)**. Interestingly, when these XRD are compared with the XRD spectrum of ZnO NWs grown on a ZnO seed layer (ZnO_ref), the NWs grown on Au seed layers show the highest (100) – ZnO peak, which leads to the observation of the (200) – ZnO peak. The texture evolution along the [002] – ZnO crystallographic direction is then evaluated by calculating the relative texture coefficient. This coefficient is determined by dividing the absolute texture coefficient C_{hkl} by the number of considered diffraction peaks N, as follows:[19,50]

$$\frac{C_{hkl}}{N} = \frac{\frac{I_{hkl}}{I_{0,hkl}}}{\sum_i^N \frac{I_{hkl}}{I_{0,hkl}}}$$

where I_{hkl} and $I_{0,hkl}$ are the intensities of the [hkl] crystallographic direction of the studied sample and a randomly oriented sample (ICDD – 00-036-1451), respectively. Thus, by considering the (100), (002), (102), (110), and (103) ZnO peaks (N=5), the relative texture coefficient along the [002] direction is 94.8, 95.2, 94.3, 94.96 and 98.0 % for ZnO NWs grown, respectively, in Au layers deposited with V_{Au} of 0.5, 0.25, 0.15, 0.10 and 0.05 nm/s. These values are slightly higher than those obtained for ZnO NWs grown on the ZnO seed layer, whose relative texture coefficient reaches 92.8 %.

Therefore, Au layers deposited by vacuum evaporation with deposition rates of 0.25 and 0.5 nm/s lead to the growth of ZnO NWs exhibiting the most suitable morphological properties for piezoelectric applications, in comparison to the other analyzed Au layers. In addition, ZnO NWs grown in Au layers depict a high texturization along the [002] direction (*c*-axis), even more pronounced than ZnO NWs grown on ZnO seed layers. However, given that the verticality of ZnO NWs is an important parameter for the performance of a PNG based on these nanostructures,[18] additional X-ray Pole Figure studies were performed and discussed in the following section.

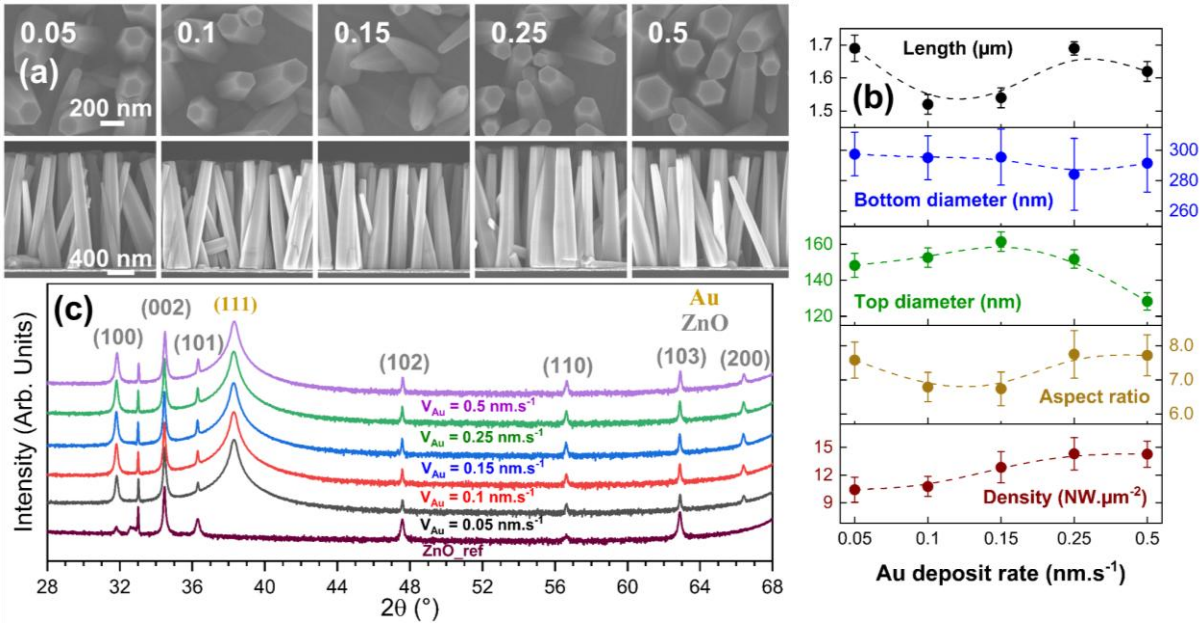

Figure IV.3-3. (a) *FESEM images (top and cross section),* ***(b)*** *morphological property summary, and* ***(c)*** *XRD patterns of ZnO NWs synthesized on Au layers grown with deposition rates of 0.05, 0.1, 0.15, 0.25, and 0.5 nm/s.*

IV.3.2.2 X-ray Pole Figure

The vertical alignment of ZnO NWs grown on the Au layers was quantified using X-ray Pole Figures. The latter was performed by fixing the X-ray source and the detector on the (002)

diffraction peak position, and by recording the associated intensity as a function of φ [0 – 360°] and χ [0 – 90°], as schematized in **Figure IV.3-4(a)**. For a given χ angle, the (002) peak intensities recorded for each ϕ angle were summed, resulting in the total, symmetrical, and normalized (002) peak intensity as a function of χ, as shown in **Figure IV.3-4(b)**. It is important to note that ZnO NWs oriented along the *c*-axis should theoretically be parallel with the normal to the substrate (χ=0°). In this study, the tilt angle between the [002]-oriented ZnO NWs and the normal to the substrate were represented by half of the FWHM of the (002) peak. However, **Figure IV.3-4(b)** depicts a progressive widening of the (002) ZnO peak bottom as the V_{Au} increases from 0.05 to 0.5 nm/s, leading to errors in fitting the recorded data with a Voigt function. This widening suggests the presence of two different populations of [002]-oriented ZnO NWs with different tilt angle, which would be consistent with REF [20]. Therefore, the recorded data fits well when considering two different ZnO NW populations, as depicted in **Figure IV.3-4(c)**. This approximation indicates a slight improvement in the verticality of the ZnO NWs when V_{Au} increases from 0.05 to 0.5 nm/s. Indeed, the χ angles slightly decrease from 2.8 to 2.4° for the first population, and from 7.0 to 6.8° for the second population, as shown in **Figure IV.3-4(d)**. In addition, the verticality seems to be enhanced through the increase in the amount of the first population at the expense of the second population, as determined by the total area of the Voigt functions. Finally, 35 nm – thick Au layers, grown by vacuum evaporation with deposition rates of 0.25 or 0.5 nm/s, are suggested to be more suitable for piezoelectric applications considering the morphological and structural properties of ZnO NWs, i.e. a high density of well vertically aligned NWs with high aspect ratio.

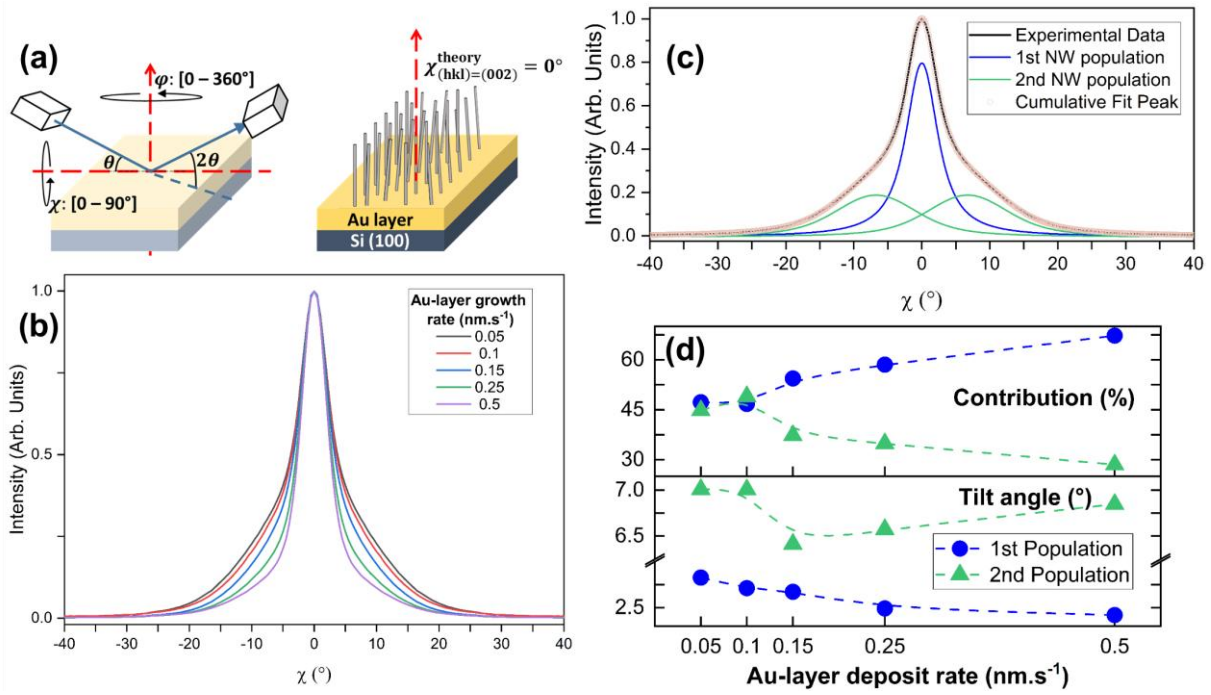

Figure IV.3-4. (a) *Schematic of X-ray Pole Figure analysis in the (002)-ZnO crystallographic position.* ***(b)*** *Normalized and symmetrical mean intensity integrated over all φ angles for a given χ angle of the X-ray Pole Figure of ZnO NWs grown on different Au layers.* ***(c)*** *Fitting of the corresponding intensity with Voight functions referring to two different populations of ZnO NWs along the c-axis.* ***(d)*** *Quantification of the amount and tilt angle of the mentioned populations.*

IV.3.3 Output voltage of a PNG based on ZnO NWs grown on Au layer

According to previous studies, the effect of an Au layer on the output voltage of PNG was evaluated. A PNG integrating a 35 nm – thick Au layer grown by vacuum evaporation with deposition rate of 0.5 nm/s was fabricated. This Au layer serves as bottom electrode of the device and as nucleation layer for the ZnO NWs, which were synthetized with the same chemical bath condition detailed in **Section IV.3.2**. The ZnO NWs exhibit a number density of 3.1 ± 0.6 NW/µm^2, a length of 3.3 ± 0.2 µm, a diameter of 381 ± 79 nm, and an aspect ratio of 17.2 ± 4.5, as shown in **Figure IV.3-5.** These morphological features differ from the precedent results summarized in **Figure IV.3-3(b)**, highlighting the strong dependence of ZnO NW morphology on the properties of the Au seed layer. Although the deposition conditions of the Au layer were maintained as in prior experiments, slight variations in its properties could have occurred involving the evaporator machine operation mode after maintenance, aging of the Au seed layer, or surface cleanliness, etc. Moreover, although the integrated ZnO NWs

displayed low density on the Au layer, their aspect ratio is high, which is important for piezoelectric applications.

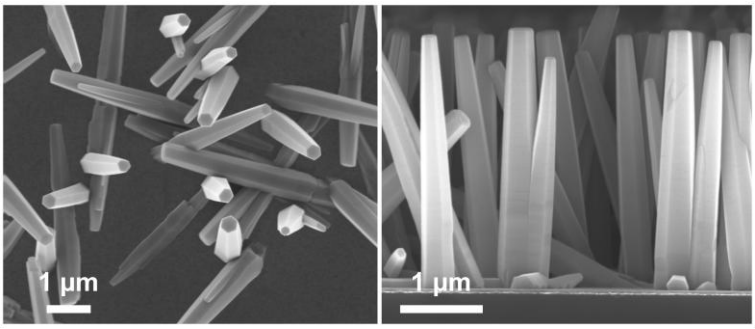

Figure IV.3-5*. Top-view (left) and cross-section (right) FESEM images of ZnO NWs grown on 35 nm-thick Au layers for the fabrication of a PNG.*

The PNG was characterized on the test bench available at the Cameleon platform of the LTM described in **Section II.5.1**. The device was subjected to sinusoidal mechanical compressions by applying a vertical force over a circular area of 0.2 cm^2 with a mechanical arm. It should be noted that the piezoelectric signal, which was amplified by a 10-factor through the Stanford Research Systems SR560 amplifier, is confirmed by changing the polarity connection of the device to achieve the inversion of the signal. During the test, several changes in the amplitude of the output signal were observed according to the mechanical excitation area of the device, as depicted in **Figure IV.3-6(a)**. By applying around 7 N at 1 Hz on 0.2 cm^2 on the top electrode (1), the output signal reaches 9 mVpp. In contrast, when the force is applied over 0.1 cm^2 on the top electrode edge (2), the highest signal of 42 mVpp is recorded. Then, by decreasing the mechanical active area, the piezoelectric signal progressively reduces, displaying values of 11 mVpp and 1.3 mVpp when the force is applied on the corner (3) and outside (4) of the top electrode, respectively. This behavior could be attributed to mechanical effects occurring during the mechanical stress mainly related to the embedding parylene-C layer, which suggests that additional studies need to be focused on the mechanical properties of this polymer layer. Moreover, by increasing the vertical force from 2.2 to 13.6 N applied on the top electrode (configuration 1), the output signal steadily increments from 3.3 to 9.6 mVpp, as depicted in **Figure IV.3-6(b)**. Although the piezoelectric signal of the device can increase depending on the applied force and the mechanical active area, its values are relatively low, which could come from the low ZnO NW density. Additionally, the morphological properties of ZnO NWs seem to be highly dependent on the properties of Au layers (i.e. deposition condition, surface cleanliness, aging of the layer, etc.),

which could lead to significant variability in the piezoelectric response of PNGs, even when following the same fabrication protocol. Consequently, alternative solutions involving AZO layers, which can serve both as a nucleation layer for ZnO NWs and as the bottom electrode of a PNG, can be considered since the morphological variability of ZnO NWs on AZO layers is less pronounced.

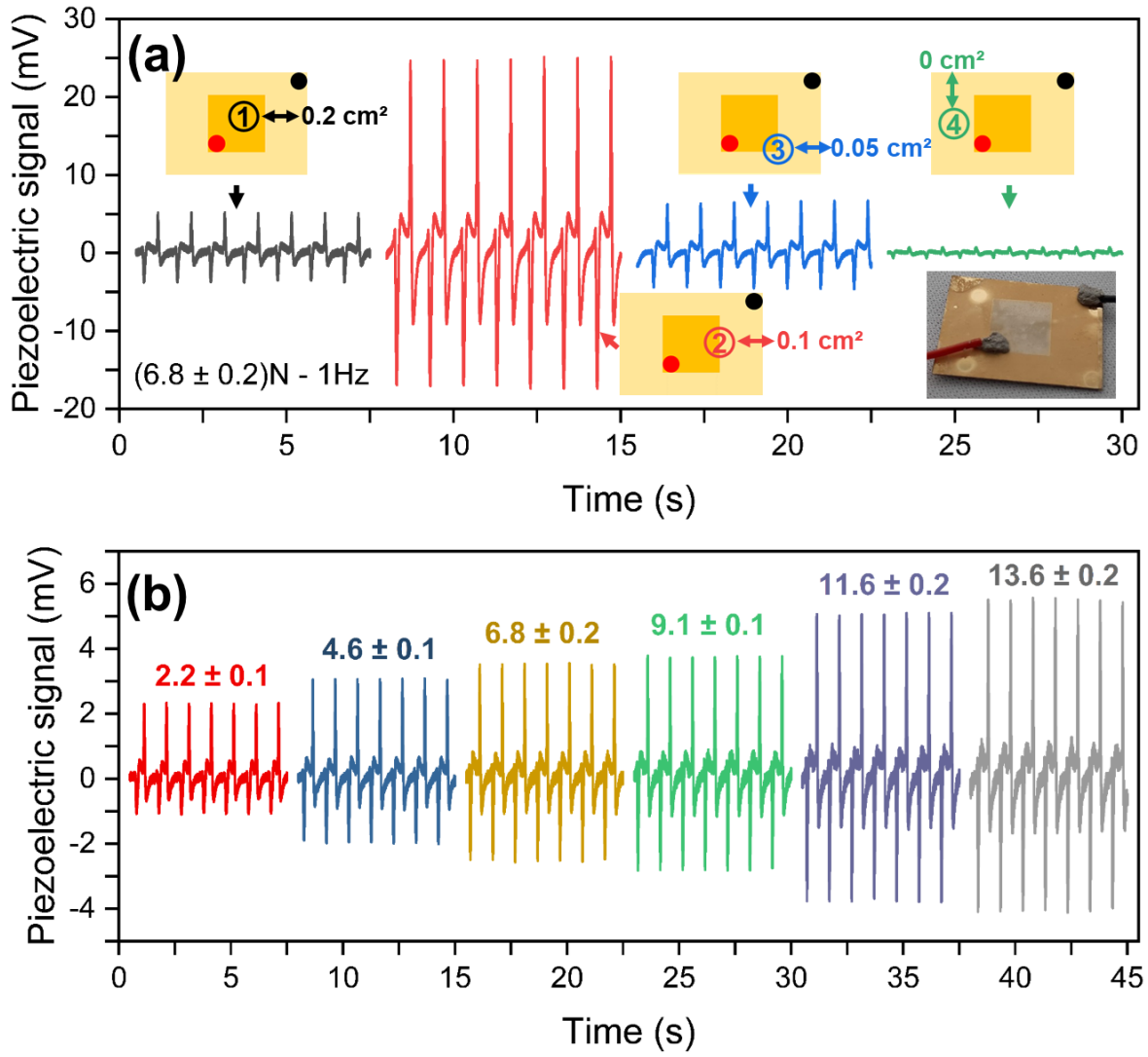

Figure IV.3-6. *Piezoelectric signal of a PNG based on ZnO NWs grown on a 35 nm-thick Au layer according to the* ***(a)*** *mechanical excitation area and* ***(b)*** *vertical sinusoidal force on the LTM's test bench. This figure displays the piezoelectric signals and the output voltage values amplified by a 10-factor using the Stanford Research Systems SR560 amplifier of the test bench for the sake of readability.*

IV.4 Conclusion

In conclusion, the use of Au and AZO layers as nucleation layers for ZnO NWs, as well as potential bottom electrodes for PNGs, was investigated.

Initially, Au layers were employed as a seed layer for ZnO NWs due to the Schottky barrier expected at their interface, which could improve the PNG performance. These Au layers were grown by vacuum evaporation at different deposition rates. FESEM, AFM, and XRD analysis have demonstrated that smooth 35 nm-thick Au films consist of a single layer of Au grains, which are strongly oriented along the [111] direction. Moreover, ZnO NWs have displayed their best morphological and structural properties for piezoelectric applications when growing on Au layers deposited at 0.25 and 0.5 nm/s. Despite these promising results, a low reproducibility of experiments on Au layers was observed. A PNG integrating an Au film, which was used as a nucleation layer for ZnO NWs and as a bottom electrode of the device, was successfully fabricated. Piezoelectric characterizations have revealed a low output voltage of such a device due to the low density of ZnO NWs, as well as mechanical effects probably arising from the parylene-C layer.

Furthermore, the effect of AZO layers on the morphology of ZnO NWs was investigated, as an Ohmic contact is expected at their interface for piezoelectric applications. These layers were grown by sputtering PVD with thicknesses of 100, 200, 300, and 400 nm. TLM measurement has demonstrated the lowest resistivity for a 200 nm-thick AZO layer. Interestingly, thermal annealing at 200 °C in an O_2 atmosphere further decreases the resistivity and enhances the transparency of AZO layers, as TLM and optical measurements have proved. Moreover, AZO layers have shown a high number of nucleation sites that lead to dense ZnO NW matrices, whose high density is not suitable for piezoelectric applications. Ongoing experimental efforts in selective area growth show potential for controlling the nucleation of ZnO NWs and thus their morphological properties. In this context, different lithographic resins were used such as 2% PMMA, 4% PMMA, and UV5, which are solubilized in an alkaline chemical bath, and consequently, spontaneous ZnO NWs grow on the AZO layer. A hard resin of SiO_2 was also tested, showing identical results to the other resins. Further investigations are thus recommended to study the behavior of lithographic resins in different chemical bath conditions to successfully grow localized ZnO NWs. This opens perspectives in the fabrication of transparent PNGs.

Bibliography

[1] R. Tao, M. Parmar, G. Ardila, P. Oliveira, D. Marques, L. Montès, M. Mouis, *Semicond. Sci. Technol.* **2017**, *32*, DOI 10.1088/1361-6641/aa691f.

[2] X. Zhang, J. Villafuerte, V. Consonni, J.-F. Capsal, P.-J. Cottinet, L. Petit, M.-Q. Le, *Nanomaterials* **2021**, *11*, 1712.

[3] H. G. Kim, E. H. Kim, S. S. Kim, *Materials (Basel).* **2021**, *14*, 1461.

[4] C. Justeau, T. S. Tlemcani, G. Poulin-Vittrant, K. Nadaud, D. Alquier, *Materials (Basel).* **2019**, *12*, DOI 10.3390/ma12162511.

[5] L. J. Brillson, Y. Lu, *J. Appl. Phys.* **2011**, *109*, DOI 10.1063/1.3581173.

[6] S. Brochen, G. Feuillet, J. L. Santailler, R. Obrecht, M. Lafossas, P. Ferret, J. M. Chauveau, J. Pernot, *J. Appl. Phys.* **2017**, *121*, DOI 10.1063/1.4977506.

[7] L. Wang, S. Guillemin, J. M. Chauveau, V. Sallet, F. Jomard, R. Brenier, V. Consonni, G. Brémond, *Phys. Status Solidi Curr. Top. Solid State Phys.* **2016**, *13*, 576–580.

[8] T. Cossuet, F. Donatini, A. M. Lord, E. Appert, J. Pernot, V. Consonni, *J. Phys. Chem. C* **2018**, *122*, 22767–22775.

[9] J. Villafuerte, F. Donatini, J. Kioseoglou, E. Sarigiannidou, O. Chaix-Pluchery, J. Pernot, V. Consonni, *J. Phys. Chem. C* **2020**, *124*, 16652–16662.

[10] K. Guruprasad, G. Marappan, S. Elangovan, S. Velappa Jayaraman, K. Kamala Bharathi, G. Venugopal, C. Di Natale, Y. Sivalingam, *Nano Express* **2020**, *1*, 030020.

[11] M. W. Allen, M. M. Alkaisi, S. M. Durbin, *Appl. Phys. Lett.* **2006**, *89*, 1–4.

[12] J.-H. Tian, J. Hu, S.-S. Li, F. Zhang, J. Liu, J. Shi, X. Li, Z.-Q. Tian, Y. Chen, *Nanotechnology* **2011**, *22*, 245601.

[13] A. M. Lord, V. Consonni, T. Cossuet, F. Donatini, S. P. Wilks, *ACS Appl. Mater. Interfaces* **2020**, *12*, 13217–13228.

[14] R. Tao, M. Mouis, G. Ardila, *Adv. Electron. Mater.* **2018**, *4*, DOI 10.1002/aelm.201700299.

[15] A. J. Lopez Garcia, M. Mouis, V. Consonni, G. Ardila, *Nanomaterials* **2021**, *11*, DOI 10.3390/nano11040941.

[16] R. Hinchet, S. Lee, G. Ardila, L. Montès, M. Mouis, Z. L. Wang, *Adv. Funct. Mater.* **2014**, *24*, 971–977.

[17] R. Tao, M. Parmar, G. Ardila, P. Oliveira, D. Marques, L. Montès, M. Mouis, *Semicond. Sci. Technol.* **2017**, *32*, DOI 10.1088/1361-6641/aa691f.

[18] R. Tao, G. Ardila, R. Hinchet, A. Michard, L. Montès, M. Mouis, in *Futur. Trends Microelectron.*, Wiley, Hoboken, NJ, USA, **2016**, pp. 291–307.

[19] S. Guillemin, V. Consonni, E. Appert, E. Puyoo, L. Rapenne, H. Roussel, *J. Phys. Chem. C* **2012**, *116*, 25106–25111.

[20] C. Lausecker, B. Salem, X. Baillin, H. Roussel, E. Sarigiannidou, F. Bassani, E. Appert, S. Labau, V. Consonni, *Nanotechnology* **2019**, *30*, DOI 10.1088/1361-6528/ab1d6e.

[21] K. Kawajiri, K. Tahara, S. Uemiya, *Resour. Environ. Sustain.* **2022**, *7*, 100047.

[22] M. Berginski, J. Hüpkes, M. Schulte, G. Schöpe, H. Stiebig, B. Rech, M. Wuttig, *J. Appl. Phys.* **2007**, *101*, DOI 10.1063/1.2715554.

[23] X. Yan, W. Li, A. G. Aberle, S. Venkataraj, *Procedia Eng.* **2016**, *139*, 134–139.

[24] K. Sekar, R. Nakar, J. Bouclé, R. Doineau, K. Nadaud, B. Schmaltz, G. Poulin-Vittrant, *Nanomaterials* **2022**, *12*, 1–20.

[25] Q. C. Bui, V. Consonni, S. Boubenia, G. Gay, C. Perret, M. Zeghouane, S. Labau, H. Roussel, X. Mescot, G. Ardila, B. Salem, *Materialia* **2023**, *31*, DOI 10.1016/j.mtla.2023.101863.

[26] P. Novák, L. Nedvědová, T. Kozák, P. Šotová, O. Bláhová, Z. Jansa, R. Medlín, M. Frank Netrvalová, J. Minár, *Thin Solid Films* **2023**, *780*, DOI 10.1016/j.tsf.2023.139942.

[27] T. Minami, H. Sato, K. Ohashi, T. Tomofuji, S. Takata, *J. Cryst. Growth* **1992**, *117*, 370–374.

[28] Y. Fei, Y. Li, Y. Li, A. Xie, Y. Li, D. Sun, *J. Mol. Struct.* **2022**, *1269*, 133804.

[29] B. Sarma, D. Barman, B. K. Sarma, *Appl. Surf. Sci.* **2019**, *479*, 786–795.

[30] J. Zhang, W. Que, Q. Jia, X. Ye, Y. Ding, *Appl. Surf. Sci.* **2011**, *257*, 10134–10140.

[31] F. Dehghan Nayeri, E. Asl Soleimani, *Exp. Tech.* **2014**, *38*, 13–20.

[32] K. E. Lee, M. Wang, E. J. Kim, S. H. Hahn, *Curr. Appl. Phys.* **2009**, *9*, 683–687.

[33] T. Dhakal, A. S. Nandur, R. Christian, P. Vasekar, S. Desu, C. Westgate, D. I. Koukis, D. J. Arenas, D. B. Tanner, *Sol. Energy* **2012**, *86*, 1306–1312.

[34] R. Raciti, R. Bahariqushchi, C. Summonte, A. Aydinli, A. Terrasi, S. Mirabella, *J. Appl. Phys.* **2017**, *121*, DOI 10.1063/1.4986436.

[35] B. D. Viezbicke, S. Patel, B. E. Davis, D. P. Birnie, *Phys. status solidi* **2015**, *252*, 1700–1710.

[36] C. Agashe, O. Kluth, J. Hüpkes, U. Zastrow, B. Rech, M. Wuttig, *J. Appl. Phys.* **2004**, *95*, 1911–1917.

[37] E. Burstein, *Phys. Rev.* **1954**, *93*, 632–633.

[38] J. D. Ye, S. L. Gu, S. M. Zhu, S. M. Liu, Y. D. Zheng, R. Zhang, Y. Shi, *Appl. Phys. Lett.* **2005**, *86*, 1–3.

[39] Y. K. Frodason, K. M. Johansen, T. S. Bjørheim, B. G. Svensson, A. Alkauskas, *Phys. Rev. B* **2018**, *97*, 104109.

[40] S. Grover, S. Sahu, P. Zhang, K. O. Davis, S. K. Kurinec, in *2020 IEEE 33rd Int. Conf. Microelectron. Test Struct.*, IEEE, **2020**, pp. 1–6.

[41] M. Willander, L. L. Yang, A. Wadeasa, S. U. Ali, M. H. Asif, Q. X. Zhao, O. Nur, *J. Mater. Chem.* **2009**, *19*, 1006–1018.

[42] R. Hinchet, S. Lee, G. Ardila, L. Montès, M. Mouis, Z. L. Wang, *Adv. Funct. Mater.* **2014**, *24*, 971–977.

[43] R. Parize, J. Garnier, O. Chaix-Pluchery, C. Verrier, E. Appert, V. Consonni, *J. Phys. Chem. C* **2016**, *120*, 5242–5250.

[44] R. Parize, J. D. Garnier, E. Appert, O. Chaix-Pluchery, V. Consonni, *ACS Omega* **2018**, *3*, 12457–12464.

[45] D. Yang, Y. Qiu, Q. Jiang, Z. Guo, W. Song, J. Xu, Y. Zong, Q. Feng, X. Sun, *Appl. Phys. Lett.* **2017**, *110*, DOI 10.1063/1.4975477.

[46] C. Lausecker, B. Salem, X. Baillin, V. Consonni, *Cryst. Growth Des.* **2023**, *23*, 2941–2950.

[47] S. Boubenia, A. S. Dahiya, G. Poulin-Vittrant, F. Morini, K. Nadaud, D. Alquier, *Sci. Rep.* **2017**, *7*, 1–10.

[48] M. Ohring, *The Materials Science of Thin Films*, Academic Press, San Diego, **2001**.

[49] G. Wang, J. Han, Y. Lin, W. Zheng, *Mater. Today Commun.* **2021**, *27*, 102279.

[50] H. R. Moutinho, F. S. Hasoon, F. Abulfotuh, L. L. Kazmerski, *J. Vac. Sci. Technol. A Vacuum, Surfaces, Film.* **1995**, *13*, 2877–2883.

IV.5 Supporting information

IV.5.1 XRD pattern of annealed 200 nm-thick AZO layer annealed in an O_2 atmosphere at different temperatures

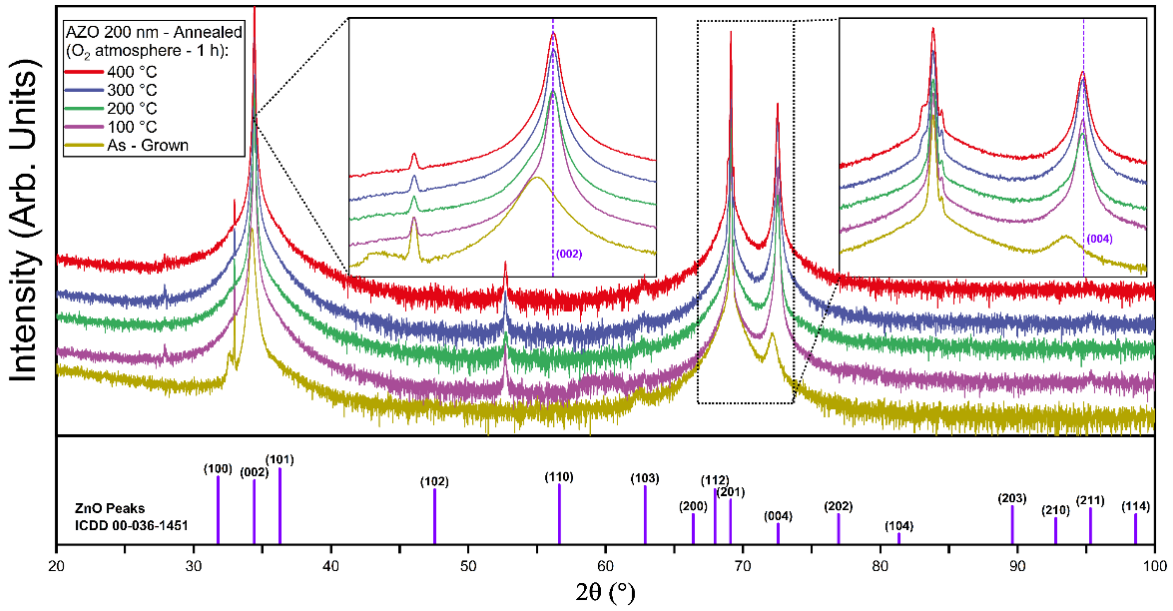

Figure SI-IV-1. XRD pattern of 200 nm-thick AZO layers annealed in an O_2 atmosphere for 1 h at different temperatures

IV.5.2 XRD pattern of ZnO nanowires grown on 200 nm-thick AZO layers

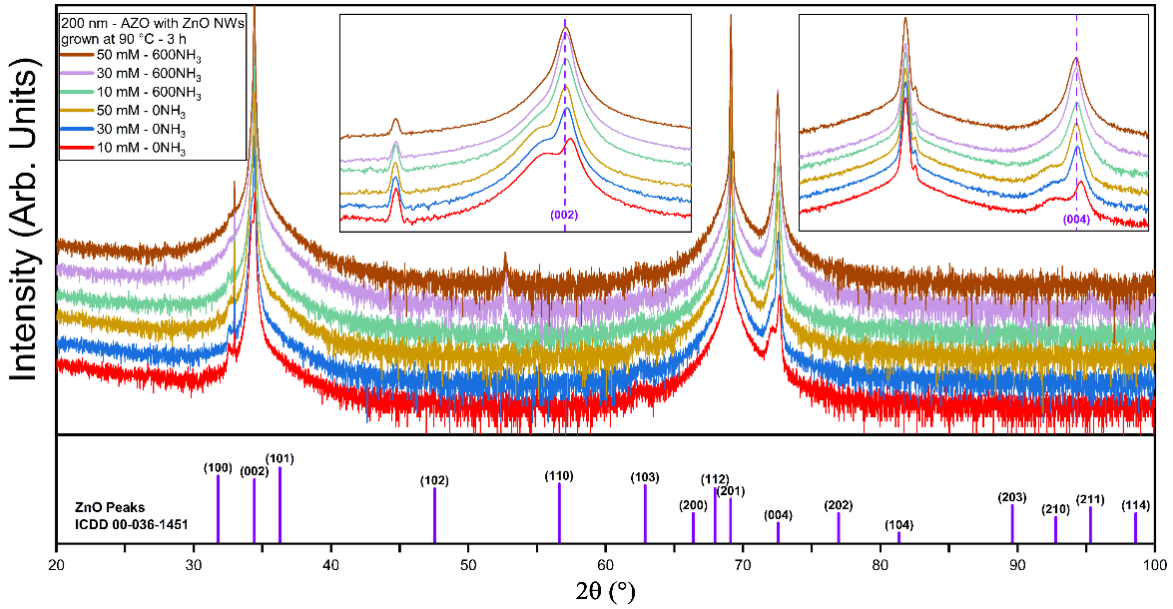

Figure SI-IV-2. XRD pattern of ZnO NWs grown on 200 nm-thick AZO layers with different concentrations in $Zn(NO_3)_2$, HMTA, and NH_3 in the chemical bath

IV.5.3 Morphology of ZnO NWs grown on annealed 200 nm-thick AZO layers

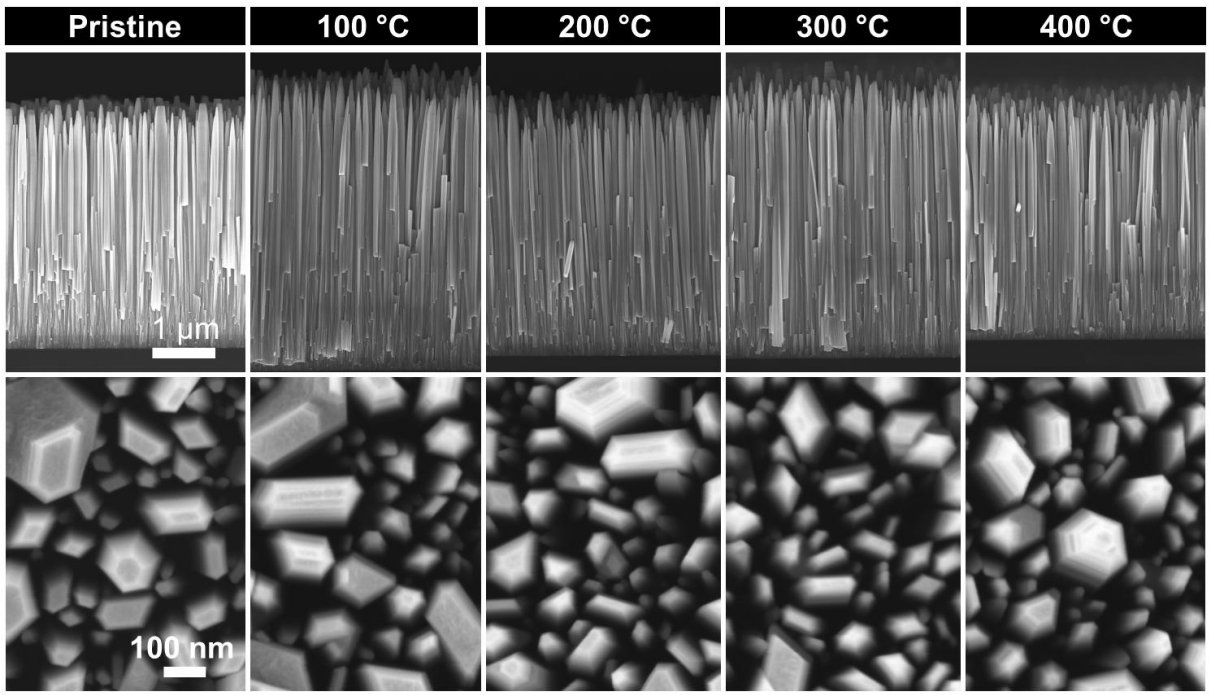

Figure SI-IV-3. ZnO NWs grown on 200 nm-thick AZO layers. The latter were annealed in an O_2 atmosphere for 1 h at 100, 200, 300, and 400 °C.

The page was intentionally left blank.

The page was intentionally left blank.

General conclusion and perspectives

This thesis, organized into four chapters, has discussed the motivation behind the research and the approaches developed to address a critical issue: the performance degradation of ZnO NW-based PNGs due to screening effects. In this work, since ZnO NWs were grown via the CBD method, they exhibit a high density of free electrons in their structure, leading to screening effects that severely deteriorate their piezoelectric properties. Therefore, this thesis explored three distinct methods designed to boost the overall performance of such PNGs.

In **Chapter I**, the theoretical background of piezoelectricity and an overview of piezoelectric materials have been provided. A focus is done on ZnO, an abundant, biocompatible, and low-cost material, which presents advantageous piezoelectric properties compared to other semiconductor materials. A detailed discussion of ZnO properties has described its spontaneous electrical polarization along its polar *c*-axis due to its wurtzite crystal structure, the formation of intrinsic point defects related only to Zn and O atoms, and the dependence of its electrical properties on the synthesis method used. Then, the dimensional advantages of ZnO for piezoelectric applications have been highlighted, justifying the choice of using ZnO NWs. The close relationship between the screening effect and the free electron density in ZnO has also been discussed. An analysis of NW-based PNGs has demonstrated the potential of ZnO for creating high-performance devices. The chosen PNG architecture has been justified due to its ease of fabrication, and suggestions for improving the performance of such a device have been provided. Finally, a detailed investigation of the growth of ZnO NWs by CBD has outlined methods to i) control the morphology of ZnO NWs via the SAG method or by defining the chemical bath conditions, and ii) modify the electrical properties of ZnO by intentional doping process with atoms other than Zn or O in the chemical bath. After introducing the context and problematic of the thesis, this first chapter concludes by outlining the objectives of the research.

Chapter II has explored the elaboration of electrically resistive ZnO NWs using compensatory Cu-doping and thermal annealing processes, followed by their integration into PNGs to evaluate their piezoelectric properties. First, $Cu(NO_3)_2$ and NH were used as additives in the chemical bath for the growth of ZnO NWs. The pH_0 level of the solution exceeding 10.6 has favored electrostatic interactions between the negatively-charged polar *c*-planes of ZnO

NWs and the positively-charged Cu(II) species in the bath, resulting in shorter and thicker ZnO NWs as the $[Cu]/[Zn]_{bath}$ ratio was increased in the solution from 0 to 10%, as FESEM images have depicted. An atomic $[Cu]/[Zn]_{NW}$ ratio around 20 – 100 ppm in the ZnO NWs was achieved with the increase of the $[Cu]/[Zn]_{bath}$ ratio up to 10%, as ICP-MS analysis have revealed. X-ray related techniques and Raman spectroscopy have demonstrated that the incorporation of Cu affects slightly the crystallographic quality of ZnO NWs. Surprisingly, XANES and XLD spectroscopy have shown that only 15-18% of the total amount of Cu in ZnO NWs substitutes for Zn sites, forming Cu_{Zn} defects. In addition, the density of Cu_{Zn} defects can be easily tuned by adjusting the concentration of Cu in the chemical bath. Two-point probe electrical measurements have reported the acceptor behavior of Cu_{Zn} defects in ZnO NWs, leading to higher resistivity. However, these electrical measurements have also suggested an influence of the pH_0 of the solution on the electrical properties of Cu-doped ZnO NWs. Furthermore, annealing the Cu-doped ZnO NWs in an O_2 atmosphere for 1h at 300, 500, and 800 °C further increased their resistivity. This increase was likely due to the migration of Cu atoms from the surface to the bulk of the NWs, potentially forming defect complexes involving Cu_{Zn} and V_{Zn} defects with unknown electrical and optical properties, as XPS, 5 K cathodoluminescence, XANES, and XLD spectroscopy have suggested. These findings highlight the need for additional DFT calculations, as well as studies of Positron Annihilation Lifetime and Doppler-broadening spectroscopy to understand the formation and properties of complex defects related to Cu_{Zn} and V_{Zn}. Finally, according to the previous studies, Cu-doped and thermally annealed ZnO NWs were integrated into PNGs, which have exhibited a notorious improvement of their generated output voltage, attributed to the reduction of free carriers in ZnO NWs through hole-electron pair recombination processes involving Cu_{Zn} defects, as well as the engineering of H- and N-related defects with thermal annealing. A study discussing the performance of PNGs based thermally annealed Cu-doped ZnO NWs would be interesting.

Chapter III has examined the modification of the surface properties of ZnO NWs by coating them with Al_2O_3 and parylene-C layers, and evaluated their piezoelectric properties through PNG characterizations. First, the thickness of the parylene-C layer was varied to assess its effect on the piezoelectric response of PNGs. Thus, four different PNGs were fabricated with 1.11, 1.98, 2.93, and 3.34 µm-thick parylene-C over the ZnO NW matrix, as FESEM and EDS images have confirmed. Interestingly, the embedding parylene-C layer did not induce mechanical stress on the ZnO NWs, but an apparent modification of their optical properties,

as Raman spectra have suggested. Then, as expected, thicker parylene-C layers have led to an increase in internal impedance of PNGs, suggesting that an adaptation of external loads could be necessary to characterize the PNGs in open-circuit. Piezoelectric characterizations have shown that the PNG with a 1.98 µm-thick parylene-C top layer generated the highest output signal, indicating that a layer of 2 µm-thick would provide an optimal balance between mechanical energy transfer and energy conversion efficiency. These findings can be complemented with theoretical calculations, bringing information about the mechanical and electrical properties of ZnO NW – parylene C composites, as explored for other polymers such as PMMA and PDMS. Furthermore, ZnO NWs were coated with amorphous Al_2O_3 shell layers with thicknesses of 1, 2, 5, and 10 nm by ALD at 300 °C. Characterization techniques such as XRD and Raman spectroscopy have reported a slight compression in ZnO NWs along their *c*-axis when coated with alumina shell layers, which can potentially modify spontaneous electrical polarization in these nanostructures. In addition, 5 K cathodoluminescence spectra have revealed an effective surface passivation of Al_2O_3-coated ZnO NWs, which exhibited a steady increase in the NBE/DLE ratio with the increment of the Al_2O_3 thickness up to 10 nm. These ZnO/Al_2O_3 core-shell heterostructures were subsequently integrated into PNGs. To discriminate the effects of the alumina coating from potential thermal effects that occurred during the ALD, a reference PNG with ZnO NWs was subjected to the same ALD conditions but without alumina deposition. Thus, piezoelectric characterizations have demonstrated that the use of a 5 nm-thick Al_2O_3 shell layer resulted in the best PNG performance, likely due to an optimal balance between surface passivation and the ability of the ZnO/Al_2O_3 heterostructures to deform under mechanical stress. Further studies could explore the surface properties of parylene-C-coated ZnO NWs. In addition, it would be valuable to investigate other heterostructures for piezoelectric applications, such as ZnO/Ga_2O_3, through DFT calculations and experiments, as there is limited information available in the literature on this topic.

Chapter IV has studied the synthesis of ZnO NWs on Au and AZO seed layers, aiming to create, respectively, Schottky and Ohmic interfaces with these NWs for piezoelectric applications. AZO layers were grown by sputtering with thicknesses of 100, 200, 300, and 400 nm on glass substrates, with perspectives in elaborating transparent PNGs. TLM measurements have revealed that the 200 nm-thick AZO layer depicts a lower resistivity than the other layers. Further thermal annealing in an O_2 atmosphere for 1h at 200 °C improved

the conductivity and transparency of the 200 nm-thick AZO layer, as optical measurements have reported. Then, the synthesis of ZnO NWs by CBD with different bath conditions on 200 nm-thick AZO layers resulted in a dense NW matrix, indicating a high density of nucleation sites in the AZO layer. Given the need for controlling the morphology of ZnO NWs for piezoelectric applications, the SAG method was investigated. Thus, distinct lithographic resins such as 2% PMMA, 4% PMMA, and UV5 of 90 nm-thick were used to pattern AZO layers by electron-beam lithography. These resins were found to solubilize in an alkaline chemical bath (high pH_0), resulting in ZnO NWs growing spontaneously on the AZO layer, as FESEM images have shown. To address the problems encountered with the chemical bath conditions, a hard 30 nm-thick SiO_2 resin was subsequently used. However, the results were identical to those of the previous resins. Therefore, additional research would be necessary to understand how lithographic resins behave in distinct chemical bath conditions, which should contribute to the successful and controlled growth of localized ZnO NWs. In addition, the fabrication and characterization of a transparent PNG based on ZnO NWs grown by SAG should be achieved. Moreover, 35 nm-thick Au layers were grown by vacuum evaporation with different deposition rates of 0.05, 0.1, 0.15, 0.25, and 0.5 nm/s. These layers were structured by a single layer of Au grains preferentially oriented along the [111] direction, as FESEM, AFM, and XRD studies have shown. After the growth of ZnO NWs by CBD, they displayed their best aspect ratio and verticality on Au layers deposited at rates of 0.25 and 0.5 nm/s, whose features are suitable for piezoelectric applications. Despite these promising findings, the morphology of ZnO NWs was found to be strongly dependent on the properties of Au layers. It suggests the need for controlling the reproducibility of morphological and structural properties of Au layers. Then, a PNG using an Au films as seed layer for ZnO NWs and as bottom electrode was fabricated. Piezoelectric characterizations have depicted the low generation of output voltage of such device due to the low density of integrated ZnO NWs. In addition, the PNG's piezoelectric response depends on the excitation area where a mechanical force is applied, revealing unexplored mechanical effects likely coming from the parylene-C layer. This phenomenon could be understood via mathematical calculations.

In conclusion, this thesis has outlined distinct approaches to enhance the performance of ZnO NW-based PNGs. Although additional studies could be required to optimize these methods, the technological processes developed in this work have potential for fabricating performant flexible and transparent PNGs. This opens up new perspectives and challenges for

the future of this topic. In addition, a new thesis will continue the current research by investigating the nanoscale effects of ZnO NWs with diameters around 20 nm on their piezoelectric properties. This upcoming work will be conducted in collaboration with the LMGP, LTM, CEA Leti, Institut Néel, and LGEF-Insa Lyon laboratories, and will be funded by the ANR as part of the IMINEM project.